STUDY OF PIEZO VIBRATION STRIKING TREATMENT FOR SURFACE ROUGHNESS AND TEXTURE MODIFICATION

By

Jisheng Chen

A DISSERTATION

Submitted to
Michigan State University
in partial fulfillment of the requirements
for the degree of

Mechanical Engineering – Doctor of Philosophy

2022

ABSTRACT

The functional performance and service life of engineering components strongly depend on the surface attributes, including surface finish, residual stress, and mechanical strength. Modifying surface attributes by mechanical surface treatment is an effective and economical way of improving the overall performance of engineering components and products. In this study, a novel mechanical surface treatment process, piezo vibration striking treatment (PVST), is proposed and realized by a piezo stack vibration device integrated into a CNC machine. Unlike existing mechanical surface treatments, PVST employs non-resonant mode tool vibration to strike the work surface, leading to better control of the induced surface plastic deformation and hence more efficient surface modification. First, the striking force, tool vibration displacement, and resulting surface deformation were investigated using four designed experiments, i.e., tool-surface approaching, single-spot striking, one-dimensional (1D) scan striking, and 2D scan striking experiments. The results demonstrate the feasibility and excellent controllability of PVST in terms of force and displacement correlation and surface deformation monitoring. Then, intrinsic surface roughness and texture produced by PVST were investigated by conducting PVST on mild steel and pure copper with an initially smooth surface ($Ra \sim 0.32$ μm). The dependency of the intrinsic roughness/texture on the process parameters was established. Finally, surface roughness/texture improvement by PVST on electron beam melted Ti6Al4V was investigated. It was found that the combined compression and sliding deformation under the negative engagement distance between the striking tool and work surface is most effective in reducing surface roughness (from 48.6 μm to 3.7 μm) and transforming surface texture from a scattered pattern to a uniform pattern. This study shows the promising potential of PVST in the post-processing of additively manufactured metal parts.

ACKNOWLEDGEMENTS

I would like to express my gratitude to many people who supported, inspired, and encouraged me in my life, especially for this dissertation and my Ph.D. study, all along the way.

Foremost, my greatest gratitude shall be paid to my advisor, Dr. Yang Guo. It is my great fortune to study and work under his persistent support, extraordinary guidance, and caring. I would like to express my most sincere appreciation to my Ph.D. committee members, Dr. Patrick Kwon, Dr. Thomas Bieler, and Dr. Firas Khasawneh, for their valuable feedback on the research work that has helped improve the overall quality of this work. I am extremely grateful to have this opportunity to work with each of you. Not only did your intelligence and expertise provide invaluable advice and significantly impact me, but your diligence, work ethic, and personal characteristics also inspired me to move forward.

Besides, great appreciation shall be expressed to all the lab peers: Juan Sandoval, Dr. Ryan Khawarizmi, Amr Saleh, Bibek Poudel, Tyler Bauder, Hawke Suen, Jack Song, Dr. Dinh Nguyen, Dr. Melih Yesili, Aaqib Ali, Max Chumley, Yang Xu, Tyler Johnson, Jianxin Zhao, Aaron O'Neil, Beytullah Aydogan, Jonathan Daman and Mike Koschmider from the ME Machine Shop, and many others that I cannot mention them all. Also, I would like to thank Jian Tang, Ming Liu, Zinan Wang, Ye Ma, Haosu Cong, Haining Du, Jiawei Lu, Tianhong Ying, Chacha Feng, Yao Xu, Guolin Yao, Fengbo Pei, Lu Gao, Su Pang, Xin Ma, Richard and Amy, Lori Leu and Bart, for the friendship we had developed over the past few years, thoughtful suggestions and selfless support for my life and study in the U.S.

Last but not least, my deepest gratitude goes to my beloved family. Thanks to my beloved parents and parents-in-law for their unreserved support and understanding throughout this endeavor. I know that this is a proud moment for them as well. Thanks to my darling and wise wife, Shengfang Song, for keeping me motivated throughout the tough years by providing stability and happiness. I want to share my happiness with them.

Time flies with a changing world, but my passion for life and Spartan Wills will not. Go Green!

TABLE OF CONTENTS

CHAPTER 1 INTRODUCTION 1

CHAPTER 2 BACKGROUND 10

CHAPTER 3 PIEZO VIBRATION STRIKING TREATMENT AND EXPERIMENTS . . 21

CHAPTER 4 CHARACTERIZATION OF PIEZO VIBRATION STRIKING TREATMENT 36

CHAPTER 5 PIEZO VIBRATION STRIKING TREATMENT ON MACHINED SURFACE 77

CHAPTER 6 PIEZO VIBRATION STRIKING TREATMENT ON ADDITIVELY MANUFACTURED SURFACE 102

CHAPTER 7 CONCLUSIONS AND FUTURE WORK 152

BIBLIOGRAPHY 154

CHAPTER 1

INTRODUCTION

Because friction, wear, corrosion, and fatigue usually occur or initiate on the surface, the functional performance and service life of metallic engineering components are very much dependent on their surface attributes, such as surface roughness, hardness, microstructure, and residual stresses [1]. Modifying these surface attributes is an effective and economical way of improving the overall performance of engineering components and products. Typically, surface treatment is applied at the end of the manufacturing process to remove defects or improve the components' mechanical properties, such as smoothing after machining or heat treatment after additive manufacturing. There are various surface treatments corresponding to the different manufacturing processes. Therefore, selection of surface treatment highly depends on the manufacturing process.

1.1 Classification of metal surface treatment

Common metal surface treatments can be generally divided into four categories. The first category of surface treatment is the material removal process, i.e., milling, drilling, and turning in machining. Machining is typically used as a pre-processing to machine the raw material to a size very close to the target geometry [2]. It can produce parts with tight tolerances and fine details from an extensive range of metals. However, the parts often come off milling and turning machines with visible tool marks. They need to be further smoothed or polished to improve their surface quality and visual appearance by reducing their surface roughness [3]. The process can also introduce tensile residual stress that decreases the fatigue life.

The second category of surface treatment is adding a protective layer to the surface of the workpiece to enhance its surface attributes by chemical, physical, or electrochemical methods. The typical processes in this category include electrophoresis deposition [4], electroplating [5], powder coating [6], anodizing [7], and physical vapor deposition [8], etc. The protective layers in these processes can enhance wear or corrosion resistance, impact resistance, and hardness of the parts' surface [6]. The coating can also add color and different high-gloss matte to increase the product's aesthetic appearance with good dimensional control, which are broadly applied in daily furniture, automobiles, and pipeline transportation industries. Nevertheless, these methods have limitations. Anodizing is only compatible with non-ferrous metals or their alloys. Powder coating is not easily applied to internal surfaces and is unsuitable for small components. Electroplating has a high risk of environmental pollution due to chemical solutions.

Abrasive treatment is another surface treatment that depends on the repeat interaction between the workpiece's surface and some flexible tools or abrasive medium to remove those rough surface features, including abrasive machining [9], polishing [10], electropolishing[11], grinding [12], and superfinishing [13]. Electrolytic polishing has the advantages of good gloss quality, high efficiency, low cost, increased corrosion resistance of the workpiece surface, and is suitable for all stainless-steel materials. Superfinishing, such as shape adaptive grinding, continuously processed polishing, elastic emission machining, and magnetic-field assisted finishing, can finish surfaces to a nano-scale level and accommodate surface finishing of 3D freeform surfaces [14], enabling the parts to be applied in the manufacture of precision instruments. Nonetheless, many influencing parameters in electropolishing make it challenging to find the correct parameters. Additional attention to safe operation is needed when using the complex composition of the electrolyte. The superfinishing methods require the initial surface finish of the workpiece to be at a specific level (slight surface roughness). Otherwise, the treatment cannot be successfully implemented. Also, it takes a long processing time to reach the nano-level precision and does not improve mechanical properties except the surface finish.

Lastly, another common method to modify surface attributes is by surface plastic deformation imposed by striking the surface with hard tool indenters. This has long been utilized in surface mechanical treatments which are usually applied at the end of the manufacturing process to reduce the unfavorable effects, such as stress concentration after welding, pores defect and rough surfaces after casting in turbo blast, engine block and cylinder head production [15], and scaling effect after steel products manufacturing (i.e., strips, plates, sheets, wires). The surface treatments can be leveraged to resist fatigue fracture, abrasive wear, fretting fatigue, and stress corrosion [16].

Although the first three surface treatment methods mentioned above have advantages, disadvantages, and applications, they cannot improve the workpiece surface roughness and material properties simultaneously compared with the fourth plastic deformation treatment method. In addition, the second category requires relatively complex process equipment and procedures, such as various electrochemical solutions and equipment, which have certain limitations. Therefore, this dissertation mainly focuses on surface treatment methods through plastic deformation and explores their potential to improve workpiece properties.

1.2 Striking-based surface treatment in conventional manufacturing

In conventional manufacturing, the most notable example of striking-based surface treatments is shot peening (SP) [17, 18, 19, 20, 21, 22, 23, 24]. In SP, a myriad of small hard balls made of steel or ceramic are impacted onto the surface by compressed air, resulting in randomly distributed strikes on the targeted surface. The process generates compressive residual stresses on the surface, thereby improving the fatigue strength of critical components and the overall fatigue life of a structure [25, 26].

Surface mechanical attrition treatment (SMAT) is another striking-based surface modification process [27]. In SMAT, hard steel balls (used as tool indenters) and the workpiece are all confined to a vibrating chamber. The workpiece is fixed within the chamber while the steel balls are free to bounce between the workpiece surface and the chamber walls, leading to repeated strikes on the workpiece surface. This process induces severe plastic deformation, transforming the surfaces into a nanocrystalline microstructure [28, 29, 30, 31, 32, 33, 34].

Alternatively, surface striking can also be realized while controlling the striking location by a single vibrating tool indenter(s) driven by either a pneumatic or ultrasonic actuator. This is demonstrated by high frequency mechanical impact (HFMI) treatment, mainly utilized to treat weld joints [35]. The HFMI equipment is usually a hand-held impact device connecting to an external power source. This enables the treatment to be carried out manually for weldments of large sizes or complex geometries. The impact device is usually directed to strike the weld toe to modify its geometry, induce compressive residual stress, and close subsurface micro-cracks, significantly enhancing the fatigue strength of the weld joints [36, 37, 38, 39, 40, 41, 42].

While treating the weld joints manually with hand-held equipment is possible, manual operation generally is not ideal for treating component surfaces. Machine hammer peening (MHP) treatment [43, 44] and ultrasonic nanocrystal surface modification (UNSM) treatment [45, 46, 47, 48, 49] are examples of such devices integrated into a computer numerical control (CNC) machine or robotic arm. MHP has been shown to effectively reduce surface roughness and increase surface hardness for machined molds and dies [50, 51]. As indicated by its name, UNSM employs ultrasonic tool vibration, which enables generating nanocrystalline surfaces and improving tribological and fatigue properties [45, 52].

1.3 Striking-based surface treatment in additive manufacturing

In metal additive manufacturing (AM), metallic parts are produced layer-by-layer using either local melting/solidification or sintering of materials, as opposed to traditional subtractive manufacturing. The increasing adaptation of AM components offers a novel extended design freedom for innovative engineering components and applications, especially in the biomedical, aircraft, and aerospace industries. AM can produce parts of intricate and complex geometries directly from 3D CAD models and offer a short lead time as a novel manufacturing technique.

The wide application of AM metal parts, however, is limited by the well-known disadvantages related to the poor mechanical integrity which emanates from the part surface, such as poor surface finish, undesirable residual stress, and volumetric defects that are intrinsic to the underlying process (lack of fusion, unmelted particles, gas porosities, micro-cracks, etc.) [53]. These defects can deteriorate the mechanical properties of AM parts, especially reducing fatigue performance. One common way of addressing these issues is to remove the bad surface layer by machining. However, this will require the AM parts to be built larger than their original design to accommodate the extra material to be removed subsequently by machining. This results in not only longer build time but also a waste of materials in the AM process. Moreover, the issue of residual stresses and subsurface pores cannot be entirely addressed by machining. In contrast, the mechanical surface treatment uses plastic deformation rather than material removal to improve surface finish, so the part does not need to be built oversized. This could lead to cost savings in both build time and materials. More importantly, the mechanical surface treatment will be more effective in generating compressive surface residual stresses, strengthening the surface by strain hardening, and possibly closing and healing the pores beneath the surface, all of which will significantly benefit the mechanical integrity together with better surface finish and improved fatigue life of AM parts.

In recent years, various mechanical surface treatments, including striking-free and striking-based methods, have been applied to AM metal parts. Striking-free surface treatments are dependent on sliding friction and compression between the tool and workpiece and apply severe plastic deformation on the treated surface, such as burnishing [54, 55, 56], where a half-spherical indenter applies compression on a rotating workpiece and deep rolling [57] in which the deep rolling pressure is applied to rolling balls that follow a milling-like kinematic process (the tool rotates and the machining is performed by a linear movement along the machining axis). Sumair Sunny et al. [58] utilized a hybrid AM process that combines laser-based powder bed fusion and interlayer burnishing to investigate the effects of microstructure and inherent (imposed) stress on the residual stress. The resulting microstructure has an anisotropic distribution of residual stress along the treated surface, as shown in Fig. 1.1.

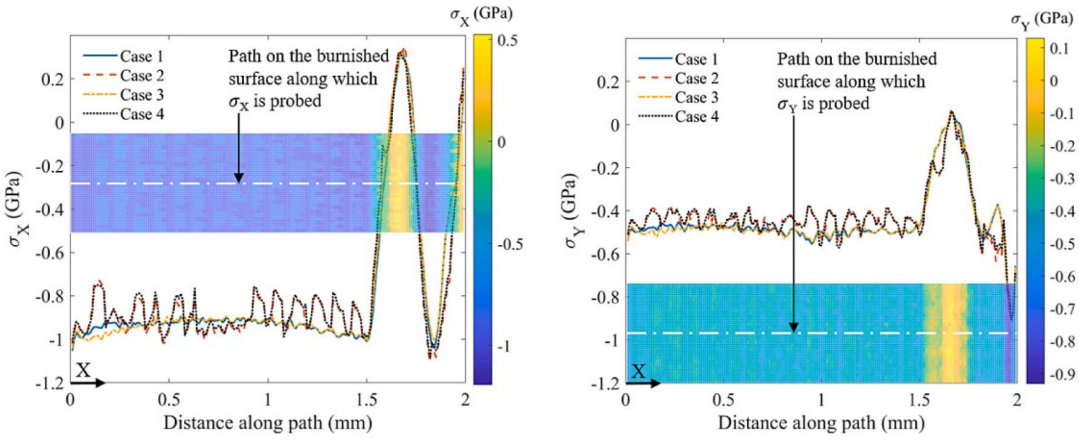

(a)

(b)

Figure 1.1 Anisotropic residual stress distribution: (a) the rolling direction (X), and (b) the axial direction (Y), along the surface of the subset [58].

In contrast, the influence of the inherent stress on the residual stress is less significant than the microstructure. Daniel Meyer et al. [59] reported that deep rolling can also be integrated into the build process of Selective Laser Melting (SLM). The interlayer interaction between deep rolling and layer deposition provides the potential to generate material-internal reinforced domains. In contrast to striking-free surface treatment, striking-based surface treatments rely on continuous dynamic impact from the tool or the shots to deform the surface material and improve the surface quality, such as SP, SMAT, HFMI, and UNSM mentioned above. Researchers utilized SP to post-process 17-4 stainless steel components fabricated by direct metal laser sintering [60], and AlSi10Mg [61] and Ti6Al4V [62] parts manufactured by SLM. The results revealed that SP induces more favorable roughness, compressive yield strength, and fatigue resistance. SMAT was performed on 316L stainless steel parts made by laser powder bed fusion [63] and Ti6Al4V ELI medical components produced by SLM [64] to introduce a nanostructured layer and improve fatigue performance. As reported in [65], hand-held HFMI was applied with directed energy deposition (DED) to enhance the fatigue life of in-situ processing Inconel 718. The results demonstrated that the hybrid AM process can produce metallic parts with refined microstructure and favorable compressive residual stress. Zhang et al. [66] and Kim et al. [67] employed UNSM to process Ti64 and AISI 316L parts by DED. It was found that UNSM resulted in a better surface finish, lower subsurface porosity, and a high magnitude of compressive residual stress, enhancing fatigue properties.

1.4 Drawbacks of current striking-based surface treatments

It is seen that the applications of current striking-based surface treatments show great potential in both conventional subtractive manufacturing and novel additive manufacturing. However, their intrinsic characteristics might limit a broader range of applications.

In SP and SMAT, the surface is struck by numerous free indenters whose kinematics are not directly controlled. The striking location, striking angle, and striking force associated with each indenter are random variables to a large extent. Therefore, the accumulated effect from these strikes is stochastic, making it difficult to control the treatment quantitatively. Since the exact locations of these random strikes cannot be strictly controlled, these processes suffer from poor reliability.

In addition, from the process control point of view, the main advantage of MHP and UNSM is that the scanning path of the vibrating tool over the surface can be precisely controlled by the CNC machine, which implies that the strikes on the surface can be much better controlled compared to SP, SMAT, and HFMI. While a CNC machine enables more precise positioning of the strikes, the control of each strike still depends on the striking device. In MHP, the striking device can be pneumatically or ultrasonically driven [36, 44, 68]. The indenter held in the front of the device is usually not rigidly connected to the actuator. When the actuator repeatedly impacts the indenter, the relative motion between the indenter and actuator cannot be strictly controlled. Therefore, the impact on the surface may be only energy controlled, similar to SP but cannot be delivered in consistent intensity [41].

In UNSM, the motion of the indenter is entirely driven by the rigidly connected ultrasonic actuator, leading to more uniform strikes on the surface [45]. However, ultrasonic vibration depends on the resonance of the vibrating structure, and thus its frequency and amplitude cannot be controlled [69]. Technically, the vibration displacement and the striking force are difficult to measure in the ultrasonic frequency regime. This makes it difficult to monitor or control surface deformation imposed by each individual strike, and the overall surface deformation resulting from the treatment cannot be quantitatively controlled. Note that imposing controllable surface deformation is a critical step toward understanding and controlling the modified surface attributes [70].

1.5 Research objective

The applications of current striking-based surface treatments in conventional and emerging additive manufacturing industries have great potential for using these techniques in a variety of products. However, randomness, high variability, and irregularity in current striking-based surface treatments make it difficult to precisely and quantitatively control the surface deformation of the treated components. This probably degrades the enhancement effect of surface quality and fatigue performance of the AM parts when these treatments are utilized as post-processing after additive manufacturing.

Unlike SP, SMAT, HFMI, and UNSM, piezo vibration striking treatment (PVST) is a novel striking-based mechanical surface treatment process realized by a piezo stack actuated vibration device integrated onto a CNC machine to exert tool strikes on the surface. Compared with ultrasonic vibration, the non-resonant mode piezo vibration is more convenient for controlling the process, as demonstrated in previous applications in modulation-assisted turning and drilling processes [71, 72, 73]. The non-resonant piezo vibration often has a lower vibration frequency but can achieve a higher vibration amplitude (up to 200 μm stroke piezo stack is commercially available). The frequency and amplitude can be independently controlled with the piezo stack actuation. Monitoring the displacement and striking force within each vibration cycle is also possible. The integration with CNC machines allows the PVST to precisely control the strike locations and scan paths, which can automate the treatment process and enhance operation efficiency. These characteristics make PVST more suitable for imposing controlled strikes and deformation on the surface.

This has motivated the present study. In this dissertation, an experimental setup for carrying out piezo vibration striking treatment was developed using a piezo stack actuated vibration device and a CNC milling center. The striking force, tool displacement, and surface topography were experimentally investigated by applying PVST on the surfaces with different initial states of different materials.

The objective of this research is to induce strikes with consistent intensity in each cycle of tool vibration, precisely control the striking intensity and striking location in the process, and identify the relationships between force and surface deformation for better monitoring surface deformation in real time based on force signals through PVST, all of which have not been realized in current striking-based surface treatments discussed above. Based on these results, promising opportunities for realizing more advanced control of surface striking treatment are envisaged.

1.6 Dissertation structure

This complete dissertation is organized as follows.

Chapter 2 surveys the current striking-based surface treatments and their applications in conventional and additive manufacturing fields and compares their advantages and disadvantages.

Chapter 3 proposes piezo vibration striking treatment for addressing the issues associated with current striking-based surface treatments. The design details and functional components of the device assembly are included. Experimental conditions, calibration of the PVST device assembly, and measurement methods are also involved.

Chapter 4 introduces the characterization of piezo vibration striking treatment using mild steel and OFHC copper samples. Striking force, vibration displacement, indentation size, surface deformation, and sliding force during the PVST process are explored in tool-surface approaching, single-spot vibration striking, and 1D scan vibration striking experiments, as well as their correlations.

Chapter 5 illustrates the application of the PVST on the mild steel and OFHC copper workpieces with an initially smooth surface to perform the tool scan in two directions. The resultant surface texture and roughness parameters are investigated under various PVST experimental settings involving changing overlap ratio, scan speed, driving voltage, tool diameter, and workpiece material. The results and correlations achieved in this chapter can provide a reference and basis for comparing the results obtained on the initially rough surface in Chapter 6.

Chapter 6 aims to investigate how to efficiently utilize PVST to improve the rough surface finish of AM metal parts (Ti-6Al-4V). The main goal is to reduce the Sa value to around 1 μm level using PVST, which can be effectively finished with further post-processing. The effects of the critical process parameters are explored to achieve this goal efficiently.

Finally, **Chapter 7** provides conclusions of the proposed research and recommendations for future study.

CHAPTER 2

BACKGROUND

Several striking-based surface mechanical treatment techniques have been developed in the past few decades based on various product requirements. This chapter mainly describes the application of these striking-based surface mechanical treatment methods and compares their advantages and disadvantages.

2.1 Shot peening

The most notable example of striking-based surface treatment is conventional shot peening [19, 20, 21]. SP is a well-established mechanical surface treatment mainly aiming to improve metallic components' fatigue life. In this process, hard spherical shots, typically made of steel or ceramic, are accelerated using pressurized airflow and directed at the target surface at high velocities. This mechanism results in randomly distributed strikes covering the surface area to be treated, hence inducing work hardening and residual stress redistribution on the targeted surface. Because of the continuous striking effect, the outer layers of the component experience an in-plane stretching plastic deformation while the elastic sub-surface tries to recover and maintain its original shape. This interaction generates compressive residual stress on the surface. The induced favorable compressive residual stresses in the surface enhance the treated components' hardness, yield stress, and high cycle fatigue performance. Thanks to this benefit, SP has been widely used in many manufacturing sectors, such as aerospace [22, 23, 24], automobile [74], ship manufacturing industries [75, 76], and critical engineering component manufacturing (gears and shafts).

Nevertheless, the SP process needs to be carefully controlled since it may lead to over-peening induced by high-velocity impacts, significant impact energy, and excessive exposure durations. The free shots introduce a lot of randomness and uncertainty, making it challenging to realize precise control in the SP process. The characteristic of single-directional (usually 90°) impacts with a narrow velocity distribution (as shown in Fig. 2.1) in the SP process is closely related to these drawbacks [77]. If the process is not well controlled, these drawbacks will induce harmful surface defects, i.e., overlaps, scales, non-uniform striking depth, and non-uniform material behavior throughout the surface [30].

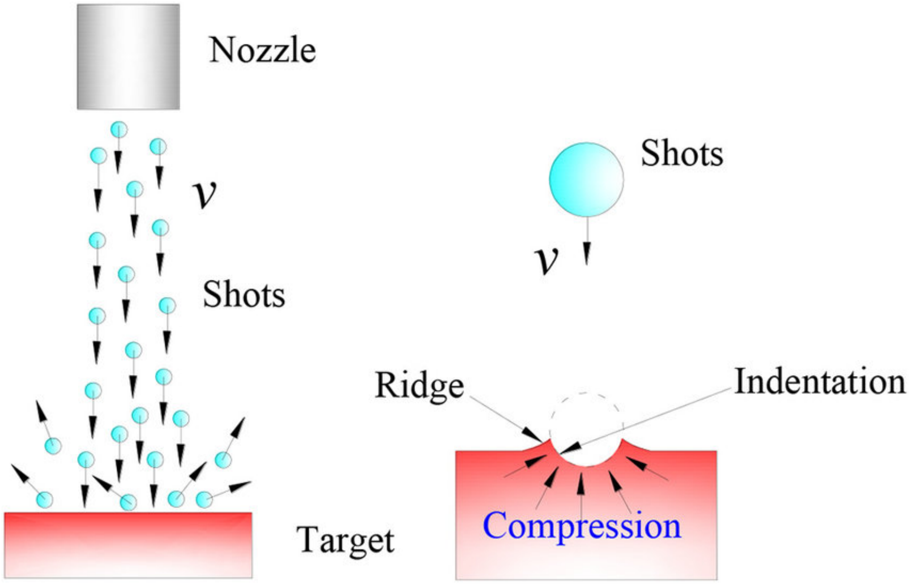

Figure 2.1 Schematic diagram of shot peening [78].

2.2 Surface mechanical attrition treatment

SMAT (including ultrasonic shot peening) is another surface modification process first proposed by K. Lu et al. in 2004 [27], involving surface striking with many steel balls as the tool indenters. Unlike SP, the loose steel balls and the fixed workpiece are all contained inside a closed chamber which is actuated to vibrate at high frequencies. The chamber vibration provides the kinematic energy for the steel balls to bounce between the workpiece surface and chamber walls, resulting in the repeated strikes on the workpiece surface. SMAT is mainly designed to induce large plastic strains on the workpiece surfaces, to generate nanostructured surfaces which possess superior strength and wear resistance [27, 77], or to process the novel gradient nano-grained materials which exhibit great potential in overcoming the strength-ductility tradeoff in conventional metals [31, 79, 80]. Compared to SP, SMAT induces a better surface quality resulting from more efficient shots and multi-directional low-speed impacts with a more extensive velocity distribution (as shown in Fig. 2.2).

Thomas Rousseau et al. [32] showed better control in SMAT over SP by investigating the effect of the number of shots used on the treated surface. The results showed that the number of shots strongly affected the number of impacts, impact depth distribution, and compressive residual

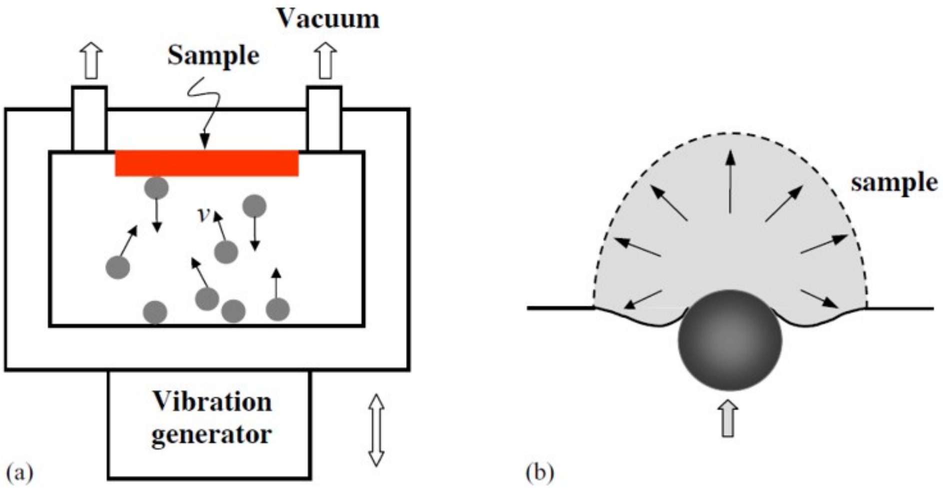

Figure 2.2 Schematic of surface mechanical attrition treatment [27]: (a) shots and sample confined in a close chamber actuated at high-frequency; (b) interaction between shots and sample.

stress distribution. S. Manchoul et al. [81] developed two 3D multi-impact models to simulate SP and SMAT processes and compare the effect of different treatments on the high-cycle fatigue strength of peened targets. The results indicated that both treatments exhibit great potential to enhance the high-cycle fatigue strength, but the fatigue performance improvement is more evident in SMAT. In the results reported by [27, 30, 33, 34], SMAT generated a deeper treated surface area of compressive residual stress and lower surface roughness than SP. Spherical balls with smooth surfaces are necessary for obtaining a nanostructured surface layer in SMAT compared to the balls with rough surfaces in SP since the rough surfaces might wear and damage the nanostructured surface layer during the treatment.

Despite better surface roughness achieved in SMAT compared to SP, the rough surface generated by the repeated impacts of the shots still exists and is a potential drawback in SMAT [82]. Experimental results suggested that the surface morphology of the treated components can be affected by processing time and shot diameter in SMAT. If they are not well controlled (i.e., overpeening, very high velocities), they likely degrade the beneficial effects of a nanocrystalline surface microstructure and induce stress concentration at specific points. This negative effect will facilitate crack initiation under fatigue conditions [83, 84, 85]. Accordingly, the surface morphology of the treated components should be predicted and controlled, and some optimization precautions must be performed to avoid unfavorable cases in SMAT [86]. Nevertheless, the intrinsic characteristic (randomness and uncertainty) of free indenters still needs to be eliminated during the process.

2.3 High frequency mechanical impact

In both SP and SMAT, the surface is struck by many free indenters where the kinematics of each indenter is not directly controlled. The striking location and orientation and the striking energy associated with each indenter are random variables to some extent. Therefore, the outcomes of these processes are stochastic. The proper evaluation of the outcomes should involve statistical methods.

In contrast to employing many free indenters, surface striking can also be realized by a single vibration tool that is directly driven by an ultrasonic or pneumatic actuator [87, 88], as shown in Fig. 2.3. This can be demonstrated by the post-welding treatment process commonly referred to as high-frequency mechanical impact [38]. This technique was first proposed by Northern Scientific and Technological Foundation in Severodvinsk, Russia, in association with Paton Welding Institute in Kyiv, Ukraine [38]. The International Institute of Welding has adopted HFMI as a generic name in which various technologies are typically associated with specific equipment manufacturers and service providers [42]. For all the HFMI techniques, the working principle is identical: cylindrical indenters are accelerated against a component or structure with high frequency (> 90 Hz). The cylindrical indenters are usually made of high-strength steel, customized by the manufacturers with different diameters (typically 2 – 8 mm), tip geometries, or indenter configurations (single or multiple).

HFMI techniques can be roughly classified as ultrasonic-based and pneumatic-based treatments, according to the summary by Yildirim [38]. Ultrasonic-based devices are named Ultrasonic Impact Treatment (UIT), Ultrasonic Peening (UP), Ultrasonic Peening Treatment (UPT), and Ultrasonic Needle Peening (UNP) and pneumatic-based devices are named High-frequency Impact Mechanical Treatment (HiFIT) and Pneumatic Impact Treatment (PIT). Among these devices, the frequencies are around 80 – 120 Hz for pneumatic-based devices and 20 – 30 kHz for ultrasonic-based devices with transducers at 200 – 300 Hz [90]. In HFMI, the vibrating indenter is mainly used to strike the

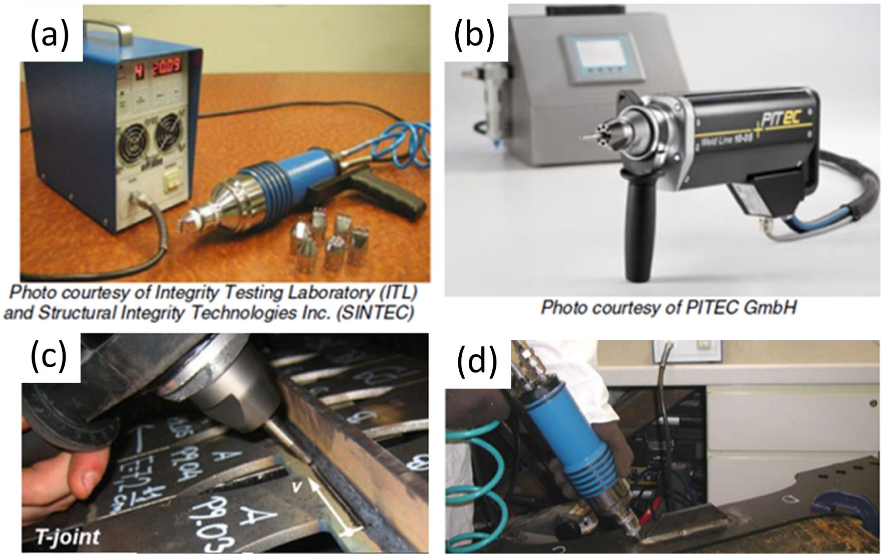

Photo courtesy of Integrity Testing Laboratory (ITL) and Structural Integrity Technologies Inc. (SINTEC)

Photo courtesy of PITEC GmbH

Figure 2.3 HFMI devices and application [87, 88, 89]: (a) ultrasonic device; (b) pneumatic device; (c) - (d) applications of hand-held HFMI in post-welding.

weld toe (i.e., the junction of the weld face and base material) to plastically deform it to a smoother profile which forms a groove after treatment, as shown in Fig. 2.3c and 2.3d. The treatment will significantly reduce the stress concentration and prevent crack initiation at the weld toe [38, 87, 88]. HFMI equipment is often hand-held and portable [39, 40, 87], so the treatment can be carried out manually for weldments of large sizes or complex geometries. Therefore, the treatment is quite effective in improving the fatigue life of welded joints [35, 87, 88, 91, 92]. Furthermore, researchers have related the groove depth or width to the fatigue life of the treatment components, which can be used as indicators for quality control in HFMI. Gary Marquis et al. [93] provided a guideline in the welding industry for qualitative and quantitative quality control in HFMI. Visual inspection can be regarded as qualitative control to evaluate the quality of the groove, where the grooves must be smooth, shiny, and continuous with no breaks. For quantitative control, the groove width and depth can be measured and used to evaluate the quality of the treatment. Rana Tehrani Yekta et al. [94] investigated the fatigue tests of welding steel components subjected to UIT at various levels (proper treatment, under-treatment, and over-treatment). The results indicated that the fatigue performance of the specimens was related to local residual stresses and the groove depth. Yanyan Feng et al. [95] studied the influence of surface topography and needle size on the surface quality after UPT. It was revealed that the dimension of the surface topography and the size of the peening needle played significant roles in forming the fold defects. The groove depth determined the dimension of fold defects in which the formation and dimension greatly influenced the surface quality and fatigue life of samples. The larger the depth, the longer the fold defects, and the deeper the fold defects layer.

The potential of HFMI has been recognized in the welding industry, but its hand-held feature limits a broader range of applications. The hand-held equipment in HFMI is unsuitable for the general treatment of component surfaces. The manual operation is time-consuming, resulting in high variability in the treatment results. Also, the intensive impacts from the vibrational devices will generate high amounts of noise and vibrations, which are transmitted to the operators' hands, making it challenging for them to apply a constant and correct angle or direction on the components for a particular time. The high amounts of noise is possible to damage the auditory system of the operators. These drawbacks weaken the repeatability and consistency of the process. If the striking tools are directed excessively at one specific location, the resulting plastic deformation of the metal can result in a crack-like feature. More importantly, dynamic energy generated by ultrasonic vibration is so powerful that the mechanical vibration transmitted to the impact pin is irregular and unstable. These characteristics probably roughen the surface and lead to the non-uniform distribution of compressive residual stress, which violates the goal of HFMI to generate smoother weld toe profiles and better fatigue performance.

2.4 Ultrasonic nanocrystal surface modification

The striking process can be implemented on a CNC machine to enable general surface treatment by a single vibrating tool and overcome the disadvantage of hand-held mode. The advantages of such a configuration are apparent. It not only eliminates the randomness and handling of loose shots or indenters but also dramatically enhances the controllability and repeatability of the treatment process. The indenter's striking locations and tool path can be defined a priori and then precisely controlled by the CNC machine. This controllability makes it possible to achieve both uniform and locally tailored/varied treatments on the workpiece surface and with a greatly enhanced process repeatability. This configuration has been used in UNSM, which employs an ultrasonic vibrating tool integrated into a CNC platform to treat the workpiece surface, as illustrated in Fig. 2.4.

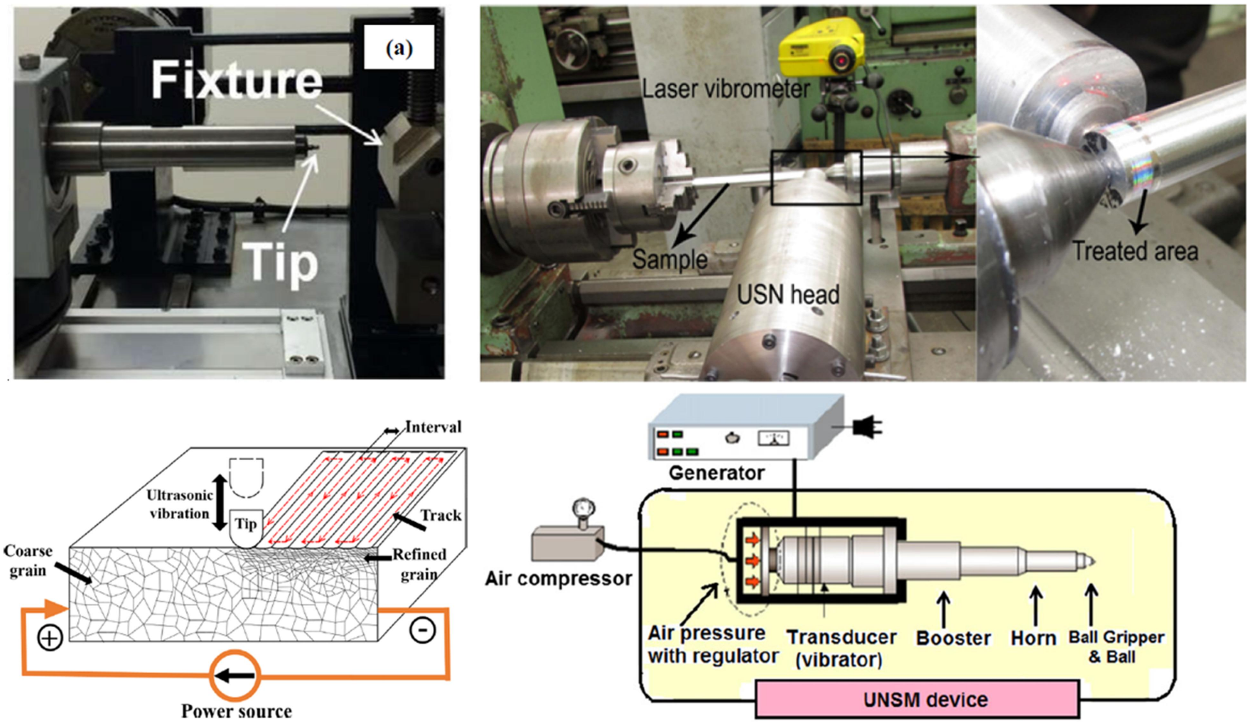

Figure 2.4 Schematic and devices of ultrasonic nanocrystal surface modification [47, 49, 96, 97]. Upper: vibration tool integrated into CNC machine; lower: mechanism of UNSM.

A. Amanov et al. [52] employed UNSM to make micro-dimples and explored their effect on the tribological characteristics of the treated workpieces. The results suggested that the friction coefficient of the UNSM-treated surface was reduced by about 25% compared to the ground surface and the wear volume loss decreased by 60%, which was a significant improvement in the tribological properties of mating surfaces. Chi Ma et al. [96] reported that the surface finish of 3D-printed AlSi10Mg alloy aluminum components decreased from 18 μm to 3.5 μm after UNSM treatment. Chang Ye et al. [98] studied the effects of UNSM on residual stress, microstructure changes, and mechanical performances of 304 steel. UNSM led to surface nanocrystallization and a high magnitude of compressive residual stress, strength, and ductility. In the work of Micheal Kattoura et al. [99], UNSM was used to improve the fatigue life of ATI 718 Plus. The nano-sized crystallites and high dislocation density in near-surface regions after USNM treatment improved the surface hardness, endurance limit, and crack propagation rates. Min-seob Kim et al. [100] investigated the variations in the metallurgical and mechanical performances of Directed Energy Deposition M4 components as treated by UNSM. The M4 austenite was transformed into martensite after the

UNSM treatment. The grain size, wear rate, and surface roughness decreased by 25.8%, 85.7%, and 88.3%, respectively.

While UNSM [52, 96, 98, 99, 100] generates nanostructured surfaces and improves the tribological and fatigue properties for a broad range of materials, the control of the treatment results, however, remains still empirical. The benefits of combining a single vibration tool with CNC motion control capability have yet to be realized. This is mainly because using ultrasonic vibration creates difficulties in controlling each strike during the treatment process. Firstly, ultrasonic vibration depends on the resonances of the vibrating mechanical structure; therefore, its frequency and amplitude cannot be conveniently varied and controlled. Secondly, the interaction of the ultrasonic vibrating tool with the workpiece surface is dynamically complicated. It has been shown that the strikes or impacts on the workpiece surface imposed by an ultrasonic vibrating tool are of varying magnitude, leading to primarily larger and secondary smaller impacts [41, 101, 102, 103]. The primary impacts occur at a much lower frequency f (e.g., 100 – 3000 Hz) than the vibrating tool ultrasonic frequency f_u (see Table 2.1), which results in various vibration amplitudes (A). Fig. 2.5a and 2.5b show the force distribution in HFMI. As shown in Fig. 2.5a, a primary impact followed by several irregular secondary impacts can be observed during the treatment process. Although the forces are significantly smoothed by filtering, irregular and unstable characteristics still exist. Fig. 2.5b also shows the comparison of force under different striking conditions, both of which consist of the primary strikes and secondary strikes. In Fig. 2.5c, the nonuniform force distribution in UIP is similar to those in Fig. 2.5a and 2.5b. As shown in Fig. 2.5d, the author theoretically divided the impact cycle into a period of several primary impacts (due to ultrasonic vibration) followed by a period of several secondary impacts to simplify the analysis. Thirdly, the tool displacement and striking force measurements in ultrasonic frequency regimes are technically very complicated. Without information on these process variables, monitoring and controlling surface deformation imposed by each strike is impossible. Thus the overall surface deformation due to the accumulation of all strikes cannot be controlled quantitatively.

Table 2.1 Experimental results from the references.

Refs.	[95]	[98]	[90]	[104]	[105]	[106]	[107]	[108]	[109]	[110]
f_u (kHz)	20	20	27	21	18.7	17	27	21.7	20	20
f (Hz)	100	—	100	3000	3000	100	200	3000	—	—
A (μm)	16	10	30	20	22	25	—	20	30	24

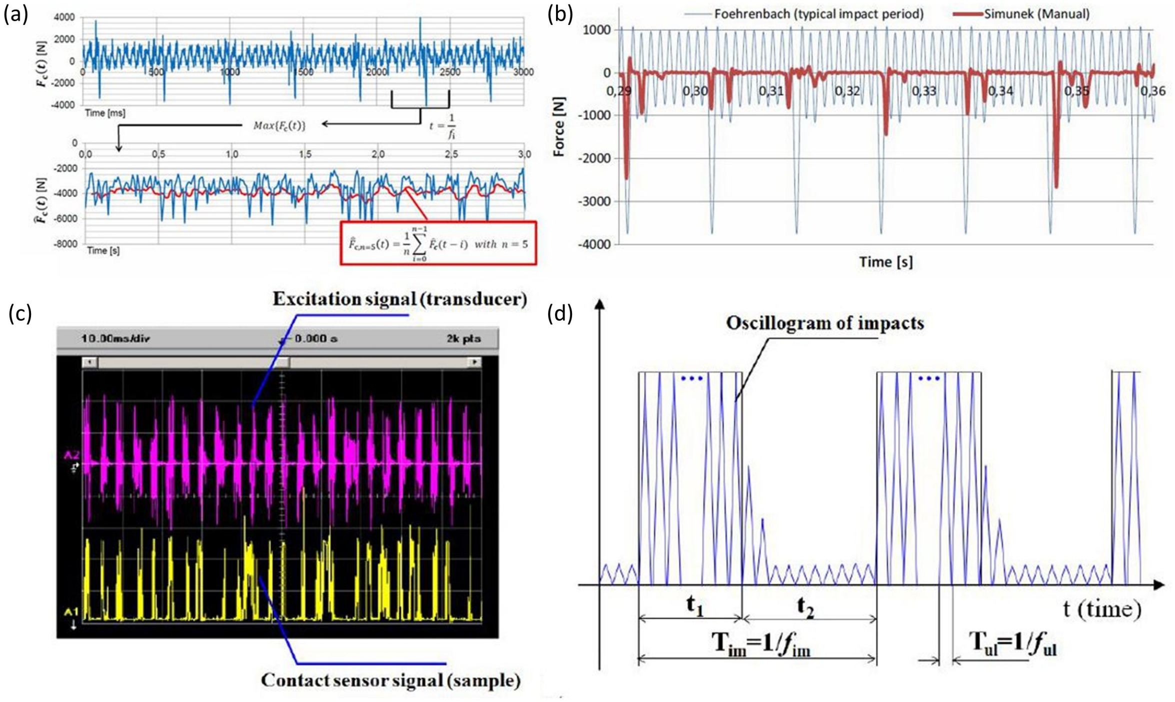

Figure 2.5 Striking force distribution: (a) Nonuniform filter striking force in HFMI; (b) Comparison of force distribution with primary impacts and secondary impacts in HFMI; (c) Force signals in UIP; (d) Theoretical definition of primary impacts and secondary impacts [41, 101, 102, 103].

2.5 Conclusions

According to the discussion above, the current striking-based surface treatments have advantages and disadvantages in different application scenarios. To better compare the characteristics of these four methods, they are briefly summarized based on the application scenario, device configuration, advantages, and disadvantages in Table 2.2.

In summary, the current issues that need to be solved urgently are the randomness and uncertainty caused by free shots in either open or closed treatment environment in SP and SMAT, the high variability caused by hand-held mode in HFMI, and the difficulty in measuring force and displacement and controlling in vibration frequency and amplitude caused by using ultrasonic

Table 2.2 Summary of striking-based surface treatments.

	SP	**SMAT**
Application	• Gears or shafts manufacturing	• Nanograined materials
Configuration	• Pressurized air flow	• High frequency vibration
		• Closed chamber
Advantage	• High speed shots	• Recovered shots
	• Improve fatigue life	• Efficient shots
	• Refine microstructure	• Multiple shot direction
		• Large speed range
		• Refine microstructure
		• Improve fatigue life
Disadvantage	• Random indenters	• Random indenters

	HFMI	**UNSM**
Application	• Post-welding treatment	• Nanostructured surfaces generation
	• Stress concentration reduction	
Configuration	• High frequency vibration	• Ultrasonic vibration
	• Ultrasonic or pneumatic actuator	• CNC platform
	• Hand-held mode	• Cylindrical shots
	• Cylindrical shots	
	• Improve fatigue life	• Enhance controllability and repeatability
	• Refine microstructure	• Improve fatigue life
	• Portable	• Refine microstructure
	• Controllable indenter	• Static load control
	• User-friendly	• CNC platform integration
	• Lightweight	
Disadvantage	• Time consuming	• Empirical process control
	• High variability	

vibration in UNSM. Also, these striking-based surface treatments currently focus more on improving mechanical properties, but less on the ability to improve surface finish. Therefore, how to effectively improve surface roughness has not been well-addressed. It is more attractive if both surface roughness and mechanical properties can be improved in the same process. The importance of controlling surface finish is to control the surface deformation during treatment. However, improving control of deformation in either hand-held or free shots is difficult to be implemented for automation, all of which require changing the process or setup and cannot be controlled in a single machine. Because of these two factors, surface treatment cannot be applied very efficiently.

In order to address these issues, a novel mechanical surface treatment, piezo vibration striking treatment (PVST), is proposed in our research. In PVST, a single striking indenter with replaceable tool tips is used to overcome the randomness and uncertainty caused by free shots. PVST device is integrated into a CNC machine, which allows better motion control of striking locations to reduce the high variability caused by hand-held mode. Instead of using ultrasonic vibration, non-resonant vibration through piezo stack actuation is utilized to independently control consistent striking intensity in each strike cycle so as to overcome the difficulty in controlling frequency and amplitude in ultrasonic vibration mechanisms. Finally, force and vibrational displacement monitoring in each strike cycle in real-time enables a better measurement of them during the process.

CHAPTER 3

PIEZO VIBRATION STRIKING TREATMENT AND EXPERIMENTS

This chapter introduces the design and mechanism of piezo vibration striking treatment and the experiments conducted in this dissertation. Calibration of the PVST device assembly and results of measurement methods are also described.

3.1 Design of piezo vibration striking treatment device

Figure 3.1 shows the components of the PVST device. A standard tool holder (CAT 40) is selected to enable PVST to work on different kinds of CNC milling machines. A device body is designed to connect the tool holder and the piezo holder, which is a hollow cylinder of variable diameter. The diameter of the outer cylinder geometry is based on the inner diameter of the tool holder so that the device body can be inserted into the tool holder completely and fixed by the bolts of the tool holder. An area on the surface of the small-diameter cylinder is machined to be flat to provide space for the tool holder to fix the device body. A through channel on the small-diameter cylinder's side surface and the large-diameter cylinder's top surface is machined to allow the piezo wire to pass through the device body in case the wire is compressed by the inner surface of the tool holder. A piezo holder is designed based on the geometry of the piezo to connect the piezo, device body, and sensor holder rigidly.

An NB ball spline connects the piezo and the striking tool using a customized spline shaft. The NB ball spline is a linear motion mechanism utilizing the rotational motion of ball elements that can sustain loads and, at the same time, can transfer torque. The NB ball spline consists of a spline shaft with raceway grooves and a spline nut. The spline nut consists of an outer cylinder (main body), retainer, side rings, and ball elements designed and manufactured to achieve a reliably smooth motion. Due to the effective contact angle between the raceway grooves and the balls, the NB ball spline can transfer large torque. By adjusting preload, it is possible to give a higher rigidity and a higher positioning accuracy. A similar through channel is machined on the side surface of the spline holder to provide space for the displacement sensor. A sensor holder clamps the sensor tightly and fixes it on the spline holder. Due to the capacitance mechanism of the displacement sensor, a sensor plate is necessary to assist the displacement measuring. By adjusting the sensor holder, the proper gap between the sensor and the plate can be achieved to realize displacement measurement in a detectable range. The striking tool consists of two components: the striking tool holder and the striking tool indenter. The holder and the indenter are press fit, and one of the ends of the holder is connected to the sensor plate rigidly. As shown in Fig. 3.1b, three tool indenters are used, sphere, tapered, and tapered SR, respectively. The sphere and tapered SR type have spherical ends with different diameters, while the tapered type has a flat surface at the end of the tool tip. The detailed geometrical parameters of the three tool indenters can be seen in Table 3.1. Note that only the sphere and tapered SR type are used in this dissertation, and the tapered type will be used in future work.

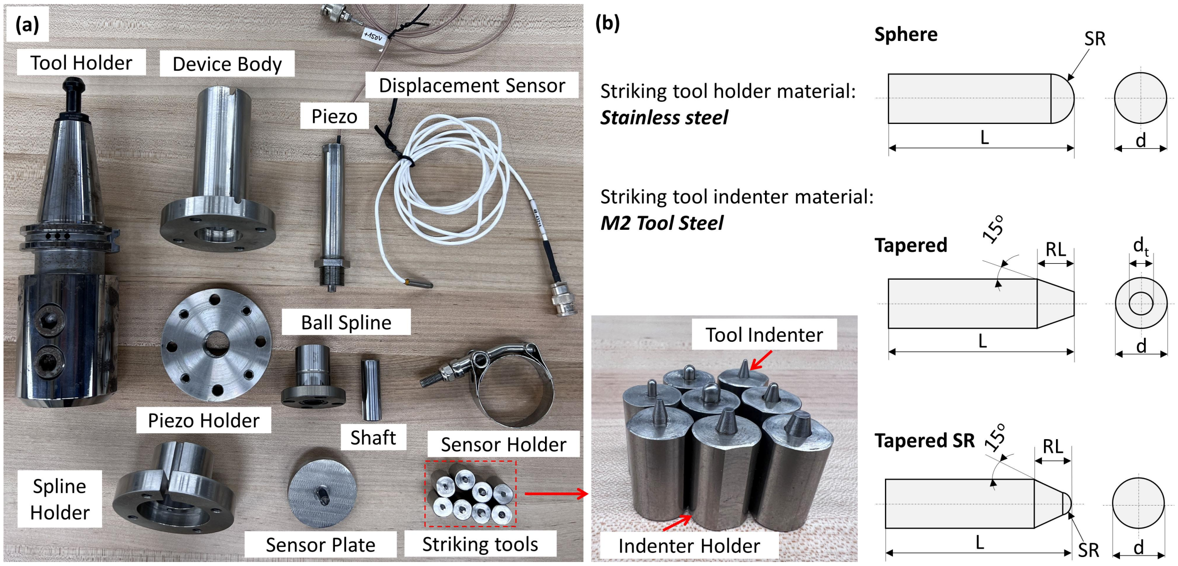

Figure 3.1 PVST: (a) components of PVST device; (b) types and geometry of striking tool tips.

Table 3.1 Geometrical Parameters of striking tool indenters.

Type	L (mm)	d (mm)	RL (mm)	SR (mm)	d_t (mm)
Sphere	10	2	-	1	-
Sphere	10	3	-	1.5	-
Sphere	10	4	-	2	-
Tapered	10	3	3.5	-	1.12
Tapered	10	4	3.8	-	1.96
Tapered	10	5	3.8	-	2.96
Tapered SR	10	3	4.2	0.5	-
Tapered SR	10	4	4.7	1	-

3.2 Mechanism of piezo vibration striking treatment

Figure 3.2 shows the experimental setup of PVST. The assembled PVST device (Fig. 3.2b) is mounted onto the spindle of a CNC vertical milling machine (HAAS Mini Mill 2, as shown in Fig. 3.3) through the standard CAT 40 tool holder. The spindle rotation function in the machine is locked to provide only the vertical motion of the striking device along the Z axis, which can control the striking distance between the striking tool and the workpiece surface. The workpiece is mounted on the machine table, which provides the horizontal motion of the workpiece in both the X and Y axes for the striking location.

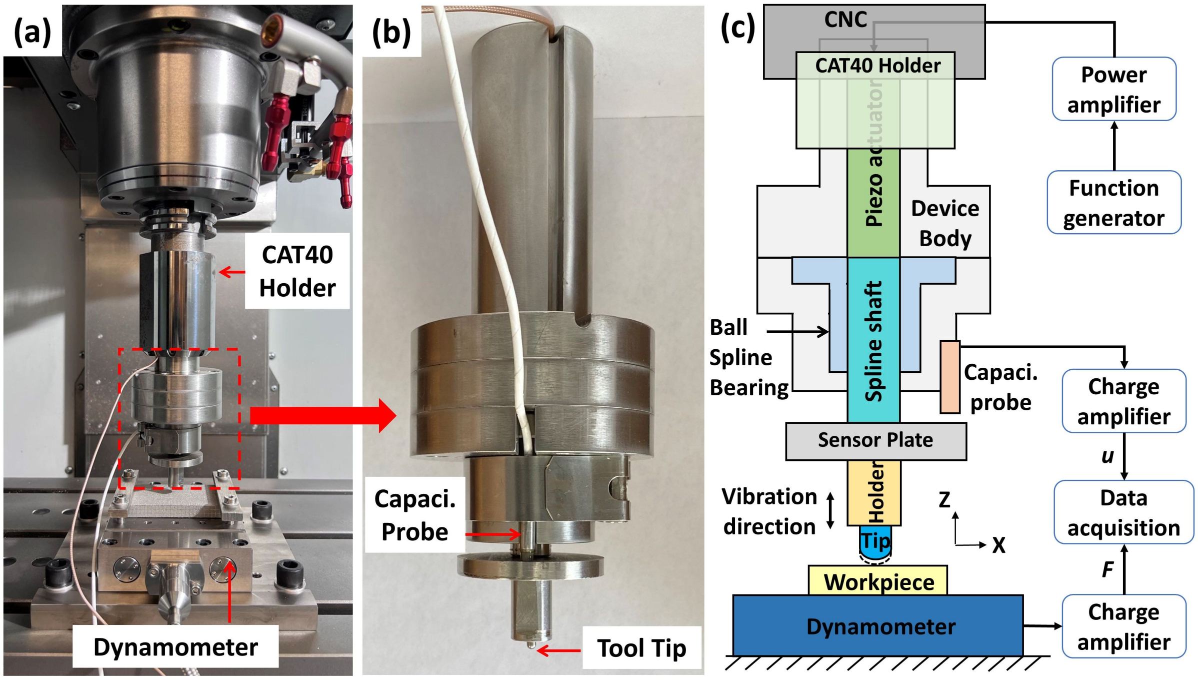

Figure 3.2 The PVST hardware (a, b) and a schematic illustration (c) of the experimental PVST setup.

The PVST device is activated using non-resonant mode piezo stack actuation. The piezo stack actuation is not dependent on the resonance of the whole system, i.e., in UNSM, as is actuated by the amplified voltage from amplifier and generator. Fig. 3.2c shows the schematic of the striking device assembly. Inside the device body, a piezo stack actuator is assembled with a spline shaft along the axial direction. The piezo stack is pre-compressed within the piezo stack housing. The ball spline is mounted on the spline shaft and fixed with the device body, which allows the linear motion of the shaft in the axial direction while restricting the bending and rotation of the shaft.

The striking tool holder with the striking tool indenter (press-fit into the tool holder), which is in the form of a small cylinder with a hemispherical end, is rigidly connected to the end of the shaft (via threaded holes in the shaft and tool holder). The indenter vibration is actuated by the extension and contraction of the piezo stack. The driving voltage generated from a waveform generator and a power amplifier (Fig. 3.3) controls the behavior of the piezo stack. The vibrational displacement of the indenter tool is measured using a capacitance displacement probe (Capacitec HPC-40) to monitor the striking process. As shown in Fig. 3.2b and Fig. 3.2c, the probe is clamped on the device body and facing the flat surface of the sensor plate. The displacement is measured based on the change in the gap between the probe and the flat surface. The striking force is measured using a dynamometer plate (Kistler 5167A) mounted on the CNC machine table. The measured displacement and force signals are recorded synchronously using a data acquisition system (NI USB 6361 + LabView). The sampling rate for both signals is 4000 per second, which is at least 40 times higher than the tool vibration frequencies used in the study; therefore, the displacement and force signals during each vibration or striking cycle can be sufficiently captured.

3.3 Workpieces

PVST experiments in this dissertation are conducted on the workpieces made of ASTM A572GR50 mild structural steel with a dimension of 120 mm × 40 mm × 20 mm, selective electron beam melted Ti-6Al-4V with a build dimension of 100 mm × 50 mm × 10 mm, and OFHC copper is 110 mm × 25 mm × 25 mm. 3D surface topography and roughness parameters (Ra, Rz, and Sa) of the treated areas are measured using KEYENCE Digital Microscope (VHX-6000). The steel and copper workpiece surfaces are prepared by grinding and machining to have an initial roughness $Sa = 0.32$ μm and $Sa = 1.1$ μm, respectively. Note that the creation of the initially smooth surface is for better characterizing the geometry of the deformed surface resulting from the striking. The workpieces are shown in Fig. 3.4.

3.4 Calibration of piezo vibration striking treatment device assembly

The frequency and amplitude of tool vibration are controlled by varying the frequency and amplitude of the sinusoidal driving voltage. The lower bound of the driving voltage is always set

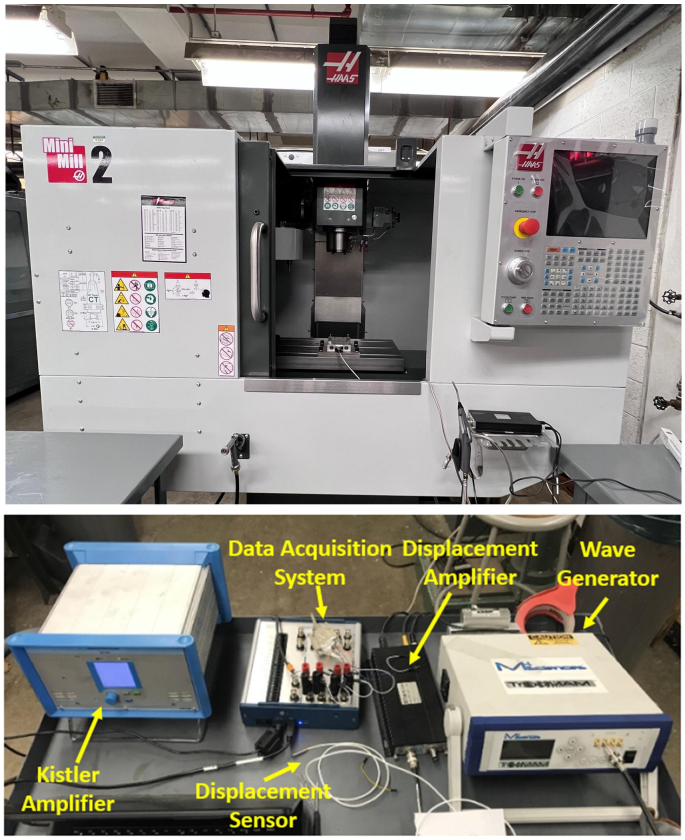

Figure 3.3 Devices used in PVST. Upper: CNC milling machine; Lower: electronic devices.

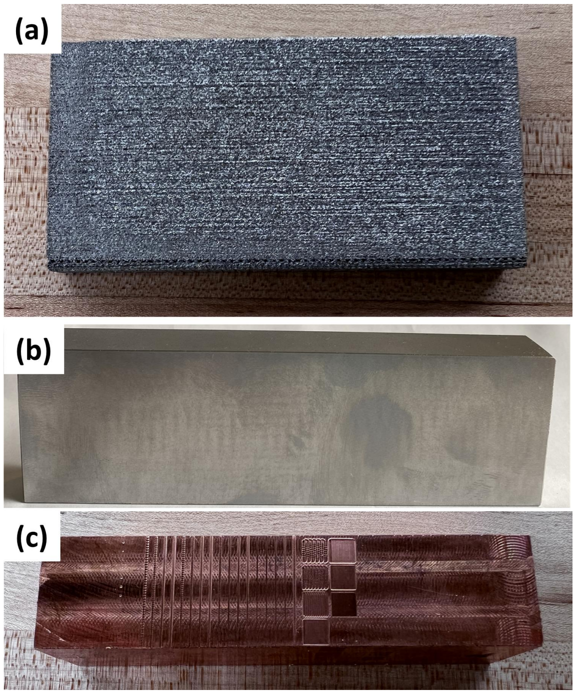

Figure 3.4 Workpieces used in the PVST experiments: (a) additive manufactured Ti-6Al-4V; (b) ASTM A572GR50 mild structural steel; (c) OFHC copper.

at zero, and thus the upper bound of the driving voltage is equal to the peak-to-peak amplitude (V_{pp}) of the voltage oscillation. The maximum driving voltage allowed for the piezo stack is 150 V. The nominal stroke of the piezo stack is 100 μm. Fig. 3.5 shows the calibrated tool vibration of the device assembly without any load at the driving voltage frequency (f) of 10 and 100 Hz and the driving voltage amplitude (V_{pp}) of 60, 90, 120, and 150 V. Fig. 3.5a shows that the vibration displacement of the tool (u) closely follows the sinusoidal driving voltage (V). The tool vibration frequency is the same as the driving voltage frequency. The tool vibration amplitude without striking (u^0_{pp}) is proportional to the driving voltage amplitude (V_{pp}) and is not significantly affected by the vibration frequency (Fig. 3.5b). The maximum vibration amplitude achieved at V_{pp} = 150 V is about 90 μm, which is 10% lower than the nominal stroke (100 μm). The calibration results indicate that the frequency and amplitude of tool vibration can be conveniently and independently controlled. Note that the driving voltage conditions calibrated here are used to conduct the vibration striking experiments in this dissertation.

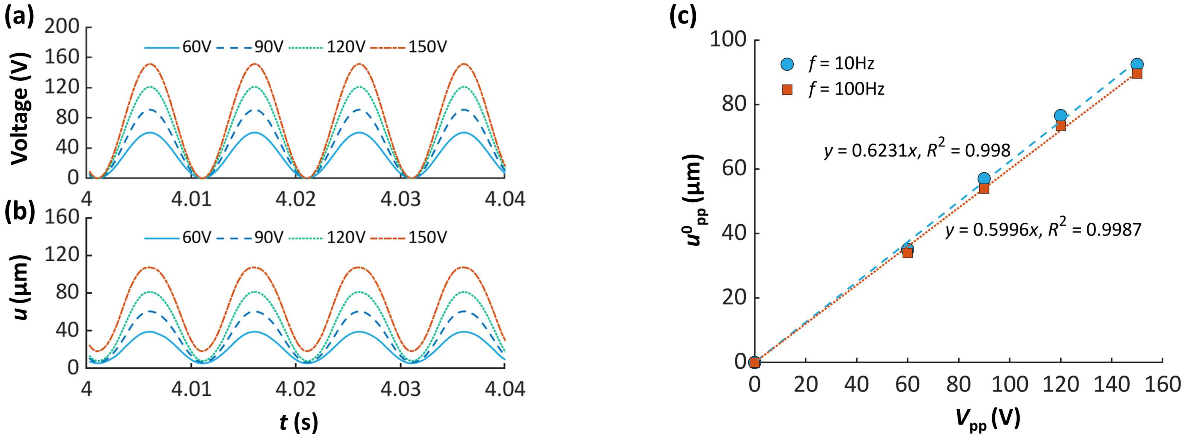

Figure 3.5 The sinusoidal driving voltage input (a) and the corresponding tool vibration displacement (b) at no striking condition for different voltage amplitudes at the same frequency (100 Hz). (c) The correlation of tool vibration amplitude with driving voltage amplitude.

Static contact tests under different loading conditions (steel workpiece, indenter diameter d = 3 mm, static loading force F_s = 100 – 700 N) were performed to determine the axial stiffness of the PVST setup. The PVST setup is mounted on the CNC milling machine while the piezo stack is not actuated. The indenter is brought into contact with the workpiece at the feed rate of 1 μm/s. When the force reaches the setting value, the movement of the indenter is stopped, and the force and displacement data are recorded.

When the piezo stack is not actuated ($V_{pp} = 0$, $f = 0$), static loading force F_s applied on the surface of the workpiece will cause a negative displacement u_s. u_s can be related to F_s as

$$F_s = -k_s u_s \tag{3.1}$$

where k_s is the axial stiffness of the device, which can be determined by the static loading experiments discussed above. The forces are positively and linearly related to the induced displacements, and k_s equals to 11.688 N/mm.

When the piezo stack is actuated, the motion equation for the oscillating mass is given by

$$m\ddot{u}^r_{pp} + b\dot{u}^r_{pp} + k_r u^r_{pp} + F_r = 0 \tag{3.2}$$

where m is the oscillating mass of the striking components; u^r_{pp} is the amplitude reduction, which is the difference between initial amplitude u^0_{pp} and actual amplitude u_{pp} achieved in the single-spot vibration striking experiment conditions; F_r is the force range, indicating the difference between maximum and minimum striking force; $m\ddot{u}^r_{pp}$ and $b\dot{u}^r_{pp}$ are the inertial force and damping force, respectively.

For the vibration at the current frequency with small mass and low friction, the inertial and damping terms in Eq. 3.2 can be ignored compared to the striking force. According to the measurements, the oscillating mass of the system was 75 g. For current vibration conditions, the inertial force ($=2\pi^2 f^2 u_{pp} m$) was estimated to a maximum of 1.4 N. Then, Eq. 3.2 becomes

$$F_r = -k_r u^r_{pp} \tag{3.3}$$

Therefore, F_r can be derived from the measurement of u^r_{pp} if k_r is known. k_r can be determined from the correlation between F_r and u^r_{pp} , which equals to 11.688 N/mm.

There is a certain constraint that defines the scope of the operation of the piezo stack vibration treatment. The controlled vibration should be in the non-resonant regime, which typically requires the frequency to be set below one-half of the resonant frequency of the system (piezo stack resonant frequency is 15 kHz). This gives

$$f < \frac{1}{4\pi}\sqrt{\frac{k}{m}} \tag{3.4}$$

Eq. 3.4 must be satisfied to ensure the proper function of the process. It serves as an important criterion in the design of the process. Substituting the values of k and m into Eq. 3.4, and the limiting frequency f of the device (1850 Hz) is achieved. The key specifications of the setup is shown in Table. 3.2.

Table 3.2 Key specifications of the PVST setup.

Specification	Value
Maximum drive voltage V_{pp}	150 V
Maximum amplitude u_{pp}	90 μm
Piezo-stack resonant frequency	15 kHz
Oscillating mass m	75 g
System stiffness k	11.688 N/mm
System resonant frequency	1850 Hz

3.5 Experiments in piezo vibration striking treatment

Figure 3.6 gives an overview of the four basic experiments conducted in this dissertation. The first experiment (Fig. 3.6a) investigates the tool-surface approaching process in which the vibrating tool is fed vertically toward the workpiece surface. The second experiment (Fig. 3.6b) investigates the single-spot striking process in which the vibrating tool repeatedly strikes the exact location on the workpiece surface from a fixed tool vertical position. The third experiment (Fig. 3.6c) investigates the 1D scan vibration striking process in which the vibrating tool strikes the workpiece surface while continuously moving along a linear path (Note that this dissertation refers to the horizontal tool feed motion as the tool scan motion). The fourth experiment (Fig. 3.6d) investigates the 2D scan vibration striking process by extending the 1D scan vibration striking to treat a 2D surface area using the vibrating tool with parallel scan path lines. In this configuration, the tool's vibration and the workpiece's two horizontal motions (along the X and Y directions) are active.

These experiments are designed to better understand the relationships among tool displacement, striking force, and surface deformation in piezo vibration striking treatment. The interval d_p between adjacent scan paths is set as 2 mm in 1D scan vibration striking to eliminate the effect of adjacent paths on each other. The scan speed v_s in 1D scan vibration striking is approximately determined by the diameter of the indentation in single-spot vibration striking. The overlap ratio

r_o of the successive indentations is proposed to represent the effect of scan speed on the surface texture. The overlap ratio is defined as

$$r_o = \frac{D - d_s}{D} \tag{3.5}$$

where D is the diameter of the permanent indentation resulting from a single-spot vibration striking and d_s is the central distance between two successive indentations (see Fig. 3.7).

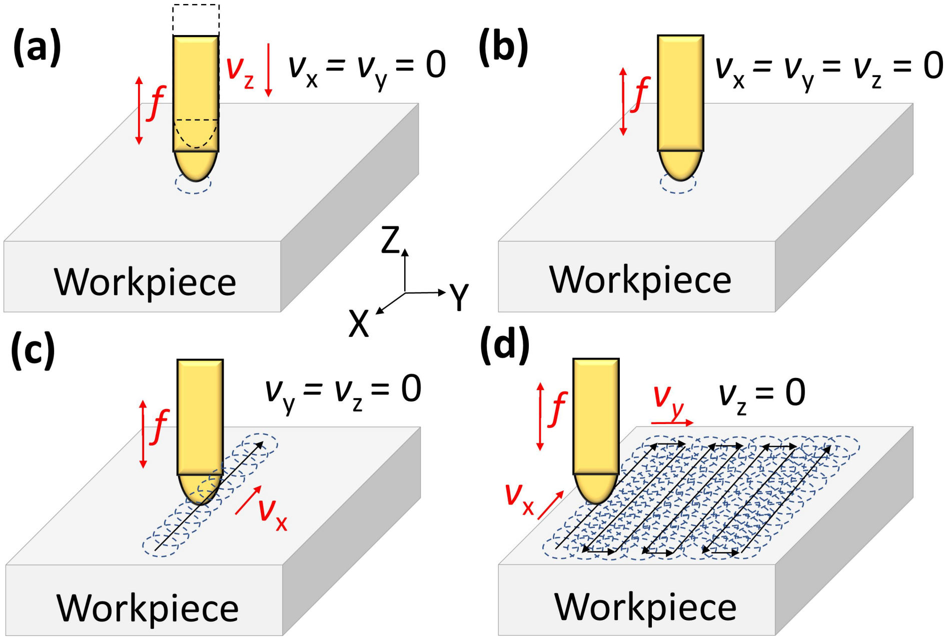

Figure 3.6 Schematic illustrations of the experiments conducted in the study: (a) tool-surface approaching; (b) single-spot striking; (c) 1D scan vibration striking; (d) 2D scan vibration striking.

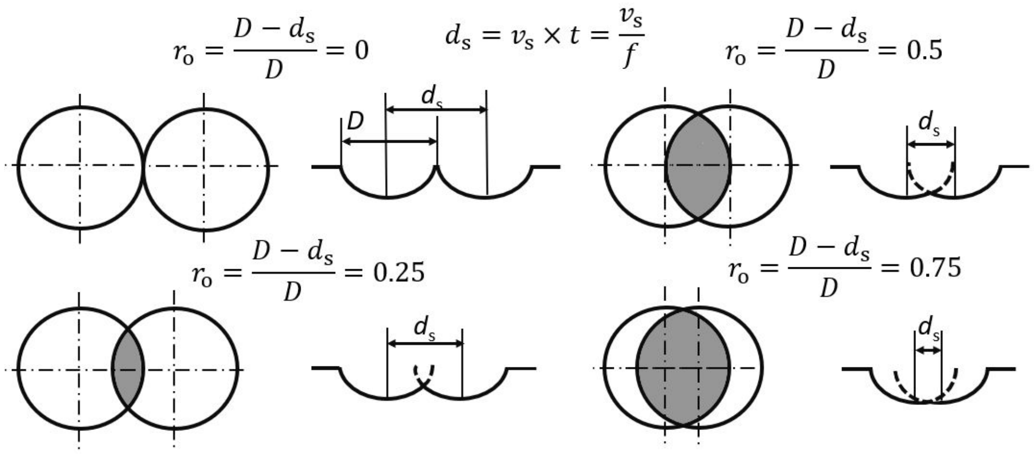

Figure 3.7 Schematic of two successive indentations under different overlap ratios.

Various experimental conditions, including static loading, free contact vibration, tool-surface approaching, single-spot vibration striking, 1D scan vibration striking, and 2D scan vibration striking, are shown in Table 3.3 - Table 3.7.

Table 3.3 Experimental conditions of static loading, free contact vibration, tool-surface approaching, and single-spot vibration striking.

Experiment type	Material	F_s (N)	V_{pp} (V)	f (Hz)	d (mm)
Static loading	Steel	100, 200, 300, 400, 500, 600, 700	0	0	3
Free contact vibration	Steel	0	60, 90, 120, 150	10, 100	3
Tool-surface approaching	Steel	0	60, 90, 120, 150	10, 100	3
Single-spot vibration striking	Steel, Copper	0	60, 90, 120, 150	10, 100	2, 3, 4

Table 3.4 1D scan vibration striking experiments using steel and copper samples.

Material	V_{pp} (V)	d (mm)	r_o
Copper, Steel	60, 90, 120, 150	2, 3, 4	0, 0.25, 0.5, 0.75

Table 3.5 2D scan vibration striking experiments using steel and copper samples.

Material	V_{pp} (V)	d (mm)	r_o	v_s (mm/min)
Copper, Steel	120	2, 3, 4	0, 0.25, 0.5, 0.75	-
Copper, Steel	60, 90, 120, 150	2, 3, 4	0.75	-
Steel	150	0.5, 1, 2	-	500, 1000, 2000, 3000

Table 3.6 2D scan vibration striking experiments using titanium alloy in single pass.

d (mm)	f (Hz)	V_{pp} (V)	Z (μm)	v_s (mm/min)
3	100	150	-150	1000, 2000, 3000
3	100, 150, 200	150	-150	3000
2	100	60, 90, 120, 150	-150	1000
0.5, 1, 2, 3	100	150	-150	1000
3	0	0	0, -50, -150, -200, -250	1000
3	100	150	10, 0, -50, -150, -200	1000
2	100	150	-170, -180, -190, -200	1000
1	100	150	-100, -120, -140, -150, -160, -170, -180, -190, -200	1000
0.5	100	150	-10, -30, -50, -70, -90, -110, -110, -130, -140, -150, -160, -170, -180, -190, -200	1000
0.5	100	60, 90, 120	-200	1000

Table 3.7 2D scan vibration striking experiments using titanium alloy in multiple passes.

d (mm)	f (Hz)	V_{pp} (V)	F_p (N)	v_s (mm/min)	Scan strategy	Pass
0.5	100	60, 90, 120, 150	100	1000	Parallel	2nd
0.5	100	150	200	1000	Parallel, Interweaving	2nd
0.5	100	60	400	1000	Parallel, Interweaving	2nd
2	100	60	400, 600	1000	Parallel, Interweaving	2nd
3	100	60	400, 600	1000	Interweaving	2nd
4	100	60	600, 800	1000	Interweaving	2nd
0.5	100	60	600, 800, 1000	1000	Interweaving	2nd
0.5	100	60	1000	1000	Parallel	2nd
0.5	100	60	1000	1000	Parallel, Interweaving	3rd

3.6 Experimental results measurement

The workpiece after PVST experiments is placed on a free-angle XYZ motorized observation system (VHX-S650E), and a KEYENCE Digital Microscope (VHX-6000) is used to characterize the 3D surface profile of the indentations, as shown in Fig. 3.8. An objective zoom lens (KEYENCE VH-Z500R, RZ x500 - x5000) and x1000 & x2000 magnifications are utilized to achieve sufficient spatial resolution (0.2 μm & 0.1 μm). Since each capture at high magnification conditions can only cover a small area, the stitching technique (22 × 22 scans in horizontal and vertical directions) is employed to achieve a sufficient capture field. Fig. 3.8b shows the cross-section profile measurement of the indentation in the single-spot vibration striking experiment. The indentation depth h is the distance from the bottom indentation surface to the reference undeformed surface of the workpiece. The indentation diameter D is the length between two transition points from the deformed surface to the reference undeformed surface.

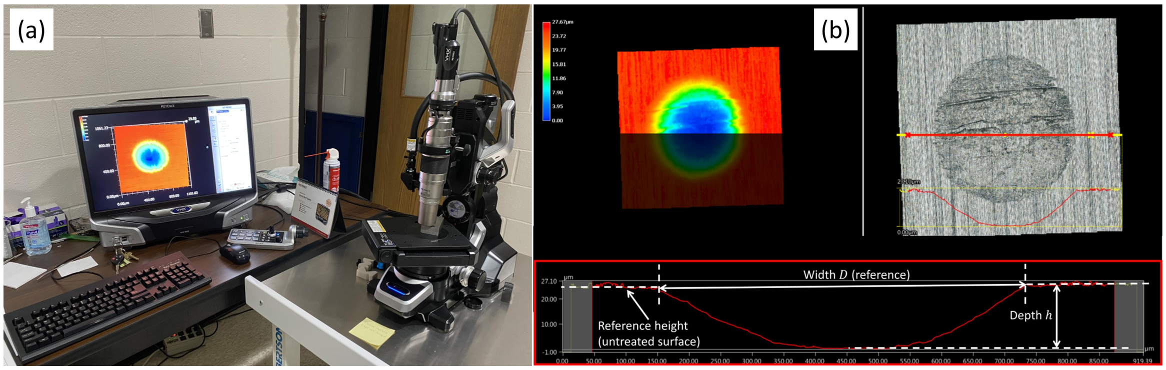

Figure 3.8 Results measurement: (a) Digit Microscope KEYENCE VHX-6000; (b) Cross-section profile measurement of the indentation in single-spot vibration striking experiment.

Figure 3.9 shows the cross-section profiles measurement of the indentation in 1D scan vibration striking experiment along the scan direction and the transverse direction. In 1D scan striking vibration experiments, there are two methods to measure the width of the indentations. One measures the distance between two ridges, while the other measures the distance between two transition points based on the reference surface, as shown in Fig. 3.10. In this dissertation, the former method is used.

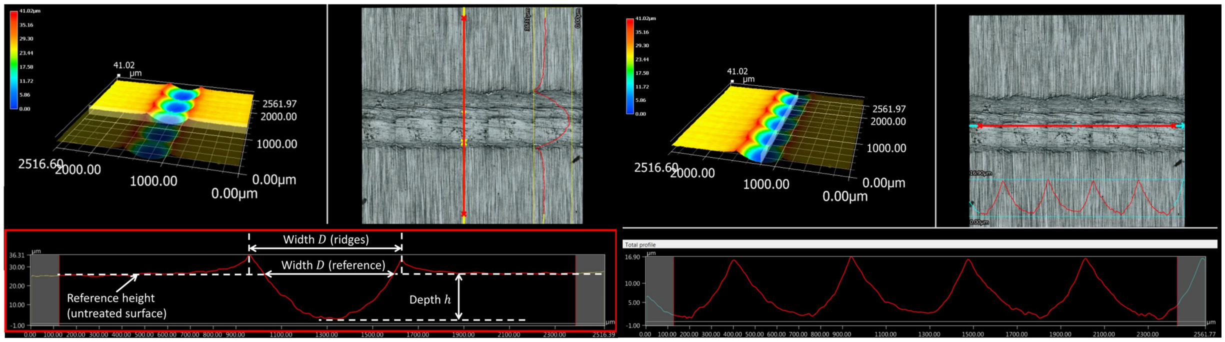

Figure 3.9 Cross-section profile measurement of the indentation in 1D scan vibration striking. Left: measurement in the transverse direction; Right: measurement in the scan direction.

In addition, to evaluate the roughness *Ra* of the treated path in 1D scan vibration striking, the cross-section profile along the scan direction is used to compute *Ra* using the arithmetic mean deviation of the contour which is the arithmetic mean of the absolute value of the distance from the average line to the profile. The formula is

$$Ra = \frac{1}{L}\int_0^L |y|dx \tag{3.6}$$

where L is the length of the estimated profile, and y is the value of the distance from the average reference line to the profile at each position along L, as shown in Fig. 3.11a.

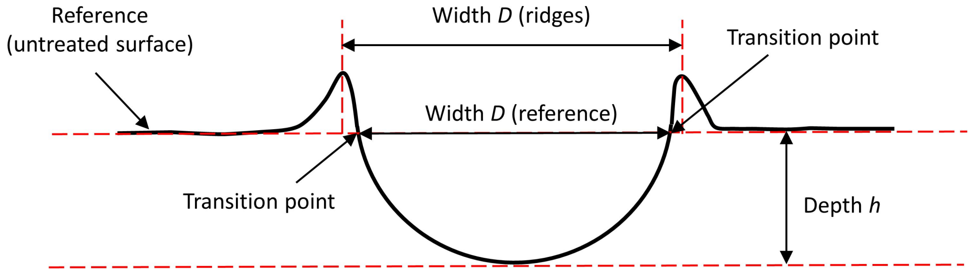

Figure 3.10 Schematic of cross-sectional profile along the transverse direction in 1D scan vibration striking.

The maximum height of the contour is the distance between the maximum peak height and the maximum valley depth, which is the average line in each sample length. Another roughness parameter Rz is the average of the maximum peak-to-valley heights in the evaluation length, which can be expressed as

$$Rz = Rp + Rv \tag{3.7}$$

where Rp and Rv are the maximum peak height and the minimum valley height along the estimated length respectively, as shown in Fig. 3.11b.

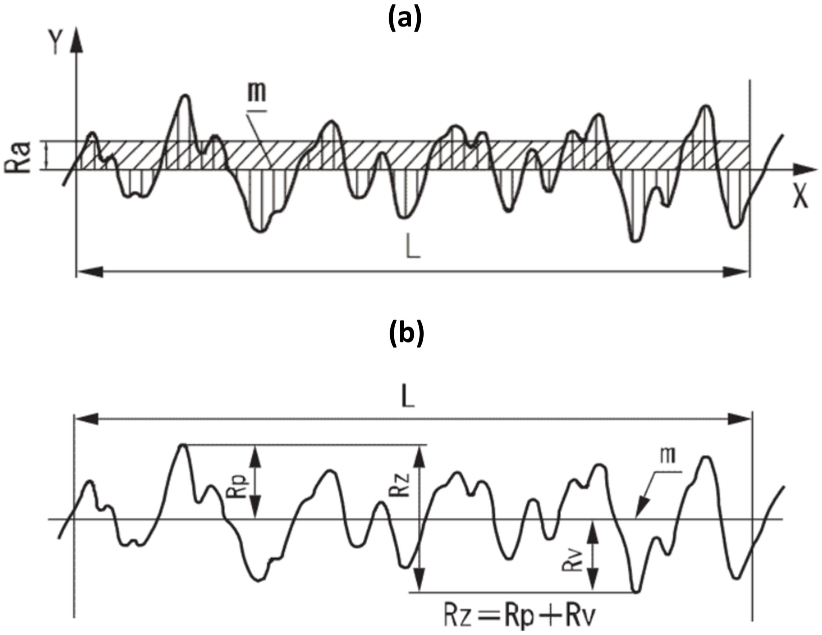

Figure 3.11 Schematics of roughness parameter measurement: (a) Ra measurement; (b) Rz measurement [111].

Figure 3.12 presents the surface texture and height contour map after the 2D area scan vibration striking experiment. In samples with the initially smooth surface, x2000 magnification is used because of the low surface roughness after PVST, and high magnification is necessary to capture all the surface features. The measured area with a size of 2.5 mm × 2.5 mm is used for surface texture data collection instead of the treated area with a size of 5 mm × 5 mm due to the same characteristic of the surface texture throughout the treated area and the computation efficiency for data processing. While in the results of samples with the initially rough surface, x1000 is sufficient to capture all the roughness features. The entire treated area is utilized for surface texture data collection as well.

The surface height data in KEYENCE is exported and processed by MATLAB to calculate the surface roughness Sa of the treated area. Similar to the computation of Ra, Sa is calculated using the arithmetic mean deviation of the surface profile, which is the arithmetic mean of the absolute value of the distance from the average plane to the surface profile. Sa can be computed using

$$Sa = \frac{1}{A}\iint_0^A |Z(x, y)|dxdy, \tag{3.8}$$

where A represents the estimated area, and $Z(x, y)$ is the value of the distance from the average reference plane to the surface profile at the position of (x, y).

Since the measuring table in the KEYENCE observation system is not perfectly flat, the collected data present a slight angle from the reference plane. A 2D fitting plane is created using the collected data to be the reference plane to address this issue. The projection of the surface profiles to this plane will be equivalent to $|Z(x, y)|$ in Eq. 3.8. Moreover, in the results of 2D area scan vibration striking experiments, the 1D roughness parameters Ra and Rz along the scan and transverse directions are also considered. Twenty cross-section profiles are selected along the scan or transverse directions. Each profile is used to compute Ra and Rz, and the average values and standard deviations of Ra and Rz are calculated statistically.

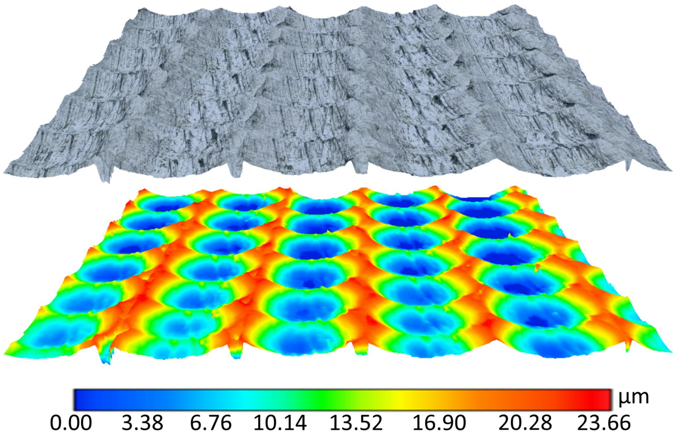

Figure 3.12 Example of surface texture and height contour map in 2D area scan vibration striking.

3.7 Conclusions

This chapter describes the components of PVST and how the PVST works in various experiments. This chapter can be concluded as follows:

1) The calibrated results of PVST, including vibration frequency, vibration amplitude, and driving voltage, indicate that the frequency and amplitude of tool vibration (driving voltage) can be conveniently and independently controlled. The linear relationship between vibration amplitude and driving voltage showcases the capability of PVST to provide a consistent strike intensity during the process and avoid the non-uniform impact as obtained in the current striking-based methods.
2) The static contact force can be derived from the measurement of amplitude reduction if the axial stiffness of the PVST device assembly is known.
3) Four basic PVST experiments and related experimental settings are introduced, involving tool-surface approaching, single-spot vibration striking, 1D scan vibration striking, and 2D scan vibration striking to study striking force, vibration displacement, and surface deformation in the PVST process.
4) Different measurement devices and standards are utilized to characterize the surface profiles after PVST.

CHAPTER 4

CHARACTERIZATION OF PIEZO VIBRATION STRIKING TREATMENT

This chapter introduces the characterization of piezo vibration striking treatment using mild steel and OFHC copper samples. Striking force, vibration displacement, indentation size, surface deformation, and sliding force during the PVST process are explored in tool-surface approaching, single-spot vibration striking, and 1D scan vibration striking experiments, as well as their correlations.

4.1 Tool-surface approaching

In the tool-surface approaching experiment (see Fig. 4.1), the tool's initial vertical position (Z) is set to 120 μm, i.e., Z = 120 μm with the reference from the workpiece surface. The tool's vibration is turned on and the tool is fed onto the surface at a speed of 1 μm/s.

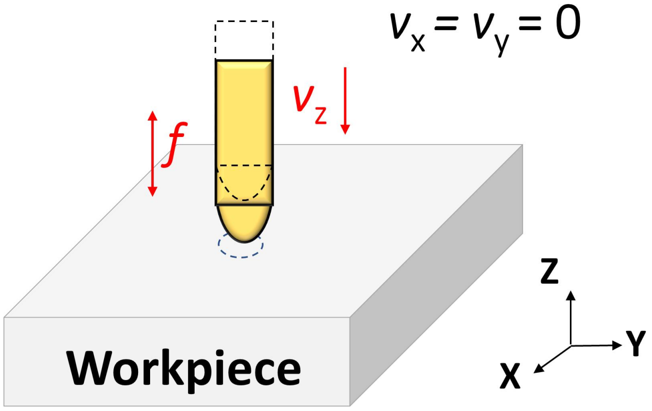

Figure 4.1 Schematic of tool-surface approaching experiment.

Figure 4.2 shows the measured striking force (F_z) and tool vibration displacement (u) plotted against the tool position (Z) as the vibrating tool is fed towards the workpiece at f = 100 Hz and V_{pp} = 60, 90, 120, 150 V. Note u refers to the displacement of the vibrating tool while Z refers to the tool position during the feed motion. As illustrated in Fig 4.2a, in regime A of the tool position (from Z = 120 μm to Z = 105 μm), the tool has no contact with the workpiece surface and correspondingly, there is no load on the vibrating tool. The vibration of the tool has a constant and calibrated amplitude. Entering regime B (from Z = 105 μm to Z = -55 μm), the vibrating tool begins to engage and disengage with the workpiece in each vibration cycle during the repeated strikes on the surface. The peak force of each successive strike increases steadily (orange) because the indentation depth reached by each successive strike increases and strain hardening caused by plastic deformation as the tool position Z decreases. At the same time, the vibration displacement of the tool decreases with Z (blue) due to the elastic compression of the vibration device by the striking force. The higher the striking force, the lower the displacement. Therefore, the maximum displacement of the tool in each successive vibration cycle (or striking cycle) decreases steadily with the tool position Z. However, the minimum displacement of the tool remains unchanged when the tool disengages, and hence no force to compress the piezo stack. Entering regime C (Z < -50 μm), the vibrating tool continuously engages with the workpiece during its vibration. As a result, the force in each vibration cycle increases steadily with the decrease of tool position Z. Correspondingly, the vibration displacement of the tool also decreases with the tool position Z. In addition, regime A's duration increases as the driving voltage decreases due to a smaller driving voltage leading to a smaller vibration amplitude. Hence, it takes longer for the striking tool to contact the workpiece surface. Also, it takes a shorter time to enter Regime C and reach the balanced period of elastic recovery and striking deformation.

As noted already, the maximum vibration displacement (u_{max}) during the striking process depends on the striking force. Fig. 4.3a and Fig. 4.3b show the relationship between the reduction in maximum vibration displacement ($\Delta u_{max} = u^0_{max} - u_{max}$) and the peak force of the strike (F_{max}) at f = 100 and 10 Hz, respectively. The relationship is based on the force and displacement data corresponding to the tool position range $0 < Z < u^0_{max}$ in the approaching experiment. Note that in this Z range, the reduction in maximum vibration displacement is the same as the reduction in vibration amplitude ($\Delta u_{pp} = u^0_{pp} - u_{pp}$). The relationship between F_{max} and Δu_{max} (or Δu_{pp}) is linear, which gives a stiffness value of 11.4 N/μm at f = 100 Hz (Fig. 4.3a) and 11.1 N/μm at f = 10 Hz (Fig. 4.3b). The axial stiffness of the vibration device assembly is nearly identical at 11.7 N/μm (Fig. 4.3c), confirmed by the static compression tests on the device (with no vibration). Therefore, the reduction in vibration displacement is due to the elastic compression of the device assembly under the striking force, which means the reduction in vibration displacement can be

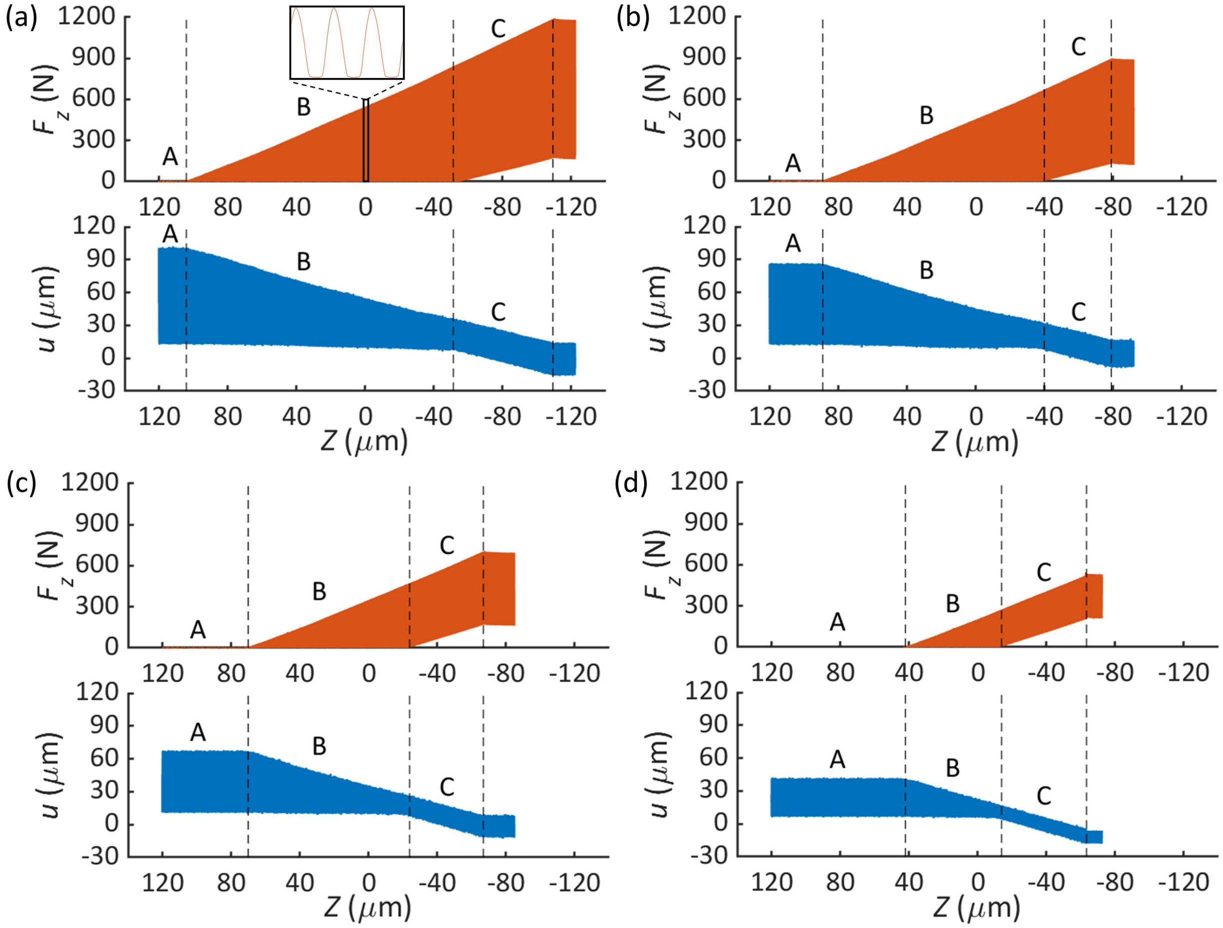

Figure 4.2 The measured striking force (top) and tool vibration displacement (bottom) plotted against the tool vertical position Z in the tool-surface approaching experiment. f = 100 Hz: (a) V_{pp} = 150 V; (b) V_{pp} = 120 V; (c) V_{pp} = 90 V; (d) V_{pp} = 60 V.

calculated from the force signal given the stiffness of the vibration device.

4.2 Single-spot vibration striking

The single-spot vibration striking experiment (see Fig. 4.4) was conducted on a single surface spot with a fixed tool position $Z = 0$. With the initial tool position Z set to zero, the vibration was turned on for 3 seconds to induce repeated strikes on the same surface spot. It is expected that the plastic deformation was imposed only within the first few strikes. After reaching a steady state, the repeated strikes only involve elastic deformation of the deformed surface.

4.2.1 Single-spot vibration striking using mild steel workpieces

The single-spot vibration striking experiments are first performed using steel workpieces under different vibration frequencies and driving voltage conditions. The deformation behavior described

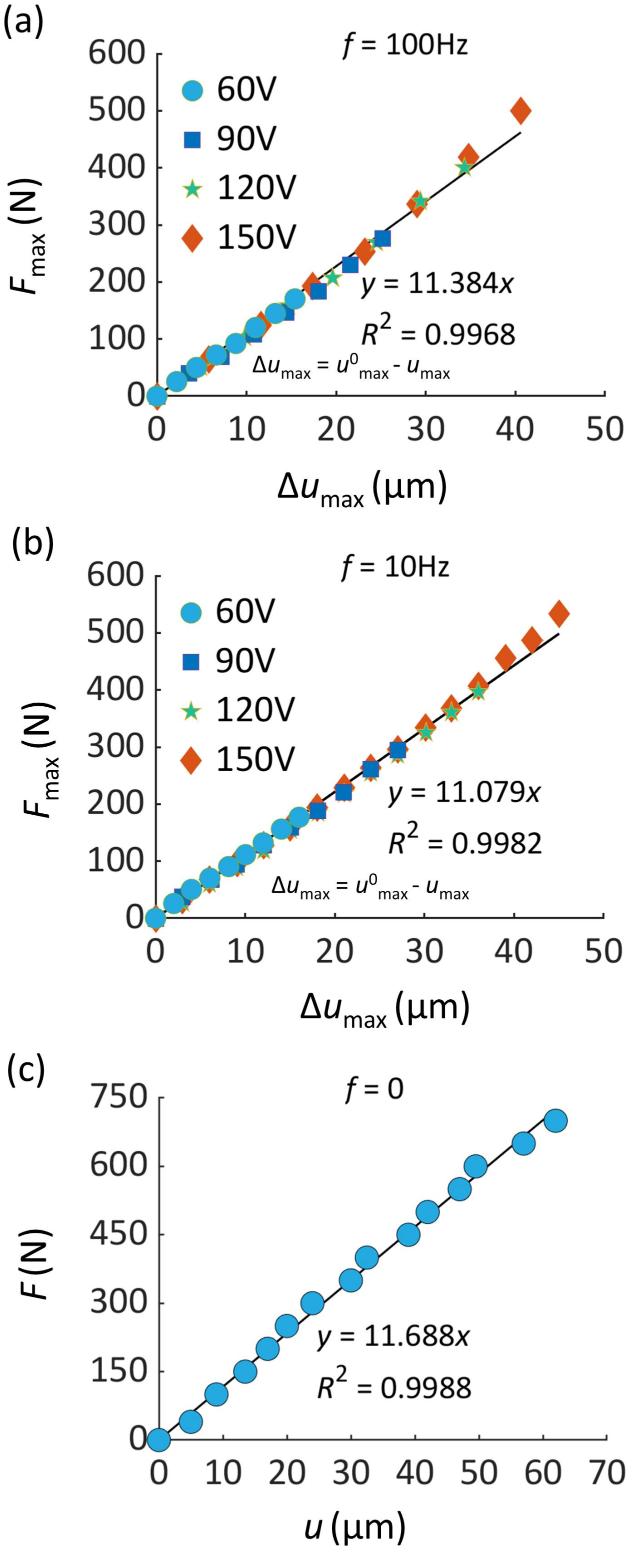

Figure 4.3 The relation between the striking peak force and the reduction in maximum tool vibration displacement at (a) f = 100 Hz and (b) f = 10 Hz. (c) The force and displacement relation in a static compression test (no vibration).

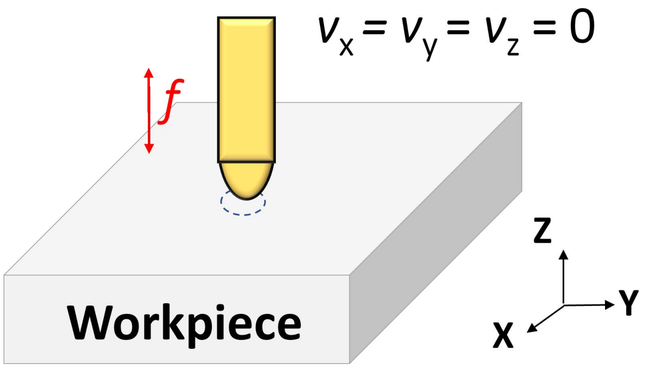

Figure 4.4 Schematic of single-spot vibration striking experiment.

above is confirmed by Fig. 4.5, which shows the measured force and vibration displacement during the repeated strikes at the vibration condition f = 10 Hz and V_{pp} = 60 V, 90 V, 120 V, 150 V. Observe that both the force and displacement signals reach steady-state oscillations nearly right after the start of the tool vibration. The peak forces (F_{max}) and the maximum vibration displacement (u_{max}) then remain constant except that F_{max} and u_{max} are different for different V_{pp} (see Table 4.1).

Table 4.1 Maximum striking force and displacement at f = 10 Hz.

Material	f (Hz)	V_{pp}	F_{max} (N)	u_{max} (μm)
Steel	10	60	163.5	22.4
Steel	10	90	256.5	37.3
Steel	10	120	359.8	49.2
Steel	10	150	441.5	60.7

To better understand the behavior of the striking tool during PVST, a single vibration cycle is selected (illustrated in Fig. 4.6). The two instants corresponding to the tool engaging and disengaging with the surface can be identified on the force and displacement profiles (i.e., t_1 and t_3). A striking cycle can be divided into four stages. From t_0 to t_1, the tool moves from its minimum displacement position toward the surface without contact, so the force is zero. From t_1 to t_2, the tool is indenting into the surface, rapidly increasing the force. From t_2 to t_3, the tool moves away from its maximum displacement position while remaining in contact with the surface due to the elastic recovery. Concurrently, the force decreases rapidly towards zero. From t_3 to t_4, the tool has completely separated from the surface and continues moving away, and force is zero. When the tool reaches its minimum displacement position, it completes the current striking cycle, and a new

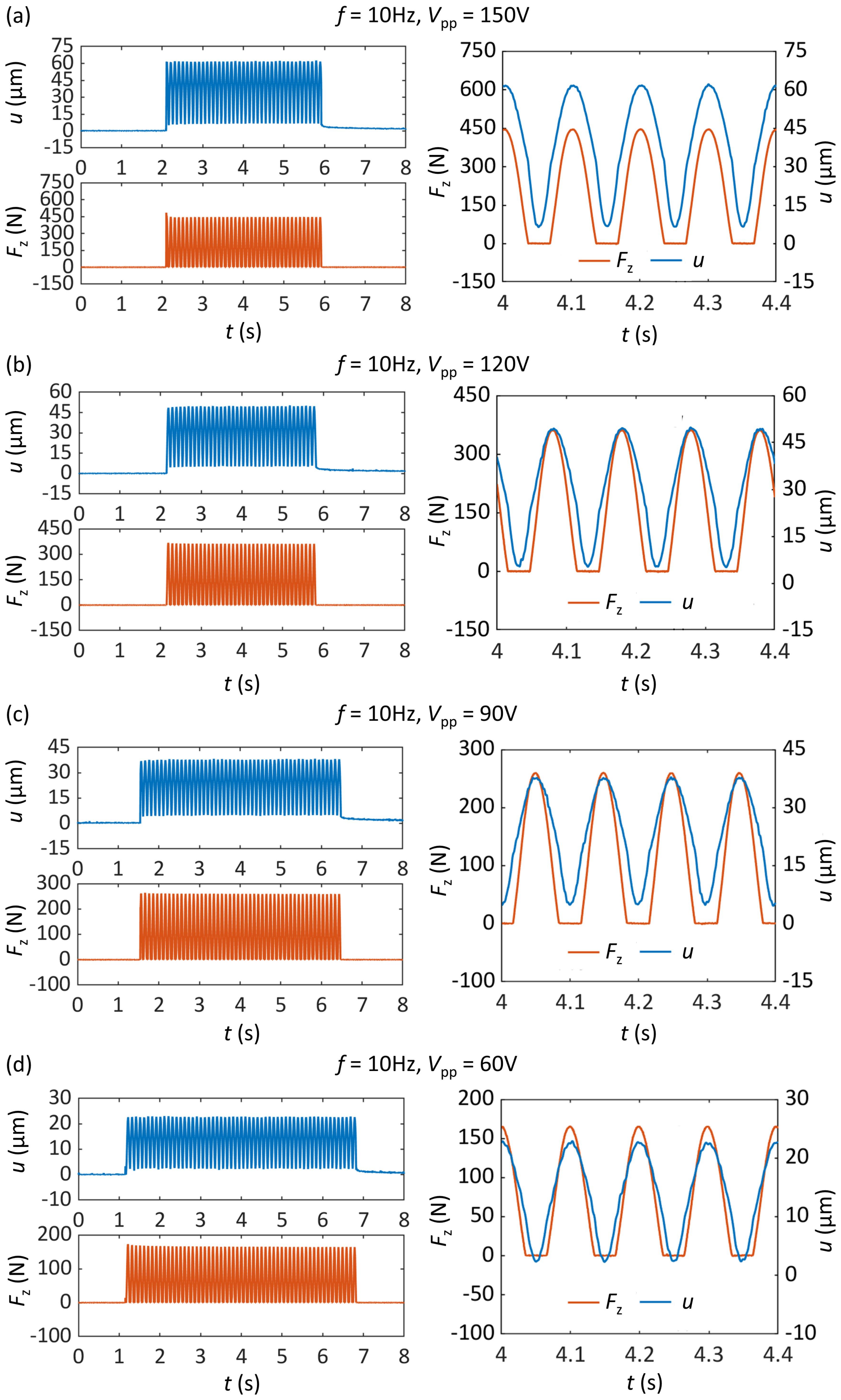

Figure 4.5 Upper left: tool vibration displacement; Bottom left: striking force. Right: variations of force and displacement within 4 vibration cycles at f = 10 Hz: (a) V_{pp} = 150 V; (b) V_{pp} = 120 V; (c) V_{pp} = 90 V; (d) V_{pp} = 60 V.

cycle begins.

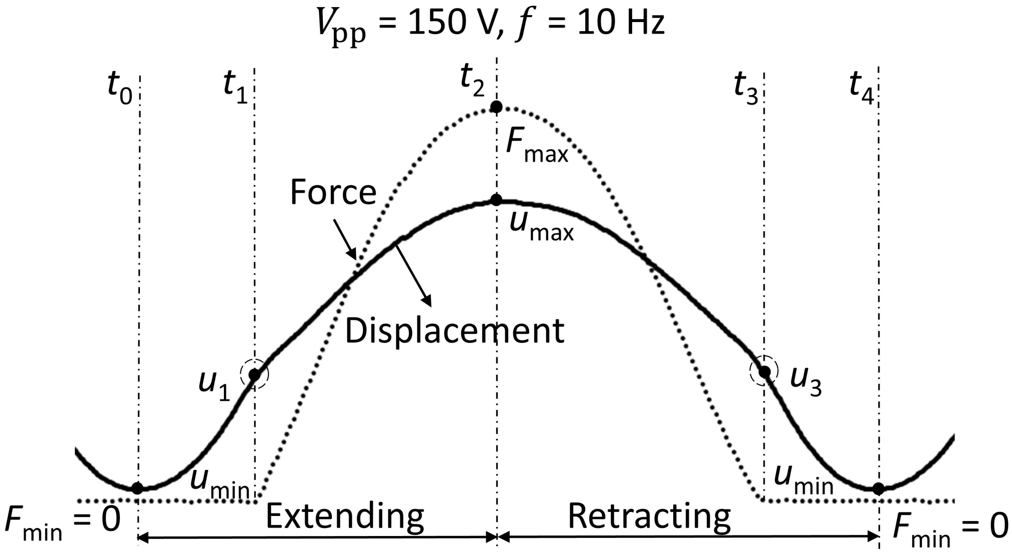

Figure 4.6 History of force and displacement in one cycle: f = 10 Hz, V_{pp} = 150 V.

Similar experiments at f = 100 Hz were conducted to see how the striking force and vibration displacement behave in high-frequency conditions. Fig. 4.7 shows the measured force and displacement at four conditions: f = 100 Hz, V_{pp} = 60, 90, 120, and 150V. The uniform and stable sinusoidal distributions of striking force and vibration displacement are still observed in each striking cycle for different driving voltages. Both the force and displacement oscillations are in a steady state, nearly right after the start of the tool vibration. The values for F_{max} and u_{max} can be seen in Table 4.2. The force and displacement profiles are consistently repeated within each vibration cycle. The force plateau still exists when the tool is not in contact with the workpiece, but it shows less stability than it does in low-frequency conditions. The force and the displacement are slightly out-of-phase as well. In addition, the positive minimum displacement is observed, caused by the mechanical movement lag of the piezo stack, and the minimum displacement is more significant than that in low-frequency conditions.

As mentioned earlier, in single-spot vibration striking, plastic deformation occurs in the first few strike cycles and the remaining repeated strikes on the surface only cause elastic deformation. Therefore, the deformation process can be divided into elastic-plastic deformation period and

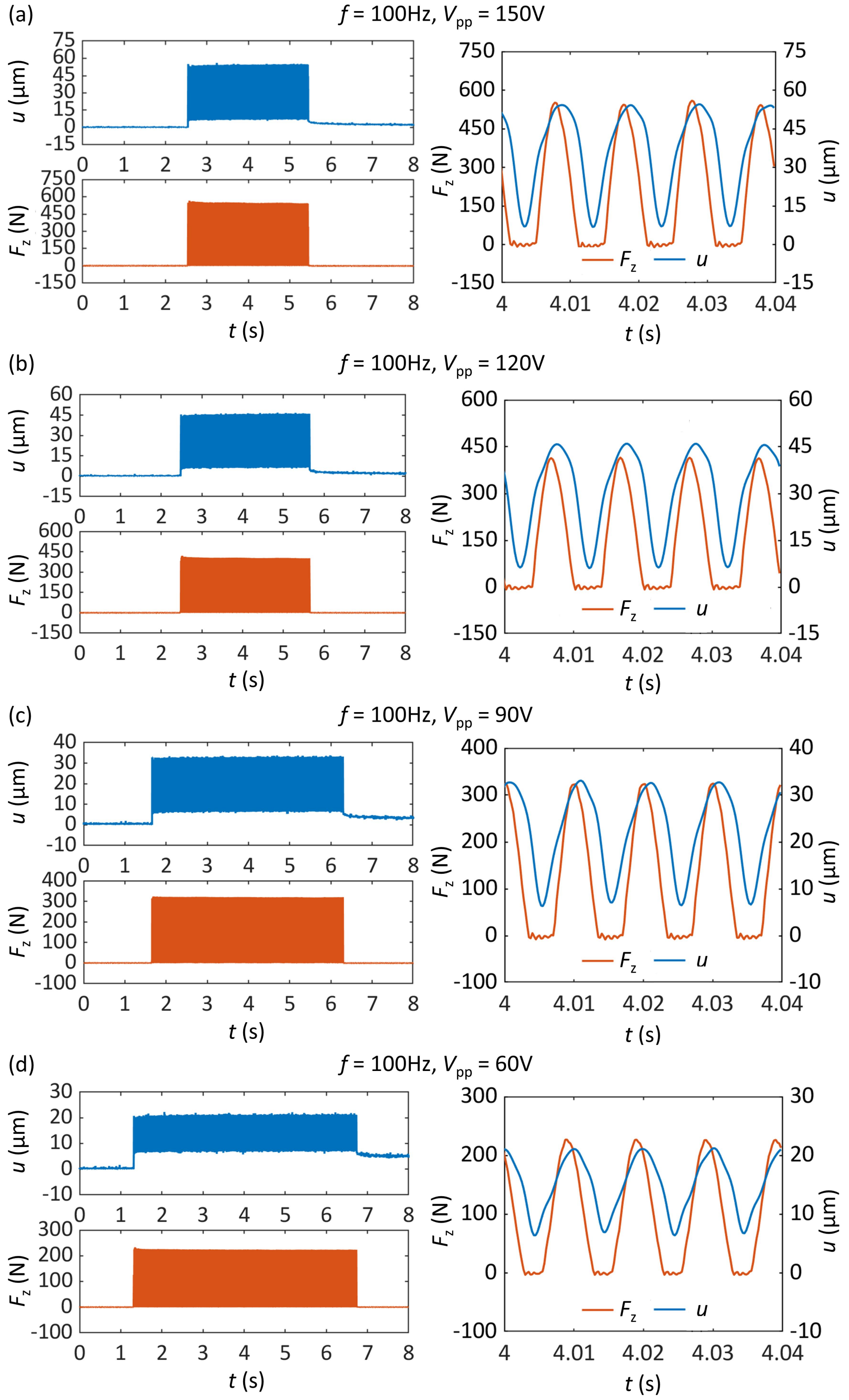

Figure 4.7 Upper left: tool vibration displacement; Bottom left: striking force. Right: variations of force and displacement signals within 4 vibration cycles at f = 100 Hz: (a) V_{pp} = 150 V; (b) V_{pp} = 120 V; (c) V_{pp} = 90 V; (d) V_{pp} = 60 V.

Table 4.2 Maximum striking force and displacement at f = 100 Hz.

Material	f (Hz)	V_{pp}	F_{max} (N)	u_{max} (μm)
Steel	100	60	224.5	21.2
Steel	100	90	323.4	33.4
Steel	100	120	412.5	46.5
Steel	100	150	549.3	55.3

purely elastic deformation period. Fig. 4.8 summarizes the measured F_{max} in the purely elastic deformation period, u_{max}, and the depth (h) and diameter (D) of a permanent indentation in single-spot vibration striking at various vibration conditions (V_{pp} = 60, 90, 120, 150 V, f = 10, 100 Hz, d = 2 mm) using steel samples. At higher frequency conditions, the striking tool needs to overcome the increased inertial force to accelerate the workpiece material when it strikes the surface. Higher frequency leads to higher acceleration during each strike and hence higher striking force. This increased striking force in elastic-plastic deformation period results in more plastic deformation (larger h and D shown in Fig. 4.8c and Fig. 4.8d) and more strain hardening of the material, thereby higher yield strength of the treated spot.

In the purely elastic deformation period, the striking force in each strike cycle is larger at higher frequency conditions due to the increased yield strength generated in elastic-plastic deformation period, as shown in Fig. 4.8a. In contrast, higher f results in lower u_{max} for a given V_{pp}. As discussed in Fig. 4.3, vibration amplitude reduction due to the device elastic compression increases as striking force increases. Therefore, higher F_{max} caused by higher f increases the amplitude reduction which makes the striking tool extend less and hence smaller u_{max}. Also, the decreased u_{max} can in turn reduce the contact area between the tool and the surface, hence deformation resistance and striking force. Based on the current observation, the increased yield strength caused by strain hardening in elastic-plastic deformation period dominates the final striking force over the effect of decreasing deformation resistance caused by smaller u_{max}. Therefore, the striking force is higher at higher frequency conditions in Fig. 4.8. Note that the comparison of F_{max} is at the steady state striking stage where the plastic deformation has already been completed, and only elastic deformation is taking place (purely elastic deformation period). As a result, the observed difference in F_{max} in Fig. 4.8a for different f is not attributed to the strain rate effect that occurs only during plastic deformation. Also, observe that F_{max}, u_{max}, h, and D increase with V_{pp} since higher V_{pp} means higher vibration amplitude.

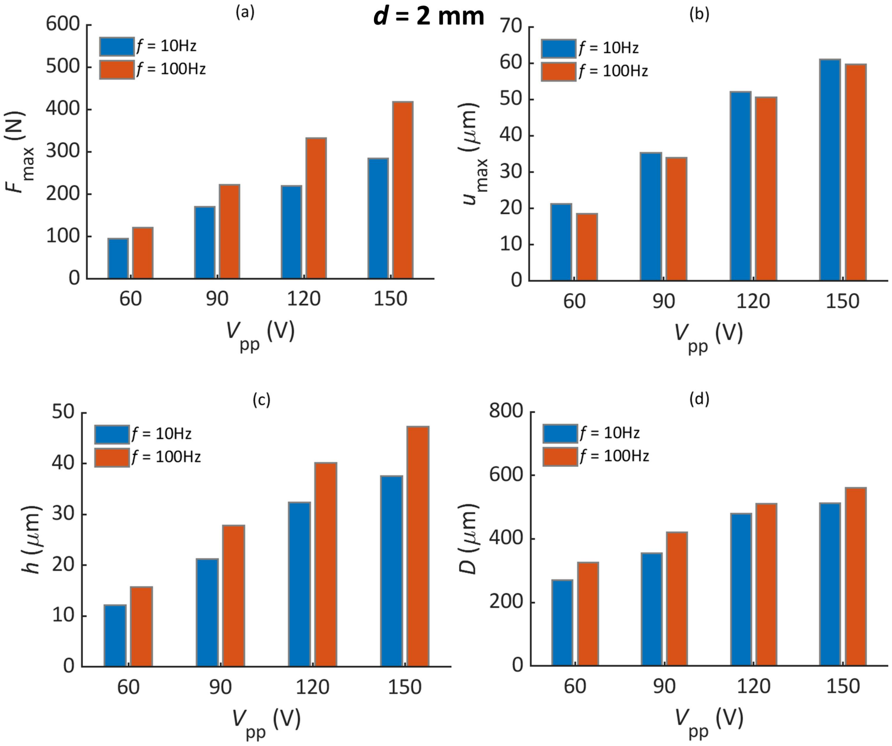

Figure 4.8 Summary of (a) striking peaking force, (b) maximum tool vibration displacement, (c) the depth, and (d) the diameter of a permanent indentation in single-spot vibration striking using steel samples at V_{pp} = 60, 90, 120, 150 V, f = 10, 100 Hz, d = 2 mm.

In addition, the tool diameter is increased to 3 mm and 4 mm to explore the effect of tool geometry on surface deformation. The single-spot vibration striking experiments at the same driving voltage and vibration frequency conditions are conducted using the two striking tools with larger diameters. The corresponding results of F_{max}, u_{max}, h, D are summarized in Fig. 4.9 and Fig. 4.10. Similar to the results at d = 2 mm, F_{max}, u_{max}, h, and D increase with more significant driving voltage at d = 3 mm and d = 4 mm. Also, higher frequency has a more evident effect on these results.

F_{max}, u_{max}, h, and D with a given V_{pp} = 150 V at d = 2, 3, 4 mm are selected to compare the effect of tool geometry of these variables more efficiently, as demonstrated in Fig. 4.11. Observe that when d increases from 2 mm to 4 mm, the maximum striking force F_{max} becomes larger. The

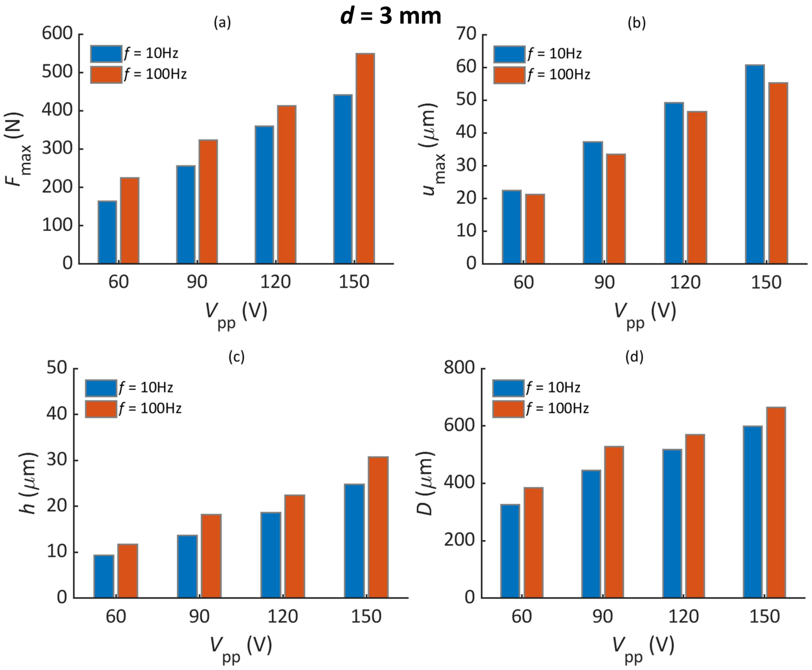

Figure 4.9 Summary of (a) striking peaking force, (b) maximum tool vibration displacement, (c) the depth, and (d) the diameter of a permanent indentation in single-spot vibration striking using steel samples at V_{pp} = 60, 90, 120, 150 V, f = 10, 100 Hz, d = 3 mm.

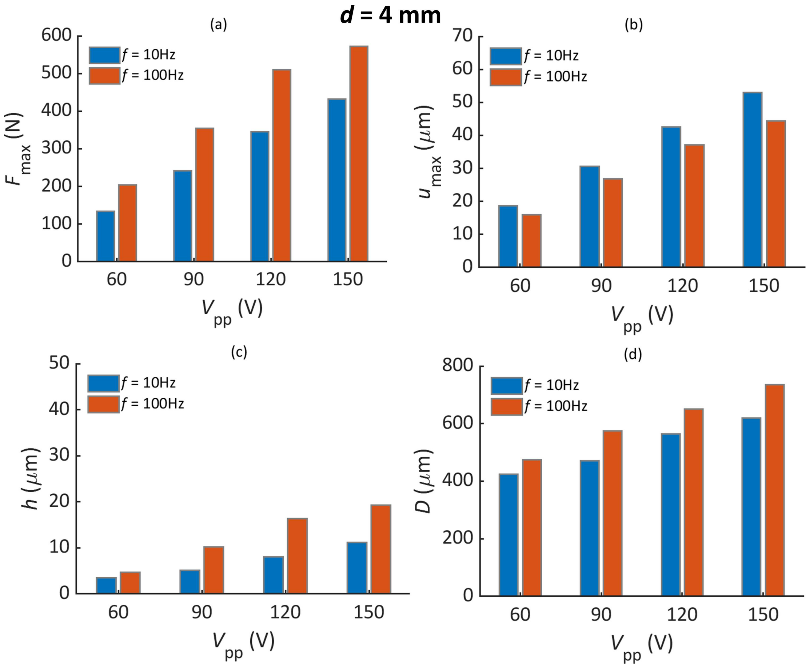

Figure 4.10 Summary of (a) striking peaking force, (b) maximum tool vibration displacement, (c) the depth, and (d) the diameter of a permanent indentation in single-spot vibration striking using steel samples at V_{pp} = 60, 90, 120, 150 V, f = 10, 100 Hz, d = 4 mm.

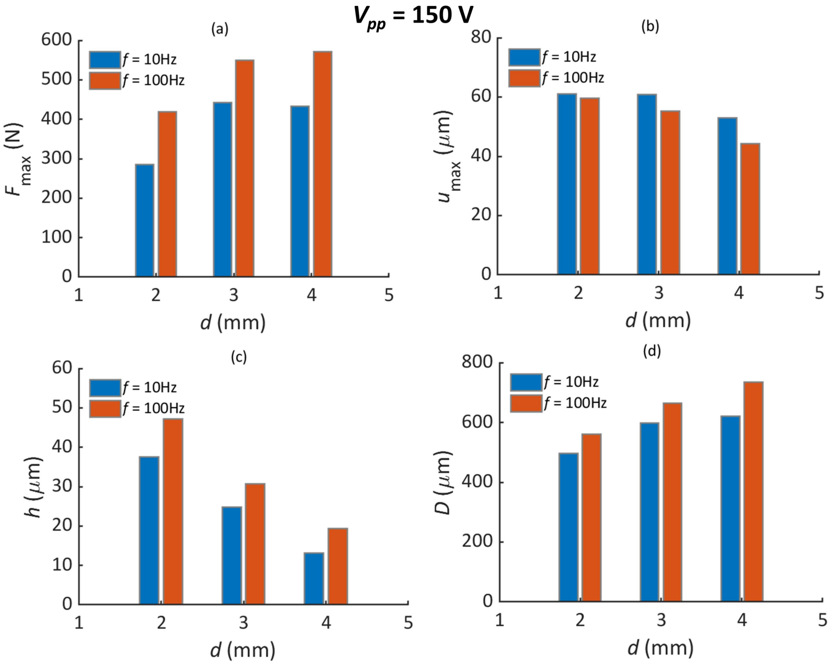

Figure 4.11 Summary of (a) striking peaking force, (b) maximum tool vibration displacement, (c) the depth, and (d) the diameter of a permanent indentation in single-spot vibration striking using steel samples at V_{pp} = 150 V, f = 10, 100 Hz, d = 2, 3, 4 mm.

increase is expected since a larger toot diameter will increase the contact area between the striking tool and the workpiece during each strike, leading to higher deformation resistance and hence more significant striking force. Accordingly, lower u_{max} is also achieved because the increasing deformation resistance causes a larger amplitude reduction of the striking tool. This reduction makes the striking tool unable to reach a position as deep as it does at minor tool diameter condition, which results in a smaller permanent depth of the indentation (Fig. 4.11c). The permanent width of the indentation becomes larger due to the larger contact area between the tool and the workpiece. Generally, the permanent depth of the indentation is negatively correlated with the tool diameter, while the diameter of the indentation is proportional to the tool diameter. To reach a similar permanent depth of the indentation in minor tool diameter conditions, a more significant driving voltage or a preload with negative Z is necessary. As mentioned earlier, higher F_{max} results in more plastic deformation, and hence larger h and D. It does not conflict with the current results of smaller h and larger D at larger tool diameter conditions since the reduced plastic deformation along the depth direction is supplemented by the increased plastic deformation along the width direction.

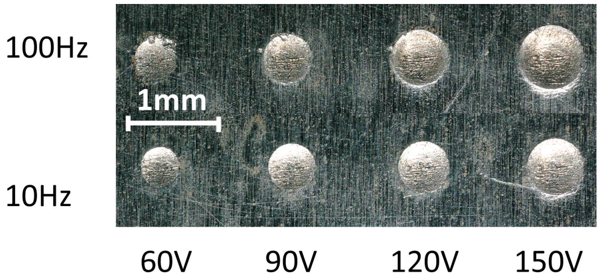

Figure 4.12 Optical photos of the permanent indentations in single-spot vibration striking at various vibration conditions (f = 10, 100 Hz, V_{pp} = 60, 90, 120, 150 V, d = 3 mm) using steel samples.

Figure 4.12 shows the resulting permanent indentations on the surface at the vibration conditions of f = 10, 100 Hz, V_{pp} = 60, 90, 120, 150 V, d = 3 mm using steel samples. It is observed that the diameter of the indentation is positively correlated with the driving voltage and vibration frequency.

Figure 4.13 shows the cross-sectional profiles of the permanent indentations grouped at f = 10 and 100 Hz with different driving voltages and tool diameters, respectively. The depth (h) and diameter (D) of the indentation increase with V_{pp}. For a given V_{pp}, higher f results in higher h and D, which is consistent with the results in Fig. 4.8c - 4.10c and Fig. 4.8d - 4.10d. Both of the above trends work for different tool diameters. As noted earlier, a higher f results in a lower u_{max} (Fig. 4.8b - Fig. 4.10b). Since the tool position is at Z = 0, u_{max} equals the maximum indentation depth reached by the strike, representing the total plastic and elastic deformation. In contrast, h represents only the plastic deformation.

Figure 4.14 shows how F_{max} is related to h and D, respectively. It is found that the size of the permanent indentation generated on the surface is linearly dependent on the peak force of the strike. It indicates that the force signal can be used to monitor the plastic deformation imposed by each strike.

4.2.2 Single-spot vibration striking using OFHC copper workpieces

To study the deformation behavior of different materials after PVST, PVST experiments at identical experimental conditions used in steel samples were carried out using OFHC copper samples. The results of F_{max}, u_{max}, h, and D at d = 2, 3, 4 mm are shown in Fig. 4.15, Fig. 4.16, and Fig. 4.17, respectively. Similar to the deformation behavior of applying PVST onto steel

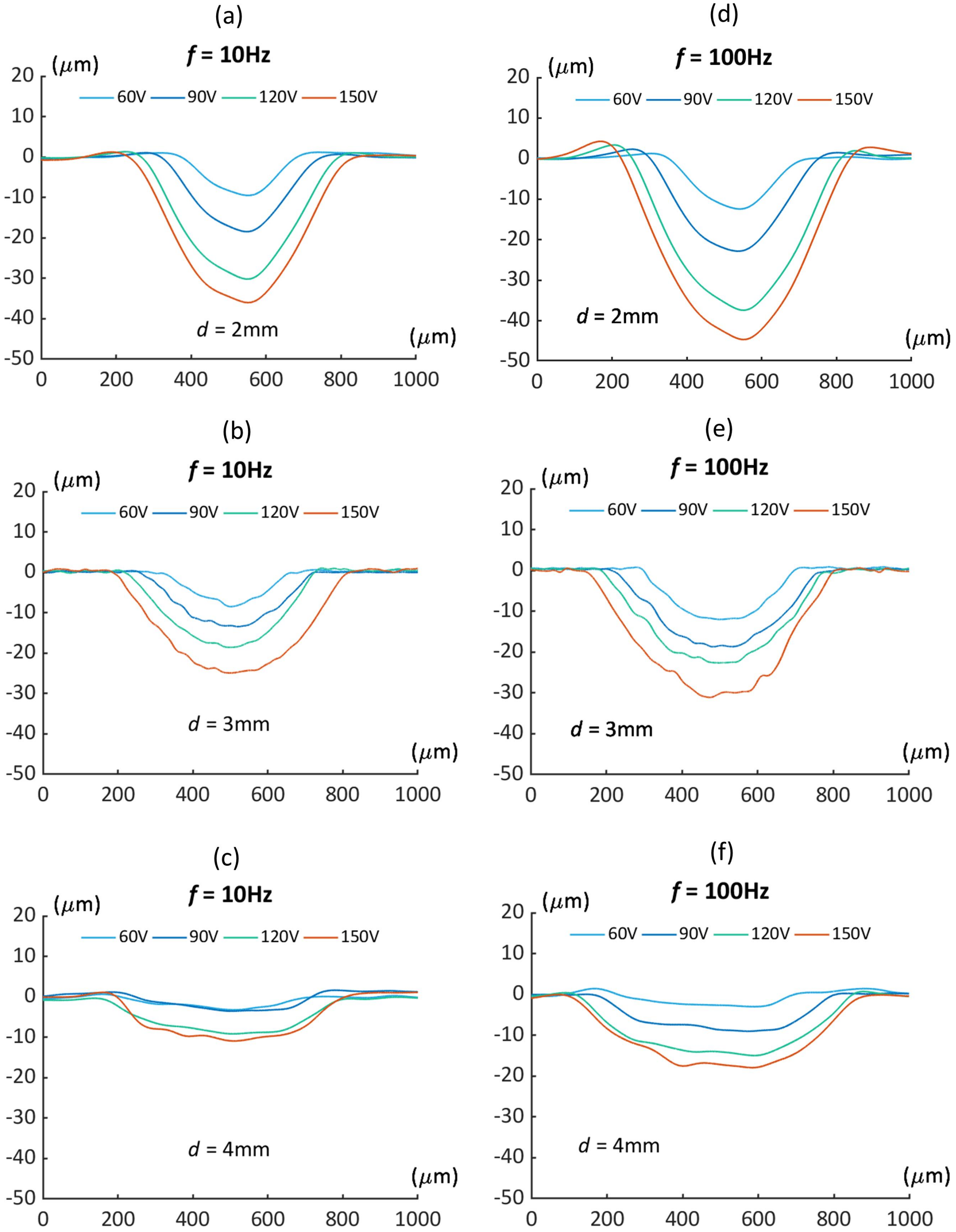

Figure 4.13 Cross-section profiles of permanent indentations at different vibration conditions using steel samples at V_{pp} = 60, 90, 120, 150 V. (a) – (c): d = 2 – 4 mm and f = 10 Hz; (d) – (f): d = 2 – 4 mm and f = 100 Hz.

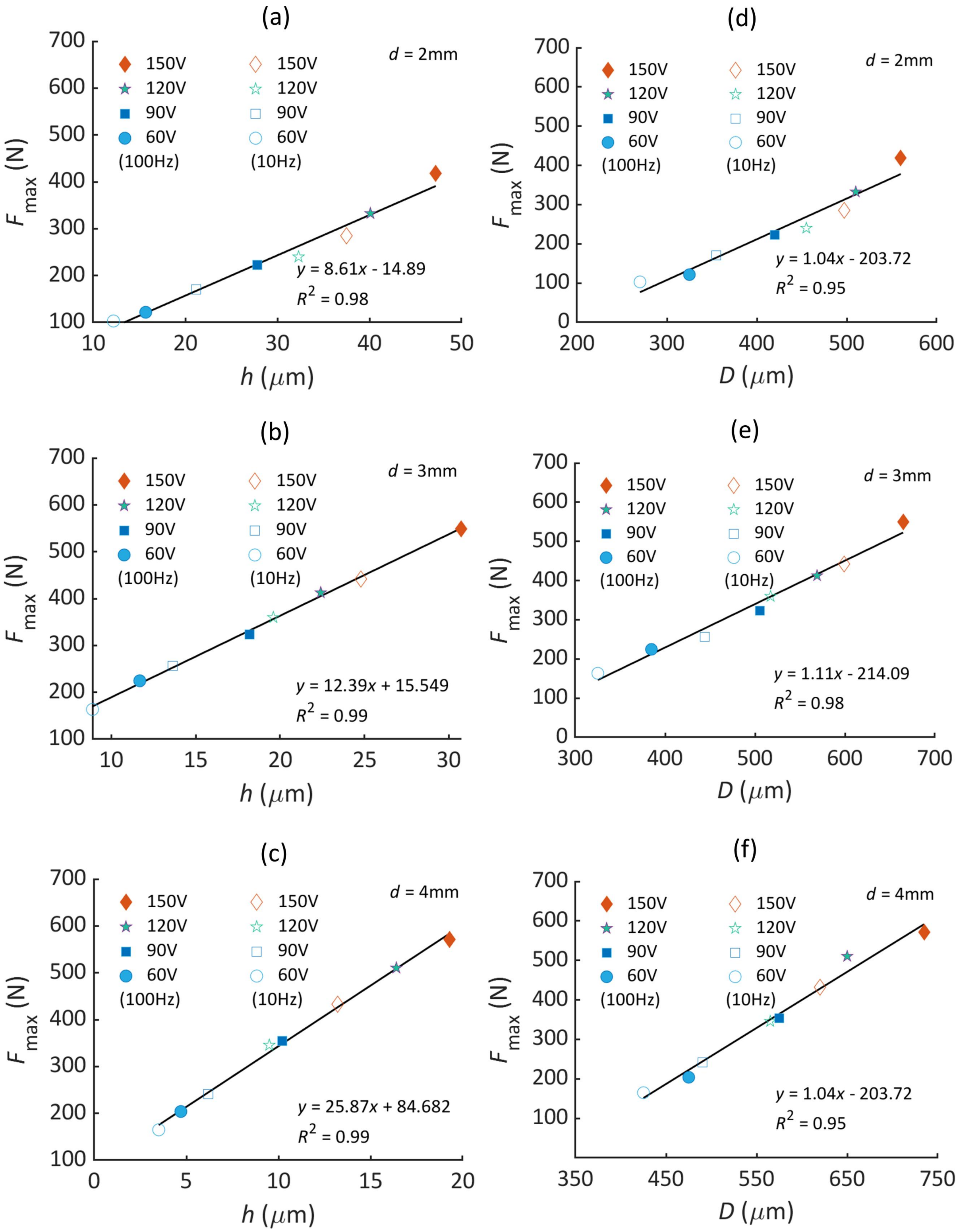

Figure 4.14 The correlation of striking peak force with the depth (upper row) and diameter (bottom row) of the permanent indentation in single-spot vibration striking at d = 2 – 4 mm using steel samples. (a) – (c): depth - force; (e) – (f): diameter - force.

samples, the experimental results show that the four variables (F_{max}, u_{max}, h, D) also increase with the increase of driving voltage. Higher vibration frequency results in greater striking force and lower vibration displacement. The maximum striking force is about 550 N in the steel samples, while it is only about 330N in the copper samples due to lower strength.

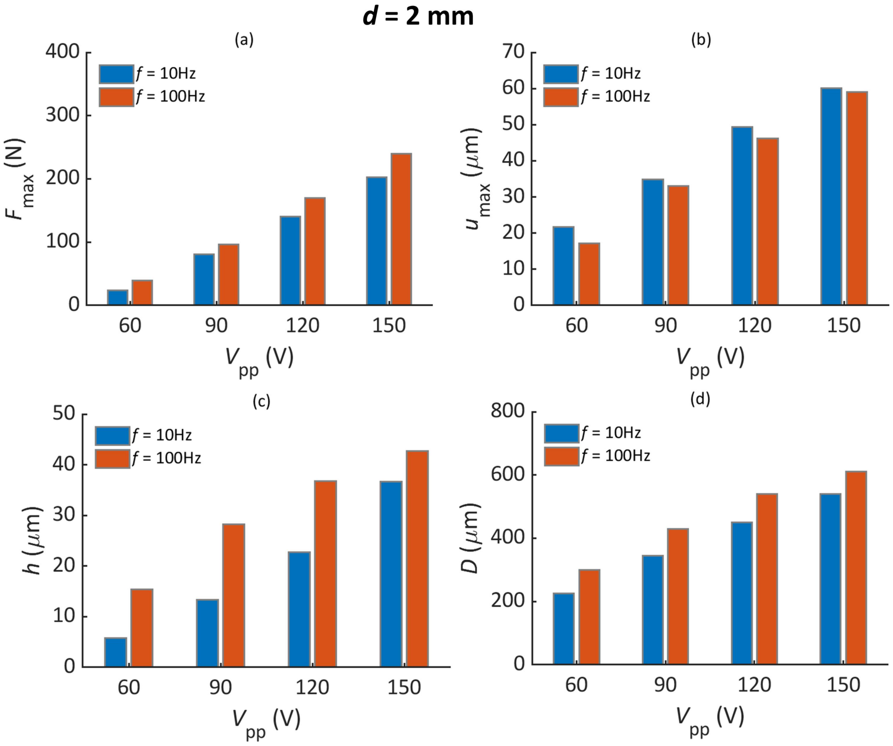

Figure 4.15 Summary of (a) striking peaking force, (b) maximum tool vibration displacement, (c) the depth, and (d) the diameter of a permanent indentation in single-spot vibration striking using copper samples at V_{pp} = 60, 90, 120, 150 V, f = 10, 100 Hz, d = 2 mm.

F_{max}, u_{max}, h, and D with a given V_{pp} = 150 V at d = 2, 3, 4 mm are selected to compare the effect of tool geometry of these variables more efficiently, as demonstrated in Fig. 4.18. Observe that F_{max} in Fig. 4.18a strictly increases and u_{max} in Fig. 4.18b strictly decreases as d increases, which is consistent with the results in the steel samples. However, the h in Fig. 4.18c does not reduce strictly with the increment of the tool diameter. Likewise, D does not increase strictly as the tool diameter increases. The values of h and D in d = 3 mm are outliers, which is inconsistent with the results in the steel samples. These outliers may be correlated with the initial surface state of the workpieces and the setting of the initial Z value. In the steel samples, the surface was ground before the PVST experiments, so it had a very low initial surface roughness. While for the copper

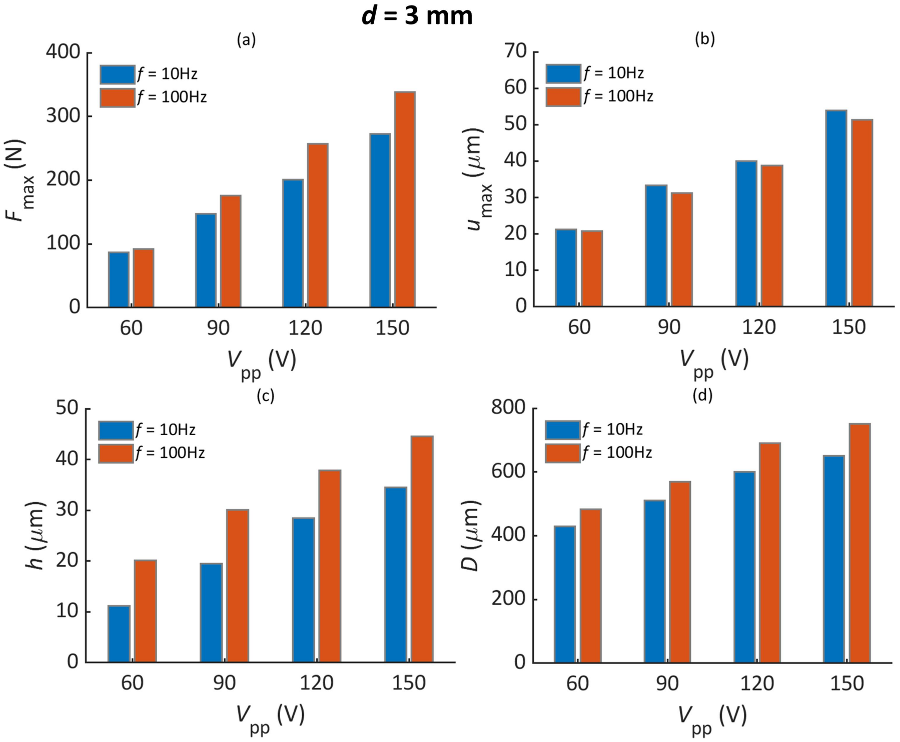

Figure 4.16 Summary of (a) striking peaking force, (b) maximum tool vibration displacement, (c) the depth, and (d) the diameter of a permanent indentation in single-spot vibration striking using copper samples at V_{pp} = 60, 90, 120, 150 V, f = 10, 100 Hz, d = 3 mm.

samples, the surface was machined without grinding before the PVST experiments. The relatively rough surface in the copper samples might cause the Z difference when setting the Z value, which can apply a preload on the surface if it is not consistent at different surface locations due to the roughness. The preload will increase the striking depth and plastic deformation, leading to a larger depth and width. In this case, the striking force at d = 3 mm could be more significant than that at d = 2 mm, and the indentation's corresponding permanent depth is also more prominent, as well as the width.

Furthermore, when comparing the elastic recovery (= u_{max} - h) of the indentation at identical experimental conditions but using different materials, it is found that the elastic recovery in the copper samples (Fig. 4.15 - Fig. 4.17) is more significant than that in the steel samples (Fig. 4.8 - Fig. 4.10). It is expected since steel has a higher Young's modulus than copper, which is more capable of resisting elastic deformation.

Figure 4.19 shows the resulting permanent indentations on the surface at the vibration conditions

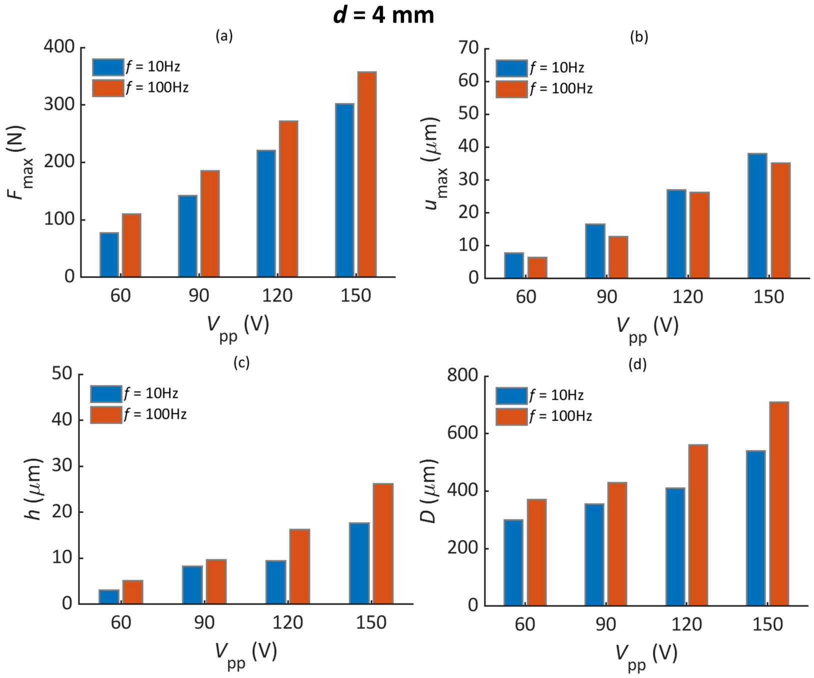

Figure 4.17 Summary of (a) striking peaking force, (b) maximum tool vibration displacement, (c) the depth, and (d) the diameter of a permanent indentation in single-spot vibration striking using copper samples at V_{pp} = 60, 90, 120, 150 V, f = 10, 100 Hz, d = 4 mm.

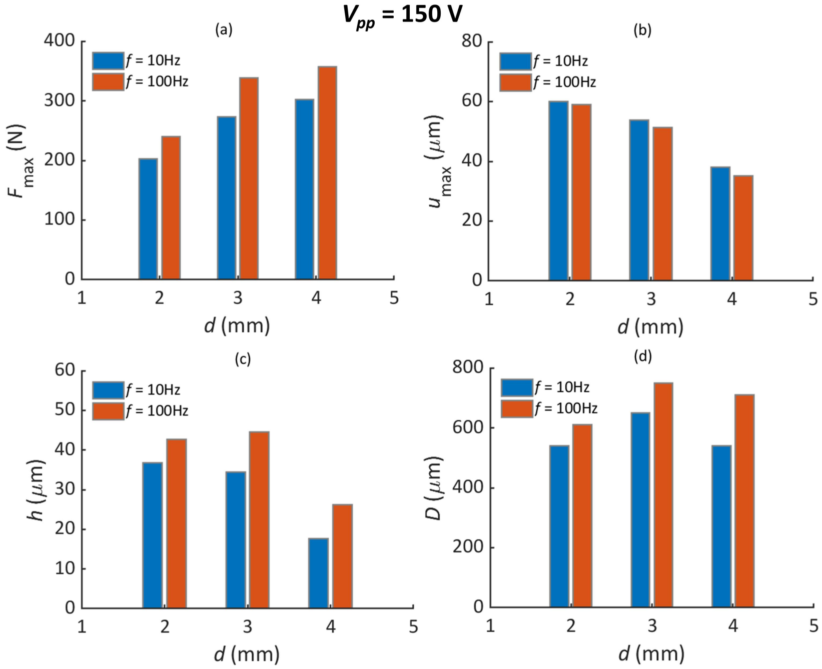

Figure 4.18 Summary of (a) striking peaking force, (b) maximum tool vibration displacement, (c) the depth, and (d) the diameter of a permanent indentation in single-spot vibration striking using copper samples at V_{pp} = 150 V, f = 10, 100 Hz, d = 2, 3, 4 mm.

of f = 10, 100 Hz, V_{pp} = 60, 90, 120, 150 V, d = 3 mm using copper samples. It is observed that the diameter of the indentation is positively correlated with the driving voltage and vibration frequency.

Figure 4.20 shows the cross-sectional profiles of the permanent indentations using copper samples at the same vibration conditions in Fig. 4.13. The increasing trend of h and D with V_{pp} still can be observed clearly. Higher frequency also leads to larger h and D. The relationships of the depth and width with the tool diameter are consistent with the results in Fig. 4.15 - Fig. 4.17, where the depth and width at d = 3 mm are more significant than that in d = 2 mm. Also, it is observed that the permanent indentation at the condition of f = 10 Hz, V_{pp} = 60 V, d = 4 mm is very shallow, which only creates a depth of 2.1 μm.

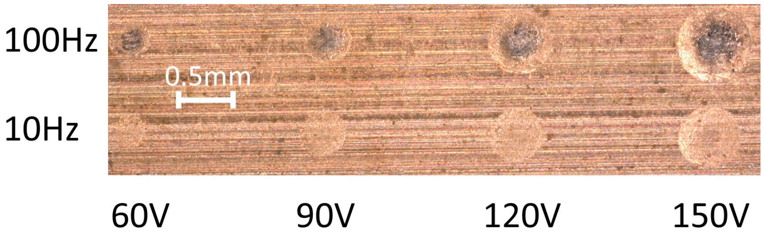

Figure 4.19 Optical photos of the permanent indentations created in single-spot vibration striking at various vibration conditions (f = 10, 100 Hz, V_{pp} = 60, 90, 120, 150 V, d = 4 mm) using copper samples.

Figure 4.21 shows how F_{max} is related with h and D, respectively. It is found that the size of the permanent indentation generated on the surface is linearly dependent on the peak force of the strike. It indicates that the linear force relationship with indentation size holds for different materials in PVST.

4.3 One-dimensional (1D) scan vibration striking

Scan speed v_s and path interval d_p (similar to indentation offset distance d_s) are crucial factors for better quality control in striking-based surface treatment. It is challenging to precisely control hand-held devices due to the high variability of human operations. Typically, v_s is an average speed instead of a constant speed during the striking process in those treatments, and d_p can only be determined empirically. For CNC-assisted devices, these two factors can be precisely controlled to generate different combinations of the parameters, i.e., d_p = 30 μm and v_s = 1000

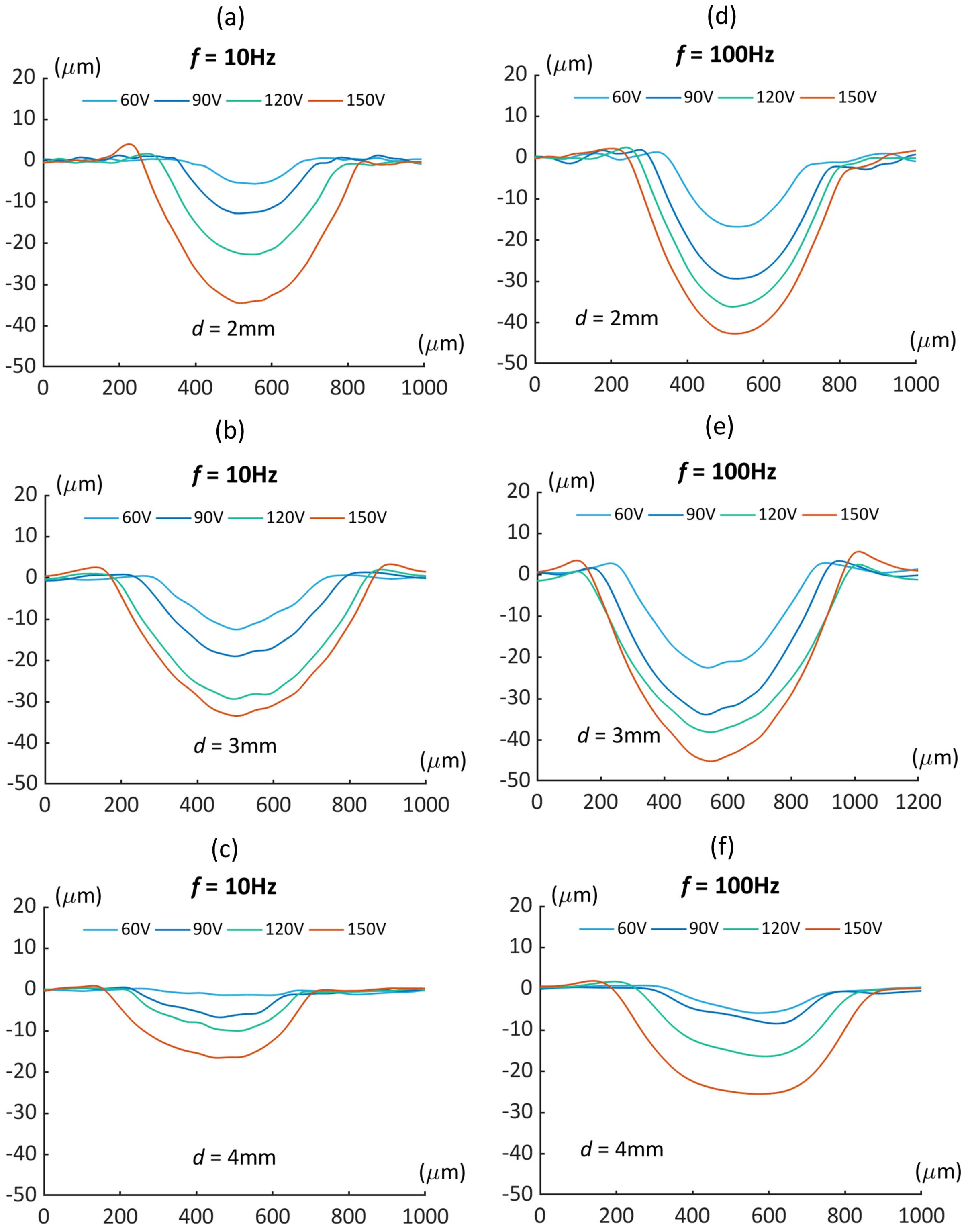

Figure 4.20 Cross-section profiles of permanent indentations at different vibration conditions using copper samples. (a) – (c): $d = 2 - 4$ mm and $f = 10$ Hz; (d) – (f): $d = 2 - 4$ mm and $f = 100$ Hz.

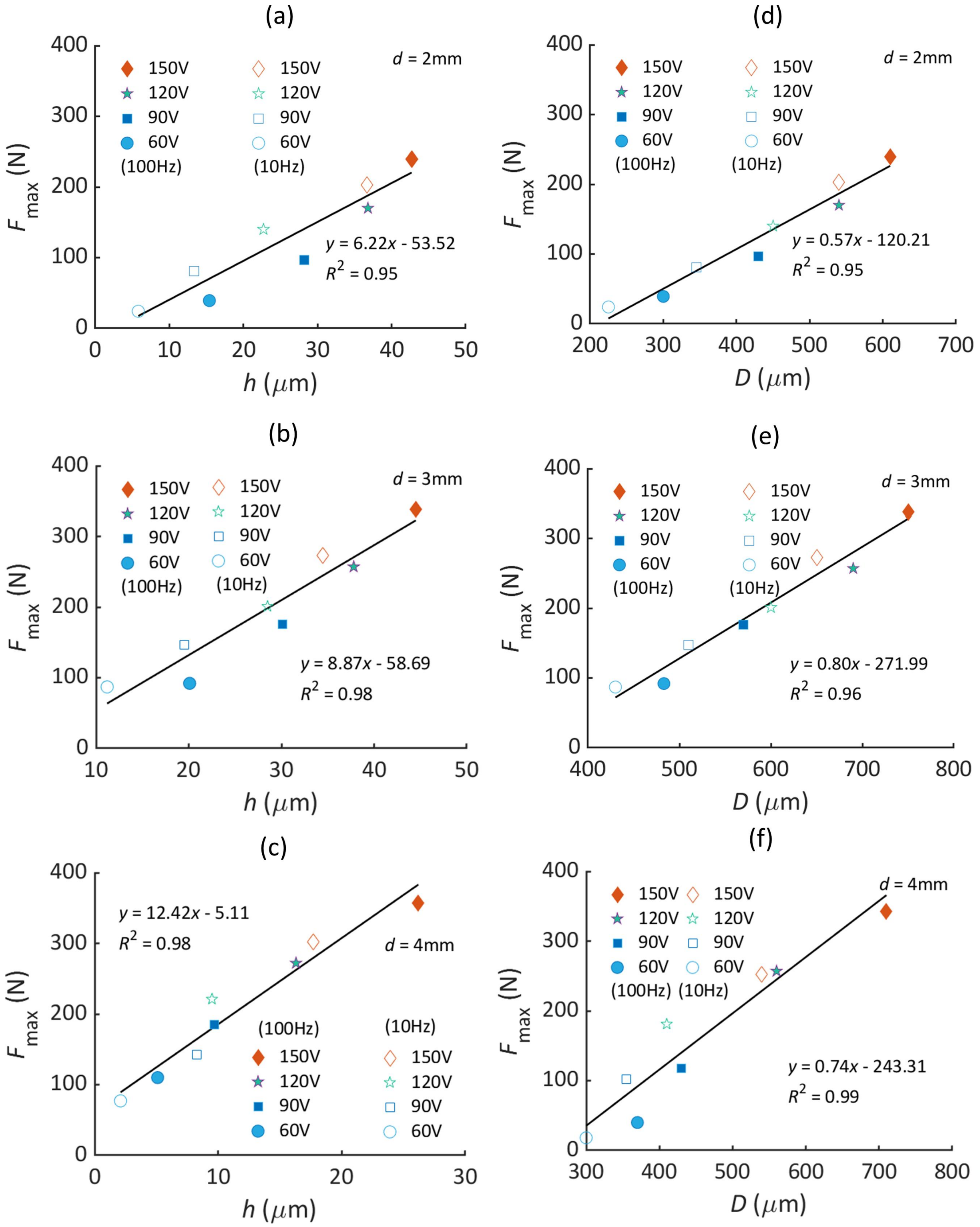

Figure 4.21 The correlation of striking peak force with the depth (upper row) and diameter (bottom row) of the permanent indentation in single-spot vibration striking using copper samples at d = 2 – 4 mm. (a) – (c): depth - force; (e) – (f): diameter - force.

mm/min [47, 99], d_p = 10 μm or 70 μm and v_s = 2000 mm/min [48, 110, 112], d_p = 10 μm and v_s = 3000 mm/min [98]. However, these references provided no guidelines for the proper scan speed selection and path interval selection. Specifically, the effect of scan speed on surface properties is not entirely understood and quantified, as two different conclusions exist about how the scan speed affects surface finish [49, 104, 113]. In the study by Farrah et al. [49], they utilized finite element simulation under UNSM to study the effect of v_s (2400 mm/min and 1200 mm/min) on surface roughness. They concluded that the surface roughness decreases with decreasing v_s. Bohdan N. Mordyuk et al. [104] explored the effect of scan speed on the surface roughness under UIP and the thickness of the nanocrystalline surface layer. The results suggested that higher v_s would diminish the surface roughness and the thickness of the nanocrystalline surface layer. The results of the effect of scan speed on the surface roughness in [49, 104] are consistent. Recent research carried out by J. Schubnell et al. [113] proposed that the term "coverage" represents the overlap degree of the successive indentations, which is closely related to v_s in HFMI and studied the effect of the coverage on the surface roughness. The results revealed that the surface roughness does not decrease with increasing coverage. These inconsistent results indicate that the investigation of the effect of scan speed on the surface finish appears particularly necessary. Therefore, in the one-dimensional (1D) scan vibration striking experiment, the effect of different scan speeds, which correspond to different overlap ratios (as defined in Fig. 3.7) on the surface properties, are explored.

In this experiment (Fig. 4.22), the tool vibration is turned on after the tool position in Z is set to zero (Z = 0). The workpiece is moved horizontally along the X-axis at a controlled speed (v_s). It leads to the vibrating tool scanning the surface while imposing successive strikes along a straight tool path. The offset distance (d_s) between two successive strikes is dependent on the vibration frequency (f) and the scan speed (v_s) as

$$d_s = \frac{v_s}{f} \tag{4.1}$$

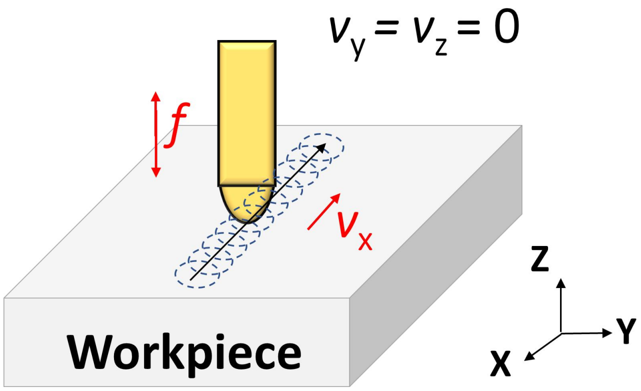

Figure 4.22 Schematic of 1D scan vibration striking.

4.3.1 1D scan vibration striking using mild steel workpieces

Figure 4.23 shows the surface grooves created with the vibration conditions of f = 100 Hz, V_{pp} = 150 V, and d = 3 mm at four scan speeds v_s = 3300, 2475, 1650, 825 mm/min using steel workpieces. These scan speeds are selected to achieve the striking overlap ratios of 0, 0.25, 0.5, and 0.75, respectively. The overlap ratio (r_o) is defined in Eq. 3.5. According to Eq. 4.1 and Eq. 3.5, a lower v_s leads to a smaller d_s and thus a higher r_o. Fig. 4.23b and Fig. 4.23c show that the 1D scan vibration striking results in a uniform indentation pattern along the tool path at each scan speed. The higher the overlap ratio, the smoother the surface in the groove.

Figures. 4.24a – 4.24c show the longitudinal section profiles of the surface grooves created in 1D scan vibration striking at various striking overlap ratio conditions using steel samples (f = 100 Hz, V_{pp} = 150 V, d = 2 – 4 mm, r_o = 0, 0.25, 0.5, 0.75). The indentation spacing d_s measured from these profiles for r_o = 0, 0.25, 0.5, and 0.75 is shown in Table. 4.3. The measured d_s values agree with the calculated d_s values using Eq. 4.1. It indicates that the vibration striking with tool scan motion can be accurately controlled. Furthermore, the measured peak-to-valley height (Rz) and line roughness (Ra) (Table. 4.4) computed using the longitudinal section profiles decrease with increasing r_o, showing that higher r_o leads to a smoother surface in the groove. Fig. 4.24d – Fig. 4.24f show the transverse section profiles of these grooves (perpendicular to the tool scan direction) taken at the center of each indentation, corresponding to the maximum depth location in the groove. As observed, the transverse section profile is not much affected by r_o. The profile appears nearly the same for different r_o. The groove depth (h) measured from the undeformed

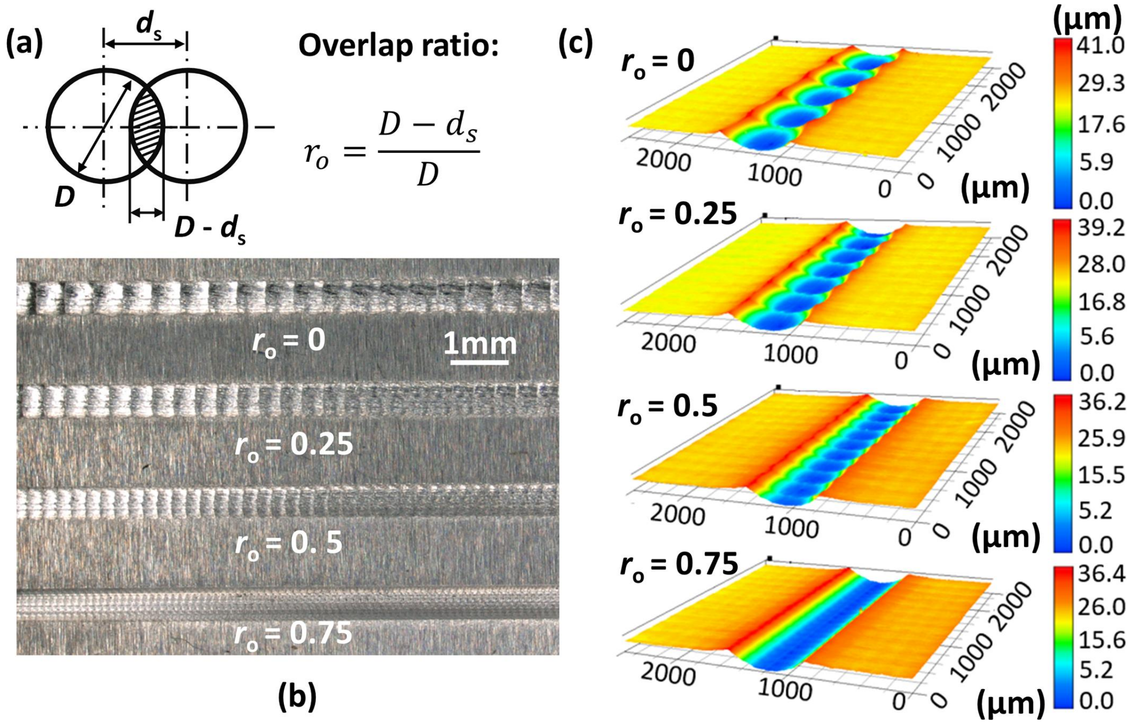

Figure 4.23 (a) Definition of striking overlap ratio; (b) optical photo and (c) measured topography of the surface grooves created in 1D scan vibration striking using steel samples: f = 100 Hz, V_{pp} = 150 V, d = 3 mm, r_o = 0, 0.25, 0.5, 0.75.

surface is about 30 μm, 24 μm, and 11 μm at d = 2 - 4 mm, respectively. The groove width (W) measured using the distance between the two ridges is about 550 μm, 645 μm, and 705 μm at d = 2 - 4 mm, respectively. The two ridges are formed by displacing material within the groove. The ridge size increases slightly with r_o as more material tends to be displaced, creating a smoother surface in the groove. Note that the left ridges at d = 3 mm are slightly higher than the opposite ridges for all overlap ratio cases, which is likely caused by the imperfect mounting of the workpiece in the experiment that results in slight tilting of the initial surface.

Table 4.3 Indentation spacing at different overlap ratios and tool diameters using steel samples.

	d = 2 mm		d = 3 mm		d = 4 mm	
r_o	Cal. d_s (μm)	Mea. d_s (μm)	Cal. d_s (μm)	Mea. d_s (μm)	Cal. d_s (μm)	Mea. d_s (μm)
0	510	530 ± 16	550	516 ± 8	735	726 ± 3
0.25	382.5	396 ± 13	412.5	392 ± 12	551.3	534 ± 17
0.5	255	266 ± 9	275	269 ± 13	367.5	261 ± 8
0.75	127.5	128 ± 3	137.5	131 ± 8	183.8	183 ± 2

Figures 4.25 - 4.27 show the measured forces corresponding to these grooves. There are two

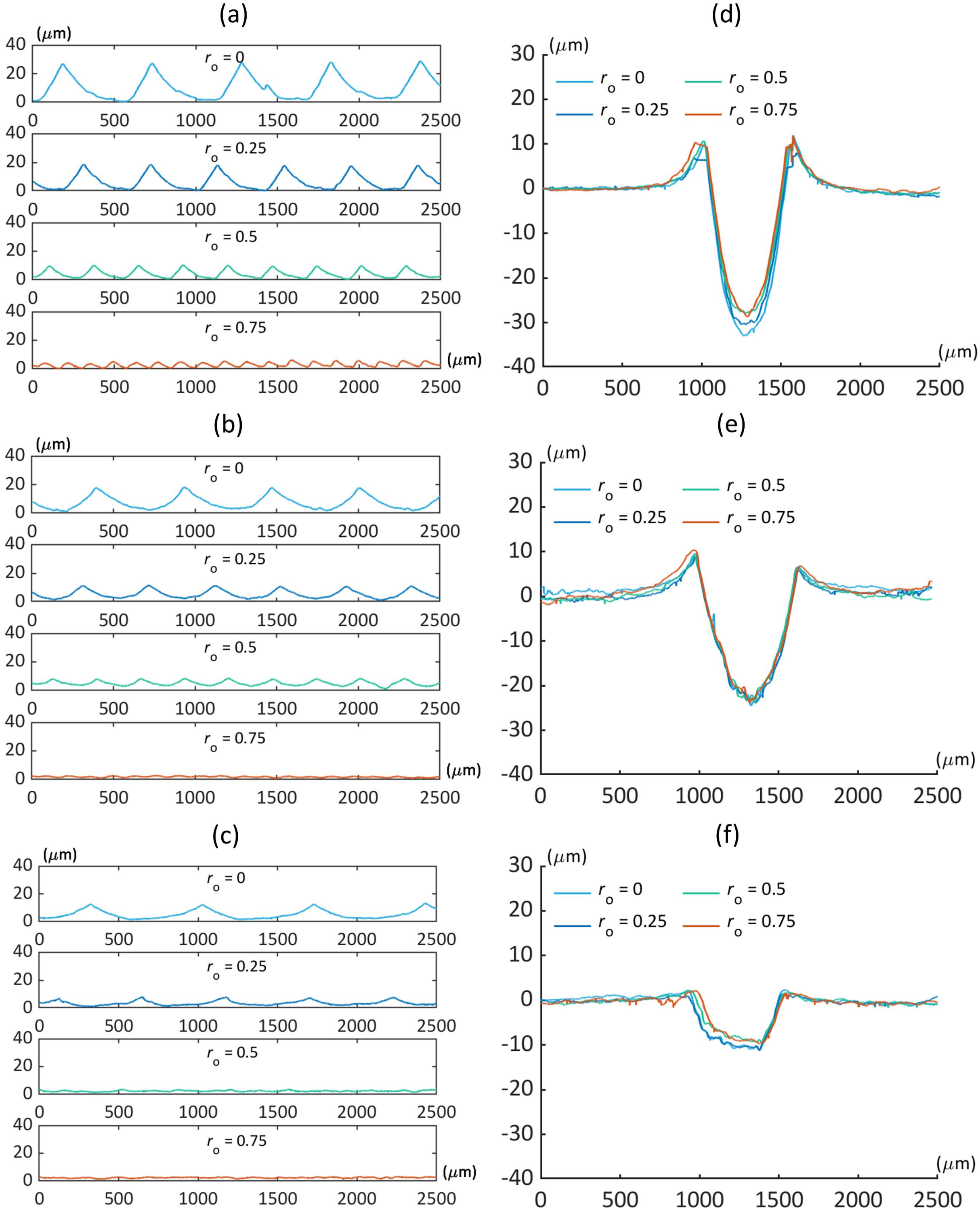

Figure 4.24 (a) – (c) Longitudinal and (d) – (f) transverse section profiles of surface grooves in 1D scan vibration striking using steel samples: f = 100 Hz, V_{pp} = 150 V, d = 2 – 4 mm, r_o = 0, 0.25, 0.5, 0.75.

Table 4.4 Measured Rz and Ra at different overlap ratios and tool diameters using steel samples.

	d = 2 mm		d = 3 mm		d = 4 mm	
r_o	Ra (μm)	Rz (μm)	Ra (μm)	Rz (μm)	Ra (μm)	Rz (μm)
0	7.1	26.7	3.9	17.0	2.6	10.6
0.25	4.5	17.3	2.6	10.5	1.3	5.7
0.5	2.3	8.8	1.5	7.6	0.7	1.5
0.75	1.2	4.1	0.6	1.6	0.3	1.1

force components during 1D scan vibration striking: the striking force (F_z) in the Z direction and the sliding force (F_x) in the X direction. Both forces are highly repetitive in the successive striking cycles, which indicates that the process is relatively stable. The primary force is the striking force which is not significantly affected by r_o. The secondary force is the sliding force which is much smaller than the striking force. The sliding force is generated due to the horizontal scan motion of the tool. Unlike the striking force, which has a symmetrical profile and is nearly independent of r_o, the sliding force decreases with increasing r_o, and the force profile becomes more asymmetrical as r_o increases. The asymmetrical profile indicates that the sliding force increases even when the tool pulls from the surface after reaching the maximum vibration displacement. This asymmetry is likely caused by the generation of pile-up material in front of the tool due to sliding. The sliding force depends on the effective engagement depth between the tool and the workpiece surface during sliding. Besides the tool vibration displacement, the effective engagement depth is also affected by the pile-up of material in front of the tool. While the tool is retracting from its maximum vibration displacement, which tends to reduce the effective engagement depth, the continuous sliding action keeps generating pile-up material in front of the tool, increasing the effective engagement depth. As a result, the occurrence of the maximum engagement depth (corresponding to the sliding force peak) lags the maximum vibration displacement (corresponding to the striking force peak), resulting in the asymmetrical profiles of the sliding force.

Besides varying r_o, the 1D scan vibration striking experiment has also been conducted while varying V_{pp} and d. Fig. 4.28 summarizes all cases' measured groove depth (h) and width (W). It shows that the groove depth and width primarily depends on V_{pp} (i.e., vibration amplitude) and less on r_o. The groove depth decreases with a larger tool diameter, especially a significant reduction in

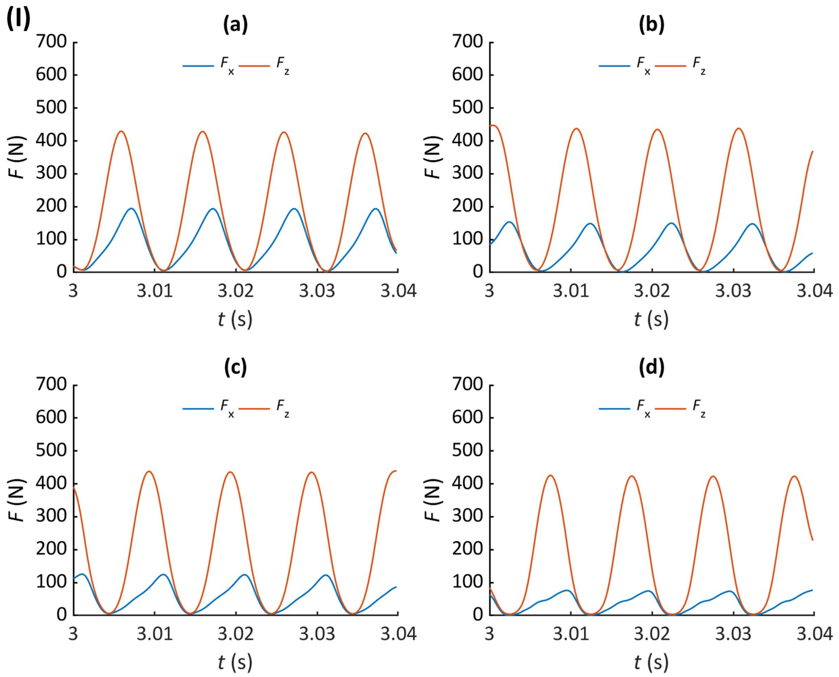

Figure 4.25 The history of sliding force and striking force in four cycles using steel samples at d = 2 mm, f = 100 Hz, V_{pp} = 150 V: (a) – (d) for r_o = 0, 0.25, 0.5, 0.75.

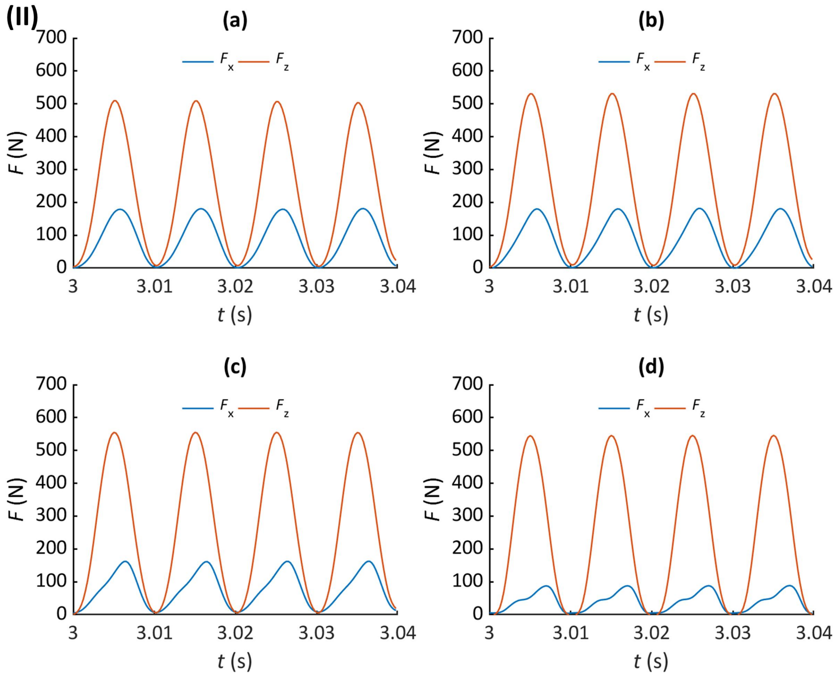

Figure 4.26 The history of sliding force and striking force in four cycles using steel samples at d = 3 mm, f = 100 Hz, V_{pp} = 150 V: (a) – (d) for r_o = 0, 0.25, 0.5, 0.75.

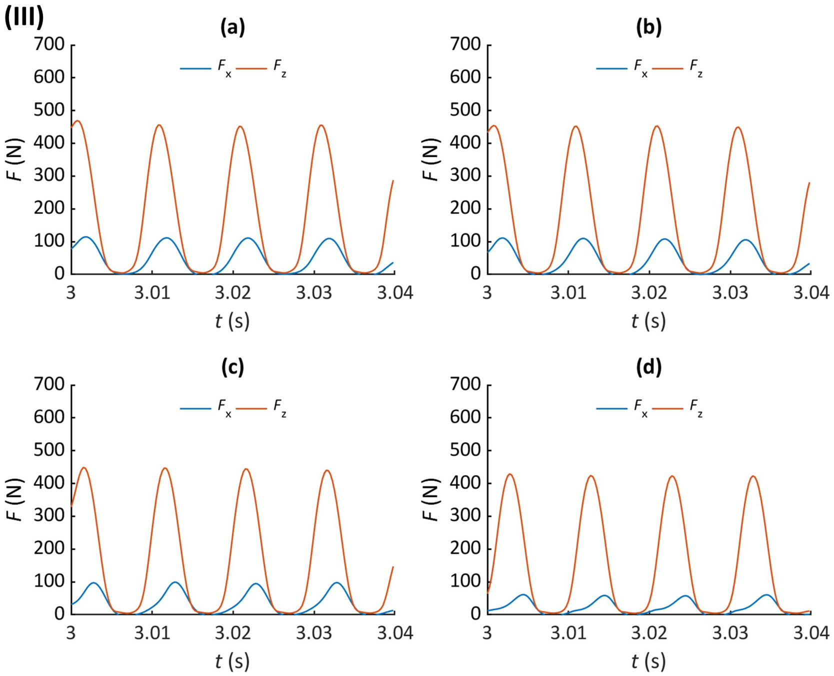

Figure 4.27 The history of sliding force and striking force in four cycles using steel samples at d = 4 mm, f = 100 Hz, V_{pp} = 150 V: (a) – (d) for r_o = 0, 0.25, 0.5, 0.75.

steel samples at d = 4 mm. The groove width increases as the tool diameter increases, likely caused by a larger contact area between the tool and the workpieces.

Moreover, it is found again that the depth and width of the groove are linearly dependent on the striking peak force (Fig. 4.29) despite the difference in the slope from the single-spot vibration striking experiment (Fig. 4.14). Therefore, the force signal can also monitor the indentation deformation resulting from each individual strike with tool scan motion for a given set of machine parameters.

4.3.2 1D scan vibration striking using OFHC copper workpieces

Figure 4.30 shows the surface grooves created under the vibration conditions of f = 100 Hz, V_{pp} = 150 V, and d = 2 mm at four overlap ratios (r_o = 0, 0.25, 0.5, 0.75) using OFHC copper workpieces. Fig. 4.30b and Fig. 4.30c show that the 1D scan vibration striking results in a uniform indentation pattern along the tool path at each overlap ratio. The higher the overlap ratio, the smoother the surface in the groove. The uniform distributions of the successive indentations are very close to the distributions in the steel samples (see Fig. 4.23), which showcases the ability of PVST to precisely control the striking effect on the samples with initially smooth surfaces despite

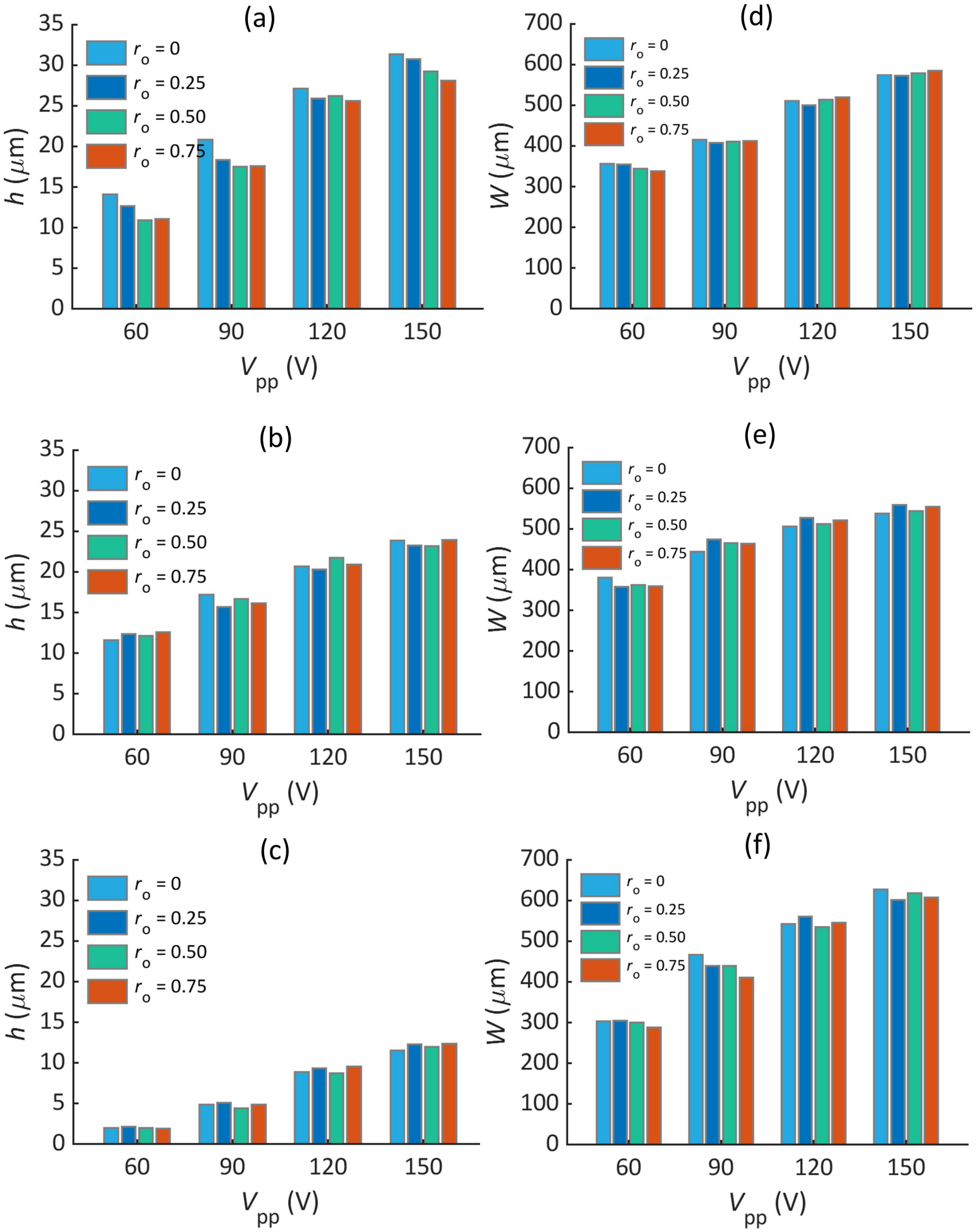

Figure 4.28 Comparisons of (a) – (c) the depth and (d) – (f) width of steel sample surface grooves resulting from 1D scan vibration striking at various V_{pp} and r_o: f = 100 Hz, d = 2 - 4 mm.

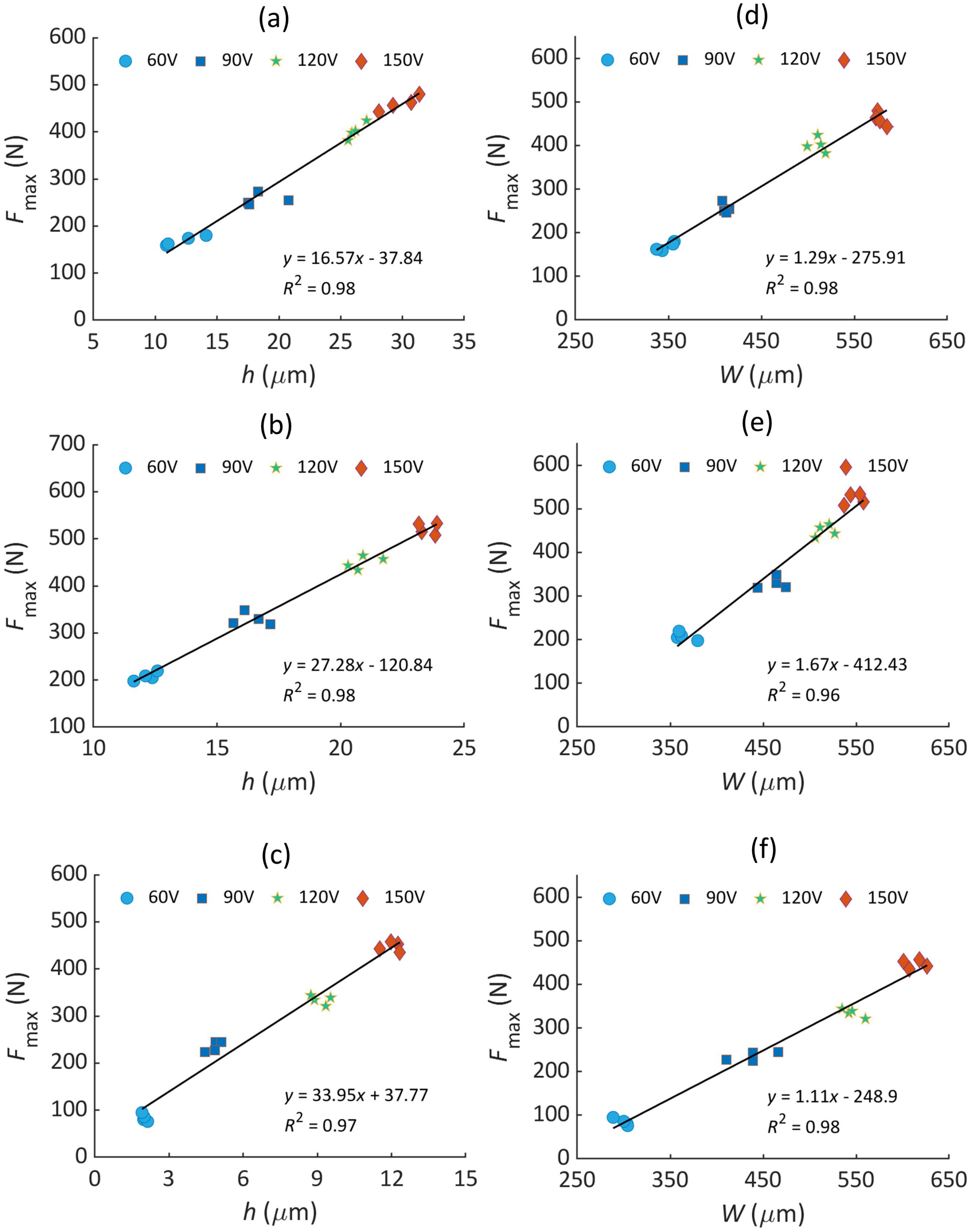

Figure 4.29 The correlation of the striking peak force with (a) – (c) the depth and (d) – (f) width of the surface groove in 1D scan vibration striking experiment at different driving voltages using steel samples: d = 2 – 4 mm.

different materials used. It is also observed that the depth of the grooves is more prominent in the copper samples than in the steel samples, which causes a higher height value of the grooves' ridges displaced by the striking tool's sliding effect.

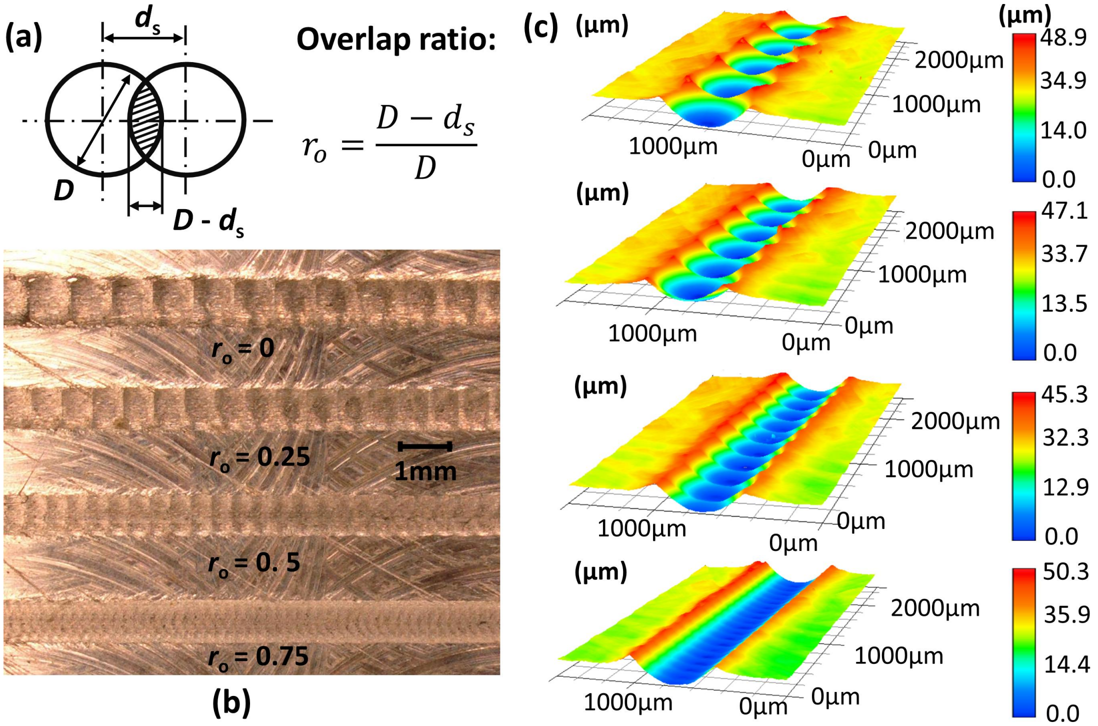

Figure 4.30 (a) Definition of striking overlap ratio; (b) optical photo and (c) measured topography of the surface grooves created in 1D scan vibration striking at various striking overlap ratios using copper samples: f = 100 Hz, V_{pp} = 150 V, d = 2 mm, r_o = 0, 0.25, 0.5, 0.75.

Figures 4.31a – 4.31c show the longitudinal section profiles of the surface grooves created in 1D scan vibration striking at various overlap ratio conditions using copper samples (f = 100 Hz, V_{pp} = 150 V, d = 2 – 4 mm, r_o = 0, 0.25, 0.5, 0.75). The indentation spacing d_s measured from these profiles for different overlap ratios are shown in Table 4.5. The measured d_s values agree with the calculated d_s values using Eq. 4.1, which are consistent with the results of the steel samples. The measured values of Rz and Ra illustrated in Table 4.6 for the longitudinal section profiles reduce with the increment of r_o, sharing the same variation trend as in the steel samples. Fig. 4.31d – Fig. 4.31f show the groove's transverse section profiles taken at the center of each indentation which corresponds to the maximum depth location in the groove. Consistent with the results of the steel samples, the transverse section profile is not much affected by r_o. The profile appears nearly the same for different r_o at d = 2 mm. Observe that there is a slight difference in the profiles at d = 3 mm for different overlap ratios and a relatively large profile at d = 4 mm and r_o = 0. It could be caused by the relatively rough surface of the copper samples compared to the steel samples with a smoother initial surface state. The groove depth (h) measured from the undeformed surface is about 28 μm, 24 μm, 21 μm at d = 2 - 4 mm, respectively. The groove width measured by the distance between the two ridges is about 605 μm, 670 μm, and 803 μm at d = 2 - 4 mm, respectively. Note that the left ridges at d = 3 mm and the right ridges at d = 2 mm are slightly higher than the opposite ridges for all overlap ratio cases, which the imperfect mounting of the workpiece might cause in the experiment that results in slight tilting of the initial surface.

Table 4.5 Indentation spacing at different overlap ratios and tool diameters using copper samples.

	d = 2 mm		d = 3 mm		d = 4 mm	
r_o	Cal. d_s (μm)	Mea. d_s (μm)	Cal. d_s (μm)	Mea. d_s (μm)	Cal. d_s (μm)	Mea. d_s (μm)
0	540	537 ± 9	710	716 ± 16	740	745 ± 3
0.25	405	407 ± 10	532.5	521 ± 14	555	565 ± 11
0.5	270	270 ± 7	355	362 ± 2	370	376 ± 6
0.75	135	135 ± 4	177.5	185 ± 2	185	187 ± 1

Table 4.6 Measured Rz and Ra at different overlap ratios and tool diameters using copper samples.

	d = 2 mm		d = 3 mm		d = 4 mm	
r_o	Ra (μm)	Rz (μm)	Ra (μm)	Rz (μm)	Ra (μm)	Rz (μm)
0	6.9	25.7	6.1	22.8	3.6	14.1
0.25	4.7	16.7	3.5	14.2	2.0	6.8
0.5	2.3	9.2	1.5	7.3	0.7	2.8
0.75	0.8	3.5	0.7	1.3	0.4	1.1

Figures 4.32 - 4.34 show the measured forces corresponding to these grooves. The striking force (F_z) and the sliding force (F_x) are highly repetitive in successive striking cycles. Consistent with the results in the steel samples, the striking force is not significantly affected by r_o, and the sliding force is much smaller than the striking force. Due to the low strength in the copper samples, the striking force is smaller than that in the steel samples, but the sliding force in the two samples is similar. Based on the hardness results in Fig.5.21, the overlap ratio does not significantly affect the hardness, which means that the sliding forces are equivalent for different ratios. It is possible that the striking effect dominates the plastic deformation of the treated surface over the sliding

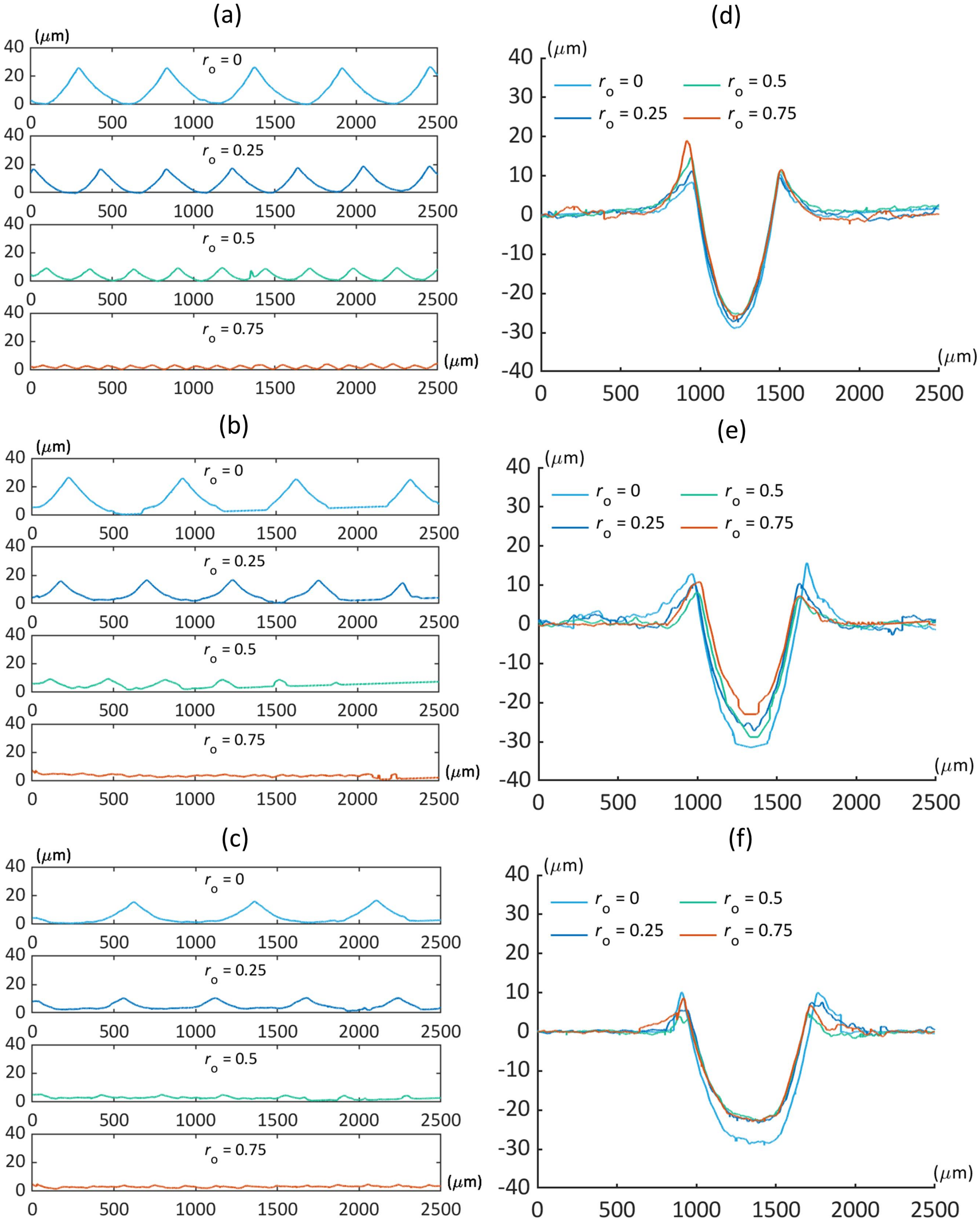

Figure 4.31 (a) – (c) Longitudinal and (d) – (f) transverse section profiles of surface grooves in 1D scan vibration striking using copper samples: f = 100 Hz, V_{pp} = 150 V, d = 2 – 4 mm, r_o = 0, 0.25, 0.5, 0.75.

effect. The symmetrical profile of the striking force and asymmetrical profile of the sliding force are still observed in the current results. Also, the sliding force reduces as the overlap ratio increases, indicating that the pile-up material and engagement effect during the PVST process is common for different materials, hence creating the asymmetrical profile of the sliding force.

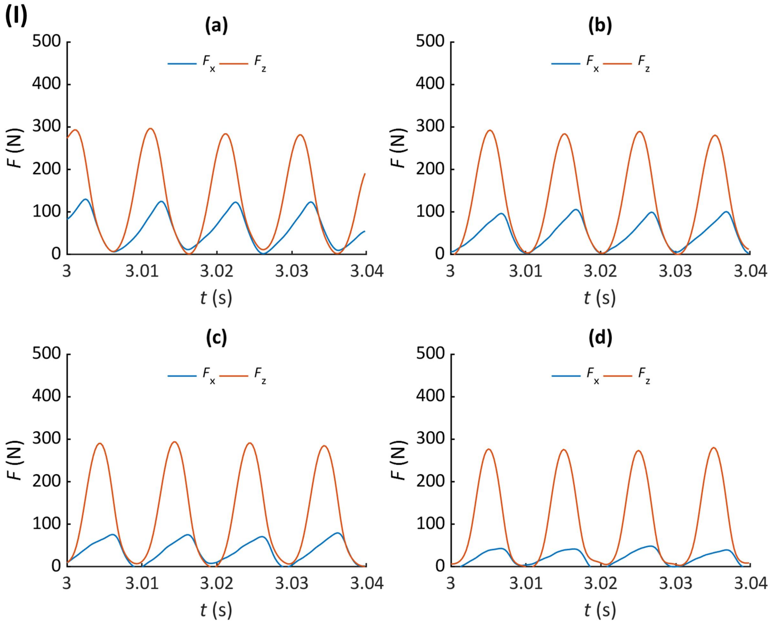

Figure 4.32 The history of sliding force and striking force in four cycles using copper samples at d = 2 mm, f = 100 Hz, V_{pp} = 150 V: (a) – (d) for r_o = 0, 0.25, 0.5, 0.75.

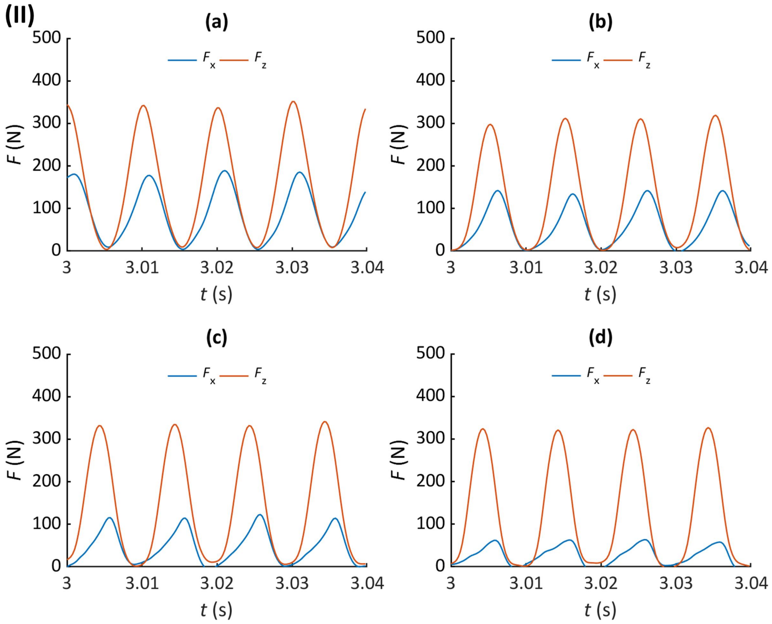

Figure 4.33 The history of sliding force and striking force in four cycles using copper samples at d = 3 mm, f = 100 Hz, V_{pp} = 150 V: (a) – (d) for r_o = 0, 0.25, 0.5, 0.75.

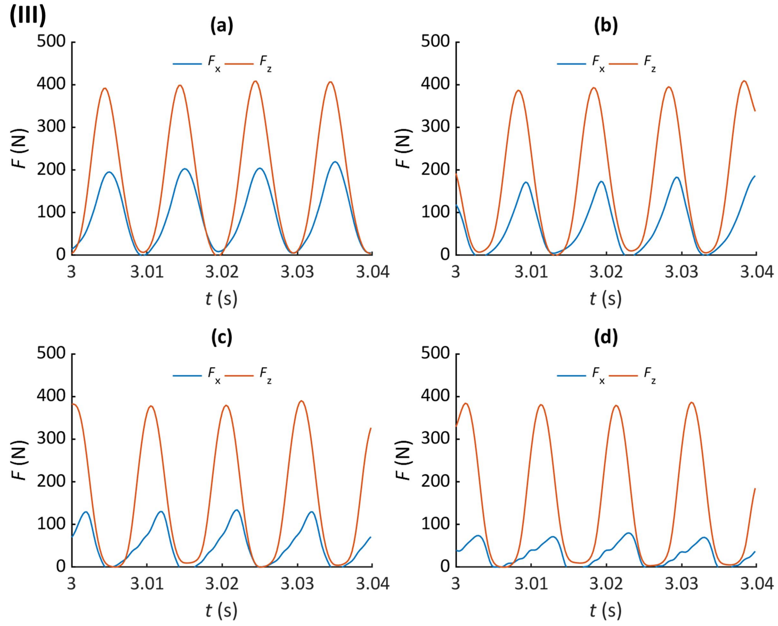

Figure 4.34 The history of sliding force and striking force in four cycles using copper at d = 4 mm, f = 100 Hz, V_{pp} = 150 V: (a) – (d) for r_o = 0, 0.25, 0.5, 0.75.

In addition, the 1D scan vibration striking experiment has also been conducted at different driving voltage and tool diameter conditions. Fig. 4.35 summarizes all cases' measured groove depth and width. Similar to the results of the steel samples, h and W are mainly correlated with V_{pp} and less with r_o. Consistent with the results of the steel samples, the groove depth decreases with a larger tool diameter in the results of the copper sample, except for a minor driving voltage condition of V_{pp} = 60 V, at which the groove depth is not influenced by the tool diameter greatly. Likewise, the groove width increases as the tool diameter increases, except for a minor driving voltage condition of V_{pp} = 60 V, at which the groove width is not significantly influenced by the tool diameter. It might be caused by the small vibration amplitude at a lower driving voltage condition and the extensive elastic recovery in the copper samples. The small vibration amplitude will not cause a large total deformation and there will be only a small part of permanent plastic deformation left after the elastic recovery of material. As demonstrated in Fig. 4.36, the linear relationship of the depth and width with the striking peak force is still achieved in the copper samples. In light of the linear relationships in Fig. 4.29 and Fig. 4.36, it reveals that the force signal can be used to monitor the indentation deformation under the current setting for these two materials, which is promising for feedback control to achieve the target surface deformation more precisely.

4.4 Discussion

The striking force and tool vibration displacement in PVST can be directly measured in real time. It is a significant advantage over the ultrasonic vibration surface treatment, for it offers an opportunity for real-time monitoring and control of the treatment process. Two kinds of linear force relationships found in PVST are beneficial in this regard. The first linear relationship is between the striking force and the reduction in tool vibration amplitude shown in Fig. 4.3. The amplitude reduction is due to the elastic deformation of the device assembly under the striking force. This linear relationship reflects the stiffness of the device assembly and is independent of workpiece material and striking tip geometry. It can be used to calculate the vibration amplitude during striking from the force signal:

$$u_{pp} = u_{pp}^{0} - \Delta u_{pp} = mV_{pp} - \frac{F_{max}}{K} \tag{4.2}$$

where m is the proportionality between the unloaded vibration amplitude and the input driving voltage; K is the proportionality between the striking peak force and the reduction in vibration amplitude, which is equivalent to the stiffness of the device assembly. Both m and K are the characteristics of the piezo vibration device and can be obtained by device calibration as shown in Fig. 3.5 and Fig. 4.3. Since V_{pp} is a directly controlled input parameter and F_{max} can be obtained from the measured force signal, it is then possible, based on Eq. 4.2, to monitor the vibration amplitude in PVST without directly measuring the vibration displacement but instead using the measured force signal. This will simplify the instrumentation for process monitoring.

The second linear force relationship is found between the striking force and the resulting indentation size (Fig. 4.14, Fig. 4.21, Fig. 4.29, and Fig. 4.36). These relationships should depend on the workpiece material and the striking tool tip geometry since both affect the plastic deformation induced on the surface. For the workpiece material (mild steel and OFHC copper) and striking tool (d = 2, 3, 4 mm) used in this dissertation, the force–indentation size relationship can be well approximated as linear. Theoretically, this relationship is nonlinear for a spherical-shaped indenter [114]. However, the indentation depth range of PVST is usually small (e.g., ~47 μm in

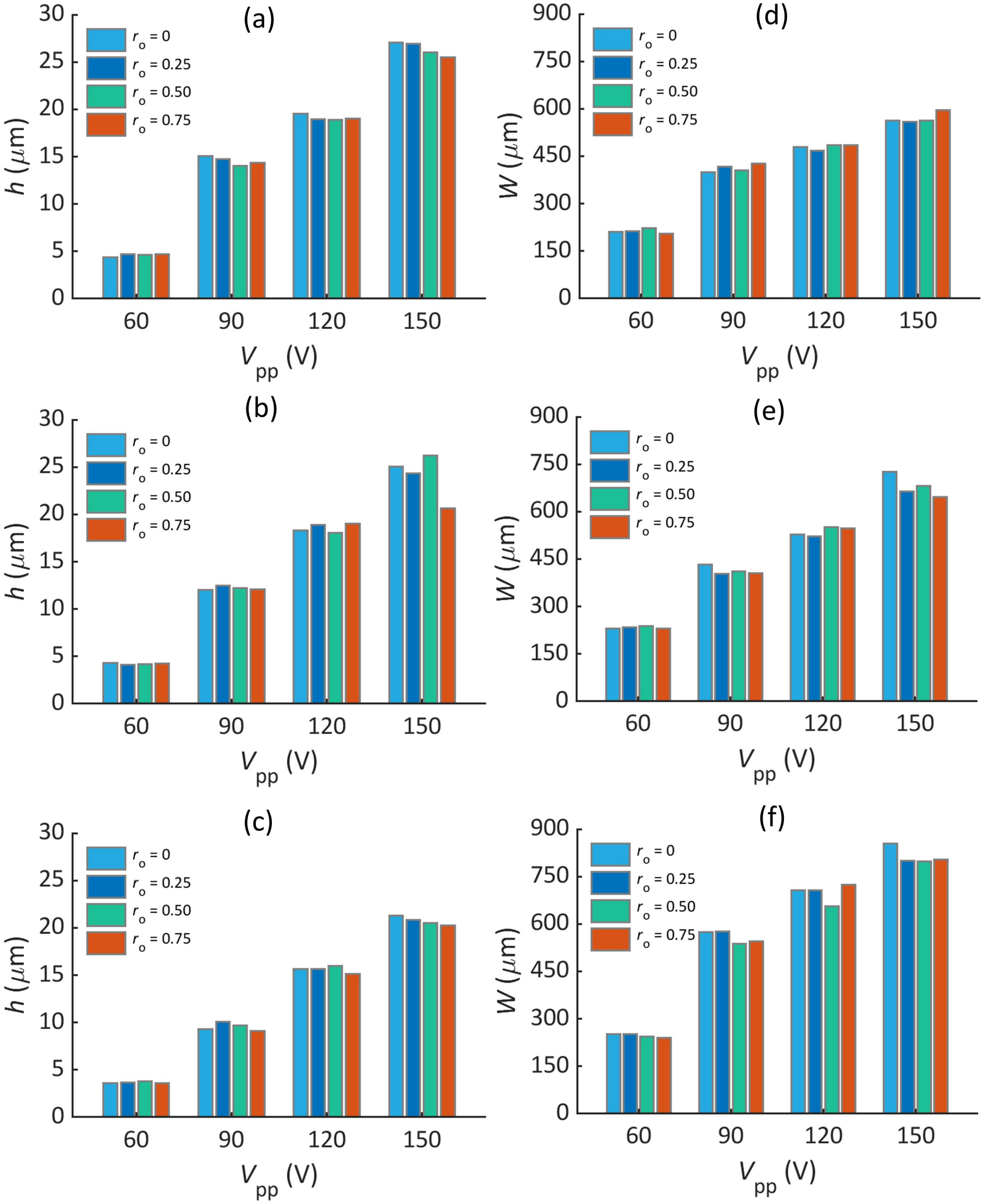

Figure 4.35 Comparisons of (a) – (c) the depth and (d) – (c) width of copper sample surface grooves resulting from 1D scan vibration striking at various V_{pp} and r_o: f = 100 Hz, d = 2 - 4 mm.

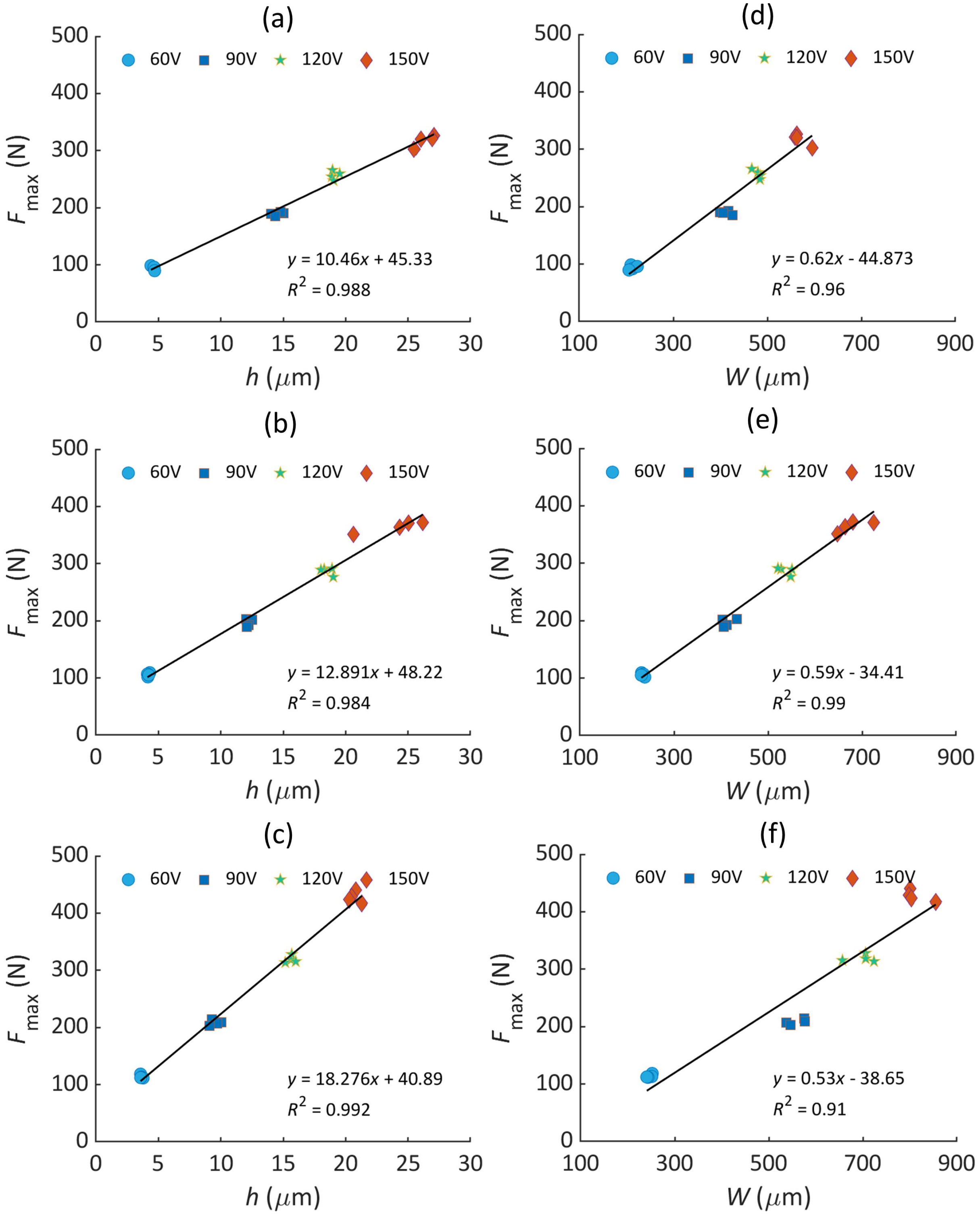

Figure 4.36 The correlation of the striking peak force with (a) – (c) the depth and (d) – (f) width of the surface groove in 1D scan vibration striking experiment using copper samples: d = 2 – 4 mm.

Fig. 4.14 and Fig. 4.21) compared to the striking tool tip diameter (2, 3, 4 mm). It is this small indentation depth range that enables a good approximation of the linear relationship between the striking force and indentation size. The quality of this linear approximation can be considered to depend on the ratio of the indentation depth range to the diameter of the striking tool tip (h/d). The smaller this ratio, the better quality has the linear approximation. It can be expected that the linear force relationship is better approximated for a harder material than a softer material because h becomes smaller for the harder material and better for a larger striking tool tip than a small tool tip. This is the second linear relationship related to Fmax-h/d instead of the first linear relationship related to the elastic compression of PVST device. In practice, the h/d ratio may still be minimal despite the changes in workpiece material or tool tip size, so the linear force–indentation size relationship may be broadly acceptable in PVST. The linear equation describing the relationship, however, will change with the workpiece material and the striking tool diameter. For a given combination of workpiece material and tool diameter, the linear force–indentation size relationship should be fixed, based on which the indentation size or plastic deformation level induced by each individual strike can be monitored using the measured force signal.

The two linear force relationships provide a basis for realizing real-time monitoring and force-based feedback control of PVST, which can significantly enhance treatment efficiency and capability. The force sensor eventually needs to be integrated into the vibration device for practical implementation. This type of integration has been demonstrated as feasible for implementing a modulation-assisted drilling process [71, 72]. In the above results, PVST is only performed on a flat workpiece surface. The force-based feedback control capability will be beneficial for performing the treatment on a freeform surface. In this case, the tool vertical position and vibration amplitude can be controlled in real time based on the striking force signal to accommodate surface height change during the tool scan. This capability will significantly enhance the automation and efficiency of the treatment process.

4.5 Conclusions

Tool-surface approaching, single-spot vibration striking, and 1D scan vibration striking experiments were carried out under various experimental settings, including varying vibration frequency, driving voltage, tool diameter, overlap ratio, and workpiece material. The force and displacement signals, involving striking force, sliding force, and vibration displacement and amplitude, are summarized to investigate the effect of process parameters on the PVST process. The size and surface texture or cross-sectional profiles of permanent indentations in single-spot vibration striking conditions or grooves in 1D scan vibration striking conditions are extracted to characterize the deformation behavior of different materials in the PVST process. The correlations between these factors and process parameters are explored to provide a reference for future study and practical application. Specific findings from this chapter are:

1) Elastic compression of the PVST device assembly under striking force causes a reduction in vibration displacement in tool-surface approaching experiments. The relationship between displacement reduction and striking force is linear, equivalent to the axial stiffness of the PVST device. It indicates that displacement reduction can be calculated from the force signal given the stiffness of the PVST device.
2) Both the force and displacement signals reach the steady-state oscillations nearly right after the start of the tool vibration in single-spot vibration striking. The peak force and the maximum vibration displacement remain constant, except that they differ for different driving voltages.
3) Maximum striking force is positively correlated with vibration frequency while maximum vibration displacement is negatively related to vibration frequency, which is caused by the increased inertial force and acceleration, and more plastic deformation and strain hardening of the material (higher yield strength) at higher frequency conditions. Striking force, displacement, and indentation diameter also increase with increasing driving voltage due to higher vibration amplitude and increasing tool diameter due to larger contact area.
4) In 1D scan vibration striking experiments, the measured indentation space agrees with the calculated value, indicating that vibration striking with tool scan motion can be accu-

rately controlled. Roughness parameters decrease with increasing overlap ratio, leading to a smoother surface. The groove depth is inversely proportional to the tool diameter, while the groove width is proportional to the tool diameter. Also, they primarily depend on driving voltage and less on overlap ratio. The transverse section profile of the groove is not much affected by the overlap ratio.

5) The force components in 1D scan vibration striking consist of striking force and sliding force. The overlap ratio does not significantly affect the symmetrical striking force, while the asymmetrical sliding force decreases with an increasing ratio. The asymmetry is likely caused by the generation of pile-up material in front of the tool due to sliding. The striking force is larger in steel samples because of higher yield strength. In contrast, the sliding forces are similar in copper and steel samples since the striking effect dominates the plastic deformation of the treated surface over the sliding effect.
6) Groove/indentation size is linearly dependent on the striking peak force both in single-spot vibration striking and 1D scan vibration striking, indicating that the force signal can monitor surface deformation resulting from each individual strike with tool scan motion. These linear relationships hold for OFHC copper and mild steel samples with initially smooth surfaces, showcasing the ability of PVST to precisely control the striking effect on the workpieces despite the differences in strength of the two materials used.

CHAPTER 5

PIEZO VIBRATION STRIKING TREATMENT ON MACHINED SURFACE

In this chapter, the PVST is applied on the mild steel and OFHC copper workpieces with an initially smooth surface to perform the tool scan in two directions. The resultant surface texture and roughness parameters were investigated under various PVST experimental settings involving changing overlap ratio, scan speed, driving voltage, tool diameter, and workpiece material. The results and correlations achieved in this chapter can provide a reference and basis for comparing the results obtained on the initially rough surface.

5.1 Two-dimensional (2D) scan vibration striking

2D scan vibration striking can be regarded as an extension of 1D scan vibration striking where a 5 mm × 5 mm area of the workpiece surface is treated by the vibrating tool following parallel line scan paths in X and Y directions. In the 2D scan vibration striking experiment, the striking tool is first brought to a position where Z equals zero, and then the vibration is turned on. The workpiece mounted on the working table moves along the X-axis at a preset scan speed. After the workpiece movement reaches the setting value (5 mm length) in the X direction, the workpiece moves along the Y-axis for a path interval d_p. Then a new line scan path starts but in the opposite X direction. For all cases, the spacing (d_p) between the path lines is set to be the same as the offset distance (d_s) between two successive striking locations along the scan path (see Fig. 5.1). It results in approximately the same striking overlap ratio r_o in both the scan and the transverse directions with respect to the scan path lines.

The effects of various experimental parameters on the topography of the treated surface are investigated using different materials. Two different initial surface states are used, including initially smooth surface (steel and copper samples) and initially rough surface (additively manufactured titanium alloy samples, see Chapter 6), to explore the application of PVST on these surface states and materials.

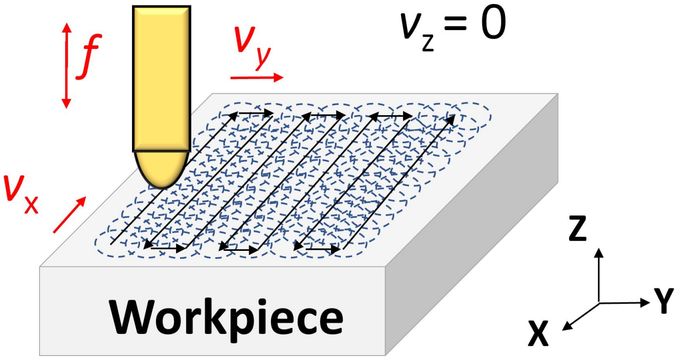

Figure 5.1 Schematic of 2D scan vibration striking experiment.

5.2 Application of PVST on the initially smooth surface

Figure 5.2 shows an overview of surface textures generated at different driving voltage and overlap ratio conditions using steel and copper samples, measured using KEYENCE at the magnification of x20. Each small square (the treated area) is measured using KEYENCE at the magnification of x1000. However, the high spatial resolution (0.2 μm) under high magnification generates enormous amounts of data points when measuring an area of 5 mm × 5mm (about 700 million data points). Because of the highly repetitive nature of the processed area, the upper left corner of the original measurement with an area of 1.4 mm × 1.4mm was selected to compute the surface roughness *Sa* to improve the measurement efficiency to save computation cost.

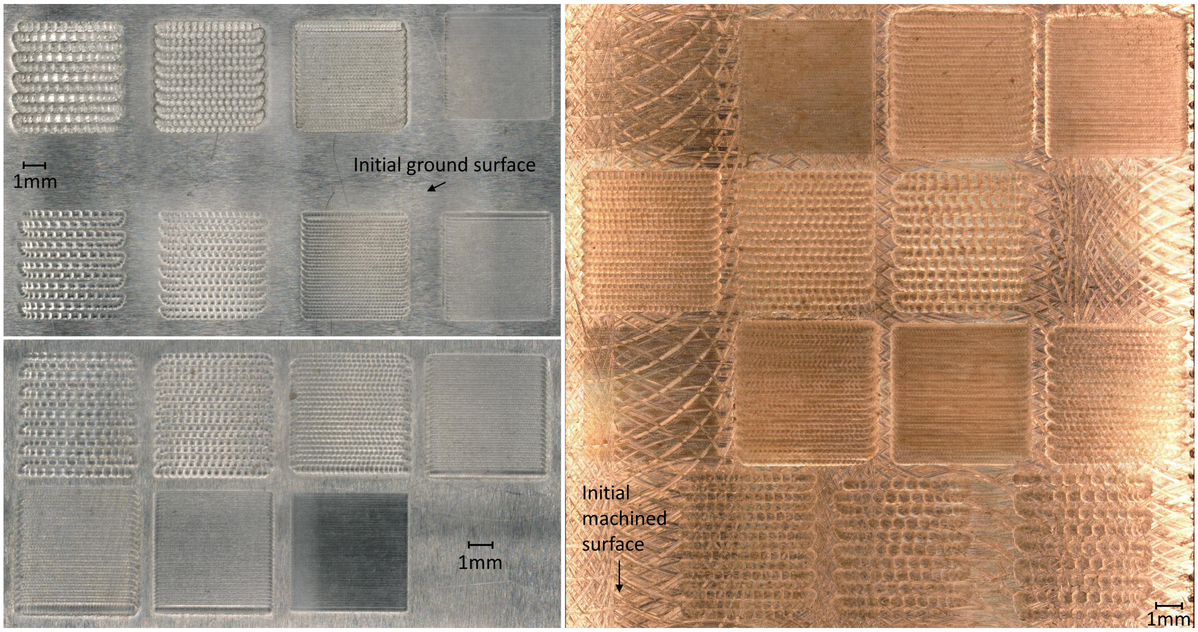

Figure 5.2 Overview of surface textures generated in 2D scan vibration striking experiments using steel and copper samples.

5.3 2D scan vibration striking using mild steel workpieces

Figure. 5.3 shows the surface topography obtained under different V_{pp} and r_o conditions at d = 2 mm and f = 100 Hz. The upper row is for different r_o (0, 0.25, 0.5, and 0.75) with a fixed V_{pp} (120 V), while the lower row is for different V_{pp} (60, 90, 120, and 150 V) with a fixed r_o (0.75). For each condition, the generated surface texture is uniform throughout the treated area, which reflects the uniform spacing and intensity of the strikes during the treatment. The r_o significantly affects the generated surface texture. With the small r_o (Fig. 5.3a and Fig. 5.3b), the surfaces have a dimple texture reflecting each surface indentation. It shows that the material is displaced to form circular ridges (red areas in the height contour maps). However, more material is displaced to the two lateral sides compared to the front and back sides with respect to the tool scan path. As r_o increases, the dimple size decreases. When r_o increases to 0.75, the individual dimple is no longer visible (Fig. 5.3d). When the surfaces generated at r_o = 0.75 are examined at a higher resolution (Fig. 5.3e - Fig. 5.3h), line ridges parallel to the tool scan path can be observed on the surfaces at higher V_{pp}. These line ridges are formed mainly by the lateral displacement of the material from inside the tool paths. The height of these line ridges decreases with decreasing V_{pp}. At r_o = 0.75 and V_{pp} = 60 V (Fig. 5.3e), the line ridges are no longer visible. The surface texture appears to have no significant difference along the scan and transverse directions, leading to a more smoother texture.

Figure 5.4 summarizes these quantified surface roughness parameters (Sa, Ra, and Rz) which are defined in Chapter 3 where describes how to compute Sa, Ra, and Rz. The 1D roughness parameters Ra and Rz are measured along both the scan and the transverse directions. It shows that all roughness parameters decrease with the increase in r_o and decrease in V_{pp}. The Ra values are close in the transverse and scan directions for all r_o, and Sa is very close to Ra (Fig. 5.4a and Fig. 5.4b). Rz is higher in the transverse direction than the scan direction because it will go across all the high ridges along the transverse direction when calculating Rz. Instead, computing Rz along the scan direction will go across several tool paths where the surface heights are smaller, generating a smaller Rz in the scan direction. For r_o = 0.75, the roughness difference in the two directions is

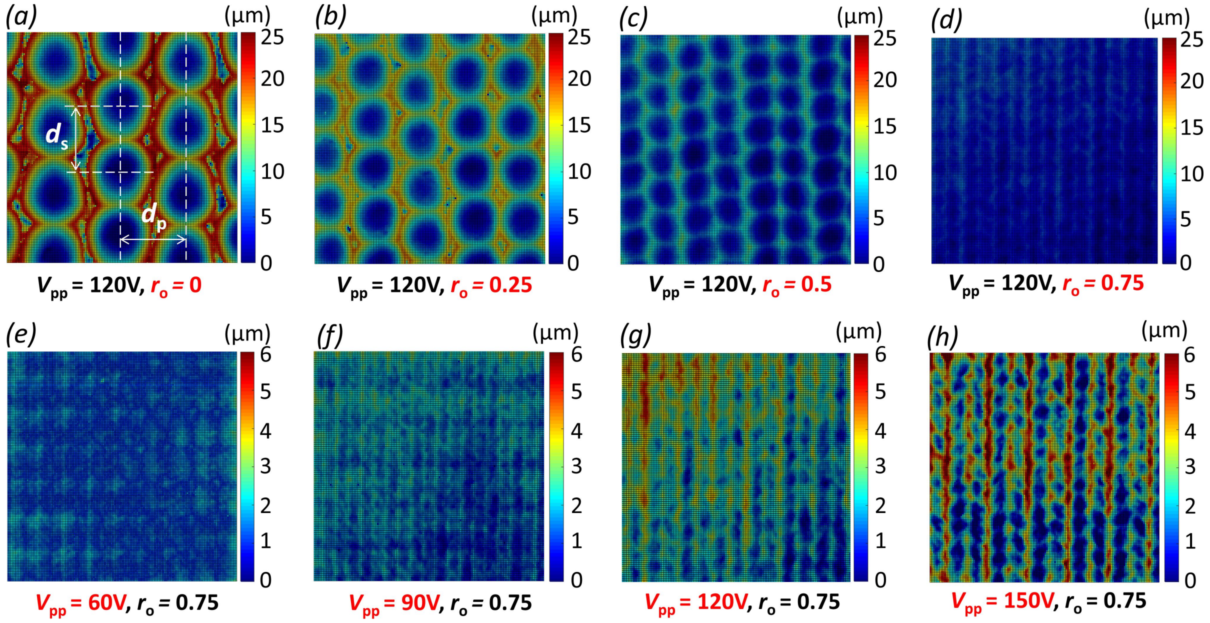

Figure 5.3 Surface topography resulting from 2D scan vibration striking at different r_o and V_{pp} using steel samples: f = 100 Hz, d = 2 mm. Measured area is 1.4 × 1.4 mm.

slight, and the difference is further reduced with decreasing V_{pp} (Fig. 5.4c and Fig. 5.4d). These changes are consistent with the transition of surface texture from the dimple type to the line ridges and eventually to the smoother type.

Figure 5.5 shows the surface topography obtained under different V_{pp} and r_o conditions at d = 3 mm. The upper row is for different r_o (0, 0.25, 0.5, and 0.75) with a fixed V_{pp} (120 V), while the lower row is for different V_{pp} (60, 90, 120, and 150 V) with a fixed r_o (0.75). The uniform surface texture throughout the treated area is still observed for each condition. The dimple texture occurs at r_o = 0, 0.25, 0.5 (Fig. 5.5a - Fig. 5.5c), and the size of dimples increases thanks to the use of larger tool diameter, compared to the dimples in Fig. 5.3a - Fig. 5.3c. The ridges at r_o = 0.25 and r_o = 0.5 become higher, indicating more material is displaced to the two lateral sides. As r_o increases, the dimple size decreases. When r_o is increased to 0.75, the individual dimple is no longer visible (Fig. 5.5d). Fig. 5.5e - Fig. 5.5h demonstrate the surfaces generated at r_o = 0.75 under different V_{pp}. Line ridges parallel to the tool scan path can be observed on the surfaces at higher V_{pp} (90 V - 150 V). These line ridges are more apparent than those at d = 2 mm in Fig. 5.3e - Fig. 5.5h. The height of these line ridges is positively dependent on V_{pp}. At r_o = 0.75 and V_{pp} = 60 V (Fig. 5.5e), the line ridges are no longer visible. A smoother texture is achieved instead, and no significant

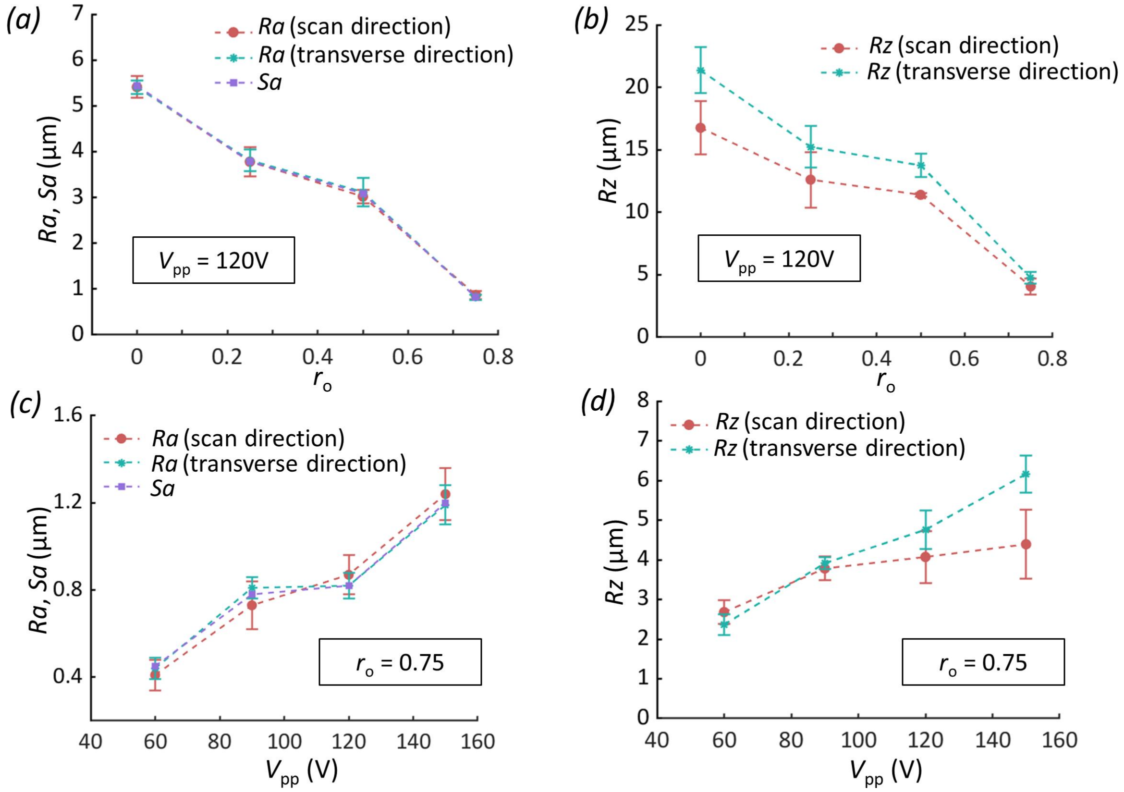

Figure 5.4 Variations of roughness parameters with r_o and V_{pp} for surfaces shown in Fig. 5.3.

difference in surface texture is observed along the scan and transverse directions.

Figure 5.6 summarizes the quantified roughness parameters (Sa, Ra, and Rz) for these surfaces in Fig. 5.5. All roughness parameters decrease with the increase in r_o and decrease in V_{pp}. For r_o < 0.5, Ra and Rz are significantly higher in the transverse direction than the scan direction, and Sa is very close to the Ra in the scan direction (Fig. 5.6a and Fig. 5.6b). For r_o = 0.75, the roughness difference in the two directions is significantly reduced, and the difference is further reduced with decreasing V_{pp} (Fig. 5.6c and Fig. 5.6d). These changes are consistent with the transition of surface texture from the dimple type to the line ridges and eventually to the smoother type.

Figure 5.7 shows the surface topography obtained under different V_{pp} and r_o conditions at d = 4 mm. The upper row is for different r_o (0, 0.25, 0.5, and 0.75) at V_{pp} = 120 V, while the lower row is for different V_{pp} (60, 90, 120, and 150 V) at r_o = 0.75. The surface texture still presents a uniform distribution of the indentations for each condition. Different from the cases at d = 2 mm in Fig. 5.3 and the cases at d = 3 mm in Fig. 5.5, the dimple texture only occurs at r_o = 0 (Fig. 5.7a) and r_o = 0.25 (Fig. 5.7b). The dimple size increases with increasing tool diameter compared to

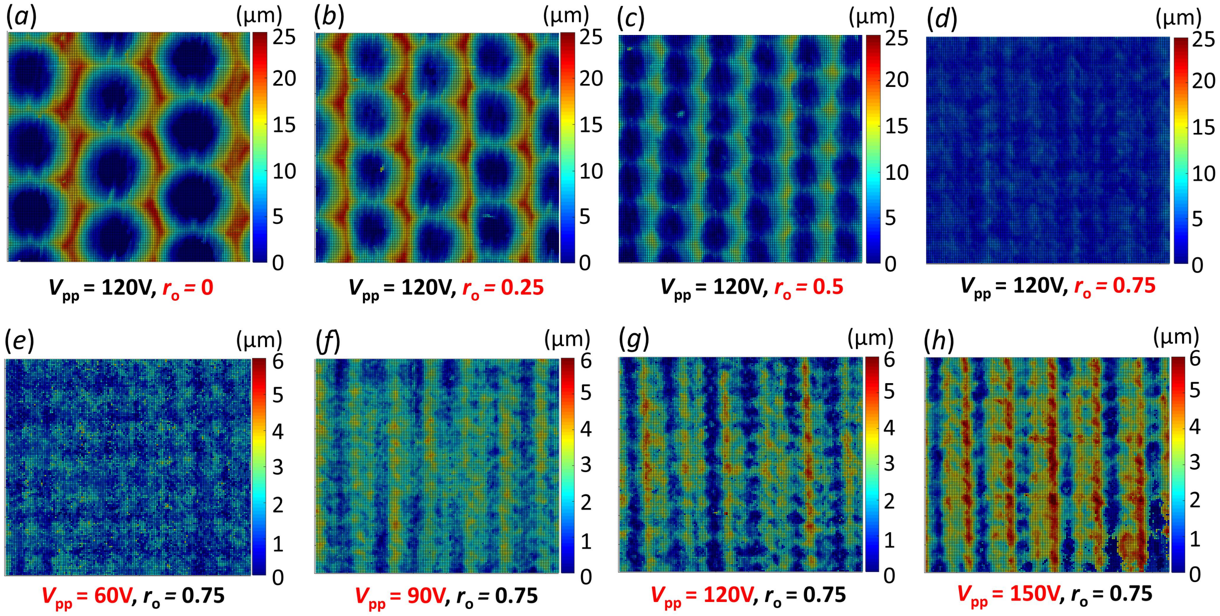

Figure 5.5 Surface topography resulting from 2D scan vibration striking using steel samples at different r_o and V_{pp}: f = 100 Hz, d = 3 mm. Measured area is 1.4 × 1.4 mm.

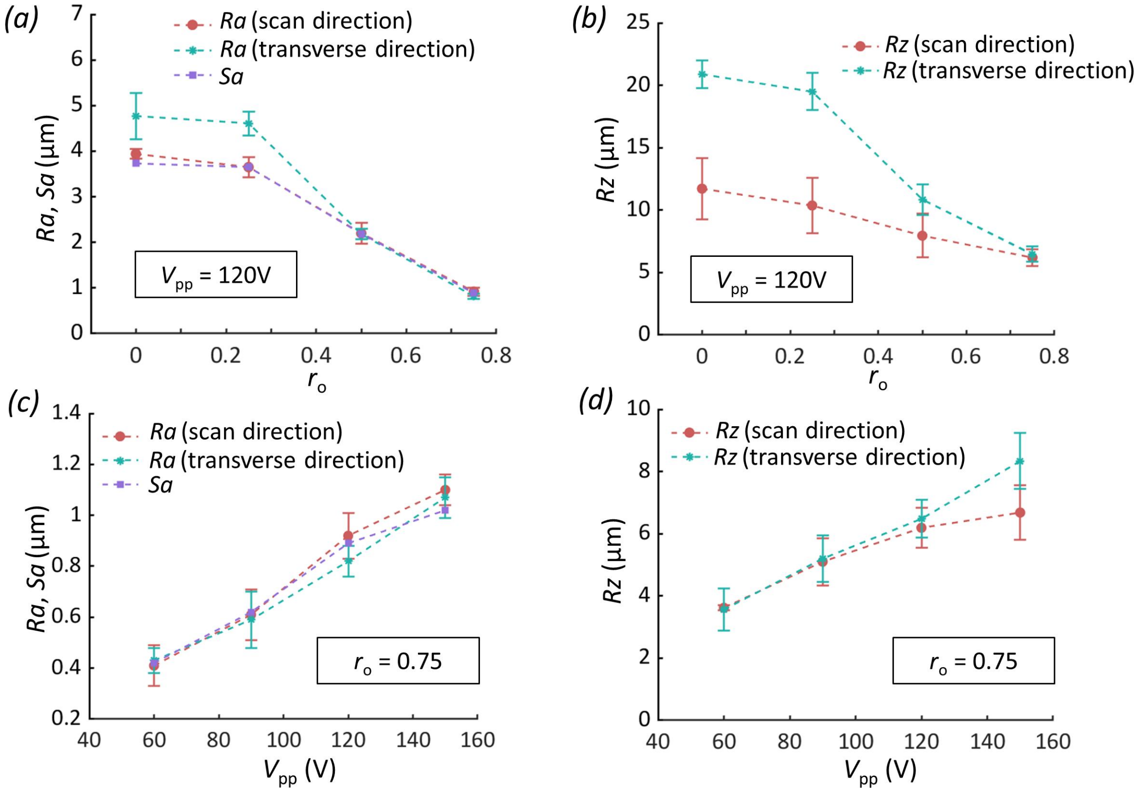

Figure 5.6 Variations of roughness parameters with r_o and V_{pp} for surfaces shown in Fig. 5.5.

the dimples in Fig. 5.3 and Fig. 5.7. The ridges significantly reduce for all the conditions. The maximum value of the ridges is only 8 μm while the value is 25 μm at d = 2 mm and d = 3 mm. It is caused by the reduced vibration amplitude when using a more prominent tool diameter, leading to less material displaced to the two lateral sides. As r_o increases, the dimple size decreases. The individual dimple is barely seen when r_o increases to 0.5 (Fig. 5.7c) or 0.75 (Fig. 5.7d). When the surfaces generated at r_o = 0.75 are examined at a higher resolution (Fig. 5.7e - Fig. 5.7h), line ridges parallel to the tool scan path can be observed on the surfaces at higher V_{pp} (120 V - 150 V). The line ridges at V_{pp} = 90 V are less pronounced than those in Fig. 5.3f and Fig. 5.5f. The surface texture at this condition is closer to the smoother texture except for some shallow line ridges. The height of these line ridges is positively correlated with V_{pp}. The maximum value of the ridges decreases to 3.5 μm (6 μm at d = 2 mm and d = 3 mm). At r_o = 0.75 and V_{pp} = 60 V (Fig. 5.7e), the line ridges are no longer visible, and the smoother texture is achieved.

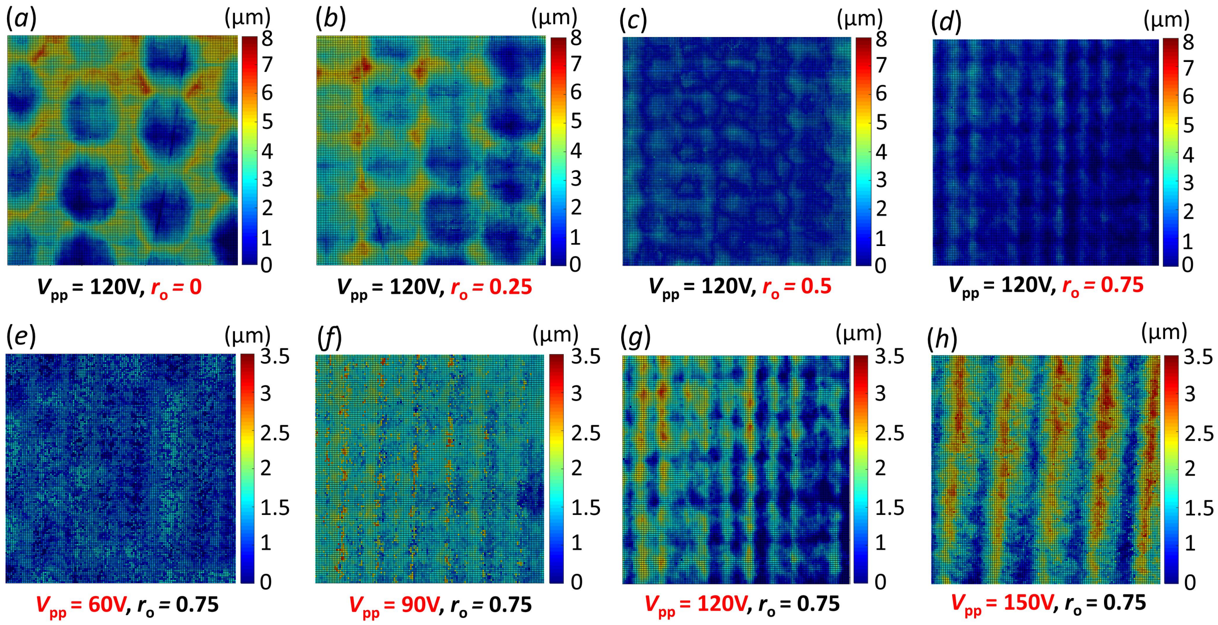

Figure 5.7 Surface topography resulting from 2D scan vibration striking using steel samples at different r_o and V_{pp}: f = 100 Hz, d = 4 mm. Measured area is 1.4 × 1.4 mm.

Figure 5.8 summarizes the quantified roughness parameters (Sa, Ra, and Rz) for the surfaces in Fig. 5.7. The roughness parameters are negatively correlated with r_o and positively dependent on V_{pp}. In comparison to the Ra and Sa at d = 2 mm and d = 3 mm, the Ra and Sa at d = 4 mm reduces greatly, and the maximum Sa is only 1.1 μm. The Sa is further reduced with decreasing V_{pp} (Fig. 5.8c and Fig. 5.8d).

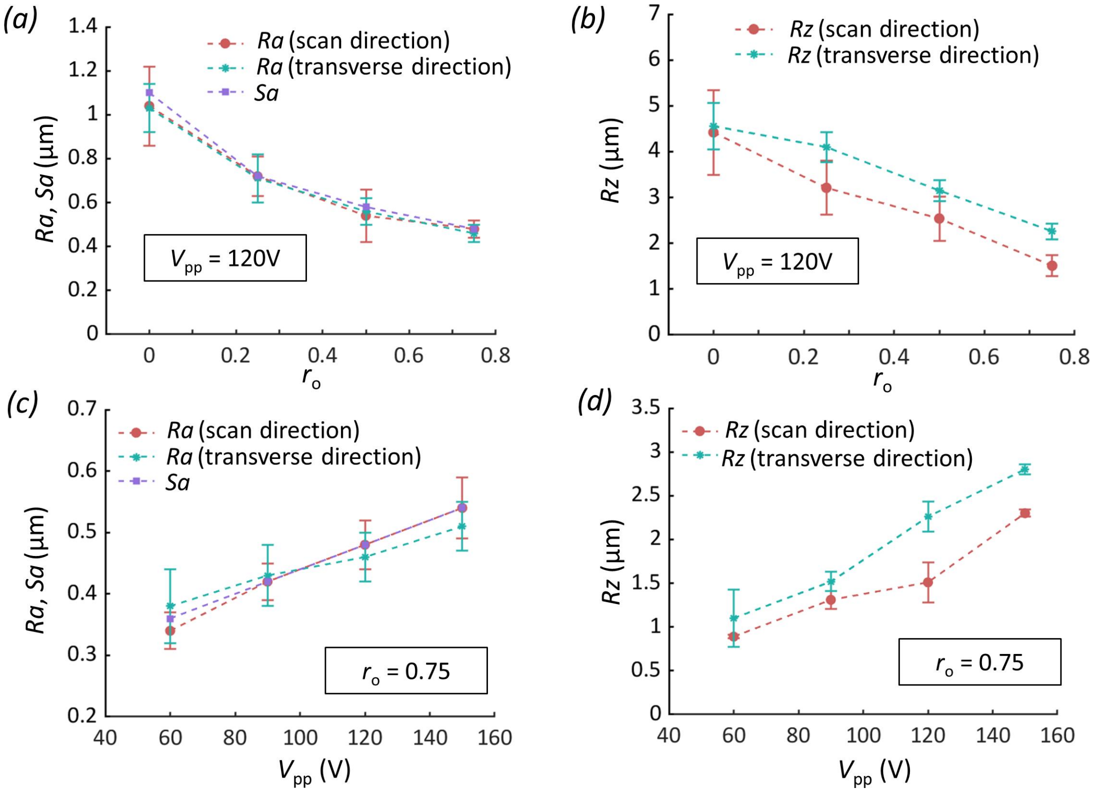

Figure 5.8 Variations of roughness parameters with r_o and V_{pp} for surfaces shown in Fig. 5.7.

Note that the roughness of the treated surfaces is higher than the ground surface's initial roughness. The smoothly ground surface is used to minimize the influence of initial surface roughness and texture such that the generated surface roughness and texture can be easily related to the processing parameters of the vibration striking treatment. Furthermore, these measured roughness parameters represent the achievable surface roughness using the corresponding treatment parameters. Among all the surfaces shown in Fig. 5.7e, the smoothest surface is obtained with V_{pp} = 60 V and r_o = 0.75 at Sa = 0.36 μm, which is only slightly higher than the initial Sa value of 0.32 μm for the ground surface. As shown by the surface texture enclosed by the red square in Fig. 5.9, the effect of PVST at this condition on the surface is much more moderate than the other conditions, and it only generates a shallow square mark on the treated surface. It can bring the striking and sliding effect to improve the surface finish but not create deep indentation marks shown in the two left squares.

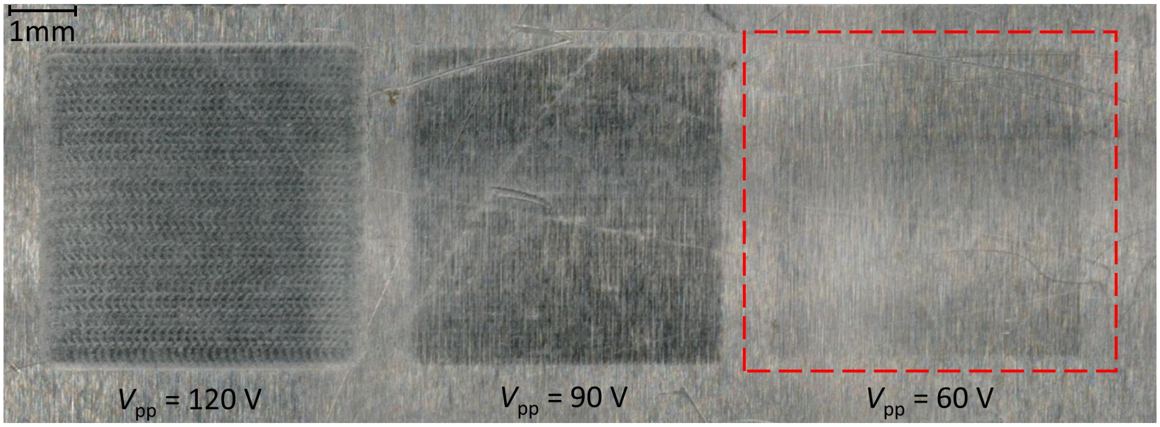

Figure 5.9 Surface texture of steel samples under the condition of V_{pp} = 60, 90, 120 V, d = 4 mm, and r_o = 0.75.

5.4 2D scan vibration striking using OFHC copper workpieces

To investigate the effect of PVST on different materials, the same experimental settings of 2D scan vibration striking experiments are carried out on the OFHC copper samples with an initially machined surface. Fig. 5.10 demonstrates the surface topography achieved under different V_{pp} and r_o conditions at d = 2 mm using copper samples. The upper row includes the surface textures at r_o = 0, 0.25, 0.5, and 0.75 with a fixed V_{pp} (120 V), while the lower row includes the surface textures at V_{pp} = 60, 90, 120, and 150 V with a fixed r_o (0.75). Consistent with the surface texture in the steel samples, the current surface texture is also uniform throughout the treated area for each condition, and the texture transition from the dimple texture to the line texture. The dimple size negatively correlates with r_o, and the individual dimple disappears at r_o = 0.75 (Fig. 5.10d). Due to the more considerable plastic deformation generated in the copper samples, the height of the ridges is much higher than that in the steel samples. The maximum height of the ridges reaches about 60 μm in Fig. 5.10a. In Fig. 5.10e - Fig. 5.10h, the line ridges parallel to the tool scan path exist for each driving voltage condition. Unlike the steel samples' results, the smoother texture is not observed at V_{pp} = 60 V and r_o = 0.75, where the line ridges dominate the surface texture. It can be explained by the fact that the more considerable plastic deformation in the copper samples leads to a more significant permanent depth of each indentation or groove and hence causes more material to be displaced to the lateral sides to form the higher line ridges.

Figure 5.11 summarizes the quantified roughness parameters (Sa, Ra, and Rz) for the surfaces

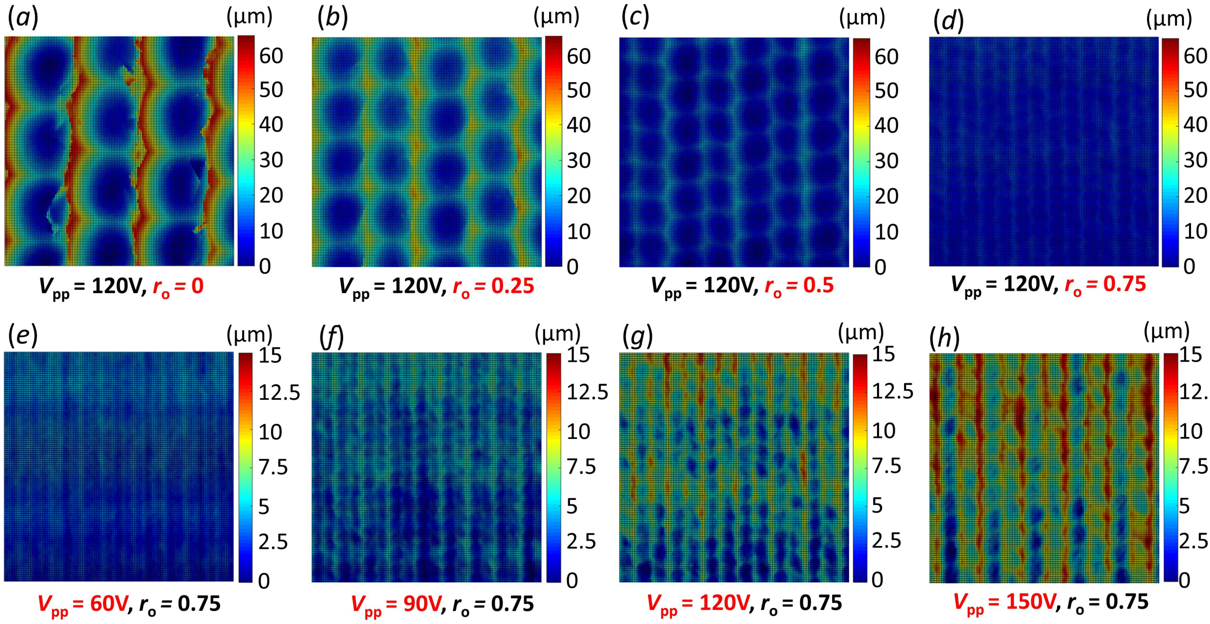

Figure 5.10 Surface topography resulting from 2D scan vibration striking at different r_o and V_{pp} using copper samples: f = 100 Hz, d = 2 mm. Measured area is 1.4 × 1.4 mm.

in Fig. 5.10. All roughness parameters decrease with the increase in r_o and decrease in V_{pp}. For all r_o, the Ra values are close in both the transverse and the scan directions, and Sa is very close to Ra (Fig. 5.11a and Fig. 5.11b). The Ra and Sa are much higher than the steel samples since the more significant depth of the successive indentations or grooves is generated in the treated area. The maximum value is about 12.5 μm. The Rz values are much higher than the steel samples as well. The Rz in the transverse direction is more significant than the scan direction because it needs to go across all the high ridges along the transverse direction when calculating Rz. For r_o = 0.75, the roughness difference in the two directions gradually declines, and the difference is further reduced with decreasing V_{pp} (Fig. 5.11c and Fig. 5.11d).

Figure. 5.12 illustrates the surface topography achieved under different V_{pp} and r_o conditions at d = 3 mm using copper samples. The upper row includes the surface textures at r_o = 0, 0.25, 0.5, and 0.75 and V_{pp} = 120 V, while the lower row includes the surface textures at V_{pp} = 60, 90, 120, and 150 V and r_o = 0.75. The height of the ridges significantly reduces compared to the height at d = 2 mm in Fig. 5.10 but is equivalent to that at d = 2 mm in Fig. 5.3. The overall distribution of the surface texture is similar to the previous results, and the smoother texture is observed again at V_{pp} = 60 and r_o = 0.75 in Fig. 5.12e. Since the vibration amplitude reduction results from using a larger

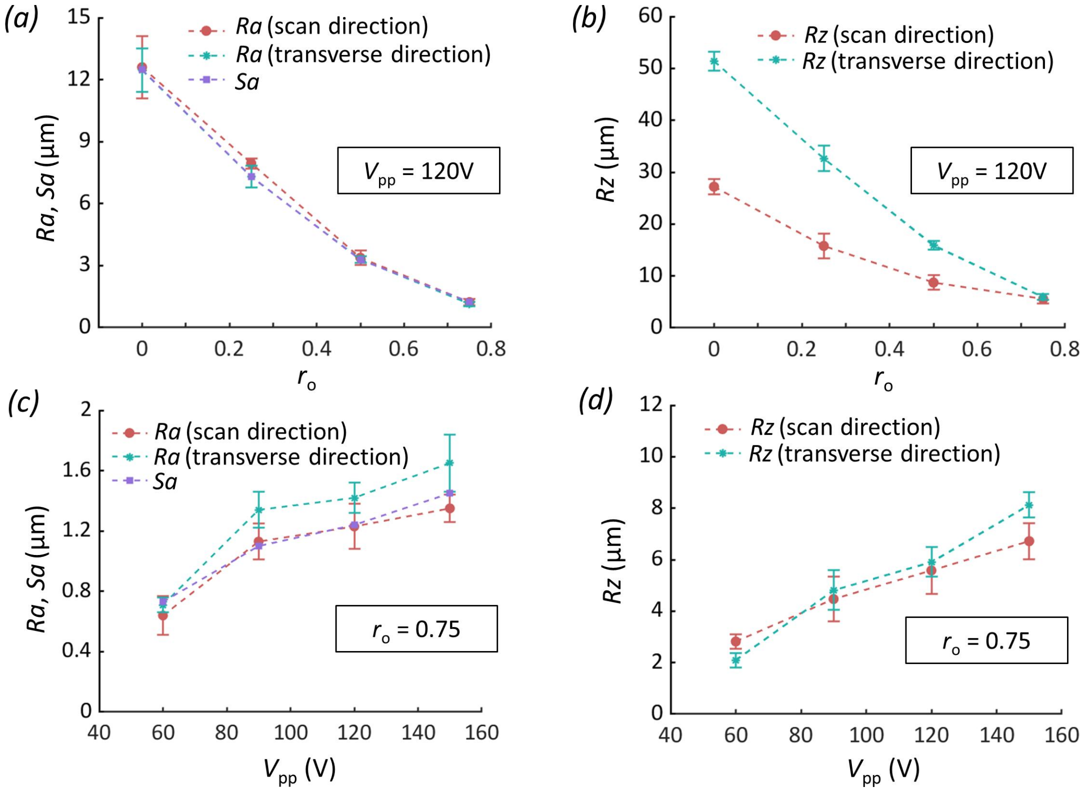

Figure 5.11 Variations of roughness parameters with r_o and V_{pp} for surfaces shown in Fig. 5.10.

tool diameter, the less plastic deformation makes the sliding effect less evident than d = 2 mm in Fig. 5.10. Hence less material is displaced to the lateral sizes to achieve the smoother texture.

Consistent with the surface texture in Fig. 5.12, the roughness parameters in Fig. 5.13 highly decrease compared to the results in Fig. 5.11. Despite the significant difference between the maximum values of Sa and Ra in the two conditions (Fig. 5.11a and Fig. 5.13a), the difference between the minimum values of Sa and Ra is relatively small, which are 0.73 μm (Fig. 5.11c) and 0.48 μm (Fig. 5.13c), respectively. Again, all roughness parameters decrease with the increase in r_o and decrease in V_{pp}.

Figure. 5.14 shows the surface topography achieved under different V_{pp} and r_o conditions at d = 4 mm using copper samples. The ridges' height in this condition is much smaller than d = 2 mm and d = 3 mm, which is similar to the variation in the steel samples. The surface texture transits from dimple texture to line ridge texture, hence smoother texture with increasing overlap ratio and decreasing driving voltage.

The roughness parameters in Fig. 5.15 are expected to reduce significantly compared to the two

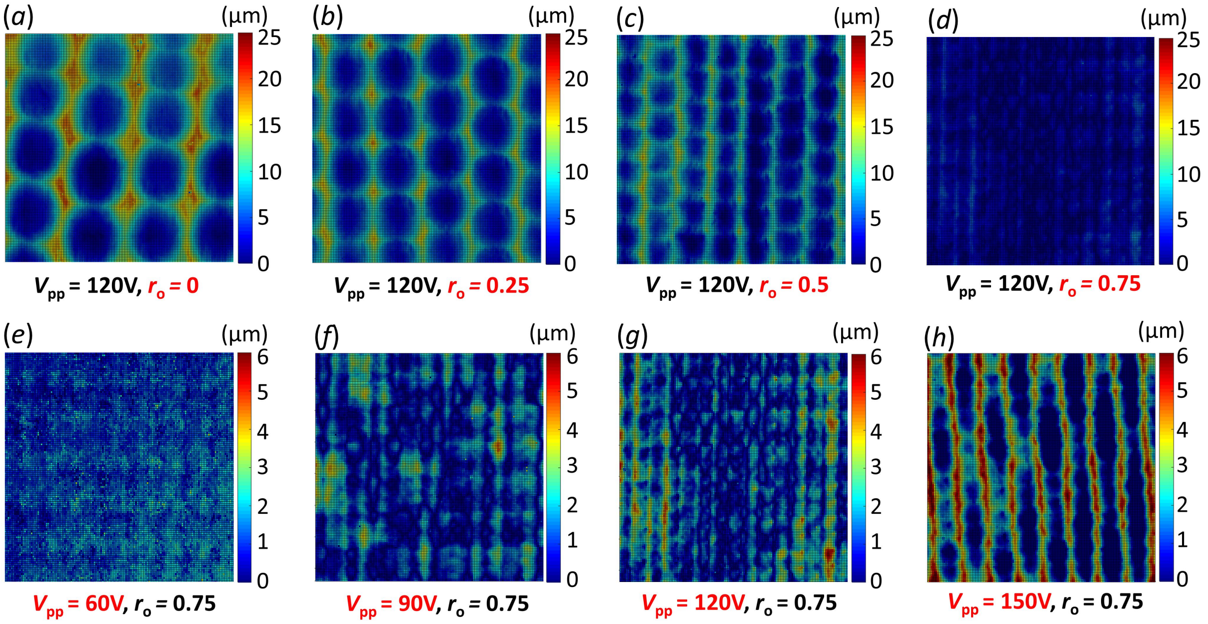

Figure 5.12 Surface topography resulting from 2D scan vibration striking at different r_o and V_{pp}: f = 100 Hz, d = 3 mm. Measured area is 1.4 × 1.4 mm.

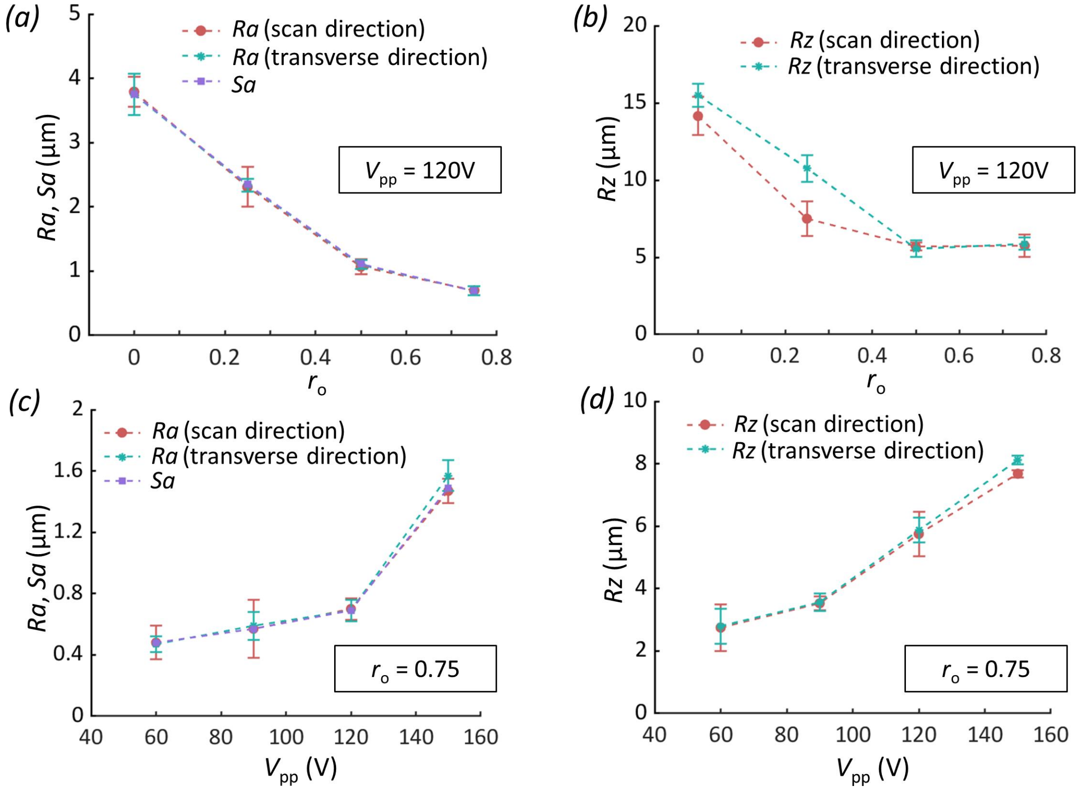

Figure 5.13 Variations of roughness parameters with r_o and V_{pp} for surfaces shown in Fig. 5.12.

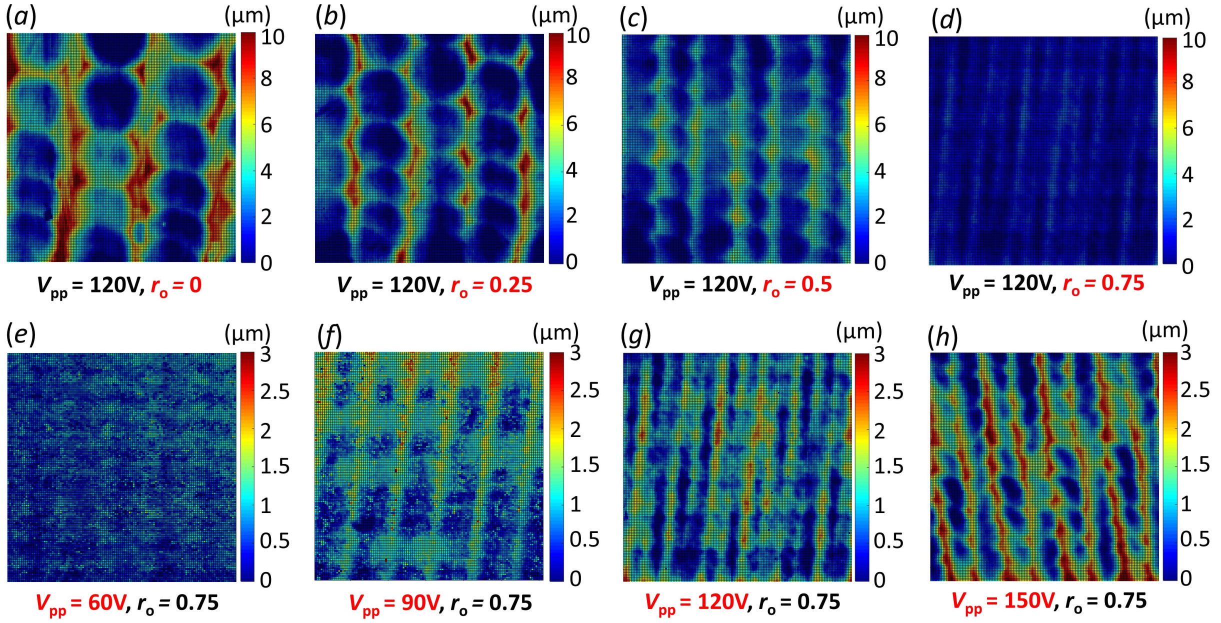

V_{pp} = 120V, r_o = 0 V_{pp} = 120V, r_o = 0.25 V_{pp} = 120V, r_o = 0.5 V_{pp} = 120V, r_o = 0.75

V_{pp} = 60V, r_o = 0.75 V_{pp} = 90V, r_o = 0.75 V_{pp} = 120V, r_o = 0.75 V_{pp} = 150V, r_o = 0.75

Figure 5.14 Surface topography resulting from 2D scan vibration striking at different r_o and V_{pp}: f = 100 Hz, d = 4 mm. Measured area is 1.4 × 1.4 mm.

previous conditions. The maximum Ra and Sa is only 1.69 μm in Fig. 5.15, and the minimum value is about 0.2 μm, which is a significant reduction of the surface roughness.

5.5 Further exploration on scan speed and tool diameter

According to the results of the steel and copper samples above, the overlap ratio highly affects the surface texture (from dimple texture to line ridge texture and smoother texture) and surface roughness (negative correlation), as shown in Fig. 5.3 - Fig. 5.14. The overlap ratio is a straightforward experimental variable because it directly represents the degree of overlap between two successive indentations, which can reflect the distribution density of the indentations on the treated path or surface. However, it is not easy to accurately calculate the overlap ratio. Although the diameter of the indentation obtained in the single-spot vibration striking experiment can be approximated as D for computing the overlap ratio in Eq. 3.5, the actual W obtained in 1D/2D vibration striking experiments is different from the D due to the additional sliding component. It indicates that the calculated overlap ratio is an approximated value and will fluctuate within a specific range. From the practical application perspective, different single-spot vibration striking experiments must be carried out for each new tool or material to determine the diameter of the

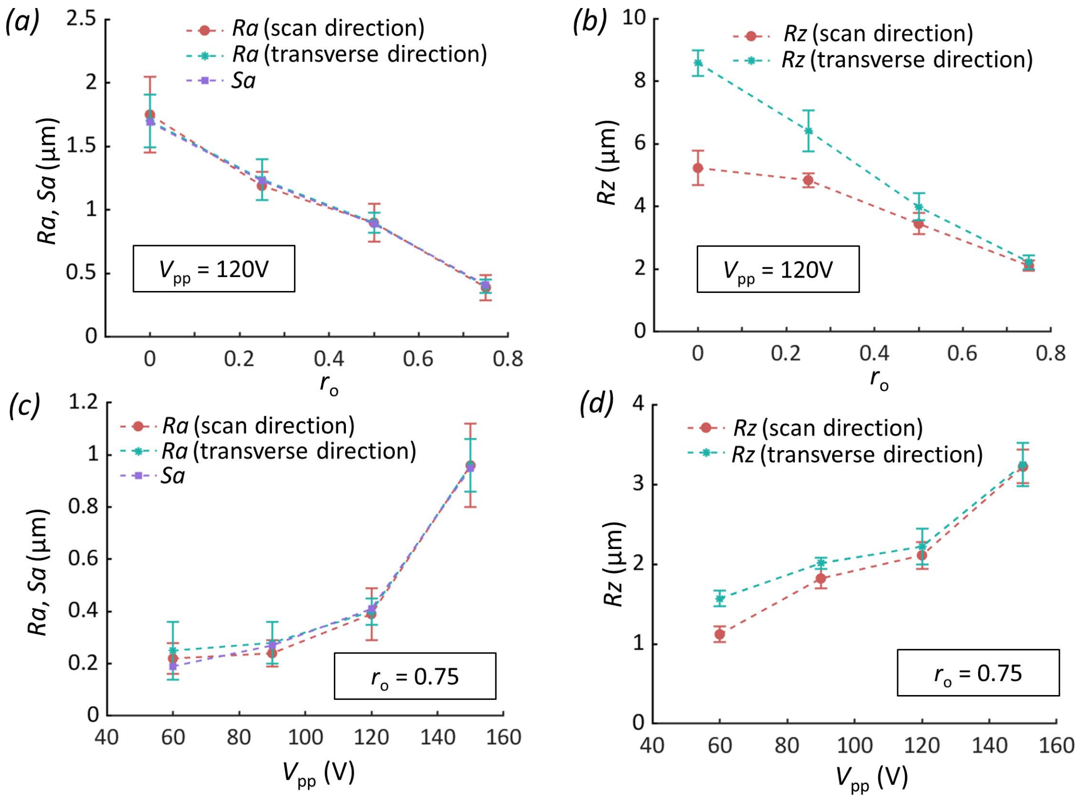

Figure 5.15 Variations of roughness parameters with r_o and V_{pp} for surfaces shown in Fig. 5.14.

indentation for each new condition so that the overlap ratio can be approximately computed. It is inefficient and time-consuming. Based on the results in Fig. 5.4a, Fig. 5.6a, and Fig. 5.8a, etc., the relationships between the surface roughness and the overlap ratio have been achieved. This general variation trend is helpful when selecting a proper overlap ratio to improve surface roughness, but it is optional to determine an exact overlap ratio in these scenarios. Instead, using scan speed that can be easily controlled in a CNC machine is a more convenient and efficient way to control the overlap density of the indentations directly. A specific range of scan speed must be used in the first few experimental trials to demonstrate the general distribution of the surface texture. Depending on the specific requirement of the workpieces and scenarios, the overlap density of the indentations can be determined by adjusting the scan speed.

To verify this method, four scan speeds (500, 1000, 2000, 3000 mm/min) are selected at d = 0.5, 1, 2 mm instead of using a particular value of the overlap ratio. Fig. 5.16 shows the texture of the surfaces generated at the conditions of f = 100 Hz, V_{pp} = 150 V, v_s = 500, 1000, 2000, 3000 mm/min, and d = 0.5, 1, 2 mm. The difference in the surface texture can be easily observed when the speed variation is considerable (i.e., 1000 mm/min). The scan speed can clearly distinguish the distribution density of the successive indentations despite the unknown overlap ratio for each treated area. Through these few simple 2D vibration striking experiments, the speed range for a specific overlap density of the surface texture can already be found. At the same time, the tool geometry can help control and generate different surface textures. These results prove that it is feasible to generate the surface texture more conveniently and efficiently by controlling the scan speed.

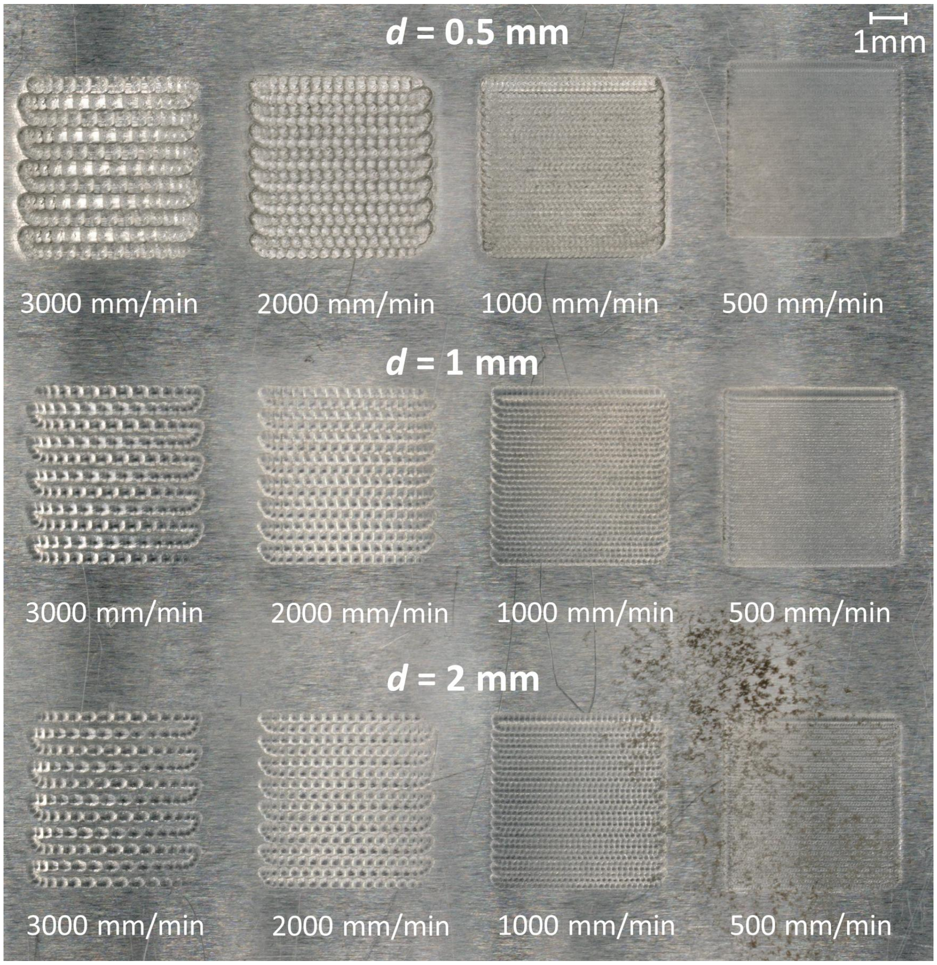

Figure 5.16 Surface textures under different scan speeds at d = 0.5, 1, 2 mm, f = 100 Hz, and V_{pp} = 150 V using steel samples.

Figure. 5.17 shows the surface topography obtained under different v_s and d conditions at f = 100 Hz and V_{pp} = 150 V from Fig. 5.16. Fig. 5.17a - Fig. 5.17d is for different v_s (500, 1000, 2000 and 3000 mm/min) with a fixed d (0.5 mm), Fig. 5.17e - Fig. 5.17h for different v_s at d = 1 mm, and Fig. 5.17i - Fig. 5.17l for different v_s at d = 2 mm, respectively. Similar to the previous results of the steel samples, the generated surface texture is uniform throughout the treated area for each condition. Different scan speeds distinguish the surface texture. With large v_s (Fig. 5.17a - 5.17b, Fig. 5.17e - 5.17f, Fig. 5.17j - 5.17i), the surfaces have a dimple texture that reflects each surface indentation. The height of the ridges increases with decreasing d. When v_s decreases to 1000 mm/min, the surface texture transitions from dimple texture to line texture where line ridges parallel to the tool scan path can be observed (Fig. 5.17c, Fig. 5.17g, Fig. 5.17k). At v_s = 500 mm/min, the line ridges are no longer visible. The surface texture appears to have no significant difference along the scan and transverse directions, leading to a more smoother texture (Fig. 5.17d, Fig. 5.17h, Fig. 5.17l).

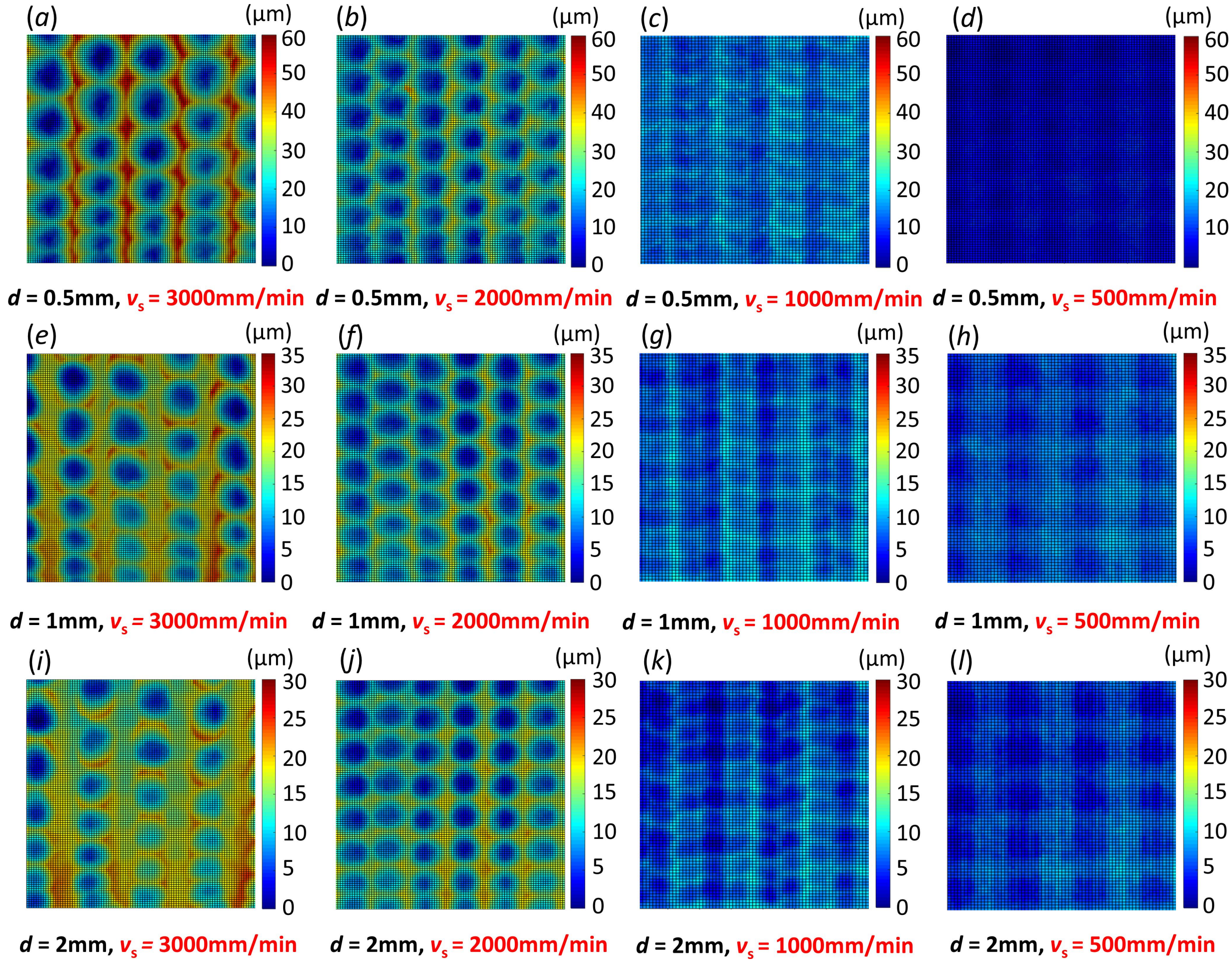

Figure 5.17 Surface topography resulting from 2D scan vibration striking at different v_s using steel samples: d = 0.5, 1, 2 mm, V_{pp} = 150 V, f = 100 Hz. Measured area is 1.4 × 1.4 mm.

Figure 5.18 summarizes the quantified roughness parameters (Sa, Ra, and Rz) for these surfaces in Fig. 5.17. All roughness parameters are positively related to v_s. For all v_s, the Ra values are close in both the transverse direction and the scan direction, and Sa is very close to Ra. Rz is higher in the transverse direction than in the scan direction. For large v_s (2000, 3000 mm/min), the roughness parameters increase with decreasing tool diameter. While for small v_s (500, 1000 mm/min), the Ra and Sa are very close for different tool diameters. It is consistent with the surface texture shown in Fig. 5.17, where the line ridge and smoother texture are achieved in these conditions.

In the above results, the Sa is inversely proportional to the overlap ratio and proportional to driving voltage and scan speed. Also, the softer the material, the larger the Sa is. Different combinations of these parameters are essential for precise control of surface roughness. The relationships between them and surface roughness can provide some reference for the practical application of PVST. Besides these parameters, another critical parameter is the tool diameter. Although different tool diameters have been used in the above results to generate different surface textures, they are not quantitatively compared at different vibration conditions. As mentioned earlier, the tool diameter affects the final indentation size and surface texture by changing the contact area between the striking tool and the workpiece. Therefore, it is worth studying its effect on Sa quantitatively. In the following results, the effects of the tool diameter on Sa under different r_o, V_{pp}, v_s, and materials are quantitatively analyzed.

Figure. 5.19 shows the relationships between the tool diameter and the surface roughness under different r_o (0, 0.25, 0.5, 0.75), V_{pp} (60, 90, 120, 150V) using steel and copper samples. Observe that Sa decreases with increasing d for each condition. For the conditions of V_{pp} = 60 V or r_o = 0.75, the difference of Sa as d increases is slight. It is suitable for a smooth surface since it does not introduce too much roughness. However, it may not be proper for those initially rough surfaces because more deformation is necessary to remove the rough features. Likewise, Fig. 5.20 displays the similar variation trend of Sa - d, where the effect of tool diameter on the surface roughness is much more apparent in significant scan speed conditions (v_s = 2000, 3000 mm/min).

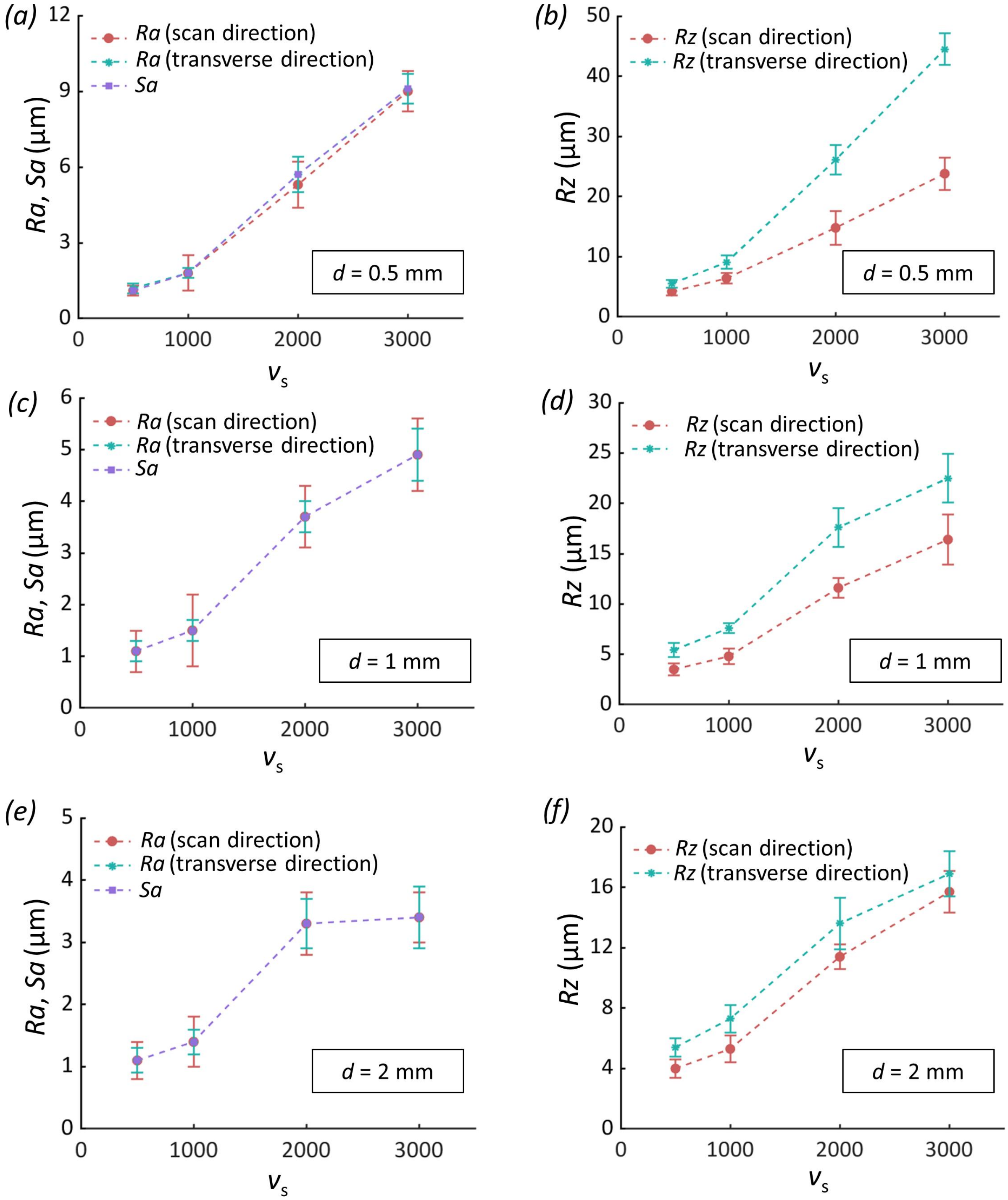

Figure 5.18 Variations of roughness parameters with v_s and d for surfaces shown in Fig. 5.17.

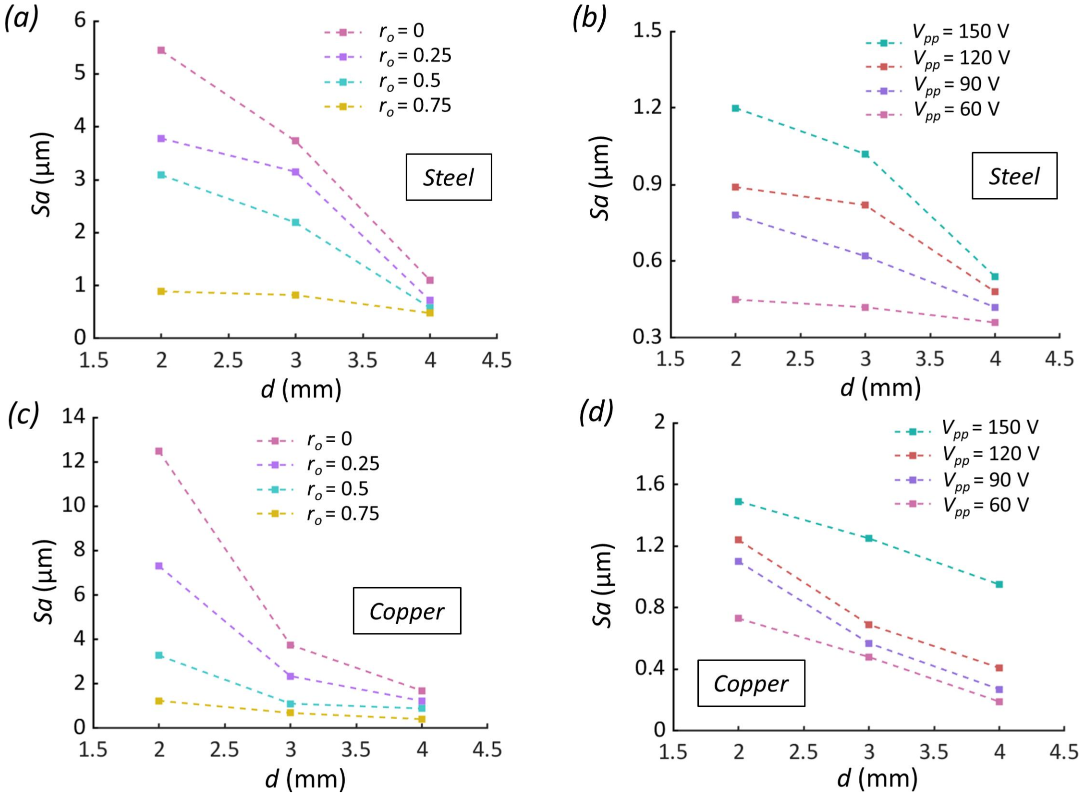

Figure 5.19 The relationships between tool diameter and surface roughness under different r_o and V_{pp} conditions using steel and copper samples.

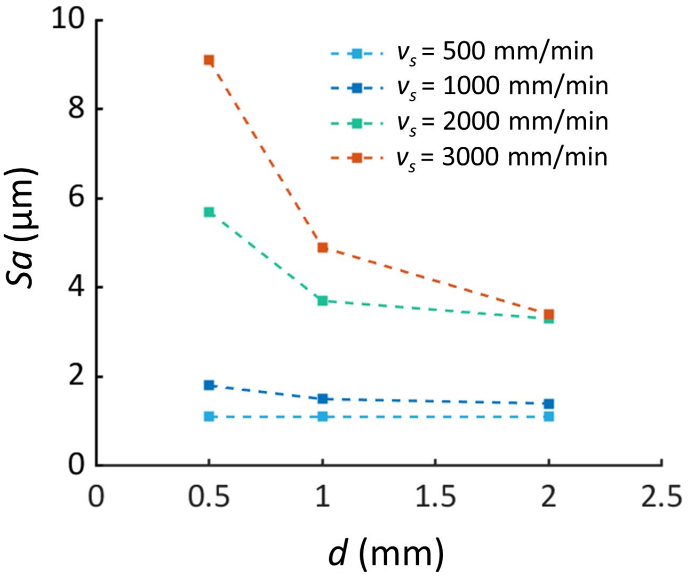

Figure 5.20 The relationships between tool diameter and surface roughness under different v_s conditions using steel samples.

5.6 Hardness testing after PVST

The effects of various process parameters, such as overlap ratio, driving voltage, tool diameter, and scan speed, on surface roughness have been investigated above. As claimed before, the deformation-based surface treatments also improve the mechanical properties of the components. In order to verify the positive effect of PVST under different process parameters on mechanical properties, hardness tests were carried out on the previously treated surfaces under the conditions of f = 100 Hz, V_{pp} = 60, 90, 120, 150 V, r_o = 0, 0.25, 0.5, 0.75, d = 2, 3, 4 mm, for ground mild steel and machined pure copper (OFHC 101, as received) samples. Brinell hardness test (1/16" ball, 100KG) was first used. Given that the hardened layer is thin after PVST, a large ball would probably cause a lot of deformation beneath the hardened surface, and the surface would not appear to be that much harder. However, it is worth doing this to illustrate the effect of the depth of hardness. Five points were selected on each treated surface and the average value was calculated to represent the hardness of the treated area. In addition, to obtain a much smaller depth of assessment, a set of microhardness measurements were conducted in Micro-Vickers hardness tests (loading: 0.2 kgF or 1.96 N; dwelling time: 15 s), which is probably more meaningful for the evaluation of PVST on the treated surfaces. Similarly, five test points were selected on each treated surface, and the average value was obtained to represent the hardness of the surface after the treatment.

Figure 5.21 shows the results of Brinell hardness tests performed under the conditions of f = 100 Hz, V_{pp} = 60, 90, 120, 150 V, r_o = 0, 0.25, 0.5, 0.75, and d = 2, 3, 4 mm for mild steel and pure copper samples. Compared with the initial hardness of the samples, the hardness results in the mild steel and pure copper samples show that PVST can improve the hardness of the treated surface. The hardness increases with decreasing tool diameter and increasing driving voltage. As discussed earlier, a larger driving voltage can generate a larger vibration amplitude, thereby applying more plastic deformation on the surface to produce a thicker hardened layer. While a striking tool with a smaller diameter results in larger indentation depth, leading to a larger ratio of h/d. The larger h/d ratio can produce more plastic strain [114] and hence higher hardness. In addition, the overlap ratio does not significantly affect the hardness which fluctuates within a certain range of values, such as

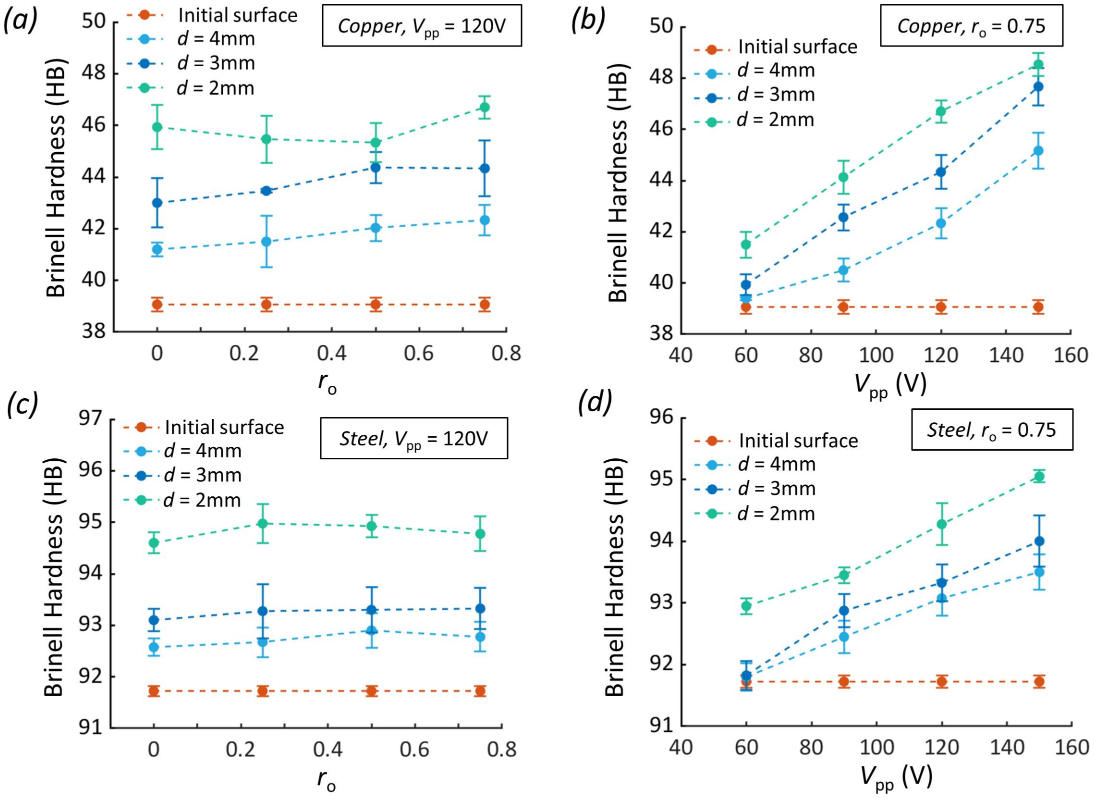

Figure 5.21 Brinell hardness of treated surfaces under various PVST conditions: f = 100 Hz, V_{pp} = 60, 90, 120, 150 V, r_o = 0, 0.25, 0.5, 0.75, and d = 2, 3, 4 mm for mild steel and pure copper samples.

46 HB, 44 HB, 42 HB at d = 2, 3, 4 mm for copper samples and 95 HB, 93 HB, 92.5 HB at d = 2, 3, 4 mm for steel samples. It is expected since the overlap ratio only changes the overlap density of the successive indentations. It does not affect the vibration amplitude in the Z direction and hence the striking depth. Also, as shown in Fig. 4.25 - 4.27 and Fig. 4.32 - 4.34, the striking force is equivalent in different overlap ratio conditions while the sliding force decreases with increasing overlap ratio. However, the sliding force is much smaller than the striking force, meaning that the striking force dominates the plastic deformation during the PVST process and the difference of the sliding force causes the fluctuation of the hardness under different overlap ratio conditions.

Observe that when the voltage is relatively small (V_{pp} = 60 V), the hardness is slightly higher than the original hardness since the applied plastic deformation is small and the strain hardening layer is thin. From all cases, it can be obtained that the maximum Brinell hardness in pure copper samples is 48.5 HB, and the improvement ratio is 24.2% compared to the original 39.1 HB. While the maximum hardness in mild steel is 95.1 HB, and the improvement ratio is 3.6% compared to the original 91.5 HB.

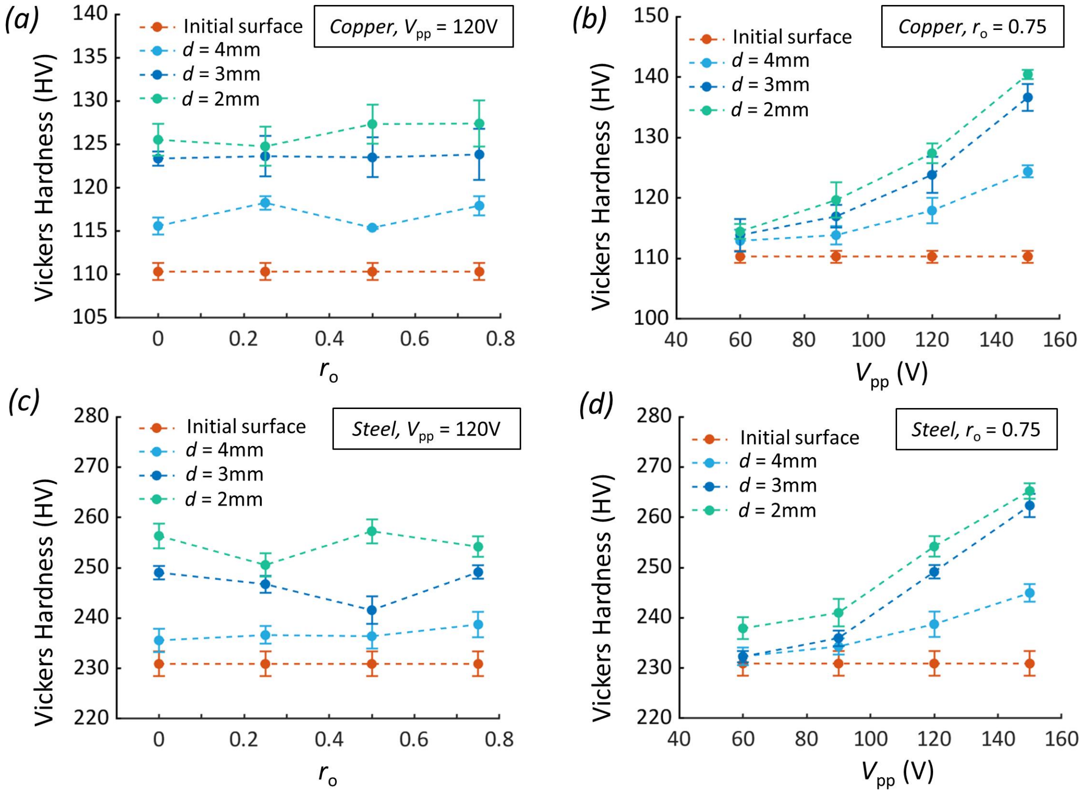

Figure 5.22 Micro-Vickers hardness of treated surfaces under various PVST conditions: f = 100 Hz, V_{pp} = 60, 90, 120, 150 V, r_o = 0, 0.25, 0.5, 0.75, d = 2, 3, 4 mm, for mild steel and pure copper samples.

Figure 5.22 illustrates the hardness measurement performed in Micro-Vickers tests. The results show that the Micro-Vickers hardness also exhibits the same variation trends with overlap ratio, driving voltage, and tool diameter. Different from Brinell hardness, the hardness variation in Micro-Vickers is much larger for different PVST conditions, such as the hardness at d = 2, 3, 4 mm. From all cases, the maximum Micro-Vickers hardness in the copper samples is 140.4 HB and the improvement ratio is 27.3% compared to the original 110.3 HB, which is close to the improvement ratio in Brinell hardness. While the maximum Micro-Vickers hardness in the steel samples is 265.2 HB, and the improvement ratio is 14.8% compared to the original 230.9 HB, which is much higher than 3.6% in Brinell hardness. Due to the thin strain-hardened layer, the results of Micro-Vickers hardness are more reasonable to reflect the effect of PVST on surface strengthening than Brinell hardness.

As mentioned earlier, scan speed is more convenient and efficient in determining the overlap density than overlap ratio. Therefore, it is also worth investigating its effect on hardness. Fig. 5.23 shows the hardness measurement under different scan speeds (f = 100 Hz, V_{pp} = 150 V, d = 0.5, 1, 2 mm, v_s = 500, 1000, 2000, 3000 mm/min for mild steel samples only). The resulting Brinell hardness and Micro-Vickers hardness show similar trends in different overlap ratio conditions as in Fig. 5.21 and 5.22, which is expected since the effect of scan speed on surface deformation is equivalent to that of the overlap ratio. It can be seen that in the case of V_{pp} = 150 V, the maximum Brinell hardness of steel is 99.5 HB, which is 8.4% higher than the original hardness. While maximum Micro-Vickers hardness is 285.9 HV, and the improvement ratio is 23.8%. The higher improvement ratios in Brinell hardness and Micro-Vickers hardness are attributed to using a smaller tool diameter (d = 0.5 mm).

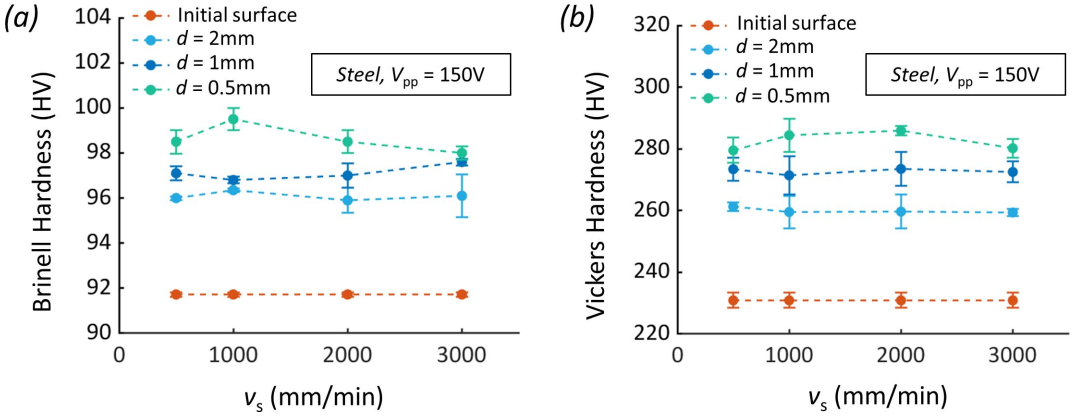

Figure 5.23 Brinell hardness and micro-Vickers hardness using steel samples.

5.7 Discussion

The 2D vibration striking experiment on the initially smooth surface has shown that surface finish can be improved by increasing r_o or decreasing V_{pp}. The trade-offs in different combinations of r_o and V_{pp}, which can achieve the same level of surface finish, are worth further discussion. In general, the same level of surface finish may be achieved by the combination of higher r_o and higher V_{pp} or the combination of lower r_o and lower V_{pp}. Higher r_o can be achieved by reducing the tool scan speed, which increases the treatment time. It can also be achieved by increasing tool vibration frequency and power consumption for piezo stack actuation. Higher V_{pp} leads to higher plastic strain and a thicker deformed layer due to higher vibration amplitude.

In contrast, the combination of lower r_o and lower V_{pp} results in faster treatment and less vibration power consumption. However, the induced plastic strain and strained layer thickness are minor. Based on these trade-offs, the higher r_o – higher V_{pp} setting is more suitable for surface microstructure refinement purposes, while the lower r_o – lower V_{pp} setting is more suitable for surface residual stress modification purpose.

5.8 Conclusions

In this chapter, 2D scan vibration striking experiments under different PVST conditions were conducted on mild steel and OFHC copper workpieces with initially smooth surfaces. Various process parameters involving driving voltage, overlap ratio, scan speed, and tool diameter are leveraged to explore their effects on the surface deformation of the treated areas. Corresponding surface textures and roughness parameters (Ra, Rz, Sa) are summarized. The major conclusions in this chapter follow:

1) Surface texture for each 2D vibration striking experiment is uniform throughout the treated area, reflecting the uniform spacing and intensity of the strikes during the treatment. Overlap ratio significantly affects the surface texture, distinguishing the texture into dimple type, line ridge type, and smoother type as the ratio increases.
2) Indentation size is negatively related to overlap ratio and positively correlated with tool diameter. The line ridges significantly reduce for all the conditions at the large tool diameter condition, caused by more amplitude reduction and less displaced material to the lateral sides. The ridge height decreases with decreasing driving voltage and increasing material strength.
3) All roughness parameters are proportional to driving voltage and scan speed, and inversely proportional to the overlap ratio and tool diameter, consistent with the transition of surface texture from the dimple type to the line ridges type and eventually to the smoother type. The

measured roughness parameters can represent the achievable surface roughness using the corresponding treatment parameters based on the initially smoothly ground surface.

4) Scan speed is a more efficient and convenient way to control the distribution density of indentation overlap than overlap ratio.
5) The higher ratio–voltage setting is more suitable for surface microstructure refinement purposes to induce considerable plastic strain and strained layer thickness, while the lower ratio–voltage setting is more suitable for surface residual stress modification purposes.
6) The results of Brinell hardness and Micro-Vickers hardness illustrate the ability of PVST in improving the surface hardness after treatment. The hardness improvement is proportional to driving voltage and inversely proportional to tool diameter. The overlap ratio does not significantly affect the hardness after treatment.

CHAPTER 6

PIEZO VIBRATION STRIKING TREATMENT ON ADDITIVELY MANUFACTURED SURFACE

This chapter investigates how to efficiently utilize PVST to improve the surface finish of AM metal parts (Ti-6Al-4V). The surface roughness of AM part is dependent on surface orientation, build layer thickness, powder size, etc. The roughness measurement Sa value is typically in the range of tens of microns. Our goal is to reduce the Sa value down to around 1 μm level using PVST, which can be effectively finished with further post-processing, i.e., Magnetic-field Assisted Finishing [14]. To achieve this goal efficiently, the effects of the critical process parameters (Table 6.1) on the plastic deformation of the rough surface layer will be investigated.

Table 6.1 Critical process parameters for PVST process.

Tool geometry control	**Vibration control**	**Motion and position control**
Size (diameter d)	Frequency f Amplitude u_{pp} (through V_{pp})	Engagement distance Z Scan speed v_s Preload F_p

Figure 6.1 compares the roughness layer of the initial workpiece surface with the roughness layers of the treated surfaces after PVST. The surface roughness Sa of the initial surface on which the rough features are scattered throughout the area is 48.6 μm (Fig. 6.1a). The surface roughness of the treated surface is reduced after PVST, as shown in Fig. 6.1b (Sa = 30.3 μm) and Fig. 6.1c (Sa = 9.5 μm). The roughness layer in Fig. 6.1b consists of scattered dark and bright areas. The bright areas represent the impacted areas that interact with the striking tool, while the dark areas are the unaffected areas that cannot be approached by the tool. In Fig. 6.1c, the roughness layer is covered by bright uniform areas with only a few dark hills or valleys. Also, the surface height contour maps show smoother characteristics in Fig. 6.1b and Fig. 6.1c than Fig. 6.1a. This dissertation mainly distinguishes the rough surface after PVST into scattered and uniform patterns. The scattered pattern represents the roughness layer consisting of the scattered dark and bright areas and the uniform pattern represents the roughness layer covered by uniform bright areas.

As mentioned in Eq. 3.5 and Eq. 4.1, the overlap ratio r_o is inversely proportional to scan

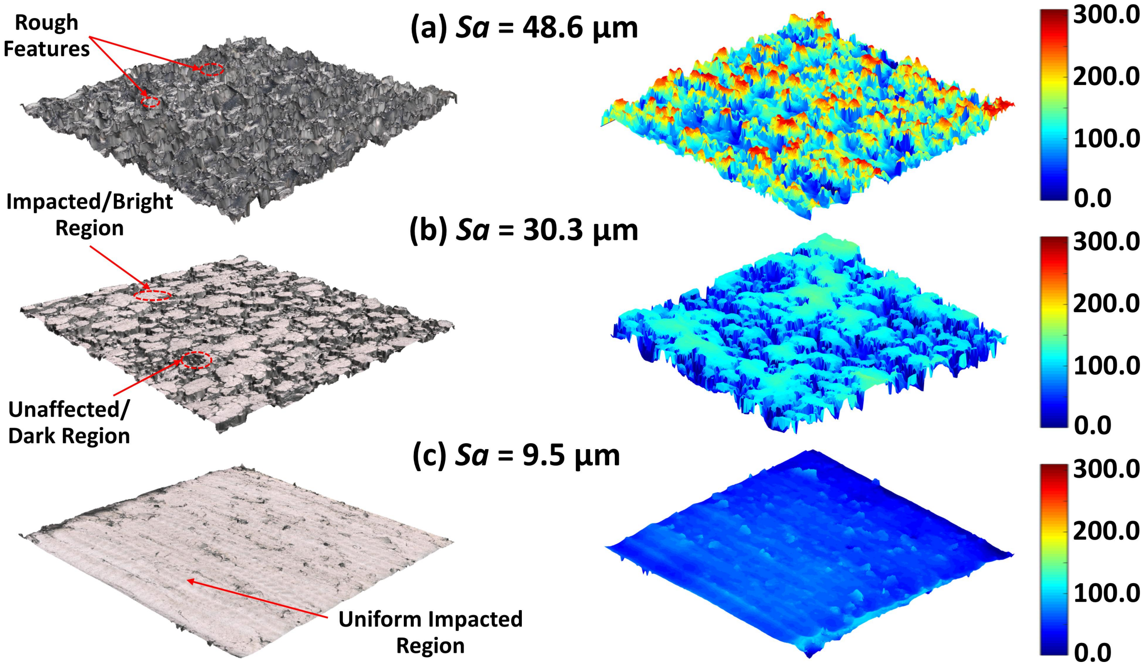

Figure 6.1 Surface textures and height contour maps: (a) initial surface pattern; (b) scattered pattern; (c) uniform pattern.

speed v_s and proportional to vibration frequency f, indicating that lower scan speed and higher vibration frequency can result in denser distribution of the successive indentations with the same treated size. This denser distribution benefits the surface finish for the copper and steel samples with the initially smooth surface. A combination of high vibration frequency and low scan speed would be a great choice to perform PVST under the ideal circumstance. Nevertheless, lower scan speed requires longer processing time and higher vibration frequency requires a more powerful actuation source, which may be time-consuming and costly. Also, the surface deformation on a rough surface may differ from that on a smooth surface, indicating that the above rules might not work in a new scenario. Therefore, how to select and balance these factors is of great significance in implementing a more economical and efficient PVST.

6.1 Effect of vibration frequency on surface deformation

To investigate the effect of the vibration frequency on surface deformation, various experiments are performed by varying f from 100 Hz to 200 Hz under v_s = 3000 mm/min, d = 3 mm, and V_{pp} = 150 V. Considering the rough and nonuniform characteristics of the initial surface, a negative engagement distance (Z = -150 μm) is selected to guarantee sufficient engagement between the striking tool and the workpiece. The following section will discuss more details about the effect of engagement distance on surface deformation.

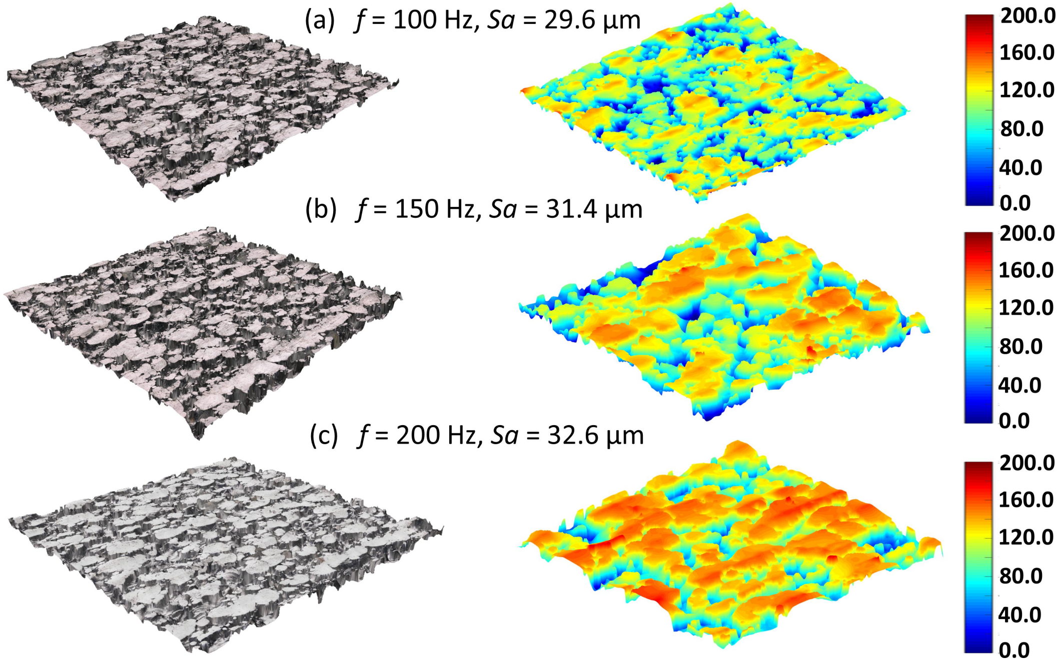

Figure 6.2 Surface textures and height contour maps after PVST under different vibration frequency conditions at d = 3 mm, V_{pp} = 150 V, v_s = 3000 mm/min, Z = -150 μm: (a) f = 100 Hz; (b) f = 150 Hz; (c) f = 200 Hz.

The left column in Fig. 6.2 illustrates the surface textures after PVST under different vibration frequency conditions. Observe that all the surface textures present a scattered pattern, and the distributions of bright and dark areas are reasonably similar for all the conditions. However, the height contour maps in the right column clearly show different surface deformation results. When f increases from 100 Hz to 200 Hz, the red areas on the uppermost layer of the treated surface increase, which means that the height difference between the flattened top layer and the bottom unaffected layer increases. The smaller vibration amplitude of the striking tool in higher frequency conditions results in the increasing height difference and more rough unapproached features. These results are consistent with the results obtained from the copper (Fig. 4.15 - Fig. 4.17) and steel (Fig. 4.8 - Fig. 4.10) samples with the initially smooth surface in Chapter 4 where higher f results in higher F_{max} but lower u_{max} for a given V_{pp}. Higher frequency leads to higher acceleration during each strike and hence more vibration displacement reduction due to the vibration device's elastic compression.

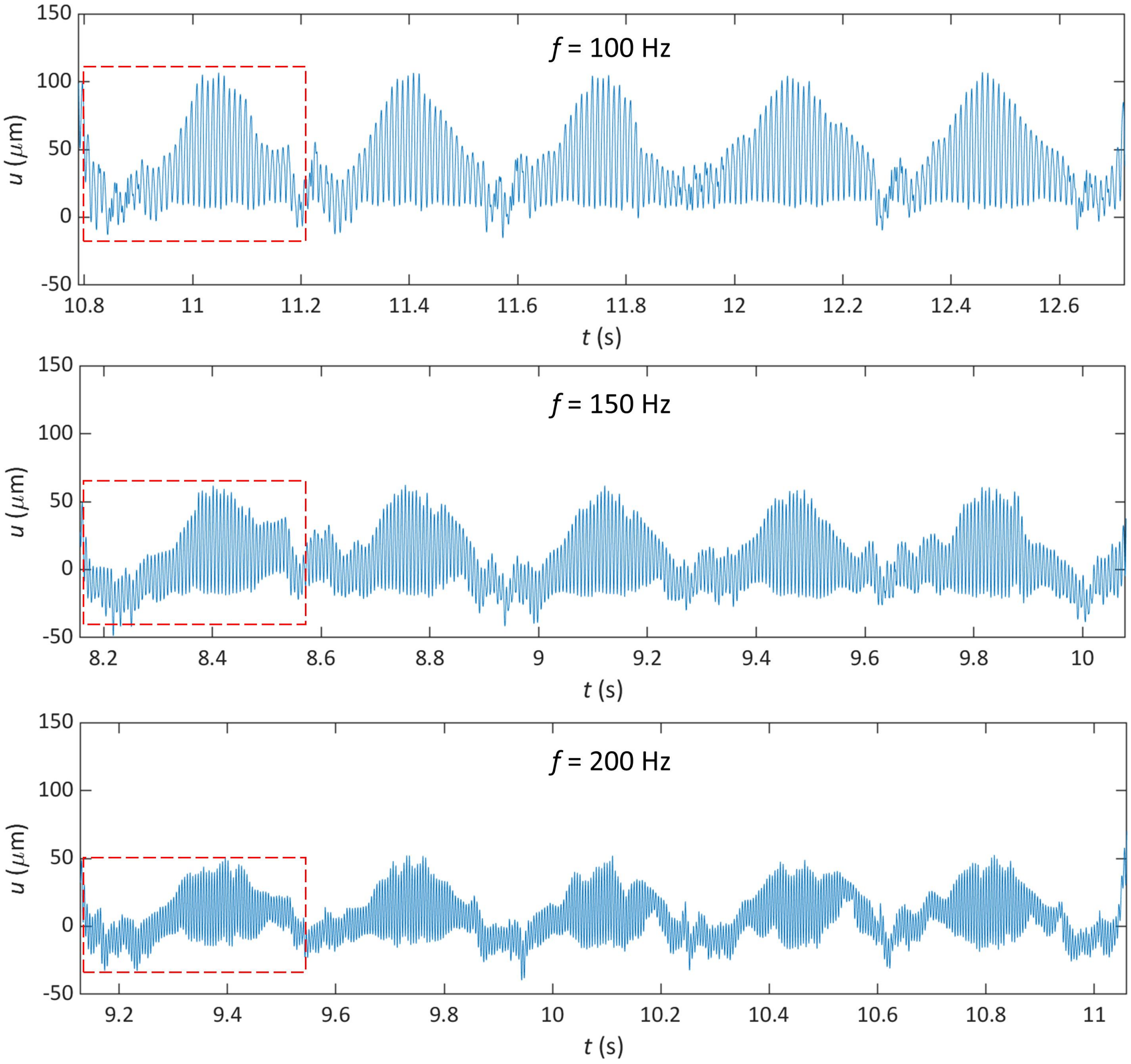

Figure 6.3 The history of vibration displacement during PVST on a treated area of 5 mm × 5mm at different vibration frequencies in Fig. 6.2.

Figure 6.3 shows the time-varying distribution of the vibration displacement during the PVST process on a 5 mm × 5 mm area under different frequency conditions in Fig. 6.2. The upper outline of each subfigure represents the farthest position the striking tool can reach at a specific spot of the treated area during the approaching process. The lower outline represents the position where the striking tool returns to the oscillating center (this new position is the starting position for the next striking cycle). Due to the rough features on the original surface, the upper and lower profiles fluctuate differently. A more extensive upper profile means the striking tool extends longer and can approach deeper areas. A smaller lower profile means the striking tool is compressed more when returning to the oscillating center, indicating that the new spot for the next strike has higher roughness than the previous one. By comparing the difference (vibration amplitude) between the upper and lower outlines at three different vibration frequency conditions, it is found that the amplitude decreases with a more significant frequency, which is consistent with the above description that the higher the frequency, the higher the amplitude reduction.

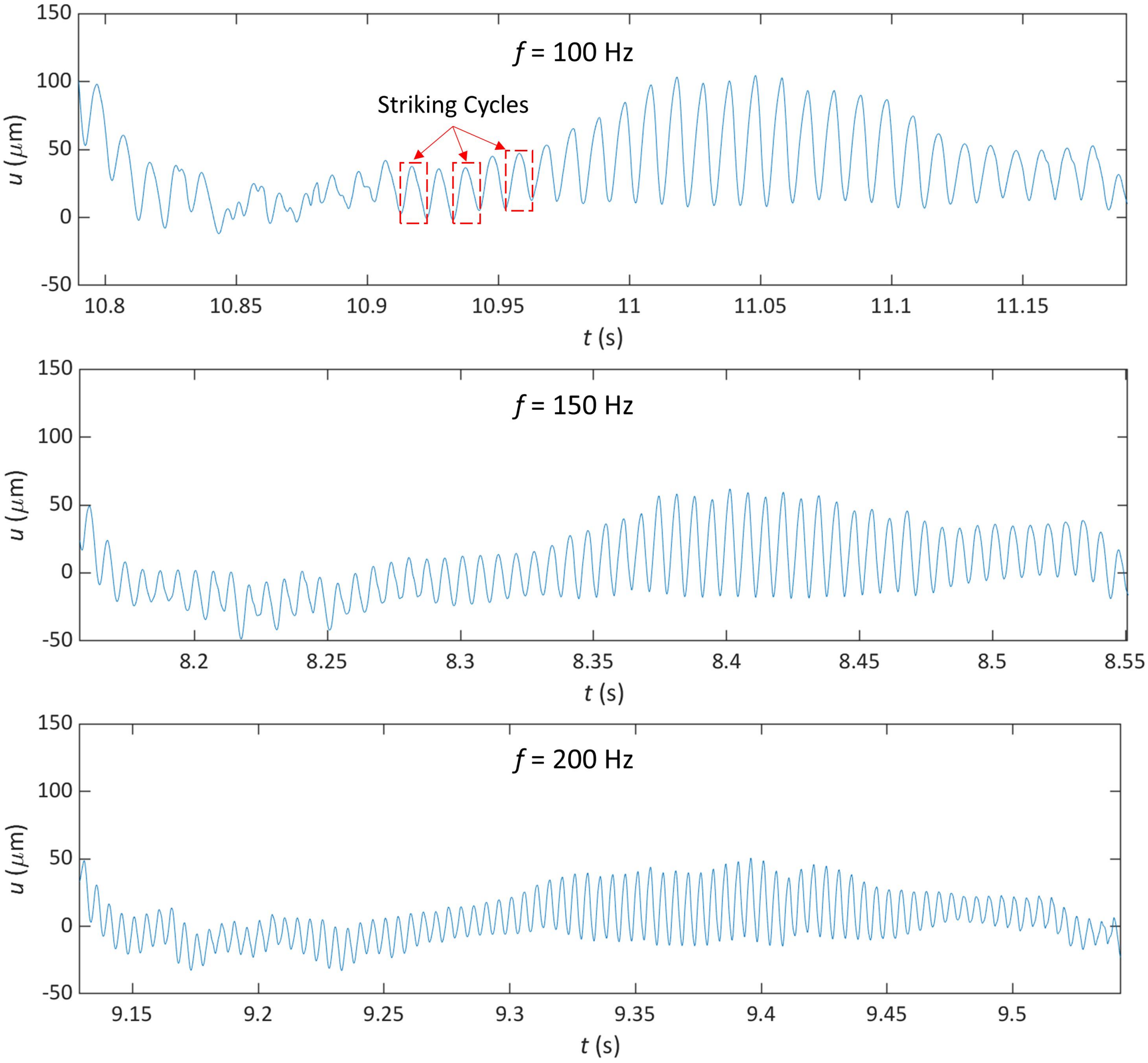

Figure 6.4 Enlarged periods of vibration displacement during PVST on a treated area of 5 mm × 5mm at different vibration frequencies in Fig. 6.3.

Fig. 6.4 shows the enlarged view circled by the red rectangle in Fig. 6.3 to observe the displacement distribution during the striking process. As seen from the figure, there are many successive fluctuating sinusoidal cycles. Each sinusoidal cycle represents a striking cycle. The upper outline described above is formed by the highest points of these sinusoidal cycles and, the lower outline by the lowest points of the cycles.

Fig. 6.5 summarizes the roughness parameters under different vibration frequency conditions to quantify the effect of the vibration frequency on the surface roughness. Sa agrees well with Ra in the scan and transverse directions, increasing as the vibration frequency increases. Rz in the transverse direction decreases slightly at f = 200 Hz, which can be attributed to the uneven and nonuniform surface rough features. The variation trends of the roughness parameters are consistent with the above surface textures under the scattered pattern. At the same time, they differ from our previous results on the thinner titanium alloy plates [115]. In the previous work, the roughness parameters were not affected too much by the vibration frequency despite the denser overlap distribution of the indentations formed at a high frequency condition. Since all of the treated surfaces after PVST at different frequency conditions present a uniform pattern and the Sa values of these surfaces are about 8 μm which is much smaller than the current Sa values (~ 30 μm), meaning they are much smoother than the current surface. Likely, the surface height difference between the flattened top layers and the bottom rough layers would lie at a similar level (these slightly smoother surfaces are still considered rough surfaces when compared to the smooth surfaces in those copper and samples with Sa = 0.32 μm). Therefore, the denser overlap distribution of the indentations does not positively affect the final surface roughness, leading to these small changes in the Sa values.

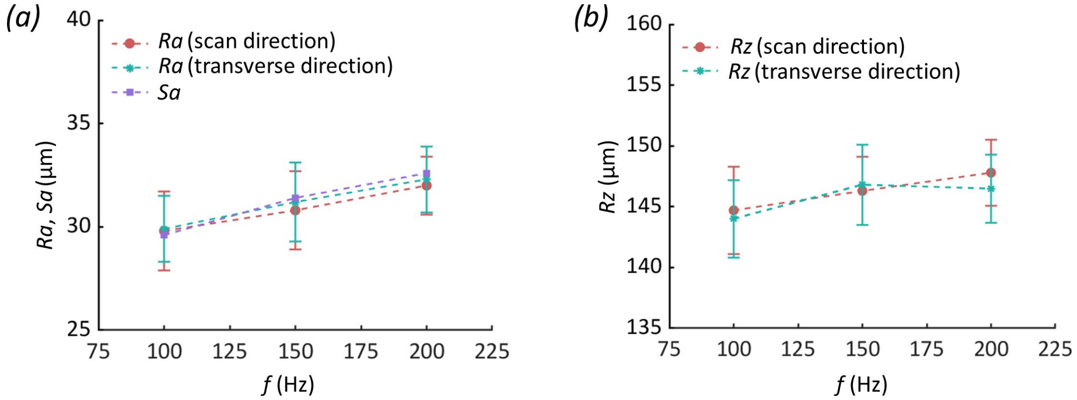

Figure 6.5 Roughness parameters (Sa, Ra, Rz) under different vibration frequency conditions at d = 3 mm, V_{pp} = 150 V, v_s = 3000 mm/min, and Z = -150 μm.

In the current scenarios, when a much rougher surface is treated using PVST, a more considerable height difference of the nonuniform rough features can be formed due to amplitude reduction, especially in the scattered pattern in which more rough features are unaffected. The positive effect brought by the denser overlap of the indentations is not pronounced in a relatively rough surface, not to mention in a much rougher surface. In addition, the calculation of the Sa value is based on the arithmetic mean deviation formula. The surface height difference significantly impacts the calculated results, which may dominate more on the Sa value compared to the distribution density of the indentations. Consequently, a higher frequency is not necessary since it has a higher requirement for the activation device and higher surface finish, based on the previous and current results. Using f = 100 Hz in the current study should be sufficient to apply the PVST on rough surfaces.

6.2 Effect of scan speed on surface deformation

Another factor closely related to the overlap of the indentations is the scan speed of the striking tool in PVST. To investigate the effect of scan speed on surface deformation, various experiments are conducted by varying v_s (v_s = 1000 - 3000 mm/min) under the condition of f = 100 Hz, d = 3 mm, V_{pp} = 150 V, and Z = -150 μm. As shown by the surface textures in the left column of Fig. 6.6, all the surface textures present a scattered pattern. The bottom unaffected areas and the top flattened areas can be observed. The bright areas increase when the scan speed decreases from 3000 mm/min to 1000 mm/min, indicating that the striking tool approaches more rough features.

Regarding the height contour maps in the right column, the connected treated areas at the top row (v_s = 1000 mm/min) seem more uniform and significant than the other two rows. There are much more blue unaffected areas at the condition of v_s = 3000 mm/min compared to that at v_s = 1000 mm/min. It is consistent with the results in the initially smooth surface conditions where lower scan speed can generate a denser overlap distribution of the indentations (see Fig. 5.17). Also, the height difference between the top treated surface and the bottom rough surface is at a similar level based on the height distribution of the contour maps.

Figure 6.7 summarizes the roughness parameters under different scan speeds. Sa agrees well with Ra in the scan and transverse directions, and increases as the scan speed decreases. Rz

(a) v_s = 1000 mm/min, *Sa* = 24.9 μm

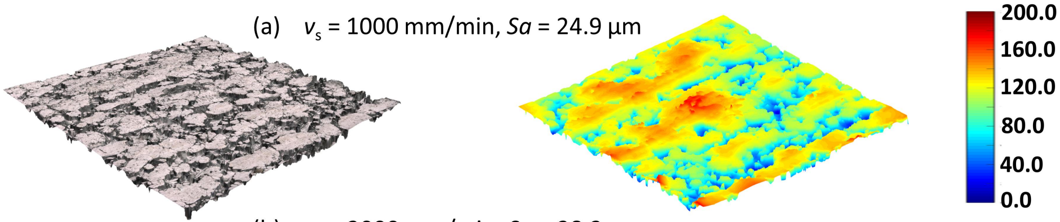

(b) v_s = 2000 mm/min, *Sa* = 28.2 μm

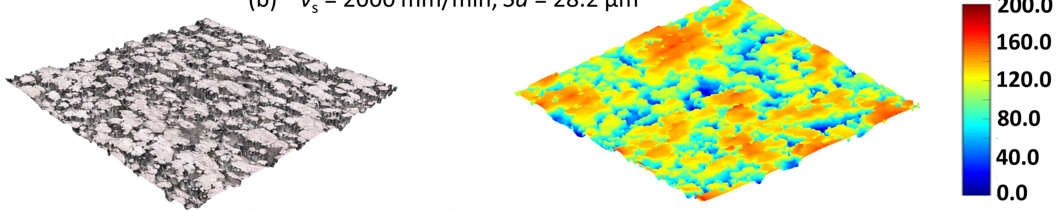

(c) v_s = 3000 mm/min, *Sa* = 29.6 μm

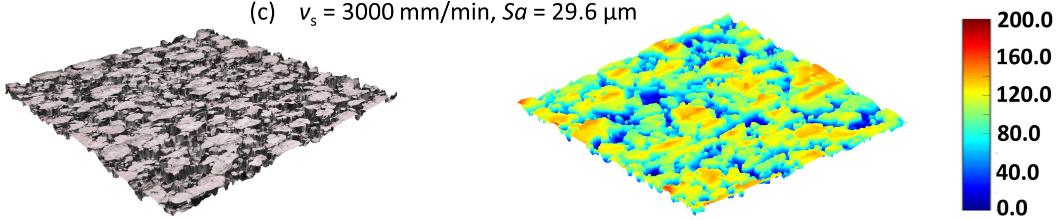

Figure 6.6 Surface textures and height maps after PVST under different scan speeds at d = 3 mm, V_{pp} = 150 V, f = 100 Hz, and Z = -150 μm: (a) v_s = 1000 mm/min; (b) v_s = 2000 mm/min; (c) v_s = 3000 mm/min.

decreases when v_s increases from 2000 mm/min to 3000 mm/min, which the nonuniform rough features may cause. The results of Sa and Ra are consistent with the above surface textures under the scattered pattern. They have the same trend as the results of the experiments using the steel samples with the initially smooth surface in Fig. 5.18 (larger scan speed, smaller surface finish, and vice versa). Similar to the results at different frequency conditions, the current results differ from our previous results on the titanium alloy plates [115], in which the scan speed does not significantly influence the roughness parameters. This inconsistency can be explained by the slight scan speed variation in the previous work, i.e., v_s = 450 mm/min, 600 mm/min, and 750 mm/min. Since the uniform pattern was achieved under v_s = 750 mm/min, a lower scan speed will not further affect the surface roughness positively, although it can generate a slightly denser distribution of the indentations. Therefore, similar roughness parameters were obtained at different scan speeds. While in current scan speed conditions, the speed variation is 1000 mm/min and large enough to produce completely distinct surface textures at the same level of surface heights, as demonstrated in the smooth surface results in Fig. 5.17 and Fig. 5.18. Since the height differences are equivalent to current scan speed conditions, the denser overlap distribution of the indentations caused by a lower scan speed will dominate the surface finish improvement.

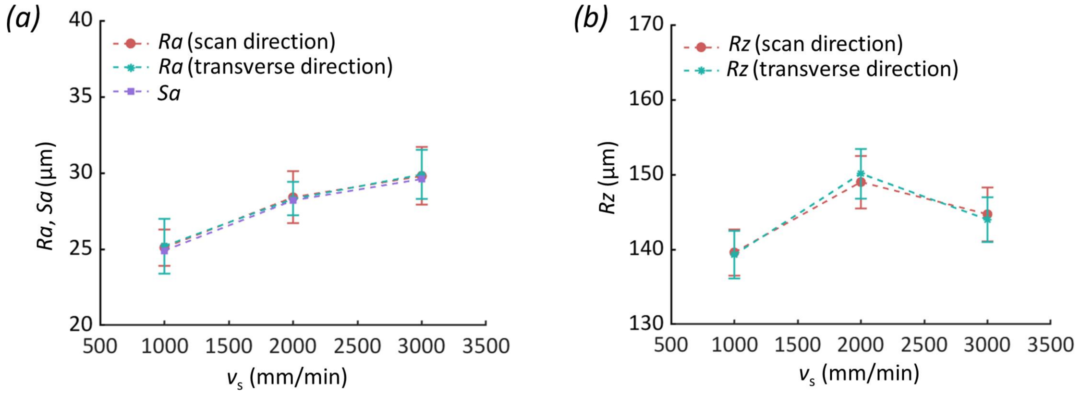

Figure 6.7 Roughness parameters (Sa, Ra, Rz) under different scan speeds at d = 3 mm, V_{pp} = 150 V, f = 100 Hz, and Z = -150 μm.

In addition, in light of the previous results, it took 45 s, 26 s, and 17 s at v_s = 450, 600, and 750 mm/min to process a targeted area of 5 mm × 5 mm in PVST, respectively. In contrast, it takes 9.9 s, 3.3s, and 1.9 s under the current scan speed conditions to process the areas of the same size. Despite the significantly reduced processing time under the conditions of v_s = 2000 mm/min and v_s = 3000 mm/min, it is not recommended to use the scan speed at this level since it is too fast to generate a dense overlap of the indentations and a better surface finish. Also, the previous work indicates that the scan speed does not highly influence the surface roughness in the range of 450 ~ 750 mm/min due to the slight speed variation. Therefore, selecting a scan speed from 750 mm/min to 1000 mm/min would be a more reasonable option. The scan speed is fixed in the following experiments at 1000 mm/min.

6.3 Effect of driving voltage on surface deformation

The amplitude of the driving voltage V_{pp} controls the vibration amplitude of the striking tool. Higher driving voltage can generate higher dynamic energy and hence higher vibration amplitude. Thus, the tool can be extended more to strike a deeper position of the roughness layer, enhancing the flattening-sliding effect to improve the surface finish.

Figure 6.8 compares the surface textures and height contour maps achieved under different driving voltage conditions (V_{pp} = 60 - 150 V, f = 100 Hz, d = 2 mm, v_s = 1000 mm/min, Z = -150

(a) V_{pp} = 60 V, Sa = 35.3 µm

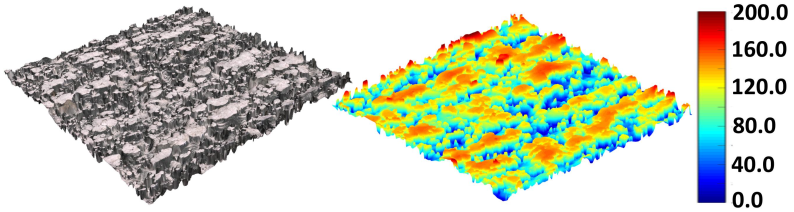

(b) V_{pp} = 90 V, Sa = 28.3 µm

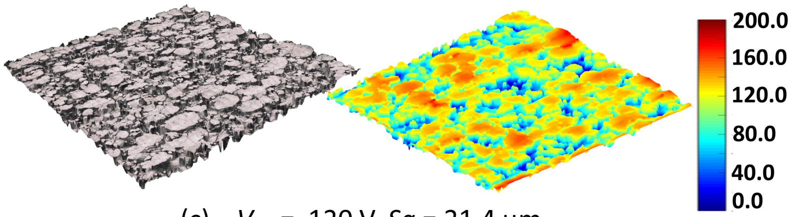

(c) V_{pp} = 120 V, Sa = 21.4 µm

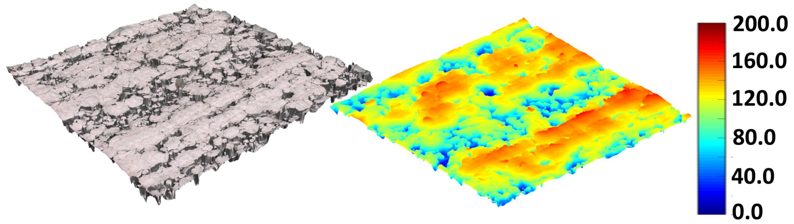

(d) V_{pp} = 150 V, Sa = 13.1 µm

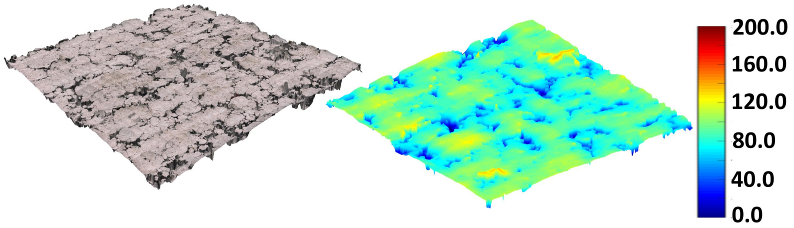

Figure 6.8 Surface textures and height contour maps after PVST under different driving voltages at d = 2 mm, v_s = 1000 mm/min, f = 100 Hz, and Z = -150 μm: (a) V_{pp} = 60 V; (b) V_{pp} = 90 V; (c) V_{pp} = 120 V; (d) V_{pp} = 150 V.

μm). More scattered bright areas are observed in the left column of Fig. 6.8 as V_{pp} increases from 60 V to 150 V. The surface texture transforms from a scattered pattern to a uniform pattern when V_{pp} reaches 150 V. This transformation is consistent with the previous results on the titanium alloy plates [115], where the scattered pattern occurs when $V_{pp} \leq 100$ V. It is also observed that the surface texture at V_{pp} = 120 V is in the transition state between the scatter pattern and the uniform pattern because many continuous block areas can be seen in the treated area despite some unapproached dark areas. When the driving voltage increases to 150 V, the continuous block areas almost cover the whole treated area, and the dark areas reduce to some path-like features or areas (more reduction of dark areas requires other proper parameters for further surface finish improvement). Since a more significant driving voltage generates a more extensive vibration amplitude, the surface height difference in the right column of Fig. 6.8 becomes smaller as V_{pp} increases from 60 V to 150 V, which is caused by the more substantial striking effect.

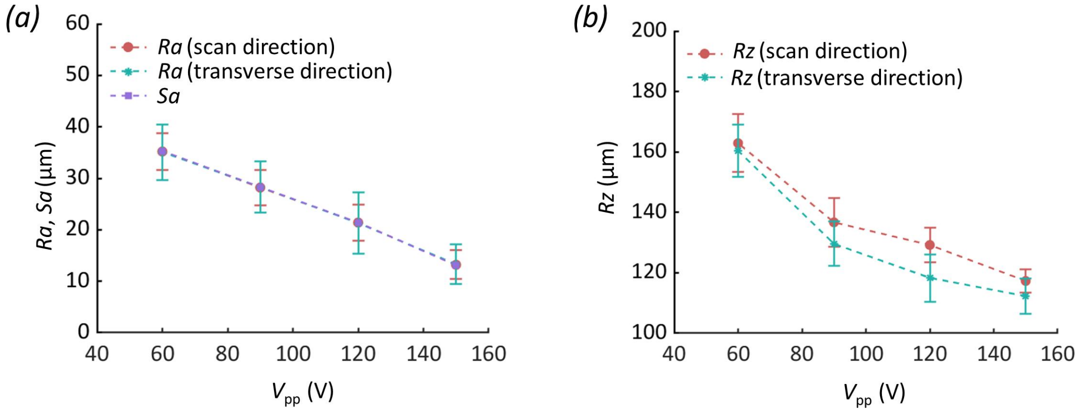

Figure 6.9 Roughness parameters (Sa, Ra, Rz) under different driving voltages at d = 2 mm, v_s = 1000 mm/min, f = 100 Hz, and Z = -150 μm.

Figure 6.9 summarizes the roughness parameters under different driving voltages. The Sa values agree well with the Ra values in the scan and transverse directions. All the parameters are negatively and linearly correlated with the driving voltage. These results are consistent with the demonstrated surface textures in Fig. 6.8, where higher driving voltages produce more bright areas and smoother surface features. They are also consistent with the previous results in [115] and inconsistent with those in the copper and steel specimens with the initially smooth surface. The inconsistency is mainly due to the initial surface state of the workpieces. In the smooth surface experiments, PVST is applied onto the smooth surface and brings the rough features to the smooth surface. It adds extra roughness to an otherwise smooth surface; hence the higher the driving voltage, the rougher the surface. Nonetheless, in the previous results of titanium alloy plates, PVST is applied onto the relatively rough surfaces (previous Sa_0 = 28.6 μm Vs. current Sa_0 = 48.6 μm) to eliminate the rough features. In this case, increasing the driving voltage and introducing a more considerable striking depth benefit the surface finish. The variation trend works for rough surfaces in two different scenarios. Therefore, a more significant driving voltage is recommended to eliminate the rough features. In the following experiments, the driving voltage is fixed at V_{pp} =

150 V, except for the conditions in multiple pass scenarios.

6.4 Effect of tool diameter on surface deformation

Striking tool diameter (d) influences the surface deformation by changing the contact area between the striking tool and the workpiece in PVST. The schematic in Fig. 6.10 illustrates the interactions between the striking tool and the workpiece in a single strike at different tool diameter scenarios. As demonstrated in Fig. 6.10a, when the striking tool with a large diameter is used, the tool has to contact more rough features during the striking process than that with a small diameter, resulting in more significant deformation resistance and hence amplitude reduction of the tool when other experimental parameters keep constant. Thus, the tool will not approach those rough features below the contact features. Instead, using the striking tool with a small diameter can improve the issue, as shown in Fig. 6.10b and Fig. 6.10c. In these scenarios, the tool has fewer contact areas with rough features in each striking cycle due to the reduced diameter. It enables the tool to extend more to strike on the lower rough features thanks to the decreasing deformation resistance. Specifically, in Fig. 6.10c, the tool with a small diameter is more likely to approach those rough features surrounded by other higher rough features by going through the gap between them and striking the lower rough features.

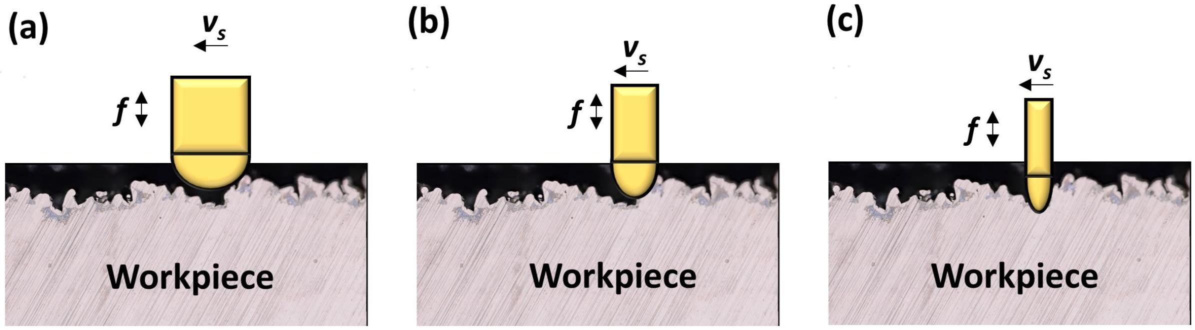

Figure 6.10 Schematic of PVST on rough surface using different tool diameters: (a) large tool diameter scenario; (b) small tool diameter scenario; (c) small tool diameter scenario when penetrating the gap between higher rough features.

Figure 6.11 demonstrates the surface textures and height contour maps after PVST under different tool diameters (f = 100 Hz, v_s = 1000 mm/min, V_{pp} = 150 V, d = 0.5, 1, 2, 3 mm, Z = -150 μm). The uniform pattern occurs only at d = 0.5 mm, while the scattered pattern occurs at

(a) *d* = 3 mm, *Sa* = 24.9 µm

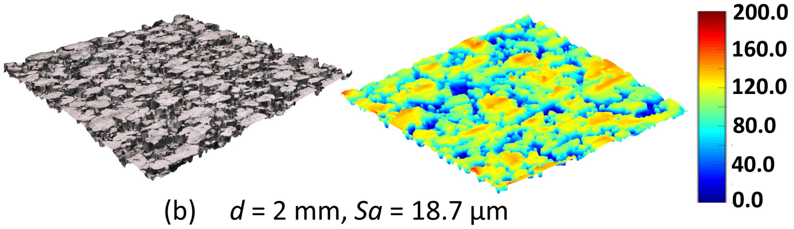

(b) *d* = 2 mm, *Sa* = 18.7 µm

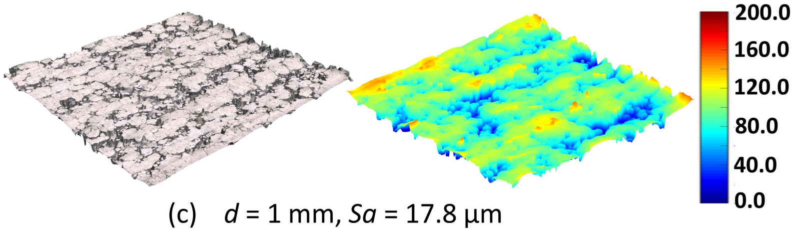

(c) *d* = 1 mm, *Sa* = 17.8 µm

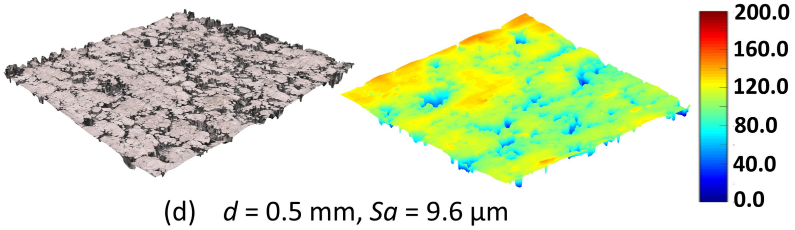

(d) *d* = 0.5 mm, *Sa* = 9.6 µm

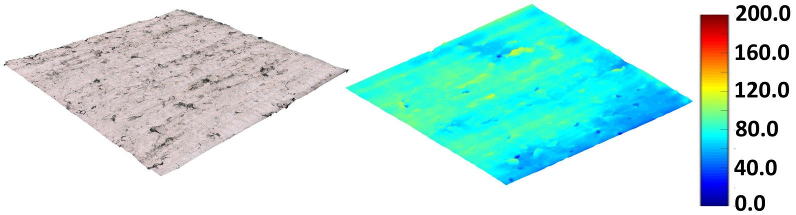

Figure 6.11 Surface textures and height contour maps after PVST under different tool diameters at V_{pp} = 150 V, v_s = 1000 mm/min, f = 100 Hz, and Z = -150 μm: (a) d = 3 mm; (b) d = 2 mm; (c) d = 1 mm; (d) d = 0.5 mm.

d = 1, 2, 3 mm, especially at d = 3 mm, where the dark areas increase significantly. The height contour maps in the right column also show a similar distribution. As seen in the figure, the surface height becomes smaller with the decrease in the tool diameter. A large uniform area with the same level of surface height can be observed at d = 0.5 mm, which indicates the uniformity and flatness of the treated area. Those navy-blue areas that represent the untreated areas are barely seen in this condition, while they are easy to be found at d = 2 mm d = 3 mm. The increasing uniformity of the treated surface with a smaller tool diameter is consistent with the previous results [115], but they behave differently. In the previous work, only d = 2, 3, 4 mm are used, and the uniform pattern occurs at d = 2 mm and d = 3 mm while the scattered pattern occurs at d = 4 mm. The uniform pattern can be achieved at d = 2 mm and d = 3 mm because the workpieces used have a less rough surface finish that does not need a very deep striking depth compared to the current scenarios. Thus, a tool diameter of 2 or 3 mm is sufficient to smooth the rough surface. While in the current scenarios, the high surface roughness necessitates a smaller tool diameter to strike the rough surface more deeply, and d = 0.5 mm is a better option (Changing engagement distance can also be another option, which will be discussed later).

In addition, all the roughness parameters in Fig. 6.12 are in good agreement with the surface textures shown in Fig. 6.11. There is a significant surface finish improvement from d = 3 mm to d = 0.5 mm (ΔSa = 15.3 μm), but only a slight improvement is obtained from d = 2 mm to d = 1 mm. A slight improvement can be observed in the Rz values from d = 3 mm to d = 1 mm, while the value reduces from 146.3 μm to 49.6 μm when d reaches 0.5 mm, which showcases the tremendous flattening effect brought by using a small tool diameter. Similar to the behavior under different driving voltage conditions, the correlation between the surface roughness and the tool diameter on the initially rough surface is opposite to that on the initially smooth surface. As discussed above, a smaller tool diameter introduces deeper striking depth for the initially smooth surface, leading to large surface roughness (see Fig. 5.19 and Fig. 5.20).

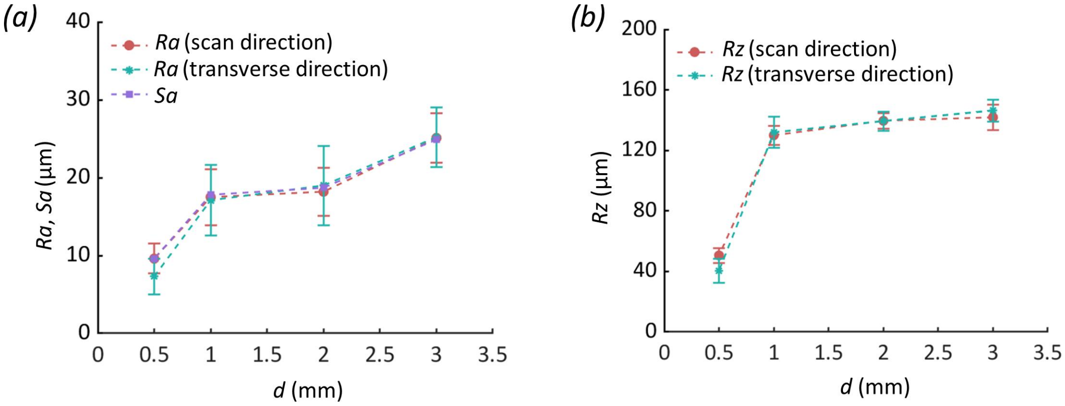

Figure 6.12 Roughness parameters (Sa, Ra, Rz) under different tool diameters at V_{pp} = 150 V, v_s = 1000 mm/min, f = 100 Hz, and Z = -150 μm.

As seen from the results in the workpieces with an initially smooth surface and the workpieces with an initially rough surface, the reasonable selection of the tool diameter is heavily dependent on the initial surface state. If the workpiece surface is relatively smooth, a large tool diameter would be a good choice since a small tool diameter can overtreat the surface and worsen the surface quality. If the workpiece surface is rough, then a small tool diameter would be a better selection to get sufficient striking depth to achieve a uniform surface. Alternatively, a combination of a large tool diameter and large engagement distance may be a feasible option, as is the combination of a small tool diameter and a small engagement distance for the smooth surface scenarios. Therefore, it is necessary to explore the effect of engagement distance on surface roughness to understand how to realize the alternatives.

6.5 Effect of engagement distance on surface deformation

In PVST, the nominal stroke of the piezo stack actuator is 100 μm under the maximum driving voltage (V_{pp} = 150 V). During the striking process, the vibration amplitude reduces because of the elastic compression of the device assembly under the striking force. To accommodate the vibration range and amplitude reduction and achieve a better surface finish, the engagement distance (Z) between the striking tool and the workpiece surface should be appropriately selected.

Figure 6.13 illustrates the possible interactions between the vibration tool and the rough surface layer in the PVST of AM part. The reference for Z is defined as the highest feature of the surface layer. In Fig. 6.13a, the tool and the surface have a positive engagement distance ($Z > 0$), i.e., the tool is above the surface at its minimum vibration displacement. In this case, the vibration amplitude needs to be larger than the engagement distance ($u_{pp} > Z$) to induce the strikes on the surface layer. The effective vibration amplitude is actually u_{pp} - Z, indicating that the vibration amplitude u_{pp} is not fully utilized. Each tool vibration leads to one strike on the roughness features. The induced deformation is more of a compression type, which would flatten the hills of the roughness features. The valleys of roughness features beyond the tool's reach will likely be unaffected. For the rougher surface with a high peak-to-valley roughness value (Rz), a larger vibration amplitude is needed for the tool to reach the bottom of the roughness layer. Since the measured average Rz throughout the targeted area of the workpiece is about 250 μm (> nominal stroke of the actuator), the striking tool cannot reach the bottom of the roughness layer in the current positive Z setting or even Z is set as 0. Therefore, the compression and flattening effect on the roughness features cannot be thoroughly realized at $Z \geq 0$.

In Figs. 6.13b - 6.13d, the tool and the workpiece surface have a negative engagement distance ($Z < 0$), i.e., the tool penetrates the roughness layer even at its minimum vibration displacement position. The tool always engages with the rough surface during its full vibration amplitude range. The required vibration amplitude to reach the bottom of the roughness layer is significantly reduced. In this case, besides compression-type deformation (Fig. 6.13b), the tool will also induce sliding-type deformation (Fig. 6.13c) due to the tool's horizontal scan at a negative engagement distance. The sliding-type deformation is likely more effective in displacing the material from the hills to the valleys for the highly rough surface (Fig. 6.13d).

Figure 6.13e illustrates the cross-section profiles of the workpiece before (lower surface) and after (upper surface) PVST measured using KEYENCE. Observe that the rough hills are flattened by the tool, and no voids or cracks exist on the flattened area compared to the initially rough surface profiles, showcasing the enhanced effect of flattening-sliding deformation on the roughness layer. Some micro-cracks and voids on the bottom of the roughness layer are still observed due to the limited striking depth, which could be eliminated with a smaller Z or larger u_{pp}. Also, the defects, such as shear lap, should be avoided during the PVST process. Otherwise, these defects will degrade the surface quality.

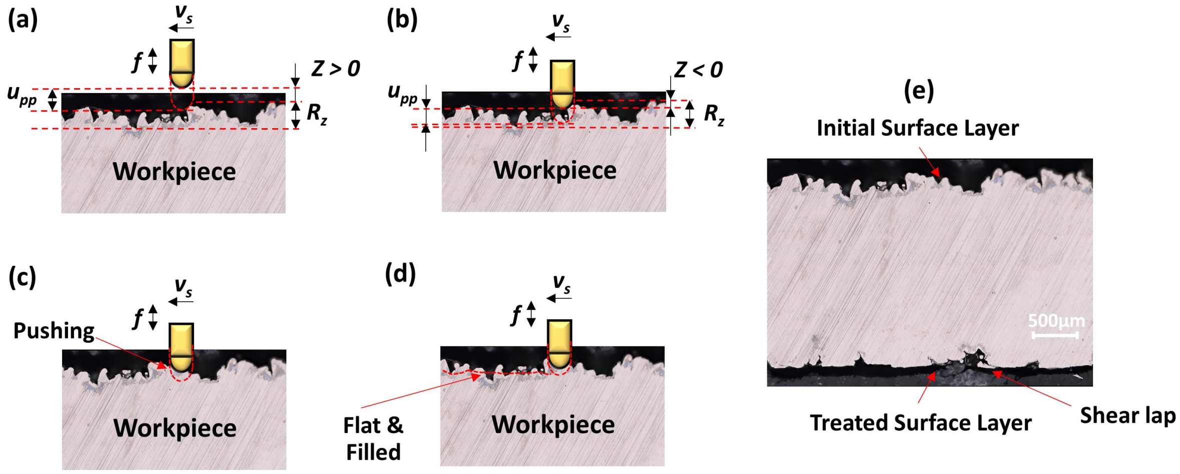

Figure 6.13 (a) – (d) The schematic illustration of tool engaging process; (e) The cross-section of the treated workpiece after PVST.

In order to explore how engagement distance works in the above three different scenarios, different treatment conditions under PVST or pure sliding without vibration are utilized. Two special conditions are first considered, which are $Z > 0$ ($Z = 10$ μm) and $Z < 0$ ($Z = -Rz = -250$ μm). $-Rz$ is chosen as the limit of negative engagement distance because the striking tool should theoretically reach the lowest position of the upper roughness layer when $Z = -Rz$. Nevertheless, there exists elastic compression of the PVST device assembly during the approaching process of the striking tool toward the workpiece surface. The actual engagement distance is smaller than the distance that the spindle of the CNC mill moves. To simplify the process, this elastic compression is ignored when exploring the effect of engagement distance on surface deformation.

The experimental data indicated that the workpiece preload was about 750 N as Z reached -250 μm. This preload is much higher than that in the previous experiment [115], where the preload is only 200 ~ 300 N when Z reaches $-Rz$. The difference is mainly caused by the relatively small Rz (= 140 μm) in the previous work, so the engagement distance at $Z = -Rz$ can be used in the previous PVST experiment. However, it is not safe to use the current engagement distance at $Z = -Rz$ in the PVST experiments since the high preload combined with the high driving voltage conditions (i.e., $V_{pp} = 150$ V) may cause the maximum striking force to exceed the maximum force range (3500 N) of the piezo stack and damage it. Therefore, to reduce the risk of damaging the piezo stack, only pure sliding without vibration was performed at this engagement distance. As for $Z = 10$ μm, the positive engagement distance indicates that the striking tool is not engaged with the workpiece at the minimum vibration displacement position. It is meaningless to perform pure sliding under this setting (due to the non-uniformity of the rough surface, pure sliding may still remove some rough features, but this is not the main focus of this research), so only PVST experiment is conducted at $Z = 10$ μm.

Figure 6.14 illustrates the surface textures and height contour maps at $Z = 10$ μm and $Z = -250$ μm under the condition of $f = 100$ Hz, $v_s = 1000$ mm/min, $V_{pp} = 150$ V, and $d = 3$ mm. Compared to the initially rough surface in Fig. 6.1, only a slight improvement of the surface roughness can be observed in Fig. 6.14a, where Sa reduces from 48.6 μm to 42.7 μm. It is seen that some of the top rough features have been flattened after PVST, and the bright areas (red areas in the height contour map) are scattered over the whole treated area. There still exists a lot of rough unaffected features in the targeted area. The results are consistent with the above analysis in the scenario of positive engagement distance. Since a positive engagement distance is used, it does not fully use the vibration amplitude and the sliding effect of the engagement, which is not beneficial to achieve a uniform surface pattern. As shown in Fig. 6.14b, the surface roughness after pure sliding is highly improved, and the Sa reduces by 34.5% (ΔSa = 16.8 μm). Several big chunks of bright areas or red areas are observed as well. Although the results present a scattered pattern, the uniform and flattened chunks showcase the positive effect of the large negative engagement distance on eliminating the rough features.

PVST

(a) Z = 10 µm, Sa = 42.7 µm

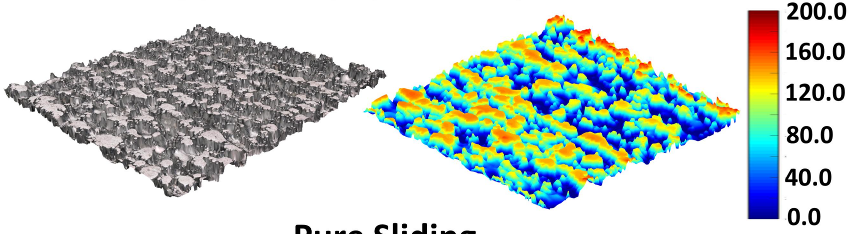

Pure Sliding

(b) Z = -250 µm, Sa = 31.8 µm

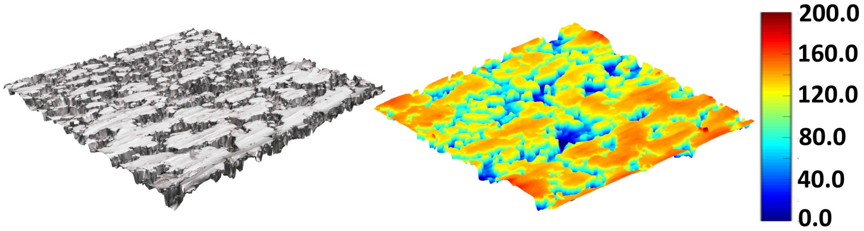

Figure 6.14 Surface textures and height contour maps after PVST or pure sliding under special engagement distance conditions at v_s = 1000 mm/min and d = 3 mm: (a) Z = 10 μm, f = 100 Hz, V_{pp} = 150 V; (b) Z = -250 μm, f = 0 Hz, V_{pp} = 0 V.

As mentioned earlier, for a uniform or low roughness surface, the striking tool should be able to theoretically approach the lowest valley of the roughness layer at $Z = -Rz$ even in a pure sliding setting. However, this might not be the case for a nonuniform surface. Due to the uneven roughness, the height may differ at distinct locations throughout the layer. In this case, the average Rz could not perfectly reflect the distance between the highest hill and the lowest valley throughout the roughness layer. As a result, the combined effect of the workpiece surface nonuniformity and the device elastic compression makes it difficult for the striking tool to reach the lowest valley in a pure sliding setting with a significant negative engagement distance. While it is still possible to use a more considerable negative engagement distance in pure sliding to reach the bottom roughness layer, that is not the main focus of the application of PVST.

According to the results of the above two conditions in Fig. 6.14, neither a positive engagement distance nor an overlarge negative engagement distance is suitable for applying PVST to obtain smoother surfaces. Therefore, the Z value in the following experiments is selected from -200 μm to 0. PVST and pure sliding are performed under the same engagement distance condition to compare and study how the striking effect in PVST affects surface roughness.

PVST **Pure Sliding**

(a) Z = -200 µm, Sa = 19.9 µm (e) Z = -200 µm, Sa = 43.5 µm

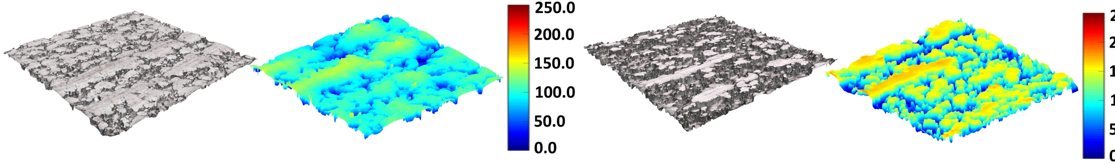

(b) Z = -150 µm, Sa = 24.9 µm (f) Z = -150 µm, Sa = 45.3 µm

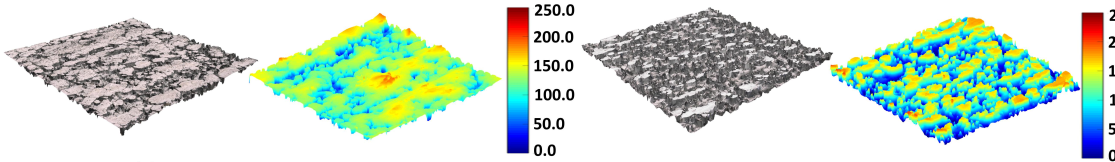

(c) Z = -50 µm, Sa = 29.6 µm (g) Z = -50 µm, Sa = 47.2 µm

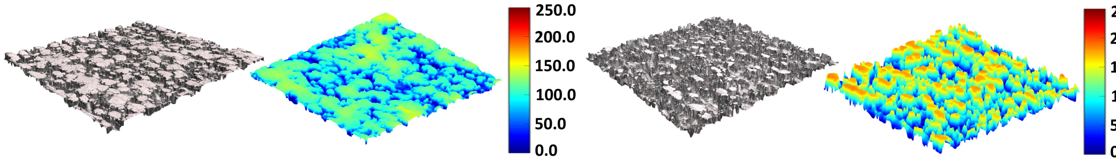

(d) Z = 0 µm, Sa = 41.4 µm (h) Z = 0 µm, Sa = 49.2 µm

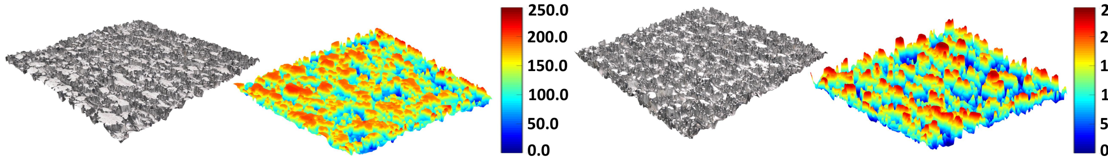

Figure 6.15 Surface textures and height contour maps after PVST or pure sliding under different engagement distances at f = 0, 100 Hz, V_{pp} = 0, 150 V, v_s = 1000 mm/min, and d = 3 mm: (a) & (e) Z = -200 μm; (b) & (f) Z = -150 μm; (c) & (g) Z = -50 μm; (d) & (h) Z = 0 μm.

Figure 6.15 demonstrates the surface textures and height contour maps under the condition of f = 0 and V_{pp} = 0 for pure sliding or f = 100 Hz and V_{pp} = 150 V for PVST at v_s = 1000 mm/min, d = 3 mm, and Z = 0, -50, -150, -200 μm. The left and right two columns are the results after PVST and pure sliding at different Z values, respectively. Both results show that the bright areas increase as the engagement distance increases (larger $|Z|$), indicating that more rough features are flattened. The surface textures present a scattered pattern at the current experimental setting despite a significant engagement distance used. The PVST results show that when Z = -200 μm, the surface pattern is very close to the uniform pattern because of the large, flattened areas with continuous chunks generated. Nevertheless, the amplitude reduction caused by a striking tool with a large diameter and the original surface roughness make it challenging to achieve a sufficiently deep striking depth to realize the uniform pattern, even with a considerable engagement distance. While more red areas in the height contour map at Z = 0 μm (Fig. 6.15d) are generated than that at Z = -10 μm (Fig. 6.15a), the surface is still rough, and Sa is 41.4 μm ($\Delta Sa\%$ = 14.8%). The value is much lower than that achieved at Z = -200 μm (Sa = 19.9 μm and $\Delta Sa\%$ = 59%). As seen from the results after pure sliding, all the surface textures are very close to the original rough surface (the largest Sa at Z = -200 μm is 43.5 μm and $\Delta Sa\%$ is only 10.5%). The results reveal that pure sliding is inefficient in improving the surface finish of a rough surface, even if a large engagement distance is used. Once the vibration is introduced, a noticeable improvement can be seen.

As mentioned above, the nominal stroke at V_{pp} = 150 V is only 100 μm. The actual vibration amplitude must be less than 100 μm due to amplitude reduction. Consider the case at Z = 0 μm after PVST (Fig. 6.15d) and the case at Z = -200 μm after pure sliding (Fig. 15e). The engagement distance difference between the two cases is 200 μm, which is much larger than the vibration amplitude of the striking tool. However, this large engagement distance difference does not significantly improve the surface finish in pure sliding. Therefore, a combination of a considerable engagement distance and the compression-sliding type of deformation in PVST is necessary for a significant surface finish improvement.

Figure 6.16 summarizes these quantified roughness parameters (Sa, Ra, and Rz). The roughness parameters are consistent with the corresponding surface textures, which decrease as Z decreases. The results achieved in pure sliding are significantly larger than those achieved in PVST. Observe that the Ra and Sa values for each condition in pure sliding (solid lines in Fig. 6.16a) fluctuate around the original Sa values except for Z = -Rz = -250 μm. Note that for pure sliding at Z = 0 μm, the effect of improving the surface finish is not apparent, and Rz after treatment is 238 μm which is very close to the original Rz value (250 μm). While for the results after PVST at Z = 0 μm and Z = 10 μm, Rz is reduced to about 180 μm. Overall, PVST has a good amount of roughness improvement when using negative engagement distance compared to pure sliding.

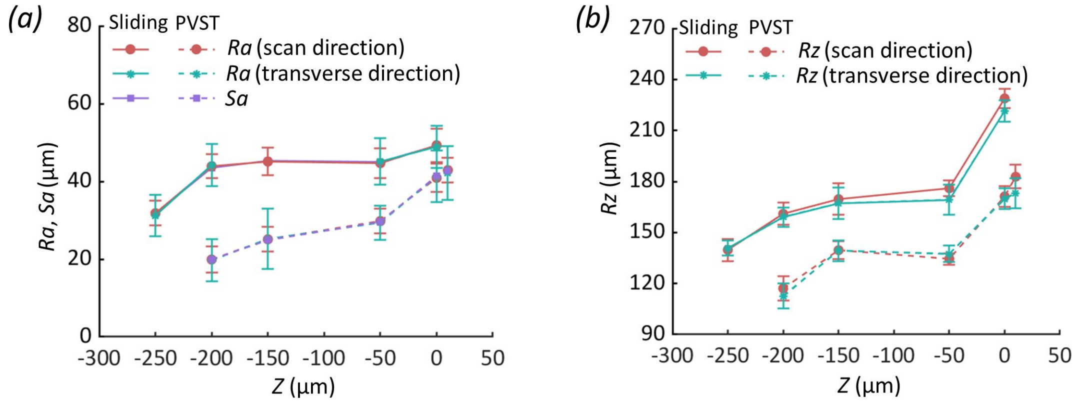

Figure 6.16 Roughness parameters (Sa, Ra, Rz) after PVST or pure sliding at f = 0, 100 Hz, V_{pp} = 0, 150 V, v_s = 1000 mm/min, d = 3 mm, and Z = 0, -50, -150, -200 μm.

Based on the above results, obtaining a uniform surface texture pattern is difficult if the engagement distance is too small. Alternatively, it can lead to overlarge striking force and damage the piezo stack if the engagement distance is too large. Thus, these two factors limit the adoption of the engagement distance. If a further roughness improvement is desired to get a uniform surface texture, reducing the tool diameter to increase the striking depth is an alternative. The experiments under d = 0.5, 1, 2 mm, and different engagement distances were performed to get the optimal combination of the tool diameter and the engagement distance.

Figure 6.17 shows an overview of the surface textures after PVST or pure sliding under different tool diameters and engagement distances at v_s = 1000 mm/min. All the small square areas enclosed by a red rectangle are treated at the same tool diameter condition. Only the ordered square areas are considered to explore the effect of the engagement distance on surface deformation. The experimental parameters and surface roughness of each treated ordered area can be found in Table.6.2.

As shown in Fig. 6.17, none of the conditions can obtain a uniform pattern at d = 3 mm.

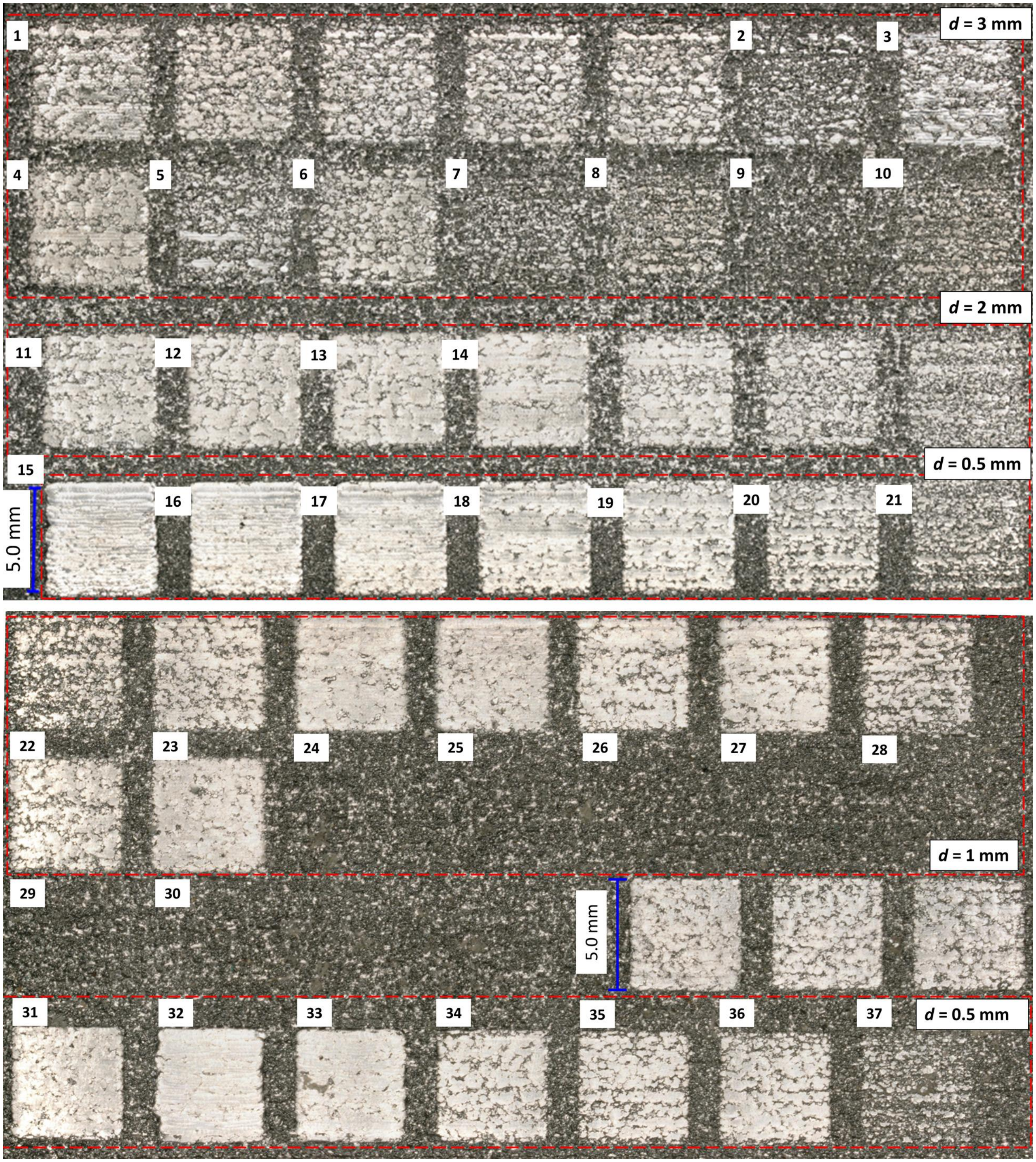

Figure 6.17 Overview of surface textures after PVST or pure sliding under different tool diameters and engagement distances. (see Table 6.2 for details)

Table 6.2 Experimental parameters and surface roughness (Sa) of the treated ordered areas.

No.	d (mm)	Z (μm)	f (Hz)	V_{pp} (V)	Sa (μm)
1	3	-150	100	150	24.9
2	3	-150	0	0	45.3
3	3	-250	0	0	31.8
4	3	-200	100	150	19.9
5	3	-200	0	0	43.5
6	3	-50	100	150	29.6
7	3	-50	0	0	47.2
8	3	0	100	150	41.4
9	3	0	0	0	49.2
10	3	10	100	150	42.7
11	2	-170	100	150	18.7
12	2	-180	100	150	16.8
13	2	-190	100	150	13.1
14	2	-200	100	150	13
15	0.5	-190	100	150	5.3
16	0.5	-170	100	150	6.5
17	0.5	-160	100	150	7.3
18	0.5	-140	100	150	11.3
19	0.5	-130	100	150	12.6
20	0.5	-50	100	150	22
21	0.5	-30	100	150	36.6
22	1	-100	100	150	29.1
23	1	-140	100	150	17.8
24	1	-180	100	150	13.1
25	1	-200	100	150	11.5
26	1	-170	100	150	14.3
27	1	-160	100	150	14.8
28	1	-120	100	150	25.9
29	1	-150	100	150	15.8
30	1	-190	100	150	12.4
31	0.5	-150	100	150	9.4
32	0.5	-200	100	150	5.8
33	0.5	-180	100	150	7.6
34	0.5	-110	100	150	15.1
35	0.5	-70	100	150	18.7
36	0.5	-90	100	150	15.8
37	0.5	-10	100	150	44.9

Although No. 14 at d = 2 mm and No. 24, No. 25, and No. 30 at d = 1 mm are much more uniform than all the conditions at d = 3 mm, many dark areas still exist. The expected uniform pattern is not achieved yet. However, when the tool diameter is reduced to 0.5 mm, the uniform pattern is achieved at several conditions, i.e., No. 15 – 17 and No. 32. Compared with a scattered pattern or the transition state of a uniform pattern, these squares with the newly achieved uniform pattern are very shiny. The indentation marks and scan paths similar to those at the initially smooth surface conditions are also observed, especially in No. 32. These results show that reducing the tool diameter at a certain engagement distance significantly facilitates getting the uniform pattern.

The PVST experiments under the conditions of Z = -130 μm ~ -200 μm, d = 0.5 mm, f = 100 Hz, v_s = 1000 mm/min, and V_{pp} = 150 V, were performed to explore the critical engagement distance to achieve the uniform pattern at d = 0.5 mm. The corresponding surface textures and height contour maps are shown in Fig. 6.18.

(a) **Z = -130 μm**, Sa = 12.6 μm

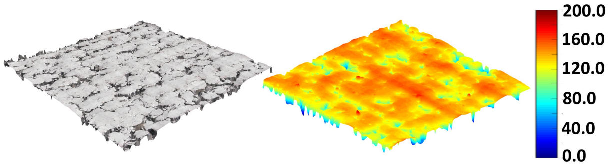

(b) **Z = -140 μm**, Sa = 11.3 μm

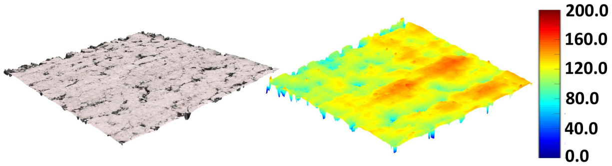

(c) **Z = -150 μm**, Sa = 9.4 μm

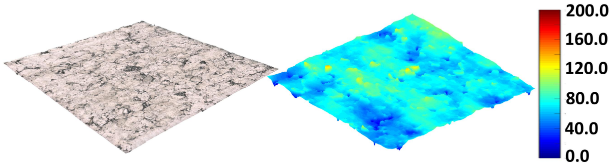

(d) **Z = -160 μm**, Sa = 7.3 μm

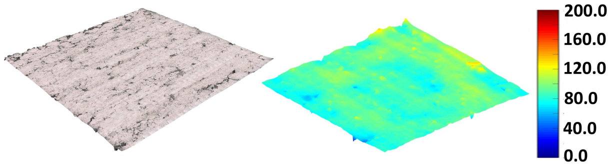

(e) **Z = -170 μm**, Sa = 6.5 μm

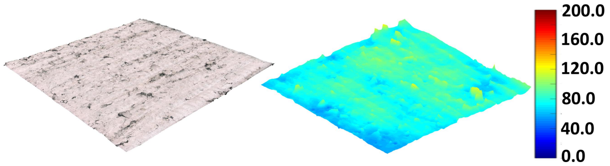

(f) **Z = -180 μm**, Sa = 7.6 μm

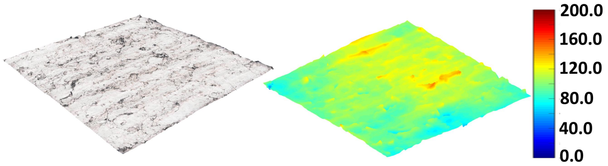

(g) **Z = -190 μm**, Sa = 5.3 μm

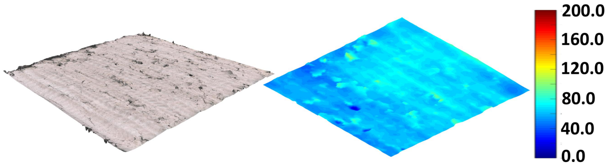

(h) **Z = -200 μm**, Sa = 5.8 μm

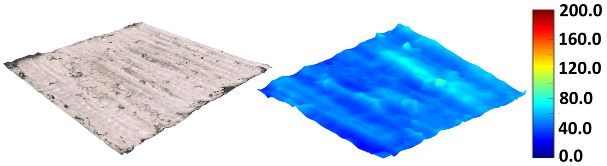

Figure 6.18 Surface textures and height maps after PVST under different engagement distances at d = 0.5 mm, f = 100 Hz, v_s = 1000 mm/min, and V_{pp} = 150 V.

It is observed that the surface textures are very close to the uniform pattern at Z = -130 μm (Fig. 6.18a) and Z = -140 μm (Fig. 6.18b), but there are still many big, flattened chunks divided by those path-like dark features or areas. In the height contour maps of these two conditions, the red chunks are easily observed to see how those unaffected features separate them. Although the dark areas still distribute on the surface, the surface quality is much better than in other tool diameter conditions. Sa reduces to 12.6 μm ($\Delta Sa\%$ = 74.1%) at Z = -130 μm and 11.3 μm ($\Delta Sa\%$ = 76.1%) Z = -140 μm, respectively. From Z = -150 μm to Z = -200 μm, it starts to enter a uniform pattern range, indicating that Z = -150 μm can be considered the critical engagement distance to get a uniform surface texture pattern. No big continuous bright chunks are observed. Instead, the surface features present a uniform surface height distribution. Most of the rough red features disappear in the height contour maps, and the height maps show a uniform color indicating the surface's flatness and uniformity. The dark features reduce gradually as the engagement distance increases, and the bright areas dominate the surface when Z reaches -200 μm.

Even though in the condition of Z = -200 μm, some dark features or defects can still be observed. It is challenging to eliminate these rough features, not only because of the rough characteristics of the surface itself but also the induced defects by the PVST process. Consider an extreme case. Even if the PVST can eliminate all the original rough features, it might still introduce the striking indentation to increase the roughness, such as the results obtained in the initially smooth surface conditions. This roughness is the intrinsic roughness created by the PVST process itself. However, compared to the original surface roughness Sa = 48.6 μm, the surface finish has been significantly improved by PVST, and the optimal improvement ratio can reach 89.1%.

Figure 6.19 summarizes the roughness parameters under the conditions of f = 100 Hz, v_s = 1000 mm/min, and V_{pp} = 150 V at different tool diameters and engagement distances. In general, the roughness parameters become smaller with the increase of the engagement distance, which is consistent with the surface textures above. The Ra and Sa at d = 1, 2, 3 mm cannot be decreased below 10 μm even if Z is reduced to -200 μm. However, the Ra and Sa values are below 10 μm when d = 0.5 mm at a relatively lower Z value (-150 μm). In addition, there are some outliers

(a) *d* = 0.5mm

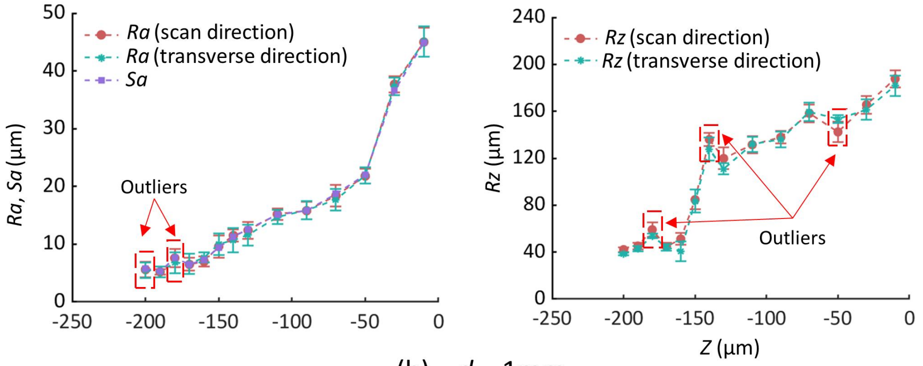

(b) *d* = 1mm

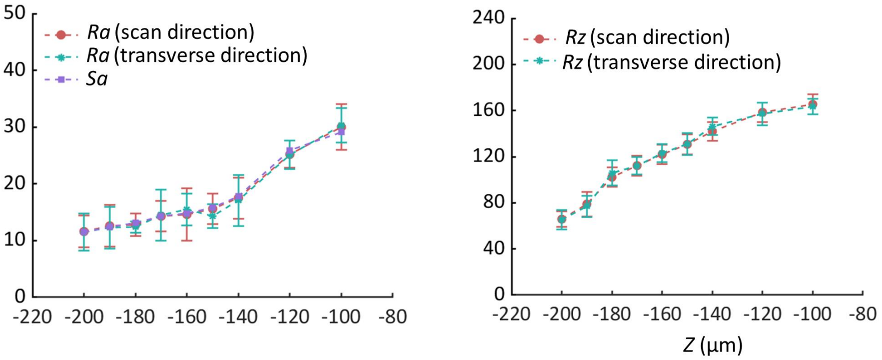

(c) *d* = 2mm

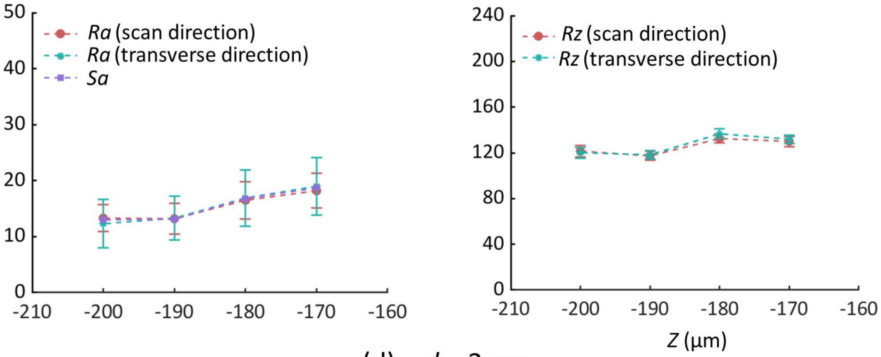

(d) *d* = 3mm

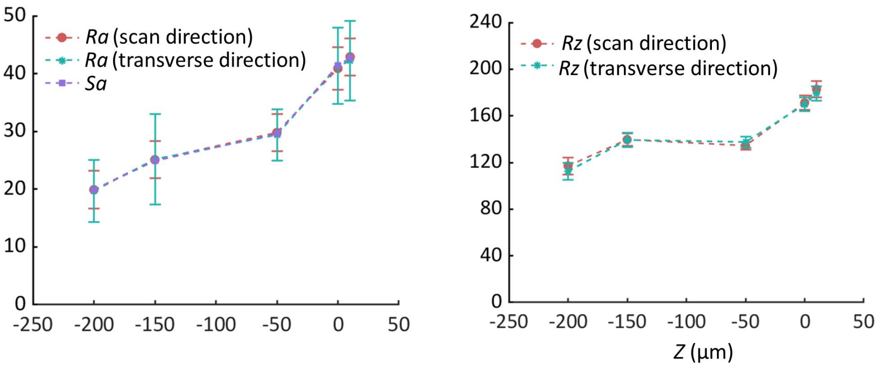

Figure 6.19 Roughness parameters (Sa, Ra, Rz) after PVST under different engagement distances and tool diameters at f = 100 Hz, v_s = 1000 mm/min, and V_{pp} = 150 V: (a) d = 0.5 mm; (b) d = 1 mm; (c) d = 2 mm; (d) d = 3 mm.

of the roughness parameters at d = 0.5 mm despite the general increasing trend. These outliers deserve attention since they reflect the nonuniformity of the rough surface. For the AM parts with high roughness, it is difficult to maintain a constant vibration amplitude during the treatment, so the selection of the Z value should be able to tackle the varied vibration amplitude and get a smooth surface. The above results show that it is a good practice to use -Rz as the starting Z value to determine the engagement distance between the striking tool and the workpiece surface. If the preload at Z = -Rz is high, then a reduced Z should be considered to prevent the pizeo stack from damage.

Nevertheless, only considering the Z value is not sufficient to guarantee an efficient and safe PVST process. Including the preload applied on the spot when setting the engagement distance can avoid inducing overlarge striking force to damage the actuation devices. The above engagement distance variation trend can only be a general guide for selecting an engagement distance. In some cases, it may be possible to use a smaller Z than -Rz to realize the flattening-sliding effect more thoroughly since Rz is a one-dimensional approximation of the peak-to-valley roughness throughout the target area and might not perfectly represent those surfaces with high roughness features.

6.6 Relationship between striking force and surface roughness

The above results show that striking force is closely related to surface roughness. A more significant striking force means more striking depth for samples with rough surfaces, which can remove more rough features and reduce surface roughness. Fig. 6.20 shows the historical distribution of the striking force throughout the PVST process based on the condition of f = 100 Hz, V_{pp} = 150 V, Z = -150 μm, d = 2 mm, and v_s = 1000 mm/min. The uneven distribution of the entire striking force history shows the nonuniform and rough characteristics of the treated surface. As seen from the enlarged view, the maximum force in each strike cycle represents the striking force that the striking tool strikes the farthest position it can reach, and it also represents the roughness at this position. The rougher the spot, the greater the striking force. The position at $F_z \approx 0$ in each cycle indicates the disengagement between the tool and the workpiece. At the moment, the tool is returning to the oscillating center after one strike. Since the rough features have been removed or flattened during the strike, there is no contact at the moment, and the force is zero.

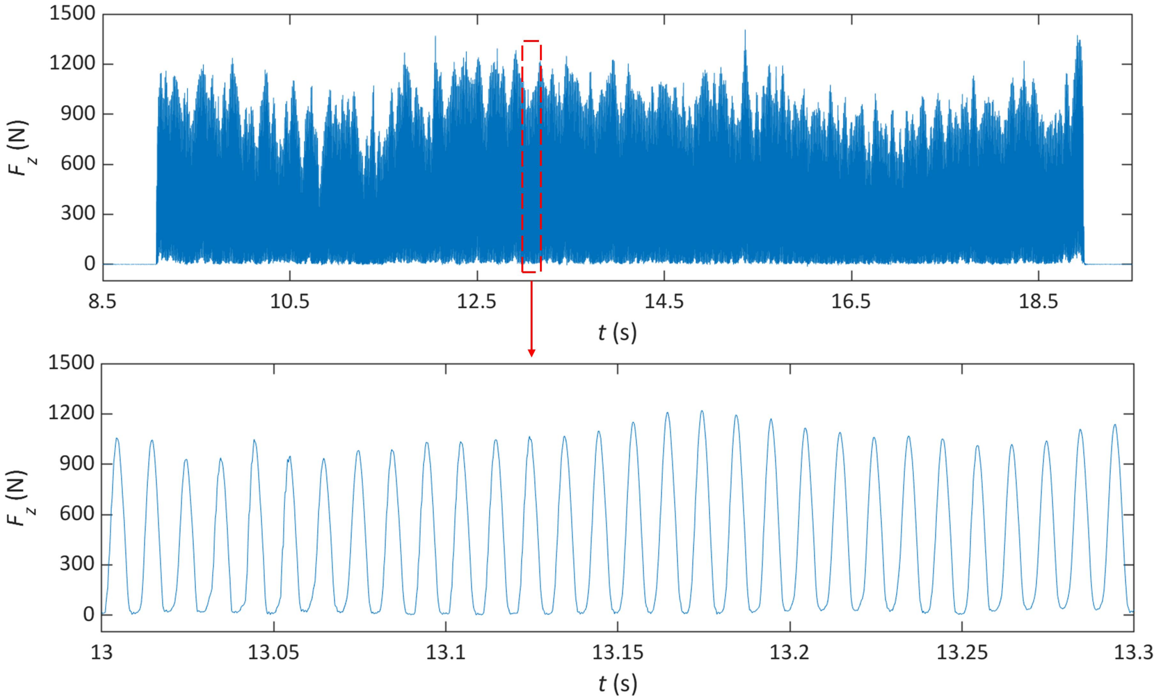

Figure 6.20 Striking force history throughout the PVST process at f = 100 Hz, V_{pp} = 150 V, Z = -150 μm, and v_s = 1000 mm/min, d = 2 mm. Upper: entire striking force history; Lower: part of striking force history.

As discussed in the results achieved from the samples with the initially smooth surface, the force–indentation size relationship can be well approximated as being linear (see Fig. 4.14, Fig. 4.21, Fig. 4.29, and Fig. 4.36). Theoretically, this relationship is nonlinear for a spherical-shaped indenter [114]. However, the indentation depth range of PVST on the smooth surface is usually minimal compared to the striking tool tip diameter, which enables a good approximation of the linear relationship between the striking force and indentation size. Moreover, the ratio of the indentation depth range to the diameter of the striking tool tip (h/d) is a good indicator to consider the quality of the linear approximation, which is negatively correlated to the quality of the linear relationship. Since the ratio is influenced by the workpiece material and tool geometry, these linear relationships might not hold on rough surfaces. In PVST experiments on samples with a rough surface, it is difficult to quantify the width and depth of each strike. A more straightforward performance of the results brought by these strikes is the surface roughness of the treated area.

Because the surface roughness after PVST is essentially determined by the width and depth of each indentation, the relationship between force and surface roughness should be equivalent to the relationship between force and indentation size.

In order to study the relationship between force and surface roughness, all the above experimental conditions are summarized. The maximum force obtained by each condition during PVST is extracted and denoted by F_z^{max}. This maximum force is significant because it can be used to determine whether the striking force exceeds the maximum force range of the piezo stack. During the entire PVST process, as long as the maximum force of one strike exceeds the maximum force range of the piezo stack, the piezo stack will be damaged, no matter how small the other forces are. In addition, the maximum force at each strike cycle during the PVST process is extracted since it characterizes the roughness of the treated location. Then the statistical analysis of the maximum force of all cycles is performed to obtain the corresponding average value and standard deviation. Each condition corresponds to a final surface roughness value Sa, as shown in Fig. 6.21. As mentioned above, the ratio h/d is a vital indicator to characterize the quality of the linear relationship, so the relationships between force and surface roughness in Fig. 6.21 are classified based on the tool diameter to represent distinct h/d scenarios despite the unknown h. Based on the results in samples with the initially smooth/rough surface, a high h is expected when d decreases; hence, a larger ratio h/d is achieved.

Similar to the linear relationships obtained in the initially smooth surface conditions, it is found that the surface roughness is linearly dependent on the striking force at large tool diameter conditions (d = 2, 3 mm). However, the relationships between the striking force and surface roughness become nonlinear at small diameter conditions (d = 0.5, 1 mm). It has been revealed in Fig. 5.19 that the striking depth increases as the tool diameter decreases and hence the surface roughness decreases. The nonlinear relationships are expected because of larger h and smaller d at the small tool diameter scenarios, thereby a larger h/d ratio is achieved. In addition, the use of negative engagement distance also increases the h values.

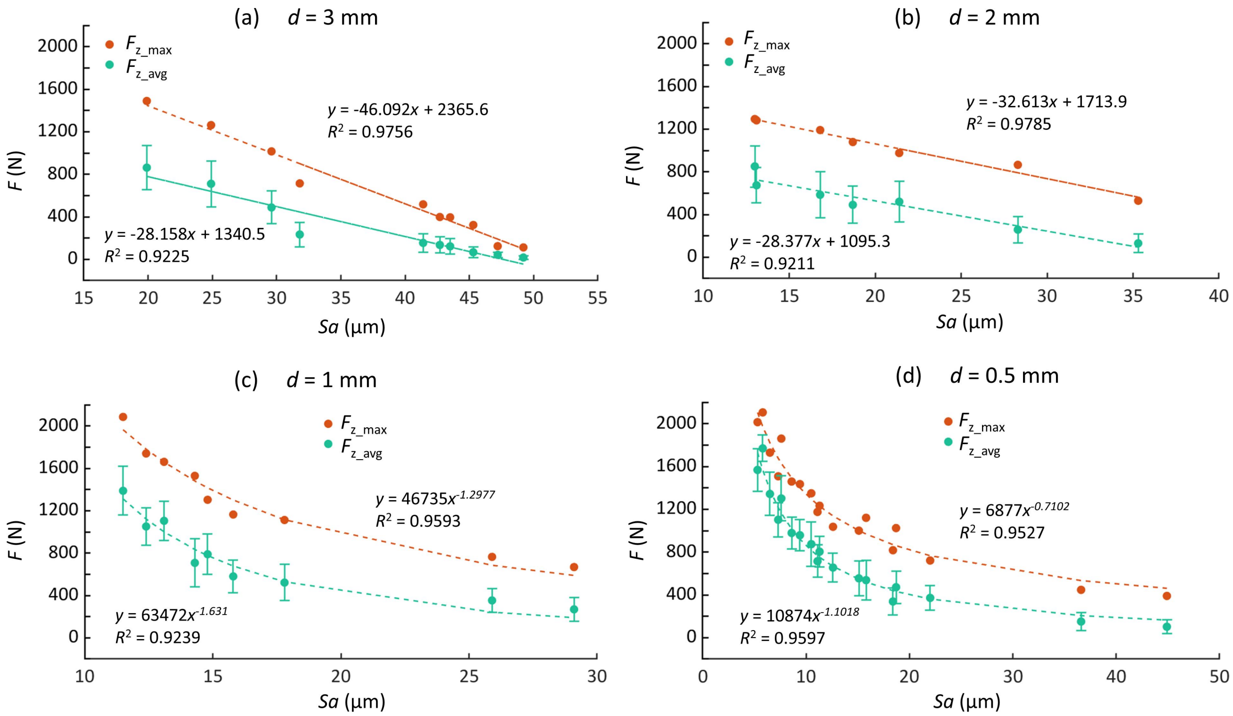

Figure 6.21 The relationships between maximum and average striking forces and surface roughness: (a) d = 3 mm; (b) d = 2 mm; (c) d = 1 mm; (d) d = 0.5 mm.

6.7 Effect of multiple passes on surface deformation

The above experiments under single pass show that scan speed, vibration frequency, and tool diameter are proportional to the surface roughness, while driving voltage and engagement distance or preload are inversely proportional to the surface roughness. The comprehensive manifestation of these parameters is to obtain a large striking force and a denser distribution of successive indentations in the PVST process, thereby obtaining a slight surface roughness. Theoretically, the greater the striking force, the better the surface roughness. However, this puts a higher requirement on the actuation device for a more extensive maximum force range. The higher striking force can increase the risk of damage to the device, which limits the application of the single pass to achieve a target surface quality.

Even if the striking force is sufficient to generate a nearly desirable surface quality, the intrinsic roughness created by PVST may, in turn, degrade the surface improvement. Balancing these issues is essential in getting a final desirable surface quality. A feasible method is to use multiple passes in PVST. The initial passes in the multiple passes process can reduce the original surface roughness to a specific level. The subsequent passes will further process the surface to reach the target surface roughness. In this regard, the striking force applied at each pass can be reduced, and the surface finish improvement can be accumulated through multiple-pass treatment. This method can not only avoid applying a considerable striking force during each strike but also reduces the dependence on the actuation equipment's ability. Also, it allows readjusting the experimental settings to improve the surface quality based on the intrinsic roughness generated by PVST (if it exists), providing more feasibility and flexibility. The design of these PVST passes will be based on considering two possible treatment phases.

Phase I (compression-sliding). Starting at a high roughness, the PVST pass will induce more compression-sliding type deformation (large engagement distance or preload, large u_{pp} or V_{pp}). It will likely densify the roughness layer more effectively by displacing the material from the hills to the valleys in the roughness layer. In this phase, the sliding effect may lead to the layer containing many surface folds (self-contacts of the original roughness surface) or pores in the layer. The mixed compression and sliding type deformation can generate an adequately combined compressive and shear stress state, leading to cold welding of the internal interfaces of these surface folds or pores. It is ideal for implementing this phase in a single pass. However, it is limited by the actuation device, as discussed earlier, because of the large striking force under the condition of large engagement distance and large driving voltage. An alternative is to divide this phase into two stages. **Stage I** mainly focuses on removing most rough features and reducing the high roughness to moderate roughness. Large driving voltage and medium engagement distance are utilized to avoid generating an overlarge striking force and achieve sufficient striking depth. Because positive engagement distance or relatively small negative engagement distance (small $|Z|$) do not significantly improve surface quality (see Fig. 6.14, Fig. 6.15, and Fig. 6.18). **Stage II** is to further process the treated area from Stage I to reach a state where PVST has created intrinsic roughness. The sliding-type deformation will dominate this stage, implying a large preload will be employed. The reason for using the preload instead of the engagement distance to present the engagement state in this stage is because the straining hardening effect caused in Stage I makes the engagement distance in Stage

II much smaller than that in Stage I to reach an equivalent preload level. It is difficult to quantify and compare the engagement distance to determine the engagement state in two different stages. Thus, preload is more straightforward than the engagement distance in this stage. A small/medium driving voltage should be used to avoid overlarge striking force. Under the combined effect of large preload and small/medium driving voltage, more unaffected rough features from Stage I will be approached, and a more uniform surface can be achieved in this stage. It is a trade-off problem for getting what kind of surface texture pattern is in the first stage and what level of sliding-type deformation is in the second stage. Suppose the scattered pattern is formed in the first stage. In that case, a more significant preload is necessary for the second stage to eliminate more rough features, which likely causes the deflection of the striking tool during the process. Conversely, if the uniform pattern is created in the first stage, a smaller preload should be sufficient in the second stage. However, a more significant striking force is necessary for the first stage, which can increase the risk of damage to the piezo stack. Balancing this problem depends on the target surface quality of the sample.

Phase II (smoothing). After the first phase, the surface roughness should be reduced significantly from the initial high value but still higher than the desired value. The PVST pass in this phase will concentrate on reducing the roughness to the final desired level ($\sim 1\ \mu$m). The consideration here is the intrinsic roughness and surface texture generated by the PVST pass (see Fig. 5.3 - Fig. 5.15 for examples). The intrinsic roughness created by the applied PVST pass needs to be smaller than the roughness of the surface to be treated. Only in this way can the roughness be further reduced after each pass of PVST. As the roughness becomes smaller, it is more suitable to induce compression-type deformation ($Z \geq 0$) to smooth the surface. Compared to sliding type deformation, the compression type deformation will create lower intrinsic roughness due to less material pileup at the two sides of the scan path. It has been demonstrated in Fig. 5.3 - Fig. 5.15 by increasing r_o and decreasing u_{pp} (V_{pp}), the intrinsic roughness due to PVST that induces primarily compression-type deformation can be reduced to below 1 μm level.

To maximize the effectiveness of roughness reduction on each pass, the characteristics of the intrinsic texture created by PVST should be considered. The created texture is mainly dependent on the tool scan path. For example, the parallel line scan path will displace the material mainly to the two sides of the scan line, forming line ridges between the scan lines (see Fig. 5.3 - Fig. 5.15). Fig. 6.22 shows two possible strategies for smoothing these line ridges more effectively on the surface. One strategy is to rotate the scan line direction by 90° from pass to pass (Fig. 6.22a). It will ensure that the scan lines in the current pass cross the line ridges formed in the previous pass. Another strategy is to keep the scan lines in the same direction but shift them laterally by half line spacing ($d_p/2$) from pass to pass (Fig. 6.22b). It will ensure that the scan lines in the current pass align with the line ridges formed in the previous pass. In this dissertation, the two strategies are represented as the interweaving scan strategy and parallel scan strategy, respectively.

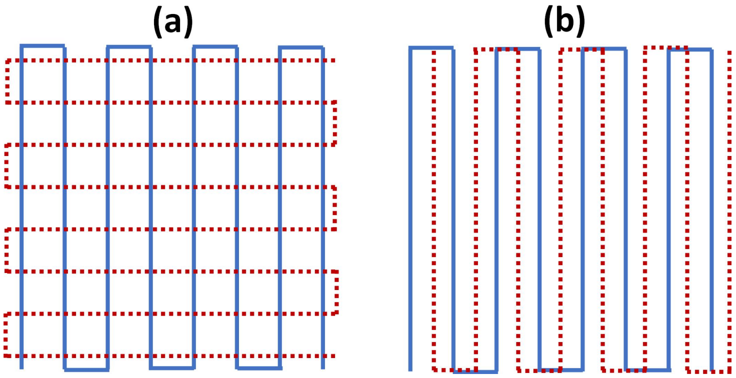

Figure 6.22 Two possible scan path designs: (a) interweaving scan; (b) parallel scan. Red dashed line is the scan path in previous pass. Solid blue line is the scan path in current pass.

The surface roughness of the areas to be treated varies at different locations of the workpiece surface due to the initial high roughness. Experimental results may be inconsistent if the PVST experiments are conducted at different spots with large starting roughness differences. Corresponding to Stage I in Phase I, the first pass covering an area of 21 mm × 21 mm is performed to ensure the treated surface for subsequent passes is flat and has statistically uniform roughness across the surface area. The preprocessing at three different levels for the first stage of Phase I is performed to get the treated areas with different starting roughness values. The three conditions are defined as f = 100 Hz, V_{pp} = 150 V, v_s = 1000 mm/min, Z = -110, -150, -190 μm (corresponding to preload F_p = 200, 300, 400 N), and d = 0.5 mm. The measurement of the surface roughness for the big square is divided into nine separate sub-square areas with a size of 5 mm × 5 mm, as shown in Fig. 6.23 at the condition of Z = -110 μm. These nine sub-square areas' average Sa value will be used as the starting roughness representing this big square. The measurements of Sa for each sub-square area can be found in Table 3. The results show that the Sa values in the same preprocessed area are similar, and the surface has statistically uniform roughness across the surface area. The average Sa values for the three big squares are 15.6 ± 1.0 μm, 10.5 ± 1.0 μm, and 8.1 ± 0.8 μm, respectively.

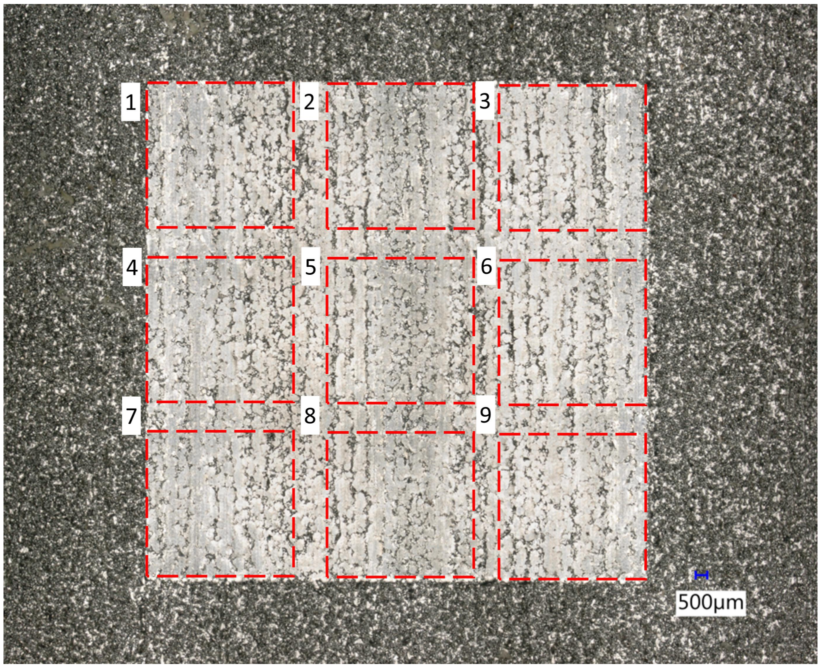

Figure 6.23 Surface texture after preprocessing with a size of 21 mm × 21 mm at Z = -110 μm, F_p = 200 N, f = 100 Hz, V_{pp} = 150 V, v_s = 1000 mm/min, and d = 0.5 mm.

Table 6.3 Surface roughness after first pass treatment at different PVST levels.

Area No.	Sa_1 (μm)	Sa_2 (μm)	Sa_3 (μm)
1	15.1	10.4	7.8
2	17.7	11.5	8.2
3	16.7	10.4	8.1
4	14.7	8.8	8.0
5	15.6	11.2	8.8
6	14.8	11.4	9.3
7	14.5	9.0	8.4
8	16	11.0	7.3
9	15.4	10.9	6.5

6.7.1 Effect of driving voltage on surface deformation in multiple passes

The surface treatment of the above three big squares adopts the vibration strategy mentioned in Stage I of Phase I where a large driving voltage and engagement distance are leveraged. The obtained Sa values are highly reduced compared to the original Sa (= 48.6 μm), and the optimization ratio can reach 67.9%, 78.4%, and 83.3%, which verifies the correctness of the strategy in Stage I of Phase I. To validate the strategy proposed in Stage II of Phase I in which a combination of small/medium driving voltage and large preload is utilized, the experiments under different driving voltage conditions are performed (f = 100 Hz, v_s = 1000 mm/min, F_p = 100 N, d = 0.5 mm, V_{pp} = 60 - 150 V). Note that Z = -30 μm corresponding to F_p = 100 N is much smaller than that in the first stage due to the strain hardening effect. A small preload used here is to avoid overlarge striking force occurring at large driving voltage conditions. A parallel scan strategy is also used, but no strict distance offset is considered.

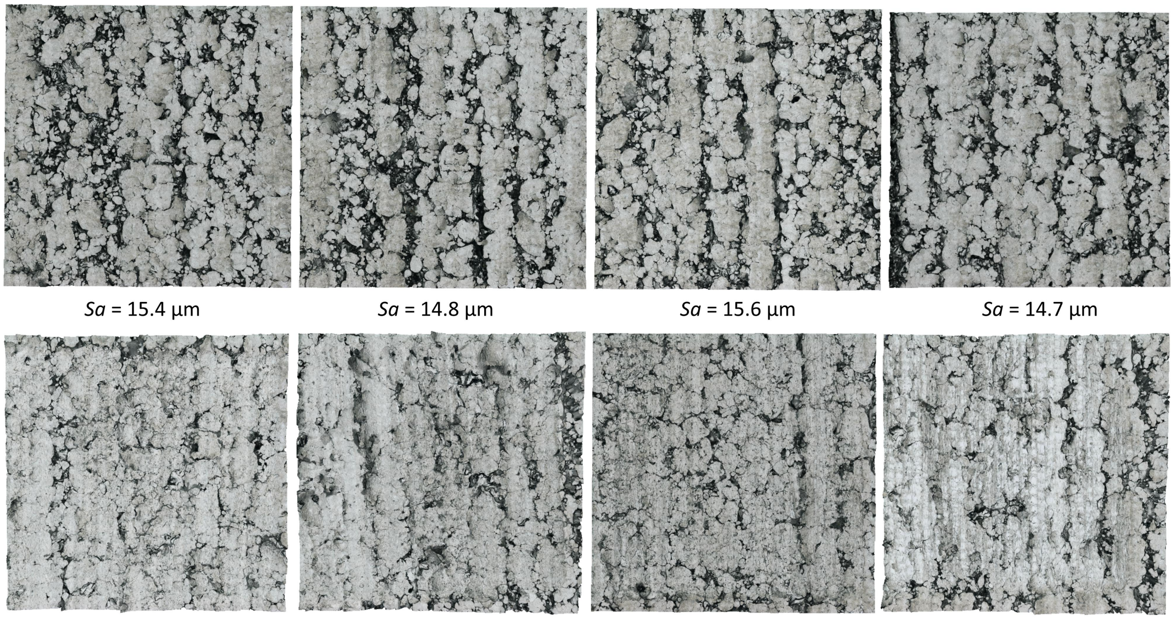

Sa = 15.4 µm
Sa = 14.8 µm
Sa = 15.6 µm
Sa = 14.7 µm

V_{pp} = 150 V, Sa = 14.1 µm
V_{pp} = 120 V, Sa = 14 µm
V_{pp} = 90 V, Sa = 12.9 µm
V_{pp} = 60 V, Sa = 12.9 µm

Figure 6.24 Surface textures in Phase I of multiple passes. Upper: Stage I; Lower: Stage II at f = 100 Hz, v_s = 1000 mm/min, F_p = 100 N, d = 0.5 mm, and V_{pp} = 60 - 150 V.

The results in Fig. 6.24 show that in the second stage of Phase I, a large V_{pp} has less improvement on the surface roughness than a small V_{pp} does. Using V_{pp} = 60 V can be a more economical and efficient consideration. Also, the improvement on the surface roughness is not significant for all the driving voltage conditions, although they do reduce the Sa values sightly. It might be caused by the insufficient preload used for the current conditions.

6.7.2 Effect of scan strategy on surface deformation in multiple passes

Before exploring the effect of preload on surface deformation, the effect of scan strategy on surface deformation is investigated. As mentioned earlier, Phase II mainly concentrates on smoothing the surface to reach the final surface finish level. Interweaving scan and parallel scan strategies can be used to further improve the surface roughness in this phase. Although the intrinsic roughness produced in the first stage of Phase I is likely to be less pronounced than that produced in the second stage, it is still worth exploring the impact of the two strategies in this phase. Since the ridges generated in the first stage are not prominent, the striking positions in the second stage are slightly offset when the parallel scan strategy is used. However, the offset is not strictly defined as the distance of $d_p/2$. Six different conditions at f = 100 Hz and v_s = 1000 mm/min represent various scenarios using the two strategies. The experimental parameters are shown in Table 6.4.

Table 6.4 Experimental parameters for two scan strategies.

No.	F_p (N)	d (mm)	V_{pp} (V)	Strategy
1	200	0.5	150	Parallel
2	200	0.5	150	Interweaving
3	400	0.5	60	Parallel
4	400	0.5	60	Interweaving
5	400	2	60	Parallel
6	400	2	60	Interweaving

Figure 6.25 illustrates the surface textures and height contour maps from the experiments in Table 6.4. It is seen that the Sa values reduce for the three conditions after employing the interweaving scan strategy. The ridges (yellow features in height contour maps) are easier to be observed in the parallel scan conditions, especially in Fig. 6.25a. While in Fig. 6.25d, the path history is less apparent, and the rough features are randomly distributed on the surface. In Fig. 6.25e and Fig. 6.25f, the new path histories are generated in the vertical directions, but the ridges are not as pronounced as seen in the parallel scan strategy conditions. Based on the results, the interweaving scan strategy is more beneficial to smooth the high rough features generated in Stage I of Phase I

under relatively high preload conditions than the parallel scan strategy. Because in the parallel scan strategy, it is more likely that the current scan path overlaps with the previous scan path from Stage I, especially at the conditions without using a strict distance offset. In this case, it is possible to displace more material to the ridges and degrade the improvement effect on the surface roughness.

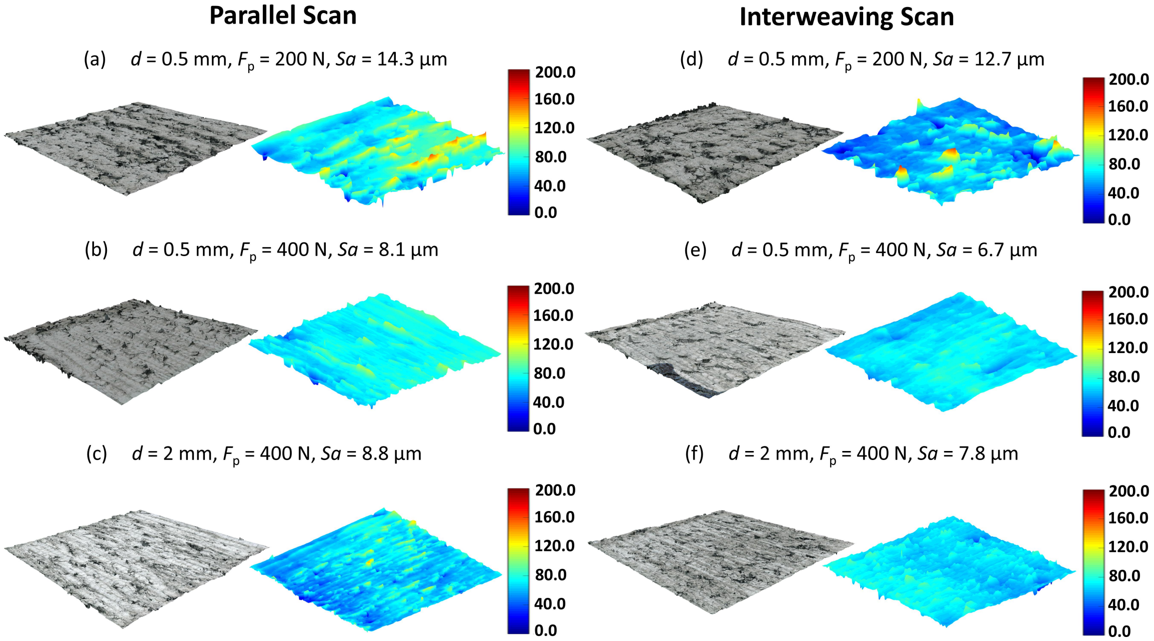
Parallel Scan

Interweaving Scan

(a) $d = 0.5$ mm, $F_p = 200$ N, $Sa = 14.3$ µm

(b) $d = 0.5$ mm, $F_p = 400$ N, $Sa = 8.1$ µm

(c) $d = 2$ mm, $F_p = 400$ N, $Sa = 8.8$ µm

(d) $d = 0.5$ mm, $F_p = 200$ N, $Sa = 12.7$ µm

(e) $d = 0.5$ mm, $F_p = 400$ N, $Sa = 6.7$ µm

(f) $d = 2$ mm, $F_p = 400$ N, $Sa = 7.8$ µm

Figure 6.25 Surface textures and height maps using different scan strategies in Table 6.4. (a) – (c): parallel scan strategy; (d) – (f): interweaving scan strategy.

6.7.3 Effect of preload on surface deformation in multiple passes

As mentioned above, combining a small driving voltage and a large preload improves the surface finish in Stage II of Phase I. To investigate how preload affects the surface roughness in this stage, the PVST experiments are conducted under the condition of f = 100 Hz, v_s = 1000 mm/min, d = 0.5 mm, V_{pp} = 60 V, F_p = 100, 400, 600 800, 1000 N, utilizing the interweaving scan strategy.

As demonstrated in Fig. 6.26a – Fig. 6.26e, the surface finish is vastly improved as the preload increases from 100 N to 1000 N. The smoothness and uniformity of the treated surface are observed in Fig. 6.26c – Fig. 6.26e, where the surface textures present a uniform pattern with pronounced indentation marks and the scan path history. The dark unaffected areas are barely seen in these treated surfaces, which showcases the significant positive effect of the large preload on the surface roughness in Stage II of Phase I. The surface texture in Fig. 6.26c – Fig. 6.26e is very similar to that generated in the initially smooth surface conditions, which is covered by the intrinsic rough features created by PVST. Surprisingly, $\Delta Sa\%$ in Fig. 6.26e is as high as 92.4%.

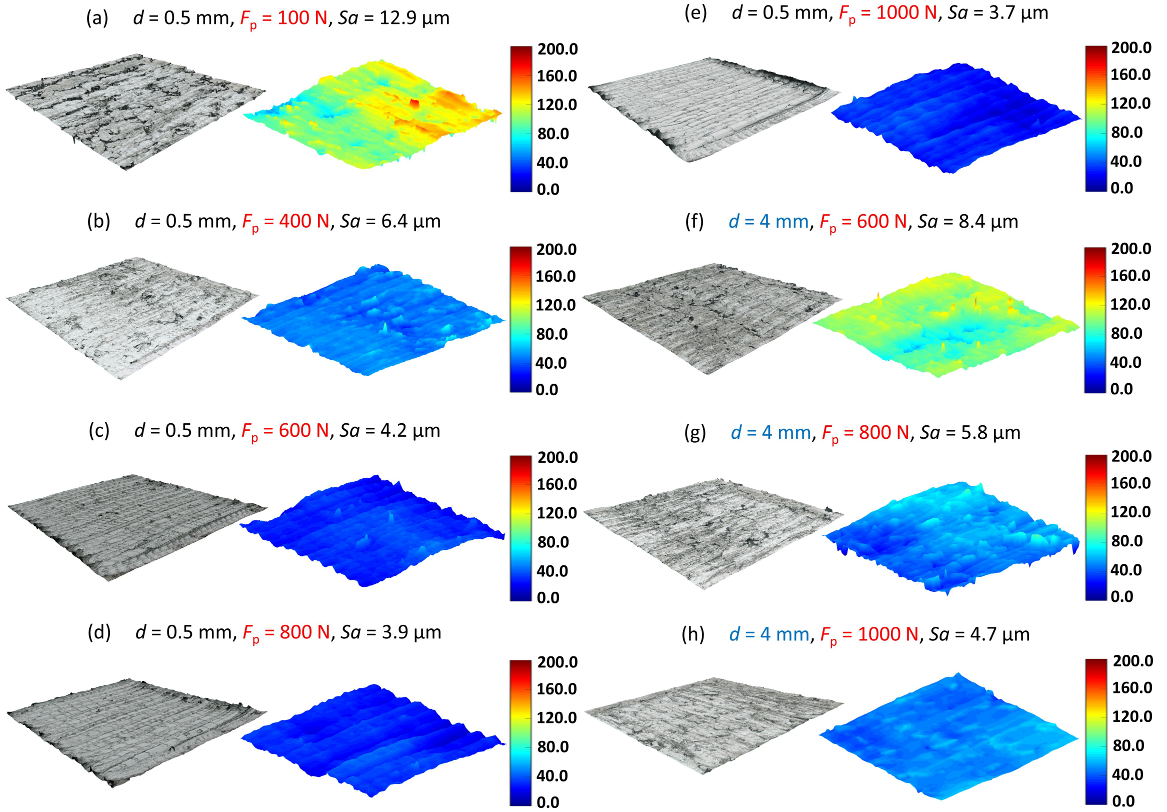

Figure 6.26 Second interweaving scan surface textures and height contour maps using different preloads at f = 100 Hz, v_s = 1000 mm/min, V_{pp} = 60 V, F_p = 100, 400, 600 800, 1000 N. (a) – (e) d = 0.5 mm; (f) – (h) d = 4 mm.

The results show that a large preload in PVST significantly improves the surface roughness at the small tool diameter conditions. However, it requires higher stiffness of the striking tool for higher preload conditions. Otherwise, it can cause deflection of the striking tool if the preload is too large. Increasing the tool diameter can increase the stiffness of the striking tool, but it also reduces the vibration amplitude for a given driving voltage, which requires a larger preload to compensate for the amplitude reduction. Theoretically, these two combinations (moderate preload + small tool diameter or large preload + large tool diameter) should achieve equivalent surface roughness improvement, given that they can create a similar striking depth to strike and smooth the surface at a specific setting.

The PVST experiments are conducted under f = 100 Hz, v_s = 1000 mm/min, d = 4 mm, V_{pp} =

60 V, F_p = 600, 800, 1000 N to validate the statement. Due to the use of large tool diameter, small preloads, i.e., F_p = 100 N and F_p = 400 N, are skipped, for they might not significantly improve surface roughness in this setting. Fig. 6.26f – Fig. 6.26h show the surface textures and height contour maps at F_p = 600 N, 800 N, and 1000 N, respectively. It is proved that using a large tool diameter combined with a large preload can achieve an equivalent surface roughness generated in a small tool diameter with moderate preload conditions. The uniformity of the treated surface and the Sa value in Fig. 6.26b (d = 0.5 mm, F_p = 400 N) are equivalent to that in Fig. 6.26g (d = 4 mm, F_p = 800 N), as well as the results in Fig. 6.26c (d = 0.5 mm, F_p = 600 N) and Fig. 6.26h (d = 4 mm, F_p = 1000 N).

In addition, the roughness parameters in Fig. 6.27 present a decreasing relationship between the preload and the surface roughness. Consistent with surface texture, all the roughness parameters (Ra, Sa, Rz) at the condition of d = 0.5 mm and F_p = 400 N are equivalent to the parameters at the condition of d = 4 mm and F_p = 800 N, as well as the roughness parameters at d = 0.5 mm and F_p = 600 N to those at d = 4 mm and F_p = 1000 N.

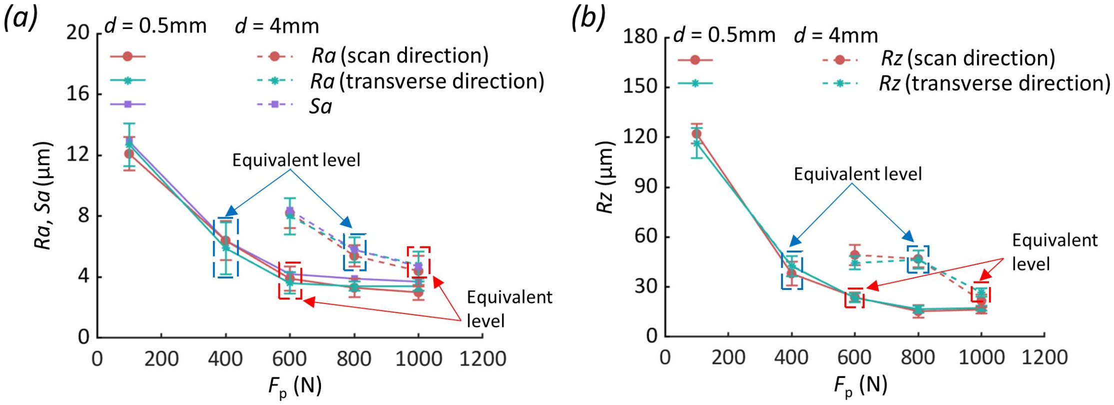

Figure 6.27 Roughness parameters (Sa, Ra, Rz) after PVST under different preloads at d = 0.5 mm and d = 4 mm in Fig. 6.26.

Although the equivalent surface roughness can be achieved through different combinations of the tool diameter and the preload, the surface textures are distinct for small and large tool diameter scenarios. In Fig. 6.26c (d = 0.5 mm, F_p = 600 N), the intrinsic rough features created by PVST are observed, and few dark regions are seen. While in Fig. 6.26h (d = 4 mm, F_p = 1000 N), the intrinsic rough features are barely seen, and there are still several dark areas on the surface. For large tool diameter conditions, a large preload (1000 N) is supposed to enable the tool to strike deeper positions and greatly remove the dark areas despite the amplitude reduction. Therefore, these dark areas may be caused by the newly generated defects by PVST or skipped by the striking tool due to the small overlap related to the scan speed instead of the reduced striking depth.

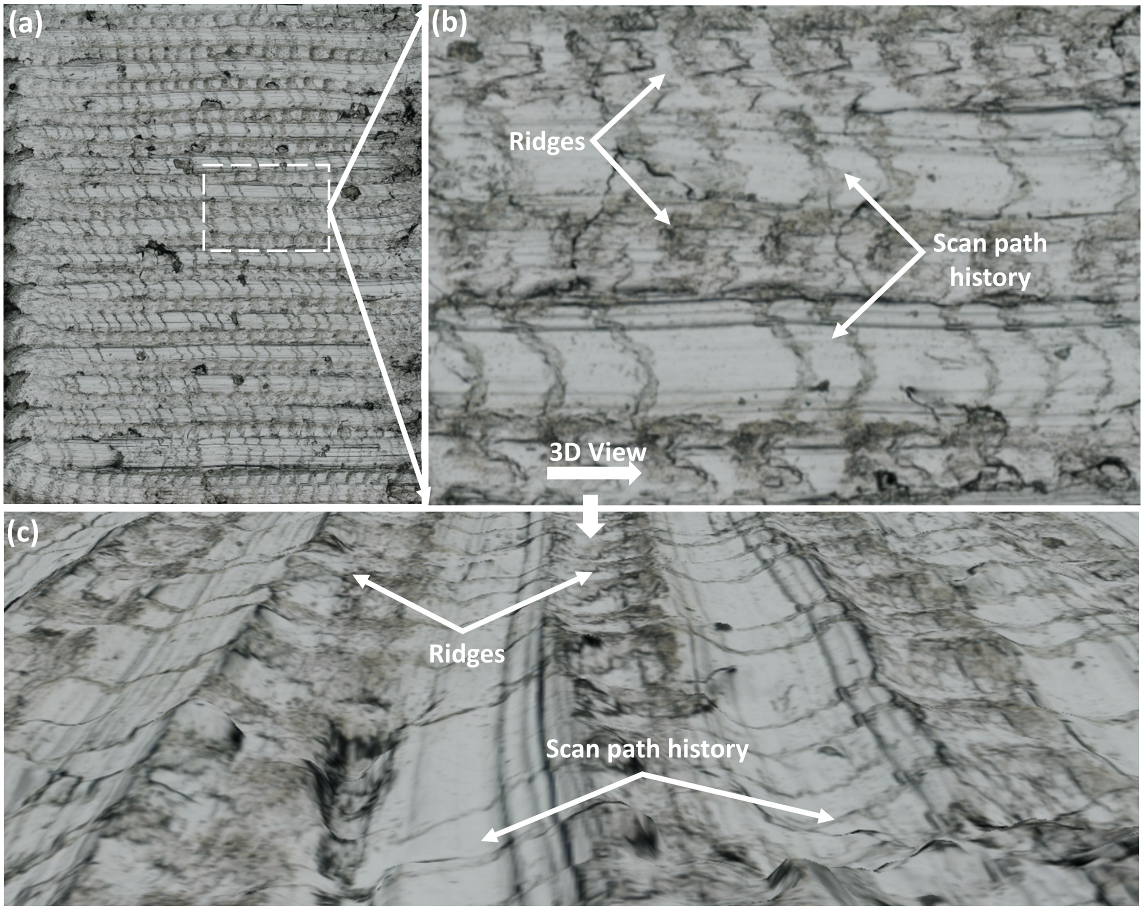

Figure 6.28 Surface texture after PVST at d = 0.5 mm and F_p = 600 N in Fig. 6.26: (a) top view; (b) magnified top view; (c) left side view in a 3D perspective (first scan parameters: d = 0.5 mm, F_p = 400 N, V_{pp} = 150 V).

To verify the cause of the dark areas in this stage, the surface textures in Fig. 6.26c and Fig. 6.26h are magnified to see the distribution of the features on the treated surface. Fig. 6.28 shows the surface texture from Fig. 6.26c at d = 0.5 mm and F_p = 600 N in three different perspectives. Fig. 6.28a illustrates the top view of the treated surface and part of which is magnified in Fig. 6.28b. Fig. 6.28c shows the side view of Fig. 6.28b in a 3D perspective to present height variation across the magnified field. The successive indentation marks are observed across the scan paths. The spacing between the marks is closely related to the scan speed. The uniform and white/bright regions indicate that the rough features have been flattened, and the gaps between the rough features are also closed. Most of the remaining dark areas or crack-like features are distributed around or on the ridges that are not approached by the striking tool. The width of the ridges is very close to that of the scan path, which means that the current scan speed is not sufficient to offer a properly dense overlap of the indentations. A lower scan speed would be better for further improving the surface roughness.

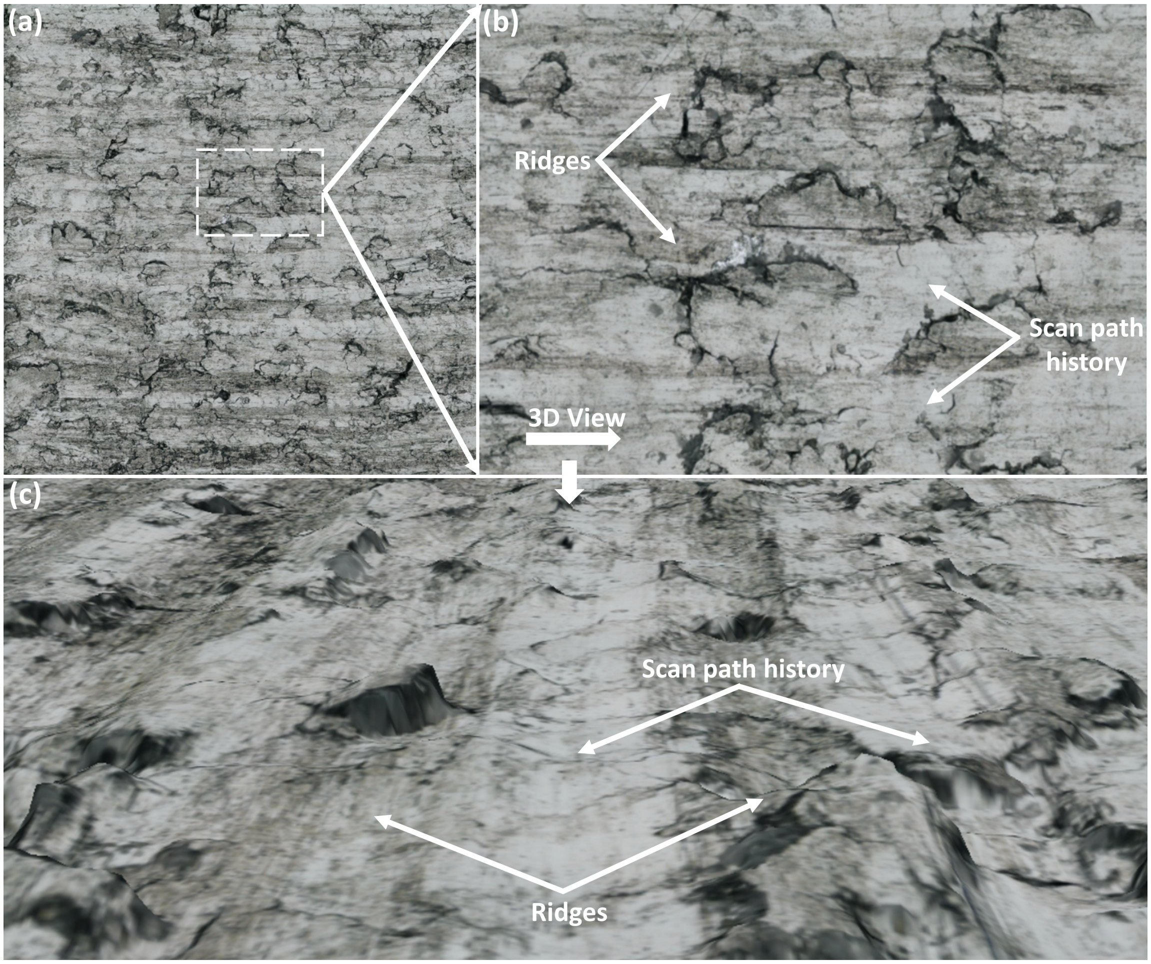

Figure 6.29 Surface texture after PVST at d = 4 mm and F_p = 1000 N in Fig. 6.26: (a) top view; (b) magnified top view; (c) left side view in a 3D perspective (first scan parameters: d = 0.5 mm, F_p = 200 N, V_{pp} = 150 V.)

Likewise, the surface texture from Fig. 6.26h at d = 4 mm and F_p = 1000 N is magnified and shown in Fig. 6.29. Although a larger preload is used, the surface texture in Fig. 6.29 differs from that in Fig. 6.28. The successive indentation marks are observed along the scan path. Many crack-like features are distributed across the surface. The scan path history can still be seen in Fig. 6.29b and Fig. 6.29c, but it is not as apparent as in Fig. 6.28b and Fig. 6.28c. Also, rough features exist on the scan path, which differs from the case in Fig. 6.28 that the rough features are removed along the scan direction. In Fig. 6.29c, the height of the ridges seems to be close to the height of the white areas, indicating a decreasing effect of the compression-sliding type deformation and less material displaced to the lateral sides. Most of the rough features are located at the ridges, which are those crack-like features seen from the top view in Fig. 6.29a. In light of the surface textures in Fig. 6.28 and Fig. 6.29, it can be known that the ridges mainly cause the surface roughness in Fig. 6.28 since the ridges are much higher than the flattened surface on the scan path. In contrast, the surface roughness in Fig. 6.29 can be mainly attributed to the remaining/unaffected features left from the first stage located at the ridges. Due to the decreasing compression-sliding type deformation, the effect of the ridges on the surface roughness in Fig. 6.29 is not as significant as in Fig. 6.28. Therefore, the mechanisms affecting the surface roughness under these combinations are distinct despite the fact that they can generate the equivalent level of surface roughness.

6.7.4 Effect of tool diameter on surface deformation in multiple passes

In the previous section, the effects of tool diameter at d = 0.5 mm and d = 4 mm on surface deformation in multiple passes have been compared. In this section, the effect of tool diameter on surface deformation is further studied. The bar chart in Fig. 6.30 shows the surface roughness results at different preloads and tool diameters. Consistent with the above results, Sa increases with tool diameter for a given preload and decreases with the increase of preload and for a given tool diameter.

Figure 6.31 shows the surface textures under the condition of f = 100 Hz, v_s = 1000 mm/min, V_{pp} = 60 V, F_p = 600 N, and d = 0.5, 2, 3, 4 mm. The upper row is the surface results processed in Stage I of Phase I, and the lower row is the results achieved in Stage II of Phase I. The two stages' scan directions are different, so the second stage adopts the interweaving scan strategy. It can be seen that the direction of the upper scan paths is displayed as vertical, and the direction of the lower scan paths is displayed as horizontal. Consistent with the results of Sa in Fig. 6.30, the surface texture becomes more uniform as the tool diameter decreases. The intrinsic rough features become

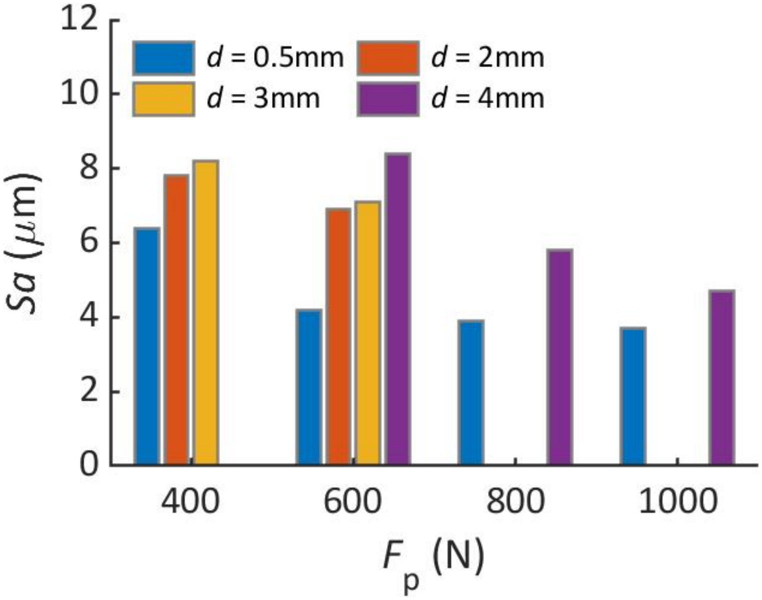

Figure 6.30 The relationship of surface roughness with tool diameter and preload in Stage II of Phase I.

more pronounced with decreasing tool diameter as well.

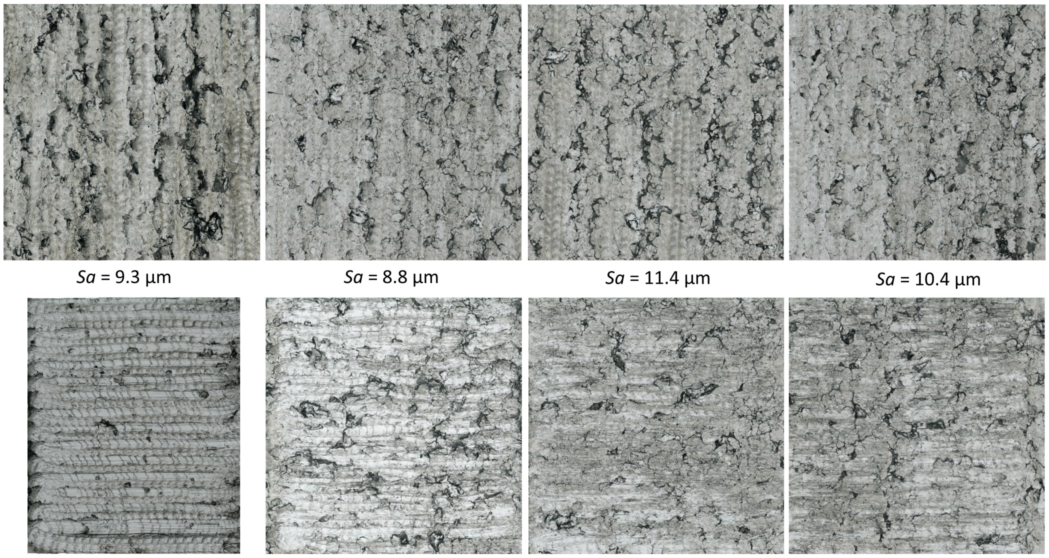

Sa = 9.3 µm *Sa* = 8.8 µm *Sa* = 11.4 µm *Sa* = 10.4 µm

d = 0.5 mm, *Sa* = 3.9 µm *d* = 2 mm, *Sa* = 6.9 µm *d* = 3 mm, *Sa* = 7.1 µm *d* = 4 mm, *Sa* = 8.4 µm

Figure 6.31 Surface textures under different tool diameters. Upper: surface texture from Stage I; Lower: surface texture from Stage II at f = 100 Hz, v_s = 1000 mm/min, V_{pp} = 60 V, F_p = 600 N, and d = 0.5, 2, 3, 4 mm (first scan parameters: d = 0.5 mm, F_p = 200, 400 N, V_{pp} = 150 V)

In the above results, in addition to the reasonable relationships between Sa and F_p, d, an abnormal phenomenon is found in Fig. 6.31 in the case of d = 0.5 mm where the treated area is a rectangular shape instead of a preset square shape (5 mm × 5 mm). Furthermore, the shortening direction corresponds to the scan direction. It is the first case since all PVST conditions have been performed so far (whether on a smooth surface or other cases on a rough surface). It is speculated that this phenomenon may be caused by the deflection of the striking tool when using a small tool diameter with a large preload. When the CNC spindle reaches the target position, the striking tool is unable to follow its motion due to a large sliding resistance; thereby the tool is bent or deflected. To verify this speculation, all the experiments in Stage II of Phase I are put together in Fig. 6.32 for a better comparison. The detailed experimental parameters and results corresponding to each treated area at f = 100 Hz and v_s = 1000 mm/min in Fig. 6.32 can be found in Table 6.5.

Based on Table 6.5, the deflection occurs in the conditions of No. 19 – No. 26, all of which are the treated areas in Square-3 in Fig. 6.32. By comparing the final size of the treated areas, it is found that when the striking tool with a small diameter (0.5 mm) is used, the deflection occurs when $F_p \geq 600$ N. For PVST with a moderate (d = 2 mm) or large diameter (d = 3, 4 mm), the deflection does not occur in all the conditions, i.e., for F_p = 600 N at d = 2, 3, 4 mm, and even for F_p = 800, 1000 N at d = 4 mm. These results demonstrate that the increased stiffness of the striking tool with a larger diameter keeps the tool from deflection at large preload conditions. When the tool diameter is reduced to a certain extent, however, the decreasing stiffness of the striking tool makes the PVST process more prone to deflect the striking tool at large preload scenarios.

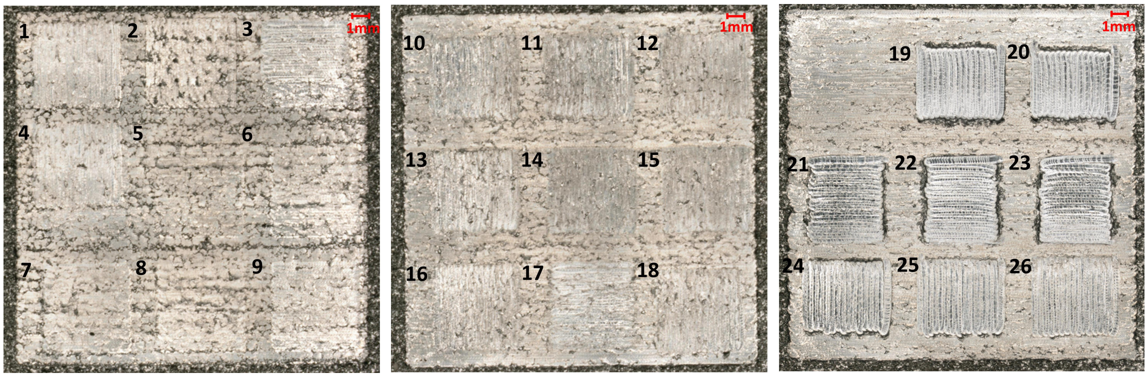

Figure 6.32 Overview of surface textures after Stage II of Phase I at different preprocessed squares from Stage I of Phase I. (a) Square-1: $Sa_1 = 15.6 \pm 1.0$ μm ;(2) Square-2: $Sa_2 = 10.5 \pm 1.0$ μm; (3) Square-3: $Sa_3 = 8.1 \pm 0.8$ μm.

It is observed that the deflection mainly occurs in the scan direction, which should be closely related to the sliding force during the PVST process. To further explore the relationship between the deflection and the sliding force, the sliding forces obtained during the PVST process are selected

Table 6.5 Experimental parameters and results corresponding to each treated area in Fig. 6.32.

No.	d (mm)	F_p (N)	V_{pp} (V)	Sa (μm)	Size (mm)
1	0.5	400	60	6.7	5 × 5
2	0.5	200	150	12.7	5 × 5
3	0.5	400	60	11.4	5 × 5
4	0.5	100	120	14	5 × 5
5	0.5	100	90	12.9	5 × 5
6	0.5	100	60	12.9	5 × 5
7	0.5	400	60	11.3	5 × 5
8	0.5	200	60	14.3	5 × 5
9	0.5	100	150	14.1	5 × 5
10	4	1000	60	4.7	5 × 5
11	4	800	60	5.8	5 × 5
12	4	600	60	8.4	5 × 5
13	2	600	60	6.9	5 × 5
14	3	400	60	8.2	5 × 5
15	3	600	60	7.1	5 × 5
16	2	400	60	7.8	5 × 5
17	2	400	60	8.8	5 × 5
18	0.5	400	60	6.4	5 × 5
19	0.5	1000	60	4.2	5 × 4.1
20	0.5	1000	60	4	5 × 4.1
21	0.5	1000	60	4.6	5 × 4.3
22	0.5	1000	60	4.7	5 × 4.1
23	0.5	1000	60	4.1	5 × 4.1
24	0.5	1000	60	3.7	5 × 4.2
25	0.5	800	60	3.9	5 × 4.5
26	0.5	600	60	4.2	5 × 4.6

Note: No. 3, No. 7, No. 19, No. 20, No. 22, No. 23 are under three passes conditions. No. 4 is covered by a failed case after the area is measured.

from No. 10 (d = 4 mm, F_p = 1000 N), No. 11 (d = 4 mm, F_p = 800 N), No. 13 (d = 2 mm, F_p = 600 N), No. 15 (d = 3 mm, F_p = 600 N), No. 18 and No. 24 – 26 (d = 0.5 mm, F_p = 400, 600, 800, 1000 N).

Figure 6.33 illustrates the sliding forces F_y under the above conditions. In Fig. 6.33a, F_y is around 50 N at F_p = 400 N and d = 0.5 mm. When F_p increases to 600 N, 800 N, and 1000 N in Fig. 6.33b – 6.33d, F_y increases to about 150 N, 170N, and 200 N, which are much larger than that in Fig. 6.33a. Also, when the tool diameter increases to 2 and 3 mm, the values of F_y are only 75 N and 55 N at F_p = 600 N. When the preload is further increased to 800 N and 1000 N in Fig. 6.33g and Fig. 6.33h, the sliding forces are about 100 N and 150 N, respectively. It is expected that the sliding forces in Fig. 6.33a and Fig. 6.33e – Fig. 6.33g will not cause the deflection of the striking tool since the forces are relatively small. Despite the sliding force in Fig. 6.33h being equivalent to that in Fig. 6.33b, the tool diameter in Fig. 6.33h is much larger than (8 times) that in Fig. 6.33b. This increases the deflection resistance of the striking tool, and hence the deflection does not occur at d = 4 mm despite using a large preload (1000 N).

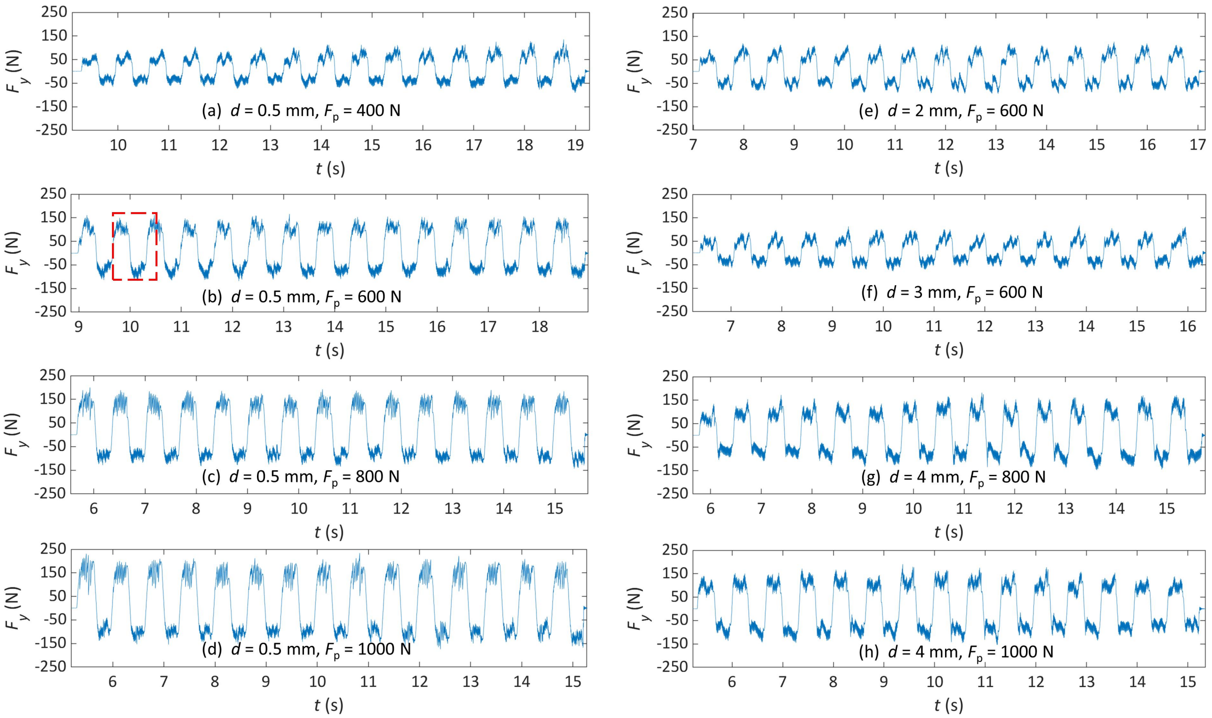

Figure 6.33 Sliding forces under different tool diameters and preloads. (a) – (d): d = 0.5 mm, F_p = 400 – 1000 N; (e) d = 2 mm, F_p = 600 N; (f) d = 3 mm, F_p = 600 N; (g) – (h) d = 4 mm, F_p = 800, 1000 N.

To better understand the behavior of the sliding forces in multiple passes, part of the scan history (red rectangular period) in Fig. 6.33b is selected, as shown in Fig. 6.34. It is seen that there are two types of sliding force. The striking tool generates a positive sliding force along the positive Y-axis. After reaching the target boundary, the tool moves along the X-axis for a step and then continues to move along the negative Y-axis to start another scan path, which creates the negative sliding force. Each path's small, jagged forces are the sliding force variation corresponding to each striking cycle.

Consequently, in Stage II of Phase I, the tool diameter and preload selection is crucial. Improper selection will increase the risk of deflection during the PVST process, thereby damaging the piezo

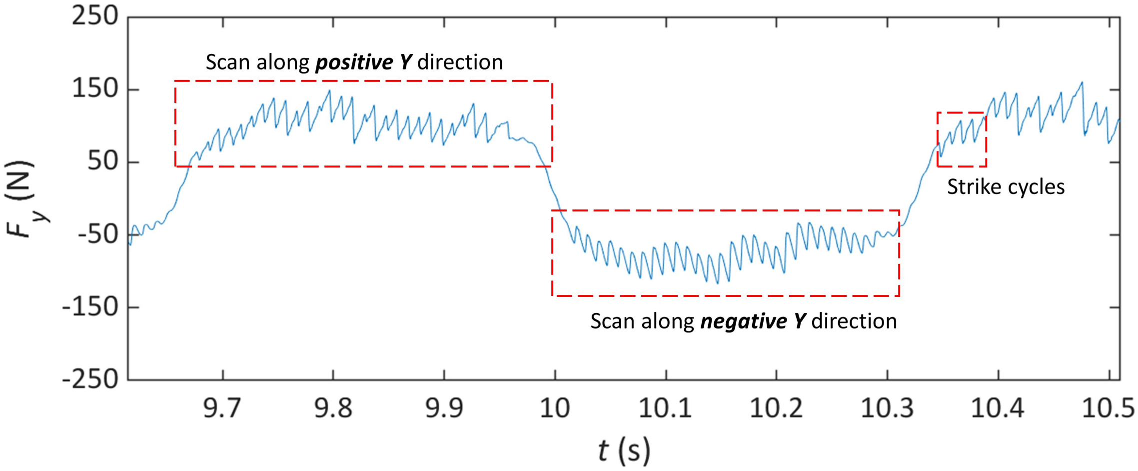

Figure 6.34 Part of sliding force history under the condition of d = 0.5 mm and F_p = 600 N.

stack and the striking tool. The above results show that a proper tool diameter is not as small as possible, and a proper preload is not as large as possible. A reasonable combination of the two factors is essential for obtaining a desirable surface finish. When one wants to obtain intrinsic roughness in the second stage of Phase I, a smaller tool diameter is better, but the preload cannot be chosen too large. If a deflection occurs, the tool diameter can be appropriately increased, thereby increasing the preload's selection range. The new combination may also play an equivalent role in improving surface roughness. Moreover, the sliding force can be used to monitor the deflection of the striking tool with a specific diameter in real-time to decrease the risk of damage to the PVST device assembly.

6.7.5 Effect of the number of passes on surface deformation in multiple passes

The optimal Sa from the above results is achieved under the condition of f = 100 Hz, V_{pp} = 60 V, v_s = 1000 mm/min, d = 0.5 mm, and F_p = 1000 N, using the interweaving scan strategy in Stage II of Phase I (Stage I of Phase I condition: f = 100 Hz, V_{pp} = 150 V, v_s = 1000 mm/min, d = 0.5 mm, and F_p = 400 N). Before applying the smoothing of Phase II on the treated surface from Stage II, a third pass is adopted to see whether it can further reduce the surface roughness in the second stage of Phase I. This third pass method is based on the idea that more repeat passes can remove more rough features if the new pass can strike on a different location to cover more unaffected areas. Therefore, four strategies are proposed to implement the third pass.

1) Use a parallel scan strategy for the third pass and follow the same experimental conditions in

the previous pass.

2) Use a parallel scan strategy for the third pass and follow the same experimental conditions in the previous pass except for readjusting the Z value to maintain the preload used in the previous pass; The reason for readjusting the Z value to get the same preload is because the second pass already changes the surface features, and the old preload setting does not work for the third pass.
3) Use an interweaving scan strategy for the third pass and follow the same experimental conditions in the previous pass.
4) Use an interweaving scan strategy for the third pass and follow the same experimental conditions in the previous pass except for Z value readjustment.

The results correspond to the four strategies can be seen in Fig. 6.32 and Table 6.5, which are No. 22, No. 23, No. 20, and No. 19, respectively. No. 21 is the reference (two passes treatment) for Strategy 1 and Strategy 2, and No. 24 for Strategy 3 and 4. Table 6.6 summarizes the Sa values from these strategies. The results show that the third pass generally does not improve surface roughness positively, except that Strategy 1 does improve the reference surface roughness slightly It is observed that applying the Z value adjustment creates a worse surface roughness. This is reasonable because the Z value adjustment likely increases the intrinsic roughness.

Table 6.6 Summary of Sa values under different strategies for the third pass.

Strategy	3rd Pass Sa (μm)	2nd Pass Sa (μm)
(1) Parallel + No Z adjustment	4.1	4.6
(2) Parallel + Z adjustment	4.7	4.6
(3) Interweaving + No Z adjustment	4.0	3.7
(4) Interweaving + Z adjustment	4.2	3.7

Overall, the above results indicate that it is not necessary to implement a third pass that is similar to the pass in Stage II of Phase I. In this regard, the smoothing in Phase II can be directly used for further improvement.

6.8 Conclusions

This chapter has experimentally explored the non-resonant PVST emphasizing striking force, surface texture, and surface finish of AM metal parts under various process parameters, including vibration frequency, scan speed, driving voltage, tool diameter, engagement distance, and multiple passes. It can be concluded that:

1) PVST can induce surface plastic deformation to improve the surface finish of the initially rough surface at different levels by controlling process parameters. Two surface texture patterns are found: scattered pattern consisting of scattered treated and untreated areas and uniform pattern with uniform treated areas throughout the surface.
2) Higher frequency results in lower vibration amplitude of the striking tool, causing a more significant surface height difference between the flattened top layer and the rough bottom layer. This difference dominates the computation of surface finish over the overlap effect of successive indentations by varying vibration frequency. Larger height difference results in less unaffected rough features, hence the surface roughness is larger.
3) Scan speed controls the overlap distribution density of the indentations and is proportional to surface roughness. A larger driving voltage generates a more extensive vibration amplitude and more substantial striking effect, decreasing the surface roughness.
4) Smaller tool diameter improves the surface finish and makes it easier to realize the uniform surface texture. A uniform pattern occurs only at small tool diameter conditions. A large uniform area with the same level of surface height at these conditions indicates the uniformity and flatness of the treated area, significantly reducing surface roughness. The effect of tool diameter on the surface finish is opposite on the initially rough surface compared to the initially smooth surface.
5) Negative engagement distance is crucial to apply a compression-sliding type of deformation to achieve a uniform pattern. Combined with a small tool diameter, the large engagement distance enables the tool to reach the bottom of the roughness layer and creates intrinsic roughness. The peak-to-valley roughness can be used as a starting engagement distance

if the corresponding preload is reasonable. A considerable engagement distance and the compression-sliding type of deformation in PVST are necessary for a significant surface finish improvement.

6) Large striking depth is more desirable than indentation overlap density to improve surface finish. A combination of small tool diameter, large preload, and large driving voltage can generate large striking depth to remove more rough features.
7) The relationship between surface roughness and striking force is linearly at large tool diameter conditions and nonlinear at small diameter conditions. The ratio of indentation depth to tool diameter increases when tool diameter decreases, increasing the nonlinearity. The relationships are beneficial for monitoring surface roughness in real time from force signals.
8) A multiple-pass process can overcome the maximum force range limitation of the actuation device. It enables PVST to be applied in multiple passes to avoid overlarge striking force and accumulate surface finish improvement. Two phases are considered. Phase I reduces the surface finish to a specific level by compression-sliding deformation. Phase II focuses on smoothing the treated surface to a target finish.
9) The driving voltage does not significantly affect surface roughness in the multiple-pass process. The interweaving scan strategy is better than the parallel scan strategy for smoothing more ridges. A combined effect of a large preload and small tool diameter is critical to creating intrinsic roughness, but deflection can occur if the preload is too large. The third pass does not improve the surface finish in the second stage of Phase I.
10) Equivalent surface roughness can be achieved by combining moderate preload and small tool diameter or large preload and large tool diameter. However, their mechanisms for improving surface roughness are different.

CHAPTER 7

CONCLUSIONS AND FUTURE WORK

In summary, this dissertation presents the design, characterization, and application scenarios (initially smooth and rough surfaces) of piezo vibration striking treatment (PVST) in the mechanical surface treatment field through plastic deformation. The results from the four experiments demonstrate the feasibility and excellent controllability of PVST in terms of force and displacement monitoring and surface deformation control. PVST can induce strikes with consistent intensity in each cycle of tool vibration. The striking intensity and striking location can be well controlled, leading to improved control of surface plastic deformation induced by the treatment. The essential process parameters for PVST are tool vertical position, tool vibration frequency and amplitude (driving voltage), striking overlap ratio (scan speed), striking tool diameter, and tool scan path. Combining a piezo stack actuated vibration device with a CNC machine allows these process parameters to be directly or indirectly controlled and monitored in real time. The piezo stack vibration device generally controls the tool vibration frequency and amplitude. In contrast, the CNC machine controls tool position in the Z direction and tool scan motion (speed and path). The control of tool vibration and tool vertical position is critical for controlling the local surface deformation imposed by each individual strike. In contrast, controlling tool scan motion is critical for controlling the locations and layout of successive strikes. Such coordinated process controllability will lead to enhanced controllable surface deformation beyond the capability of current striking-based treatment processes, such as SP, SMAT, MHP, and UNSM. Consequently, PVST has the potential to realize more efficient deformation-based surface engineering, including finish, residual stress, hardness, and microstructure, for enhancing components' performance, such as fatigue life and wear resistance.

In this dissertation, the current research only presents these results in conventionally and additively manufactured metals and specific experimental setups. However, the potential of non-resonant vibration combined with CNC control or robot arms is foreseeable. They can be further applied to surface treatment systems or manufacturing processes to improve the surface quality and material properties of the manufactured components, which will be helpful for rapid development in the novel manufacturing industry.

The following future work is recommended within the scope of novel surface treatment and advanced manufacturing using piezo vibration striking treatment.

- Force monitoring and feedback control using PVST can be implemented by extending the current design to integrate a force sensor with the PVST device assembly. In that case, the force signals are synchronized inside the PVST system instead of using an additional dynamometer to record the force.
- Material properties after PVST, such as strength, hardness, residual stress distribution, microstructure, sub-surface properties, and fatigue life, should be further investigated using the current PVST process.
- The verification of the smoothing effect in Phase II of the multiple-pass process needs to be conducted to achieve an optimal condition to reach a surface finish level below ~ 1 μm.
- It is promising to use PVST as a pre-processing method for those superfinishing processes, such as MAF, to explore their combined effect on getting a desirable surface finish.
- PVST can also be integrated into additive manufacturing processes to strike the surface for each printed layer, which will help densify the layer and reduce the porosity and volumetric defects in the process.

BIBLIOGRAPHY

[1] R. M'saoubi, J. Outeiro, H. Chandrasekaran, O. Dillon Jr, and I. Jawahir, "A review of surface integrity in machining and its impact on functional performance and life of machined products," *International Journal of Sustainable Manufacturing*, vol. 1, no. 1-2, pp. 203–236, 2008.

[2] J. P. Davim, *Machining*. London: Springer, 2008.

[3] M. A. A. Khan, M. Hussain, S. K. Lodhi, B. Zazoum, M. Asad, and A. Afzal, "Green Metalworking Fluids for Sustainable Machining Operations and Other Sustainable Systems: A Review," *Metals (2075-4701)*, vol. 12, pp. 1466–N.PAG, Sept. 2022.

[4] T. . . . Taib, M. . . Johan, 3), and W. . . . Basirun, "Enhanced Optical and Ragged Metamaterials Properties of Silver Silica Nanocomposite Thin Film via Sol-Gel and Electrophoresis Deposition Technique," *Journal of Nano Research*, vol. 74, pp. 11–24, Jan. 2022. Num Pages: 24 Publisher: Trans Tech Publications Ltd 11.

[5] O. A. Abonosimov, S. I. Lazarev, P. A. Khokhlov, and V. V. Mamontov, "Tubular Electrobaromembrane Apparatus Having Uniform Filtration Area for Electroplating Wastewater Treatment and Method for Its Calculation," *Chemical & Petroleum Engineering*, vol. 58, pp. 202–206, July 2022.

[6] C. Gosselin, "METALLIC AND PEARLESCENT PIGMENTS: for Powder Coatings," *CoatingsTech*, vol. 19, pp. 54–60, Sept. 2022.

[7] F. Abroug, E. Pessard, G. Germain, and F. Morel, "Effect of end milling, grinding and tartaric-sulfuric anodizing on the fatigue behavior of AA7050 alloy," *The International Journal of Advanced Manufacturing Technology*, pp. 1–20, Sept. 2022. Place: London Publisher: Springer London.

[8] M. Hein, "Influence of Physical Vapor Deposition on High-Cycle Fatigue Performance of Additively Manufactured Ti-6Al-7Nb Alloy," *Crystals (2073-4352)*, vol. 12, pp. N.PAG–N.PAG, Sept. 2022.

[9] H. S. Farwaha, D. Deepak, and G. S. Brar, "Investigation of a novel ultrasonically aided electrochemical magnetic abrasive machining process for SS 316L," *The International Journal of Advanced Manufacturing Technology*, pp. 1–17, Sept. 2022. Place: London Publisher: Springer London.

[10] J. Lu, Z. Ma, and X. Lv, "Study on Polishing of Polycrystalline AlN Using Sol–Gel Polishing Tool," *IEEE Transactions on Semiconductor Manufacturing, Semiconductor Manufacturing, IEEE Transactions on, IEEE Trans. Semicond. Manufact.*, vol. 35, pp. 641–649, Nov. 2022. Publisher: IEEE.

[11] S. Jiang, D. Guo, L. Zhang, K. Li, B. Song, and Y. Huang, "Electropolishing-enhanced, high-precision 3D printing of metallic pentamode metamaterials," *Materials & Design*, vol. 223, Nov. 2022. Publisher: Elsevier Ltd.

[12] Y. Nogi, S. Sakaino, and T. Tsuji, “Force Control of Grinding Process Based on Frequency Analysis,” *IEEE Robotics and Automation Letters, Robotics and Automation Letters, IEEE, IEEE Robot. Autom. Lett.*, vol. 7, pp. 3250–3256, Apr. 2022. Publisher: IEEE.

[13] I. . . . Qasem, A. . . . Hussien, A. . . . Janvekar, P. . . . Kataraki, M. . . . Pracki, and M. . . . Abdul Mujeebu, “Experimental study for optimizing superfinishing process parameters of high-quality alloy bearing steel,” *Surface Topography: Metrology and Properties*, vol. 10, Sept. 2022. Publisher: Institute of Physics.

[14] B. Poudel, P.-H. Lee, G. Song, H. Nguyen, K. Kim, K. Jung, C. Shao, P. Kwon, and H. Chung, “Innovative Magnetic-Field Assisted Finishing (MAF) Using Nano-Scale Solid Lubricant: A Case Study on Mold Steel,” *International Journal of Precision Engineering and Manufacturing-Green Technology*, vol. 9, Nov. 2021.

[15] S. o. M. Engineers, *Tool and Manufacturing Engineers Handbook Vol 7: Continuous Improvement*. Dearborn, Mich: Society of Manufacturing Engineers, 4th edition ed., Sept. 1993.

[16] H. Huang, Z. Wang, J. Gan, Y. Yang, X. Wang, J. He, and X. Gan, “The study of universality of a method for predicting surface nanocrystallization after high energy shot peening based on finite element analysis,” *Surface and Coatings Technology*, vol. 358, pp. 617–627, Jan. 2019.

[17] M. Torres and H. Voorwald, “An evaluation of shot peening, residual stress and stress relaxation on the fatigue life of aisi 4340 steel,” *International Journal of Fatigue*, vol. 24, no. 8, pp. 877–886, 2002.

[18] S. Tekeli, “Enhancement of fatigue strength of sae 9245 steel by shot peening,” *Materials letters*, vol. 57, no. 3, pp. 604–608, 2002.

[19] Y. F. Al-Obaid, “Shot peening mechanics: experimental and theoretical analysis,” *Mechanics of Materials*, vol. 19, pp. 251–260, Jan. 1995.

[20] M. Kobayashi, T. Matsui, and Y. Murakami, “Mechanism of creation of compressive residual stress by shot peening,” *International Journal of Fatigue*, vol. 20, pp. 351–357, May 1998.

[21] S. Bagherifard, R. Ghelichi, and M. Guagliano, “A numerical model of severe shot peening (SSP) to predict the generation of a nanostructured surface layer of material,” *Surface and Coatings Technology*, vol. 204, pp. 4081–4090, Sept. 2010.

[22] M. P. Nascimento, R. C. Souza, W. L. Pigatin, and H. J. C. Voorwald, “Effects of surface treatments on the fatigue strength of AISI 4340 aeronautical steel,” *International Journal of Fatigue*, vol. 23, pp. 607–618, Aug. 2001.

[23] G. Lu, Y. Song, R. Wang, Q. Wang, and X. Wang, “Numerical Simulation of 300M Steel Residual Stress Field Caused by Shot-peening,” *China Surface Engineering*, vol. 26, pp. 72–76, Aug. 2013.

[24] N. Ben Salah, "Shot Peening Applications and Future Research in the Aerospace Industry," in *International Conference on Shot peening At Montreal, Canada*, vol. 13, Sept. 2017.

[25] S. Wang, Y. Li, M. Yao, and R. Wang, "Compressive residual stress introduced by shot peening," *Journal of Materials Processing Technology*, vol. 73, no. 1-3, pp. 64–73, 1998.

[26] S. Wang, Y. Li, M. Yao, and R. Wang, "Fatigue limits of shot-peened metals," *Journal of Materials Processing Technology*, vol. 73, no. 1-3, pp. 57–63, 1998.

[27] K. Lu and J. Lu, "Nanostructured surface layer on metallic materials induced by surface mechanical attrition treatment," *Materials Science and Engineering: A*, vol. 375-377, pp. 38–45, July 2004.

[28] T. Roland, D. Retraint, K. Lu, and J. Lu, "Fatigue life improvement through surface nanostructuring of stainless steel by means of surface mechanical attrition treatment," *Scripta Materialia*, vol. 54, no. 11, pp. 1949–1954, 2006.

[29] N. Tao, Z. Wang, W. Tong, M. Sui, J. Lu, and K. Lu, "An investigation of surface nanocrystallization mechanism in fe induced by surface mechanical attrition treatment," *Acta materialia*, vol. 50, no. 18, pp. 4603–4616, 2002.

[30] S. Manchoul, R. Seddik, R. Ben Sghaeir, and R. Fathallah, "Finite element modeling of ultrasonic and conventional shot peening: A comparison of the effect of both processes on surface conditions," *Proceedings of the Institution of Mechanical Engineers, Part L: Journal of Materials: Design and Applications*, vol. 233, pp. 930–941, May 2019. Publisher: SAGE Publications.

[31] T. Chaise, J. Li, D. Nélias, R. Kubler, S. Taheri, G. Douchet, V. Robin, and P. Gilles, "Modelling of multiple impacts for the prediction of distortions and residual stresses induced by ultrasonic shot peening (USP)," *Journal of Materials Processing Technology*, vol. 212, pp. 2080–2090, Oct. 2012.

[32] T. Rousseau, T. Hoc, P. Gilles, and C. Nouguier-Lehon, "Effect of bead quantity in ultrasonic shot peening: Surface analysis and numerical simulations," *Journal of Materials Processing Technology*, vol. 225, pp. 413–420, Nov. 2015.

[33] J. Marteau, M. Bigerelle, P. E. Mazeran, and S. Bouvier, "Relation between roughness and processing conditions of AISI 316L stainless steel treated by ultrasonic shot peening," *Tribology International*, vol. 82, pp. 319–329, Feb. 2015.

[34] J. Badreddine, S. Remy, M. Micoulaut, E. Rouhaud, V. Desfontaine, and P. Renaud, "CAD based model of ultrasonic shot peening for complex industrial parts," *Advances in Engineering Software*, vol. 76, pp. 31–42, Oct. 2014.

[35] H. C. Yildirim and G. B. Marquis, "Fatigue strength improvement factors for high strength steel welded joints treated by high frequency mechanical impact," *International Journal of Fatigue*, vol. 44, pp. 168–176, Nov. 2012.

[36] M. Malaki and H. Ding, "A review of ultrasonic peening treatment," *Materials & Design*, vol. 87, pp. 1072–1086, 2015.

[37] S. Roy, J. W. Fisher, and B. T. Yen, "Fatigue resistance of welded details enhanced by ultrasonic impact treatment (uit)," *International Journal of Fatigue*, vol. 25, no. 9-11, pp. 1239–1247, 2003.

[38] H. C. Yildirim and G. B. Marquis, "Overview of Fatigue Data for High Frequency Mechanical Impact Treated Welded Joints," *Welding in the World*, vol. 56, pp. 82–96, July 2012.

[39] n. W. Engelhardt, Imke, T. Ummenhofer, T. Nitschke-Pagel, K. Dilger, and H. Eslami, "FATIGUE BEHAVIOUR OF WELDED HIGH-STRENGTH STEELS AFTER HIGH FREQUENCY MECHANICAL POST-WELD TREATMENTS," *Welding in the World, Le Soudage Dans Le Monde*, vol. 53, pp. R322–R332, Nov. 2009.

[40] M. Khurshid, Z. Barsoum, and G. Marquis, "Behavior of Compressive Residual Stresses in High Strength Steel Welds Induced by High Frequency Mechanical Impact Treatment," *Journal of Pressure Vessel Technology*, vol. 136, Apr. 2014.

[41] C. Ernould, J. Schubnell, M. Farajian, A. Maciolek, D. Simunek, M. Leitner, and M. Stoschka, "Application of different simulation approaches to numerically optimize high-frequency mechanical impact (HFMI) post-treatment process," *Welding in the World*, vol. 63, pp. 725–738, May 2019.

[42] E. Mikkola, G. Marquis, P. Lehto, H. Remes, and H. Hänninen, "Material characterization of high-frequency mechanical impact (HFMI)-treated high-strength steel," *Materials & Design*, vol. 89, pp. 205–214, Jan. 2016.

[43] F. Bleicher, C. Lechner, C. Habersohn, E. Kozeschnik, B. Adjassoho, and H. Kaminski, "Mechanism of surface modification using machine hammer peening technology," *CIRP annals*, vol. 61, no. 1, pp. 375–378, 2012.

[44] V. Schulze, F. Bleicher, P. Groche, Y. Guo, and Y. Pyun, "Surface modification by machine hammer peening and burnishing," *Cirp Annals*, vol. 65, no. 2, pp. 809–832, 2016.

[45] X. J. Cao, Y. S. Pyoun, and R. Murakami, "Fatigue properties of a S45C steel subjected to ultrasonic nanocrystal surface modification," *Applied Surface Science*, vol. 256, pp. 6297–6303, Aug. 2010.

[46] C.-M. Suh, G.-H. Song, M.-S. Suh, and Y.-S. Pyoun, "Fatigue and mechanical characteristics of nano-structured tool steel by ultrasonic cold forging technology," *Materials Science and Engineering: A*, vol. 443, no. 1-2, pp. 101–106, 2007.

[47] J. Liu, S. Suslov, S. Li, H. Qin, Z. Ren, G. L. Doll, H. Cong, Y. Dong, and C. Ye, "Electrically Assisted Ultrasonic Nanocrystal Surface Modification of Ti6Al4V Alloy," *Advanced Engineering Materials*, vol. 20, no. 1, p. 1700470, 2018. _eprint: https://onlinelibrary.wiley.com/doi/pdf/10.1002/adem.201700470.

[48] A. Amanov and Y.-S. Pyun, “Local heat treatment with and without ultrasonic nanocrystal surface modification of Ti-6Al-4V alloy: Mechanical and tribological properties,” *Surface and Coatings Technology*, vol. 326, pp. 343–354, Oct. 2017.

[49] F. F., B. S., F. Karimzadeh, and L. SM, “Finite Element Modeling of Ultrasonic Surface Nanocrystallization Process,” *International Journal of Nanotechnology and Nanomedicine Research*, vol. 1, pp. 7–21, Aug. 2017.

[50] J. Berglund, M. Liljengren, and B.-G. Rosén, “On finishing of pressing die surfaces using machine hammer peening,” *The International Journal of Advanced Manufacturing Technology*, vol. 52, no. 1, pp. 115–121, 2011.

[51] R. Mannens, D. Trauth, P. Mattfeld, and F. Klocke, “Influence of impact force, impact angle, and stroke length in machine hammer peening on the surface integrity of the stainless steel x3crnimo13-4,” *Procedia Cirp*, vol. 71, pp. 166–171, 2018.

[52] A. Amanov, I. Cho, Y. Pyoun, C.-S. Lee, and I. Park, “Micro-dimpled surface by ultrasonic nanocrystal surface modification and its tribological effects,” *Wear*, vol. 286, pp. 136–144, 2012.

[53] H.-W. Mindt, O. Desmaison, M. Megahed, A. Peralta, and J. Neumann, “Modeling of Powder Bed Manufacturing Defects,” *Journal of Materials Engineering and Performance*, vol. 27, pp. 32–43, Jan. 2018.

[54] V. P. Kuznetsov, S. Y. Tarasov, and A. I. Dmitriev, “Nanostructuring burnishing and subsurface shear instability,” *Journal of Materials Processing Technology*, vol. 217, pp. 327–335, Mar. 2015.

[55] M. Sanguedolce, G. Rotella, M. R. Saffioti, and L. Filice, “Burnishing of AM materials to obtain high performance part surfaces,” *Journal of Industrial Engineering and Management*, vol. 15, pp. 92–102, Feb. 2022. Number: 1.

[56] R. Raaj, P. Anirudh, K. C, K. Chidambaram, A. Jahagirdar, S. Joshi, and A. S. S. Balan, “Exploring grinding and burnishing as surface post-treatment options for electron beam additive manufactured Alloy 718,” *Surface and Coatings Technology*, vol. 397, p. 126063, June 2020.

[57] B. Denkena, A. Krödel, S. Heikebrügge, K. Meyer, and P. Pillkahn, “Surface topography after deep rolling with milling kinematics,” *Production Engineering*, vol. 15, pp. 587–593, June 2021.

[58] S. Sunny, R. Mathews, H. Yu, and A. Malik, “Effects of microstructure and inherent stress on residual stress induced during powder bed fusion with roller burnishing,” *International Journal of Mechanical Sciences*, vol. 219, p. 107092, Apr. 2022.

[59] D. Meyer and N. Wielki, “Internal reinforced domains by intermediate deep rolling in additive manufacturing,” *CIRP Annals*, vol. 68, pp. 579–582, Jan. 2019.

[60] B. AlMangour and J.-M. Yang, “Improving the surface quality and mechanical properties by shot-peening of 17-4 stainless steel fabricated by additive manufacturing,” *Materials & Design*, vol. 110, pp. 914–924, Nov. 2016.

[61] N. E. Uzan, S. Ramati, R. Shneck, N. Frage, and O. Yeheskel, “On the effect of shot-peening on fatigue resistance of AlSi10Mg specimens fabricated by additive manufacturing using selective laser melting (AM-SLM),” *Additive Manufacturing*, vol. 21, pp. 458–464, May 2018.

[62] S. Slawik, S. Bernarding, F. Lasagni, C. Navarro, A. Periñán, F. Boby, S. Migot-Choux, J. Domínguez, and F. Mücklich, “Microstructural analysis of selective laser melted Ti6Al4V modified by laser peening and shot peening for enhanced fatigue characteristics,” *Materials Characterization*, vol. 173, p. 110935, Mar. 2021.

[63] Q. Portella, M. Chemkhi, and D. Retraint, “Influence of Surface Mechanical Attrition Treatment (SMAT) post-treatment on microstructural, mechanical and tensile behaviour of additive manufactured AISI 316L,” *Materials Characterization*, vol. 167, p. 110463, June 2020.

[64] X. Yan, S. Yin, C. Chen, R. Jenkins, R. Lupoi, R. Bolot, W. Ma, M. Kuang, H. Liao, J. Lu, and M. Liu, “Fatigue strength improvement of selective laser melted Ti6Al4V using ultrasonic surface mechanical attrition,” *Materials Research Letters*, vol. 7, pp. 327–333, Aug. 2019. Publisher: Taylor & Francis _eprint: https://doi.org/10.1080/21663831.2019.1609110.

[65] Y. Wang and J. Shi, “Microstructure and Properties of Inconel 718 Fabricated by Directed Energy Deposition with In-Situ Ultrasonic Impact Peening,” *Metallurgical and Materials Transactions B*, vol. 50, pp. 2815–2827, Dec. 2019.

[66] H. Zhang, R. Chiang, H. Qin, Z. Ren, X. Hou, D. Lin, G. L. Doll, V. K. Vasudevan, Y. Dong, and C. Ye, “The effects of ultrasonic nanocrystal surface modification on the fatigue performance of 3D-printed Ti64,” *International Journal of Fatigue*, vol. 103, pp. 136–146, Oct. 2017.

[67] K. T. Kim and Y. S. Kim, “The Effect of the Static Load in the UNSM Process on the Corrosion Properties of Alloy 600,” *Materials (Basel, Switzerland)*, vol. 12, p. E3165, Sept. 2019.

[68] G. Telljohann and S. Dannemeyer, “Hifit–technische entwicklung und anwendung,” *Stahlbau*, vol. 78, no. 9, pp. 622–626, 2009.

[69] Y. Altintas, “Manufacturing Automation: Metal Cutting Mechanics, Machine Tool Vibrations, and CNC Design,” Jan. 2012. ISBN: 9780511843723 Publisher: Cambridge University Press.

[70] Y. Guo, C. Saldana, W. D. Compton, and S. Chandrasekar, “Controlling deformation and microstructure on machined surfaces,” *Acta materialia*, vol. 59, no. 11, pp. 4538–4547, 2011.

[71] Y. Guo, S. E. Lee, and J. B. Mann, “Piezo-actuated modulation-assisted drilling system with integrated force sensing,” *Journal of Manufacturing Science and Engineering*, vol. 139, no. 1, 2017.

[72] Y. Guo and J. B. Mann, “Control of chip formation and improved chip ejection in drilling with modulation-assisted machining,” *Journal of Manufacturing Science and Engineering*, vol. 142, no. 7, p. 071001, 2020.

[73] Y. Guo, T. Stalbaum, J. Mann, H. Yeung, and S. Chandrasekar, “Modulation-assisted high speed machining of compacted graphite iron (cgi),” *Journal of Manufacturing Processes*, vol. 15, no. 4, pp. 426–431, 2013.

[74] B. G. Scuracchio, N. B. de Lima, and C. G. Schön, “Role of residual stresses induced by double peening on fatigue durability of automotive leaf springs,” *Materials & Design*, vol. 47, pp. 672–676, May 2013.

[75] K. J. Kirkhope, R. Bell, L. Caron, R. I. Basu, and K. T. Ma, “Weld detail fatigue life improvement techniques. Part 2: application to ship structures,” *Marine Structures*, vol. 12, pp. 477–496, Aug. 1999.

[76] T. Deguchi, M. Mouri, J. Hara, D. Kano, T. Shimoda, F. Inamura, T. Fukuoka, and K. Koshio, “Fatigue strength improvement for ship structures by Ultrasonic Peening,” *Journal of Marine Science and Technology*, vol. 17, pp. 360–369, Sept. 2012.

[77] Y. Todaka, M. Umemoto, and K. Tsuchiya, “Comparison of Nanocrystalline Surface Layer in Steels Formed by Air Blast and Ultrasonic Shot Peening,” *Materials Transactions*, vol. 45, no. 2, pp. 376–379, 2004.

[78] C. Wang, L. Yongbin, W. Long, and W. Chuanli, “Dislocation-based study on the influences of shot peening on fatigue resistance,” *Surface and Coatings Technology*, vol. 383, p. 125247, Dec. 2019.

[79] N. R. Tao, M. L. Sui, J. Lu, and K. Lua, “Surface nanocrystallization of iron induced by ultrasonic shot peening,” *Nanostructured Materials*, vol. 11, pp. 433–440, June 1999.

[80] X. Wu, N. Tao, Y. Hong, B. Xu, J. Lu, and K. Lu, “Microstructure and evolution of mechanically-induced ultrafine grain in surface layer of AL-alloy subjected to USSP,” *Acta Materialia*, vol. 50, pp. 2075–2084, May 2002.

[81] S. Manchoul, R. Seddik, R. B. Sghaier, and R. Fathallah, “Prediction and comparison of high-cycle fatigue behavior of ultrasonic and conventional shot-peened parts,” *The International Journal of Advanced Manufacturing Technology*, vol. 103, pp. 2091–2108, Aug. 2019.

[82] F. Yin, L. Hua, X. Wang, M. Rakita, and Q. Han, “Numerical modelling and experimental approach for surface morphology evaluation during ultrasonic shot peening,” *Computational Materials Science*, vol. 92, pp. 28–35, Sept. 2014.

[83] K. Dai, J. Villegas, and L. Shaw, “An analytical model of the surface roughness of an aluminum alloy treated with a surface nanocrystallization and hardening process,” *Scripta Materialia*, vol. 52, pp. 259–263, Feb. 2005.

[84] L. Dai, J. Villegas, Z. Stone, and L. Shaw, “Finite element modeling of the surface roughness of 5052 Al alloy subjected to a surface severe plastic deformation process,” *Acta Materialia*, vol. 52, pp. 5771–5782, Dec. 2004.

[85] S. Manchoul, R. Seddik, R. Grissa, R. B. Sghaier, and R. Fathallah, “A predictive approach to investigate the effect of ultrasonic shot peening on a high-cycle fatigue performance of an AISI 316L target,” *The International Journal of Advanced Manufacturing Technology*, vol. 95, pp. 3437–3451, Apr. 2018.

[86] R. Seddik, A. Bahloul, A. Atig, and R. Fathallah, “A simple methodology to optimize shot-peening process parameters using finite element simulations,” *The International Journal of Advanced Manufacturing Technology*, vol. 90, pp. 2345–2361, May 2017.

[87] J. Berg and N. Stranghöner, “Fatigue Strength of Welded Ultra High Strength Steels Improved by High Frequency Hammer Peening,” *Procedia Materials Science*, vol. 3, pp. 71–76, Dec. 2014.

[88] H. C. Yıldırım, G. Marquis, and C. M. Sonsino, “Lightweight design with welded high-frequency mechanical impact (HFMI) treated high-strength steel joints from S700 under constant and variable amplitude loadings,” *International Journal of Fatigue*, vol. 91, pp. 466–474, Oct. 2016.

[89] M. Leitner, M. Stoschka, and W. Eichlseder, “Fatigue enhancement of thin-walled, high-strength steel joints by high-frequency mechanical impact treatment,” *Welding in the World*, vol. 58, pp. 29–39, Jan. 2014.

[90] C. Ernould, J. Schubnell, and M. Farajian, “Numerical Simulation of Pin Kinetic and its Influence on the Material Hardening, Residual Stress Field and Topography during High Frequency Mechanical Impact (HFMI) Treatment,” Mar. 2017.

[91] H. Yıldırım and G. Marquis, “A round robin study of high-frequency mechanical impact (HFMI)-treated welded joints subjected to variable amplitude loading,” *Welding in the World*, vol. 57, May 2013.

[92] M. Leitner, S. Gerstbrein, M. Ottersböck, and M. Stoschka, “Fatigue Strength of HFMI-treated High-strength Steel Joints under Constant and Variable Amplitude Block Loading,” *Procedia Engineering*, vol. 101, Dec. 2015.

[93] G. Marquis and Z. Barsoum, “Fatigue strength improvement of steel structures by high-frequency mechanical impact: proposed procedures and quality assurance guidelines,” *Welding in the World*, vol. 58, pp. 19–28, Jan. 2014.

[94] R. Tehrani Yekta, K. Ghahremani, and S. Walbridge, “Effect of quality control parameter variations on the fatigue performance of ultrasonic impact treated welds,” *International Journal of Fatigue*, vol. 55, pp. 245–256, Oct. 2013.

[95] Y. Feng, S. Hu, D. Wang, and H. Zhang, “Influence of surface topography and needle size on surface quality of steel plates treated by ultrasonic peening,” *Vacuum*, vol. 132, pp. 22–30, Oct. 2016.

[96] C. Ma, Y. Dong, and C. Ye, “Improving Surface Finish of 3D-printed Metals by Ultrasonic Nanocrystal Surface Modification,” *Procedia CIRP*, vol. 45, pp. 319–322, Dec. 2016.

[97] M. Khan, M. Fitzpatrick, Q. Wang, Y. Pyoun, and A. Amanov, “Effect of ultrasonic nanocrystal surface modification on residual stress and fatigue cracking in engineering alloys,” *Fatigue & Fracture of Engineering Materials & Structures*, vol. 41, no. 4, pp. 844–855, 2018. _eprint: https://onlinelibrary.wiley.com/doi/pdf/10.1111/ffe.12732.

[98] C. Ye, A. Telang, A. S. Gill, S. Suslov, Y. Idell, K. Zweiacker, J. M. K. Wiezorek, Z. Zhou, D. Qian, S. R. Mannava, and V. K. Vasudevan, “Gradient nanostructure and residual stresses induced by Ultrasonic Nano-crystal Surface Modification in 304 austenitic stainless steel for high strength and high ductility,” *Materials Science and Engineering: A*, vol. 613, pp. 274–288, Sept. 2014.

[99] M. Kattoura, S. R. Mannava, D. Qian, and V. K. Vasudevan, “Effect of ultrasonic nanocrystal surface modification on elevated temperature residual stress, microstructure, and fatigue behavior of ATI 718Plus alloy,” *International Journal of Fatigue*, vol. 110, pp. 186–196, May 2018.

[100] M.-s. Kim, W.-j. Oh, G.-y. Baek, Y.-k. Jo, K.-y. Lee, S.-h. Park, and D.-s. Shim, “Ultrasonic nanocrystal surface modification of high-speed tool steel (AISI M4) layered via direct energy deposition,” *Journal of Materials Processing Technology*, vol. 277, p. 116420, Mar. 2020.

[101] Y. Kuilin and Y. Sumi, “Modelling of ultrasonic impact treatment (UIT) of welded joints and its effect on fatigue strength,” *Frattura ed Integrità Strutturale*, pp. 476–486, Oct. 2015.

[102] J. Foehrenbach, V. Hardenacke, and M. Farajian, “High frequency mechanical impact treatment (HFMI) for the fatigue improvement: numerical and experimental investigations to describe the condition in the surface layer,” *Welding in the World*, vol. 60, pp. 749–755, July 2016.

[103] J. Föhrenbach and T. Seifert, *Fatigue life prediction of High Frequency Mechanical Impact (HFMI) treated welded joints: by numerical simulation and damage mechanics approaches : Master Thesis im Fachgebiet Mechanical Engineering*. Fraunhofer Institute for Mechanics of Materials IWM, 2015. OCLC: 1011087119.

[104] B. N. Mordyuk and G. I. Prokopenko, “Ultrasonic impact peening for the surface properties' management,” *Journal of Sound and Vibration*, vol. 308, pp. 855–866, Dec. 2007.

[105] B. N. Mordyuk, G. I. Prokopenko, P. Y. Volosevich, L. E. Matokhnyuk, A. V. Byalonovich, and T. V. Popova, “Improved fatigue behavior of low-carbon steel 20GL by applying ultrasonic impact treatment combined with the electric discharge surface alloying,” *Materials Science and Engineering: A*, vol. 659, pp. 119–129, Apr. 2016.

[106] S. Hu, C. Guo, D. Wang, Z.-J. Wang, and C. Huang, “Finite element analysis of residual stress evolution with multiple impacts on one point in ultrasonic impact treatment process,” *Proceedings of the Institution of Mechanical Engineers, Part B: Journal of Engineering Manufacture*, vol. 232, Sept. 2016.

[107] H.-P. Günther, U. Kuhlmann, and A. Dürr, “Rehabilitation of Welded Joints by Ultrasonic Impact Treatment (UIT),” *IABSE Symposium Report*, vol. 90, pp. 71–77, Jan. 2005.

[108] Y. N. Petrov, G. I. Prokopenko, B. N. Mordyuk, M. A. Vasylyev, S. M. Voloshko, V. S. Skorodzievski, and V. S. Filatova, “Influence of microstructural modifications induced by ultrasonic impact treatment on hardening and corrosion behavior of wrought Co-Cr-Mo biomedical alloy,” *Materials Science & Engineering. C, Materials for Biological Applications*, vol. 58, pp. 1024–1035, Jan. 2016.

[109] H. Park, J. Kim, Y. Pyun, A. Auezhan, and Y. S. Choi, “Numerical and Experimental Studies on Subscale Behaviors of Ultrasonic Surface Peening,” *Metals and Materials International*, vol. 25, pp. 606–616, May 2019.

[110] C. Ma, H. Qin, Z. Ren, S. C. O’Keeffe, J. Stevick, G. L. Doll, Y. Dong, B. Winiarski, and C. Ye, “Increasing fracture strength in bulk metallic glasses using ultrasonic nanocrystal surface modification,” *Journal of Alloys and Compounds*, vol. 718, pp. 246–253, Sept. 2017.

[111] J. T. Inc., “Surface roughness measurement and symbol - JRY Technology.”

[112] C. In Sik, C.-S. Lee, C.-H. Choi, H.-G. Lee, M. Lee, and Y. Jeon, “Effect of the Ultrasonic Nanocrystalline Surface Modification (UNSM) on Bulk and 3D-Printed AISI H13 Tool Steels,” *Metals*, vol. 7, p. 510, Nov. 2017.

[113] J. Schubnell, C. Eichheimer, C. Ernould, A. Maciolek, J. Rebelo-Kornmeier, and M. Farajian, “The influence of coverage for high frequency mechanical impact treatment of different steel grades,” *Journal of Materials Processing Technology*, vol. 277, p. 116437, Mar. 2020.

[114] D. Tabor, “A simple theory of static and dynamic hardness,” *Ser. A. Math. Phys. Sci.*, vol. 192, no. 1029, 1948.

[115] J. Chen, Y. Xu, P. Kwon, and Y. Guo, “A preliminary study on improving surface finish of electron beam melted Ti-6Al-4V using piezo vibration striking treatment,” *Manufacturing Letters*, vol. 33, pp. 461–468, Sept. 2022.